The Dissertation Committee for Mingsong Wang Certifies that this is the approved version of the following Dissertation:

Hybrid Systems of Plasmonic Nanostructures and Functional Materials for Light-Matter Interactions and Active Plasmonic Devices

Committee:

Yuebing Zheng, Supervisor

Adela Ben-Yakar

Delia Milliron

Wei Li

Hybrid Systems of Plasmonic Nanostructures and Functional Materials for Light-Matter Interactions and Active Plasmonic Devices

by

Mingsong Wang

Dissertation

Presented to the Faculty of the Graduate School of

The University of Texas at Austin

in Partial Fulfillment

of the Requirements

for the Degree of

Doctor of Philosophy

The University of Texas at Austin

August 2018

Dedication

To my parents for their endless love and support

Acknowledgements

First, I would like to express my sincerest gratitude to my advisor, Professor Yuebing Zheng, for his constant guidance and support to my journey to a doctoral degree. Under his supervision, I learned invaluable lessons of how to generate insightful ideas and conduct good researches. Furthermore, Dr. Yuebing Zheng has set me a good example of how to build a successful career and become an inspiring leader.

I also want to thank the members of my dissertation committee: Dr. Adela Ben-Yakar, Dr. Delia Milliron and Dr. Wei Li for their constructive guidance to my research projects, and my collaborators: Dr. Andrea Alù, Dr. Alex Krasnok, Dr. Andrew Dunn, Dr. Chong Xie, Dr. Deji Akinwande, Dr. Gyeong Hwang, Dr. Luis M. Liz-Marzán, Dr. Mauricio Terrones, Dr. Leonardo Scarabell, Dr. Evan P. Perillo, Dr. Jeremy W. Jarrett, Dr. Xiaoling Wei, He Liu, Gregory Hartmann, Wei Li and Tianyi Zhang for their tremendous help for providing me important materials, theoretical analysis and technical assistance. I would also like to express my thanks to all group members in Zheng research group, including Dr. Linhan Lin, Dr. Jiayong Gan, Dr. Abhay Kotnala, Dr. Eric Hill, Dr. Kan Yao, Dr. Zilong Wu, Bharath Bangalore Rajeeva, Xiaolei Peng, Yaoran Liu, Jingang Li and Pavana Kollipara, for their helps and efforts to make our group a great team.

I also acknowledge the Beckman Young Investigator Program, the Office of Naval Research Young Investigator Program (N00014-17-1-2424), National Science Foundation (CBET-1704634), GS University Graduate Continuing Fellowship and the Texas Advanced Computing Center (TACC) at The University of Texas at Austin for supporting my studies.

Finally, I want to express my deepest gratitude to my parents. They not only gave me life, but also taught me how to become a man of wisdom, courage, responsibility and benevolence. Without their endless support and unconditional love, I wouldn't have the opportunity to come to America for pursuing my doctoral degree and make my dream come true.

Abstract

Hybrid Systems of Plasmonic Nanostructures and Functional Materials for Light-Matter Interactions and Active Plasmonic Devices

Mingsong Wang, PhD

The University of Texas at Austin, 2018

Supervisor: Yuebing Zheng

Advances in nanofabrication and characterization of nanomaterials enable the development of plasmonic nanostructures with unique optical properties. Plasmonic nanostructures have been extensively studied for their potential applications in optical sensing, photothermal therapy, photovoltaics, and photocatalysis. In this dissertation, we present studies of light-matter interactions in hybrid systems consisting of plasmonic nanostructures and functional materials. These studies are focused on four major types of light-matter interactions in plasmonic nanostructures: (1) plasmon-induced resonance energy transfer (PIRET); (2) plasmon-enhanced spontaneous emission; (3) Fano interference between plasmonic nanostructures and emitters; and (4) strong plasmon-exciton coupling. We also achieved the tuning of light-matter interactions by modifying the physical properties of functional materials or plasmonic nanostructures. In addition, the active control of light-matter interactions was demonstrated by integrating plasmonic nanostructures with switchable materials, such as photochromic dyes.

Specifically, we first demonstrated the blue-shifted PIRET from a single gold nanorod (AuNR) to dye molecules. AuNRs enable the energy transfer from plasmonic

donors to dye acceptors with light having a longer wavelength and lower intensity, compared to dye donors. Secondly, we studied the tuning of plasmon-trion and plasmon-exciton resonance energy transfer from a single gold nanotriangle (AuNT) to monolayer MoS_2. We achieved these phenomena by the combination of rationally designed monolayer MoS_2-plasmonic nanoparticle hybrid systems and single-nanoparticle measurements. Thirdly, we realized the large modulation of hybrid plasmonic waveguide mode (HPWM) in single hybrid molecule-plasmon nanostructures through the strong molecule-plasmon coupling. The HPWM features both the capacity of plasmonic nanostructures to manipulate light at the nanoscale and the low loss of dielectric waveguides. Fourthly, we demonstrated the photoswitchable plasmon-induced fluorescence enhancement. This large switchable modulation of fluorescence was derived from the large near-field enhancement at the subnanometer gap between Au nanoparticles and switchable intersystem crossing as a nonradiative decay channel in photochromic dyes. Finally, we achieved tunable Fano resonances and plasmon-exciton coupling in two-dimensional (2D) WS_2-AuNT hybrid structures at room temperature. The tuning of Fano resonances and plasmon-exciton coupling were achieved by the active control of the WS_2 exciton binding energy and dipole-dipole interaction through controlling the dielectric constant of the surrounding medium.

Table of Contents

List of Tables

List of Figures

Chapter 1 Introduction*

1.1 PLASMONICS

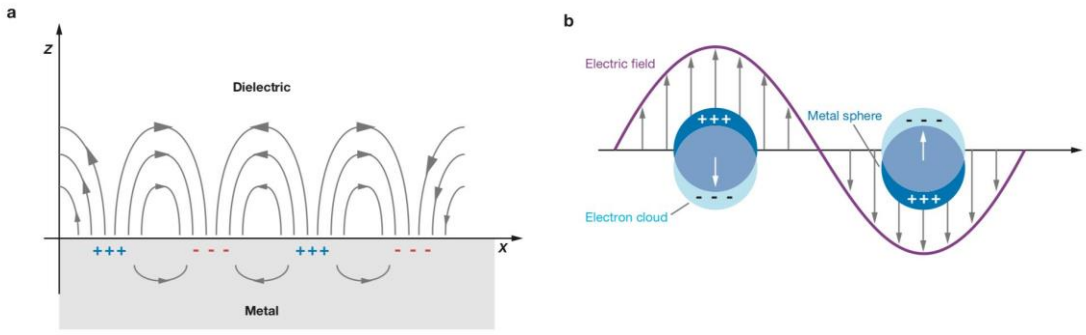

Figure 1.1: Schematic diagrams of surface plasmon polaritons (a) and localized surface plasmon resonances (b).[1] Reproduced with permission from ref 1. Copyright 2007 Annual Reviews.

Optical devices have played a critical role in people's daily life and modern scientific research. Those devices include lasers, optical sensors, solar cells, etc., and having been extensively used in numerous applications such as medical diagnosis, photo-thermal therapy, environmental monitoring and solar energy harvesting. However, the conventional optical devices have disadvantages like the bulky size and high cost, due to the diffraction limit and expensive optical components. These disadvantages impede the miniaturization and large-scale applications of conventional optical devices. In recent decades, plasmonics—a field dedicated to the fundamental study and applications of surface plasmons (SPs) has emerged for facing those challenges. SPs are the light-coupled

* Wang, M.; Bangalore Rajeeva, B.; Scarabelli, L.; Perillo, E. P.; Dunn, A. K.; Liz-Marzán, L. M.; Zheng, Y., Molecular-Fluorescence Enhancement via Blue-Shifted Plasmon-Induced Resonance Energy Transfer. *J. Phys. Chem. C* 2016, 120 (27), 14820-14827.
Lin, L.; Wang, M.; Wei, X.; Peng, X.; Xie, C.; Zheng, Y., Photoswitchable Rabi Splitting in Hybrid Plasmon–Waveguide Modes. *Nano Letters* 2016, 16 (12), 7655-7663.
Wang, M. carried out the experimental work and participated in the preparation of manuscript.

coherent oscillations of free electrons at the interfaces between metals and dielectric materials.[2-4] SPs are commonly classified into two types: surface plasmon polaritons (SPPs) and localized surface plasmon resonances (LSPRs), as schematically illustrated in Figure 1.1. SPPs are electromagnetic waves that propagate at the flat interface between a metal and a dielectric.[1, 5] Commonly, to excite SPPs a glass prism is used to compensate the momentum mismatch between evanescent modes at the metal-dielectric interface and the electromagnetic incident wave through the total internal reflection.[1, 5] Arrays of sub-wavelength holes or grooves in the metal films can be also used for the compensation of the momentum mismatch. Different from SPPs, LSPRs are the localized collective oscillations of electrons in plasmonic nanoparticles. Plasmonic nanoparticles work as nanoantennas and own highly concentrated electromagnetic field at specific spots, known as "hot spots". Through Drude mode, we can estimate the peak frequency of LSPR through the bulk plasma frequency of the metal for designing the plasmonic nanostructure for different working wavelength ranges, as shown in Figure 1.2a.[6] Furthermore, new types of colloidal semiconductor nanocrystals and graphene enable LSPRs in the IR region. In addition, the resonance frequency, the location of "hot spots" and the electromagnetic field enhancement also depend on the size and shape of plasmonic nanostructures, as shown in Figure 1.2b and c.[7-8]

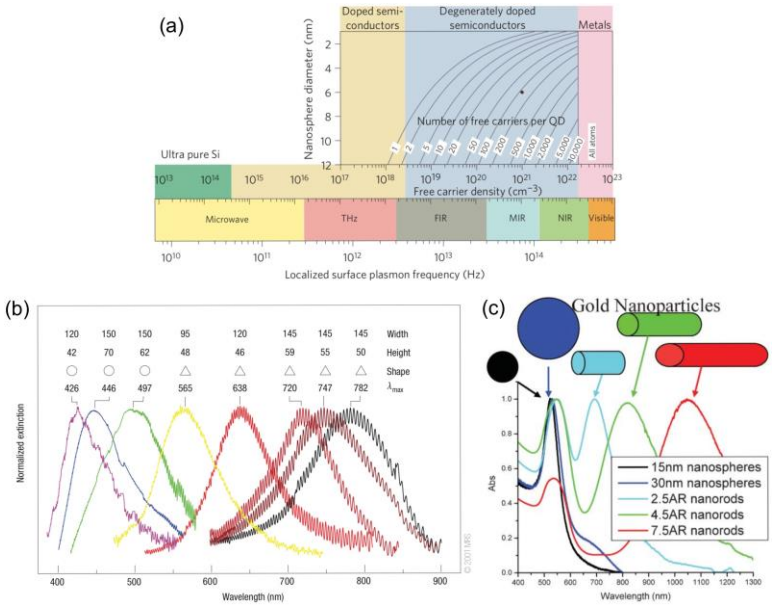

Figure 1.2: (a) Dependence of localized surface plasmon resonance frequency of a spherical nanoparticles on the density of its free charges.[6] Reproduced with permission from ref 6. Copyright 2011 Springer Nature. (b) Effects of size and shape on the extinction spectra of silver nanoprisms and nanodiscs.[7] Reproduced with permission from ref 7. Copyright 2008 Springer Nature. (c) Effects of size and shape on the absorption spectra of gold nanoparticles.[8] Reproduced with permission from ref 8. Copyright 2006 The Royal Society of Chemistry.

1.1.2 Light scattering and absorption by small particles

Plasmonic nanoparticles can strongly scatter and absorb light owing to the excitation of surface plasmons. Hence, optical spectroscopy is a powerful tool to study the plasmonic properties of small particles. Herein, we introduce some basic theoretical approaches of understanding the light scattering and absorption by small particles.

1.1.2.1 Quasi-static approximation

When the size of a metallic spherical particle is much smaller than the wavelength of light (<100 nm), a quasi-static approximation can be used to describe its light scattering properties by solving the Laplace equation for the scalar electric potential: $\nabla^2\Phi = 0$ and

$E = -\nabla\Phi$. By applying continuous boundary condition, the effective dipole moment of the metal nanoparticles can be expressed as:[9]

$$P = 4\pi\varepsilon_m a^3 \frac{\varepsilon_p - \varepsilon_m}{\varepsilon_p + 2\varepsilon_m} E_0 \tag{1.1}$$

where ε_p is the complex dielectric constant of metal nanoparticles and ε_m is the dielectric constant of the surrounding medium. The frequency-dependent ε_p can be expressed by the Drude model:[6]

$$\varepsilon_p = \varepsilon' + i\varepsilon'' = \varepsilon_\infty - \frac{\omega_p^2}{\omega^2 + i\omega} \tag{1.2}$$

where ε' and ε'' are the real and imagery part of the dielectric constant; ε_∞ is the contribution from the bound electrons; ω_p is the bulk plasma frequency of the metal and equates $Ne^2/\varepsilon_0 m^*$, where N is the free electron density, e is the charge of an electron, ε_0 is the vacuum permittivity, and m^* is the effective mass of an electron. Through this dipole moment, one can obtain the cross-sections of scattering (C_{sc}) and absorption (C_{abs}) of this dipole by:

$$C_{sc} = \frac{8\pi}{3} a^2 q^4 \left| \frac{\varepsilon_p - \varepsilon_m}{\varepsilon_p + 2\varepsilon_m} \right|^2 \tag{1.3}$$

$$C_{abs} = 4q \,\mathrm{Im}\left(\frac{\varepsilon_p - \varepsilon_m}{\varepsilon_p + 2\varepsilon_m} \right) \tag{1.4}$$

where q is dimensionless size parameter and equates ka and k is the wave vector in the medium. By comparing Equations 1.3 and 1.4, it is known that the scattering cross-section increases faster than absorption cross-section does when the radius of the particle increases. This implies that for metal nanoparticles with a large radius the scattering is dominating, while small metal nanoparticles have very weak light scattering. These two equations also unravel that the resonant enhancement of scattering and absorption is achieved when $\varepsilon_p = -2\varepsilon_m$, known as Fröhich condition.

1.1.2.2 Mie theory

When the radius of the metal spheres is larger than 100 nm, the quasi-static approximation is no longer valid. In this scenario, Mie theory should be applied. In 1908, Gustav Mie had developed a general theoretical solution to describe the scattering of an electromagnetic plane wave by a homogeneous sphere of arbitrary materials in the frame of electrodynamics. The Mie solution is obtained by applying Maxwell's equations with appropriate boundary conditions, and the obtained extinction, scattering and absorption cross sections are given by:[10]

$$\sigma_{ext} \approx \frac{2\pi}{q^2}\sum_{l=1}^{\infty}(2l+1)\,\mathrm{Re}(a_l + b_l) \tag{1.5}$$

$$\sigma_{sca} \approx \frac{2\pi}{q^2}\sum_{l=1}^{\infty}(2l+1)\left\{|a_l|^2 + |b_l|^2\right\} \tag{1.6}$$

$$\sigma_{abs} \approx \sigma_{ext} - \sigma_{sca} \tag{1.7}$$

where l represents the order of spherical multipole excitation in the particle (e.g., l=1 corresponds to dipole). a_l and b_l are electric and magnetic amplitude, respectively. They are defined by the Mie formulas:

$$a_l = \frac{F_l^{(a)}(q,\varepsilon)}{F_l^{(a)}(q,\varepsilon) + iG_l^{(a)}(q,\varepsilon)} \tag{1.8}$$

$$b_l = \frac{F_l^{(b)}(q,\varepsilon)}{F_l^{(b)}(q,\varepsilon) + iG_l^{(b)}(q,\varepsilon)} \tag{1.9}$$

at small q:

$$F_l^{(a)}(q,\varepsilon) \approx q^{2l+1}\frac{l+1}{[(2l+1)!!]^2}(\varepsilon - 1) \tag{1.10}$$

$$G_l^{(a)}(q,\varepsilon) \approx \frac{l}{2l+1}\left\{\varepsilon + \frac{l+1}{l} - q^2\frac{\varepsilon - 1}{2}\left[\frac{\varepsilon}{2l+3} + \frac{l+1}{l(2l-1)}\right]\right\} \tag{1.11}$$

$$F_l^{(b)}(q,\varepsilon) \approx \frac{q^2}{2l+1}F_l^{(b)}(q,\varepsilon) \tag{1.12}$$

$$G_l^{(b)}(q,\varepsilon) \approx \varepsilon\left[1 + \frac{1-\varepsilon}{l(2l+1)}q^2\right] \tag{1.13}$$

where $F_l^{(a)}(q,\varepsilon)$, $G_l^{(a)}(q,\varepsilon)$, $F_l^{(b)}(q,\varepsilon)$, and $G_l^{(b)}(q,\varepsilon)$ are related to the spherical Bessel and Neumann functions.

1.1.3 Light-matter interactions in plasmonic nanostructures

The ability of SPs to concentrate and manipulate light at the nanoscale leads to numerous intriguing light-matter interactions in plasmonic nanostructures such as plasmon-induced resonance energy transfer (PIRET), plasmon-enhanced spontaneous emission, Fano resonance and strong plasmon-exciton coupling.

1.1.3.1 Plasmon-Induced Resonance Energy Transfer

PIRET is a process through which the energy of SPs transfers from plasmonic nanostructures to adjacent semiconductors via the dipole-dipole interaction. Akin to well-known Förster resonance energy transfer (FRET), PIRET can be utilized in numerous applications such as molecular rulers, biomedical imaging and photocatalysis. However, compared with dye molecule donors in Förster resonance energy transfer (FRET), plasmon NP donors in PIRET have advantages toward applications in biosensing and bioimaging in three main aspects: First of all, AuNP donors require incident light with lower intensity to excite acceptors than that required for dye molecule donors, because AuNPs have larger absorption cross-section than dye molecules (4-5 orders of magnitude larger than that of conventional dyes) due to the excitation of surface plasmons.[11-13] Second, the energy transfer efficiency of PIRET decays more slowly when the NP-molecule distance is increased, as compared to FRET.[14-15] Last but not least, PIRET has the ability to enhance molecular fluorescence using excitation light with longer wavelengths (i.e., lower energy) than that of the molecular absorption peak (more detailed description is in Figure 1.3).

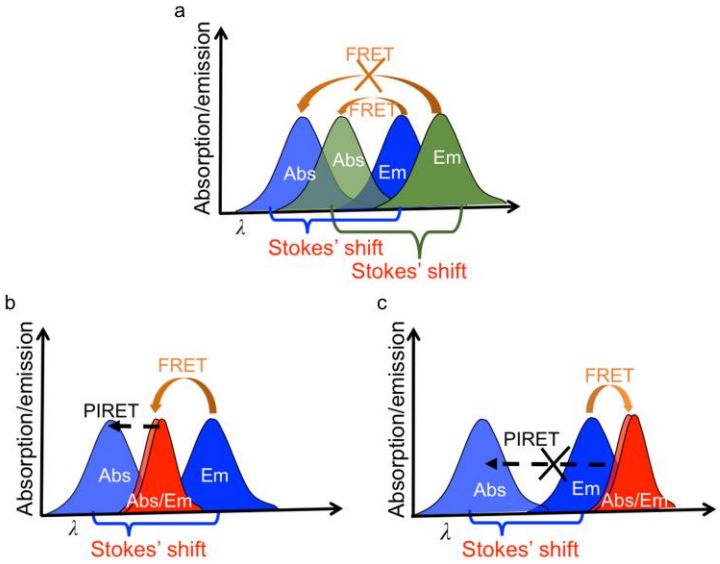

Figure 1.3: Schematics of different energy transfer scenarios in NP-molecule hybrids: (a) Scheme showing energy transfer between a pair of fluorophores. Due to Stokes shift, the emission of an acceptor (green) does not overlap with the absorption of a donor (blue) and FRET does not occur between them. The partial overlap between the emission of the donor (blue) and the absorption of the acceptor (green) leads to FRET from donor to acceptor. (b) Scheme of energy transfer between fluorophores and AuNPs. No obvious Stokes shift occurs to the LSPR-associated absorption and emission spectra of AuNPs (red). As expected, FRET from fluorophores to AuNPs occurs due to the spectral overlap between dye fluorescence (blue) and AuNP absorption. We demonstrate here that PIRET from AuNPs to fluorophores can occur to enhance the molecular fluorescence even if the absorption peak wavelength of the AuNPs is longer than that of fluorophores. PIRET is contingent upon a spectral overlap between the scattering/emission of AuNPs and the absorption of fluorophores, as further described in (c). (c) Scheme showing energy transfer between fluorophores and AuNPs. When there is no spectral overlap between the scattering of AuNPs and the absorption of fluorophores, PIRET does not occur. FRET from fluorophores to AuNPs occurs due to the spectral overlap between dye fluorescence and AuNP absorption.

PIRET has been also utilized to enhance the efficiency of solar energy harvesting owing to the advantages of plasmonic nanoparticles, such as the large absorption coefficient, broad absorption spectrum and stability. Recently, Nianqiang Wu and co-workers demonstrated that blue-shifted PIRET can harvest visible and near-infrared region

sunlight with energy below the band edge of semiconductors commonly used in photoelectrochemical cells, photocatalysts and photovoltaics.[16] By overcoming the constraints of band-edge energetics for those semiconductors with the help of blue-shifted PIRET, enhanced efficiency of solar energy harvesting can be achieved.

1.1.3.2 Plasmon-Enhanced Spontaneous Emission

Controlling the spontaneous emission of fluorophores at the nanoscale is critical to the development of nano-lasers, single-photon sources and high-resolution fluorescence biomarkers, for applications in information processing, biosensing and bioimaging.[17-24] When an emitter is placed in an optical cavity, the spontaneous emission rate can be strongly enhanced, which is known as Purcell effect. However, the minimum size of conventional optical cavities is limited to several-hundred-nm scale due to the diffraction limit, which does not fulfill the requirement of nanophotonic devices.

Since then, tremendous development of nanophotonic technology has enabled exploring the control over the spontaneous emission of fluorophores at the nanoscale and below.[17, 21-22, 25-31] Among many nanophotonic systems, plasmonic nanostructures present multiple advantages for controlling fluorescence, including: (1) strong electromagnetic field enhancement upon excitation of surface plasmons; (2) small size of plasmonic nanostructures for device miniaturization; (3) highly confined “hot spots”, relevant to single fluorophores in size; and (4) high chemical stability of noble metals in plasmonic nanostructures.[4, 8, 13, 32-38]

The strongly confined electromagnetic field derived from the coherent oscillation of electrons on plasmonic cavities allows them to process a much smaller size, compared to conventional cavities. This also makes plasmonic nanostructures to obtain ultrasmall mode volume. Since the Purcell factor is given by $F_p = \frac{3}{4\pi^2}\left(\frac{\lambda_c}{n}\right)^3\left(\frac{Q}{V}\right)$, where Q is the

quality factor, λ_c is the wavelength of light and n is the refractive index of the medium, the ultrasmall mode volume can bring a large enhancement in the spontaneous emission rate despite that the Q factor of plasmonic nanostructure is smaller than that of conventional optical cavities.

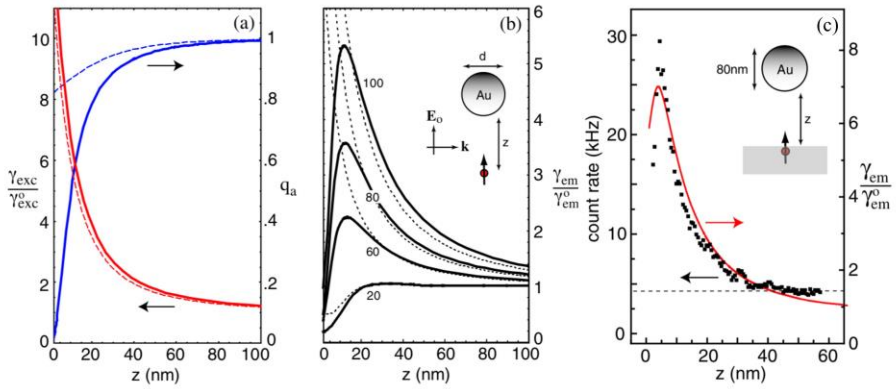

Figure 1.4: (a) Calculated excitation enhancement (red) and quantum yield (blue) as a function of molecule-particle separation (z). The solid curves are the result of MMP calculations while the dashed curves are the dipole approximation. The particle diameter is 80 nm. (b) Calculated emission enhancement as a function of z. The numbers near solid curves indicate the diameter of gold nanoparticles. (c) Theoretical (solid) and experimental (doted) results of the fluorescence rate as a function of z. The dashed line indicates the background level.[25] Reproduced with permission from ref 25. Copyright 2006 American Physical Society.

Lukas Novotny and co-workers studied the enhancement in the molecular fluorescence near plasmonic nanoparticles by controlling the distance between a gold nanoparticle attached to the end of a pointed optical fiber and a single dye molecule.[25] They concluded that the enhancement in fluorescence quantum efficiency and excitation rate originates from the increase of local density of states gained by the enhanced electromagnetic field at the "hot-spots" of the plasmonic nanoparticle. The excitation

enhancement, quantum yield and fluorescence rate of a single molecule as a function of the molecule-particle separation are shown in Figure 1.4.

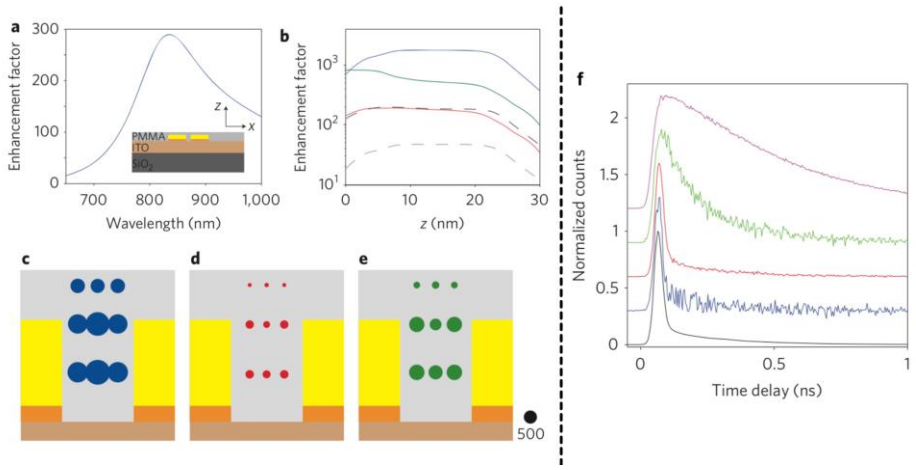

Figure 1.5: (a) Calculated electric field intensity enhancement in the center of a Poly(methyl methacrylate) (PMMA)-covered gold bowtie with a 14-nm gap as a function of wavelength. The thickness of PMMA layer is 30 nm. Inset is the cross section of the simulated structure. (b) Red and green curves show radiative and non-radiative enhancement factors along the center of the gap at a wavelength of 820 nm, respectively; *z* is the distance above the indium tin oxide/PMMA interface. The black dashed, blue and grey dashed lines represent the local optical intensity enhancement at 780 nm, the fluorescence enhancement factor for molecules with a quantum efficiency of 2.5% and molecules with a quantum efficiency of 100%, respectively. The blue (c), red (d) and green (e) circles show the regions of fluorescence, radiative and non-radiative enhancement factors for a molecule emitting at a wavelength of 820 nm, respectively. (f) Time delay curves of bulk TPQDI in PMMA without bowtie nanoantenna (magenta), SM on bowtie nanoantenna (green), SM on bowtie nanoantenna, excitation polarization parallel or perpendicular to the long axis (red or blue), instrument response function (black).[39] Reproduced with permission from ref 39. Copyright 2009 Springer Nature.

The dramatically enhanced emission rate can reduce the lasing threshold and lead to a fast radiative rate as well, which is critical to the development of singe photon sources.

By using a gold bowtie nanoantenna to enhance the emission of a single fluorescent molecule (SM) (Figure 1.5), Anika Kinkhabwala et al demonstrated a maximum fluorescence enhancement rate of 1690 and a lifetime of SM *N*,*N′*-bis(2,6-diisopropyl-phenyl)-1,6,11,16-tetra-[4-(1,1,3,3-tetramethylbutyl)phenoxy]quater-rylene-3,4:13,14-bis(dicarboximide) (TPQDI) shorter than 10 ps.[39]

1.1.3.3 Fano resonance

The spectral shape of optical resonances generally follows the Lorentzian formula.[10] The Lorentzian spectral shape is a sum of the intensity of individual resonances. Hence, symmetrical Lorentzian spectral shape does not present the interference between individual resonances. In 1961, Ugo Fano discovered a new type of resonance lineshape during a study of the autoionizing states of atoms. He attributed the origin of Fano resonance to the constructive and destructive interference between a narrow discrete resonance with a broad spectral line or continuum.[10, 40] Based on Fano's original theory, the spectral shape of a scattering cross section can be described in a convenient mathematical form:[40]

$$\sigma_{\text{sct}} = \frac{\left(2\frac{(E-E_F)}{\Gamma}+q\right)^2}{\left(2\frac{(E-E_F)}{\Gamma}\right)^2+1} \tag{1.14}$$

where E_F is the resonant energy and Γ is the linewidth of the discrete state, q is phenomenological shape parameter as a ratio of the transition probabilities to the mixed state and the continuum. Equation 1.14 suggests that when $q=\infty$, the interference between the discrete mode and the broad mode leads to a Lorentzian peak, while in the situation $q=0$ the interference causes a Lorentzian-like dip in the broad resonance. The asymmetrical

Fano profile of the mixed state is obtained in the case of q=1. These three scenarios are illustrated in Figure 1.6.[40]

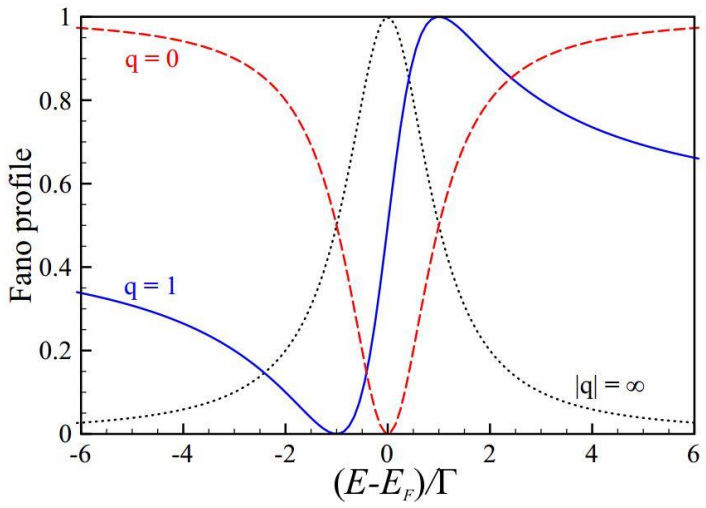

Figure 1.6: Normalized Fano lineshapes with q equates ∞, 1 and 0.[40] Reproduced with permission from ref 40. Copyright 2010 American Physical Society

Fano resonance in plasmonic nanostructures is commonly derived from the interference of a broad bright mode with a narrow dark mode. For instance, Federico Capasso and co-workers have observed Fano resonance in a self-assembled plasmonic heptamer. The heptamer consists of a central particle surrounded by six nanoparticles with the same size.[41] Because of its specific symmetry (Figure 1.7a), collective plasmonic modes of the heptamer include a bonding mode having all the dipoles of nanoparticles oscillating in phase and an antibonding mode with the dipole of the central nanoparticle oscillating out of phase with the dipoles of the other six nanoparticles. The later one results in a subradiant plasmonic mode (dark mode), which induces a sharp Fano dip in the broad scattering spectrum of the super-radiant plasmonic mode (bright mode) derived from the bonding mode. Intriguingly, the symmetry breaking in plasmonic nanostructures can also

induce Fano resonances. Peter Nordlander and co-workers demonstrated that when there is a symmetry break in the concentric ring/disk cavity (CRDC), tunable Fano resonances can be achieved by modifying the displacement of the disk with respect to the center of the peripheral ring (Figure 1.7b).[42] Moreover, asymmetry in plasmonic nanostructures can enable an effective interaction between electric modes and magnetic modes, and leading to the observation of a magnetic-based Fano scattering resonance at optical frequencies, as shown in Figure 1.7c.[43]

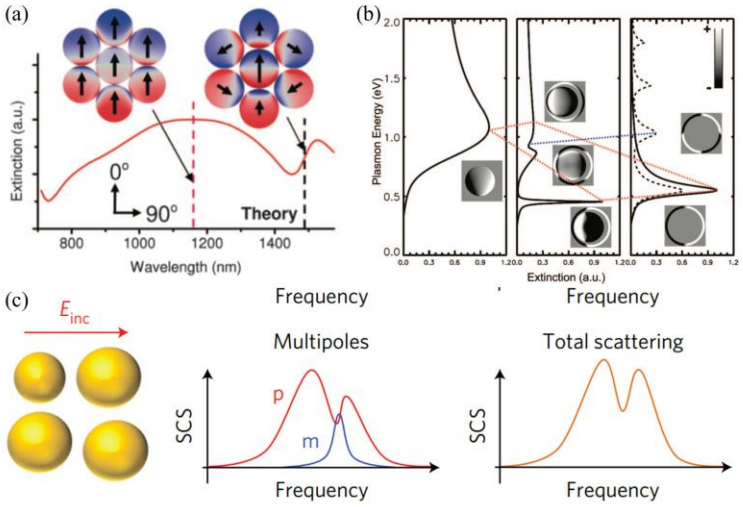

Figure 1.7: (a) Calculated extinction spectrum and charge density profiles for a heptamer excited by the normal incident light. A Fano dip in the bright mode is observed at 1450 nm.[41] Reproduced with permission from ref 41. Copyright 2010 American Association for the Advancement of Science. (b) The plasmon hybridization diagram of CRDC. The blue dashed line shows the Fano coupling between the quadrupole mode of the ring and the dipole mode of the disk.[42] Reproduced with permission from ref 42. Copyright 2008 American Chemical Society. (c) Schematic diagrams of Fano interference between an electric dipole and a magnetic dipole.[43] Reproduced with permission from ref 43. Copyright 2013 Springer Nature.

Besides rising from the interaction between different plasmonic modes, Fano resonance can be obtained in plasmon-exciton hybrid systems, where the excitonic resonance of an emitter can interfere with surface plasmon resonances. For example, Fano

resonance had been observed in hybrid systems consisting of plasmonic nanostructures and J-aggregates. The strong Fano interference of excitons with surface plasmons is derived from the large oscillator strength of J-aggregates and the intense electromagnetic field of plasmonic nanostructures.

1.1.3.4 Strong plasmon-exciton coupling

When an emitter is placed near a plasmonic nanostructure, usually only its spontaneous emission rate is modified while the emission frequency keeps the same.[44] However, if the coupling between the emitter and plasmonic nanostructure is strong enough to surpass the losses of the hybrid system, the energy levels responsible to the emission are changed. This phenomenon is known as the strong coupling. Typically, for a two-level system, when the strong coupling region is achieved, the original excited energy level splits into two energy levels, known as the upper polariton state and lower polariton state. The energy difference between these two states is called Rabi splitting, as shown in Figure 1.8. A commonly used criterion to determine whether a system achieves strong coupling or not is:[44]

$$\Omega = \sqrt{\frac{\gamma_{ex}}{2} + \frac{\gamma_{SP}}{2}} \tag{1.15}$$

where Ω is the Rabi splitting energy; γ_{ex} and γ_{SP} are the linewidth of excitonic and surface plasmon resonance, respectively.

In the classical case, Rabi splitting can be calculated by:

$$\Omega = \sqrt{\frac{N}{V}} \frac{e}{\sqrt{\varepsilon_0 m}} \tag{1.16}$$

where N is the number of the coupled emitters and V is the mode volume.

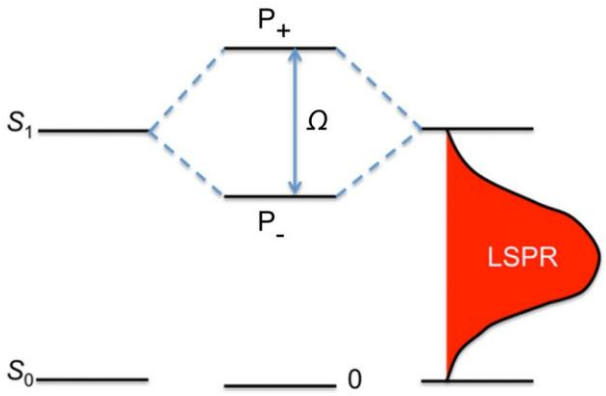

Figure 1.8: Schematic drawing of Rabi splitting. S_0 and S_1 are the ground state and excited state of a two-level system respectively. P_+ and P_- are the upper polariton state and lower polariton state respectively.

It is known from Equation 1.16 that although plasmonic nanoparticles have strong dissipative losses, the ultrasmall mode volumes allow a large Rabi splitting, which can overcome the dissipative losses to reach the strong coupling region. For example, J. Bellessa et al. reported the strong coupling between surface plasmons and excitons by depositing cyanide dye J-aggregates on a silver film.[45] The J-aggregates are chosen due to their large oscillator strength, because Rabi splitting in the coupled system is directly proportional to the oscillator strength of emitters.

Most recently, the strong single-molecule coupling at room temperature is demonstrated in nanoparticle-on-mirror (NPoM) geometry by Jeremy J. Baumberg and co-workers.[46] This strong coupling at single-molecule resolution is realized by leveraging the ultrasmall effective mode volume of NPoM. The comparison of different plasmonic nanocavities and dielectric optical cavities is illustrated in Figure 1.9.

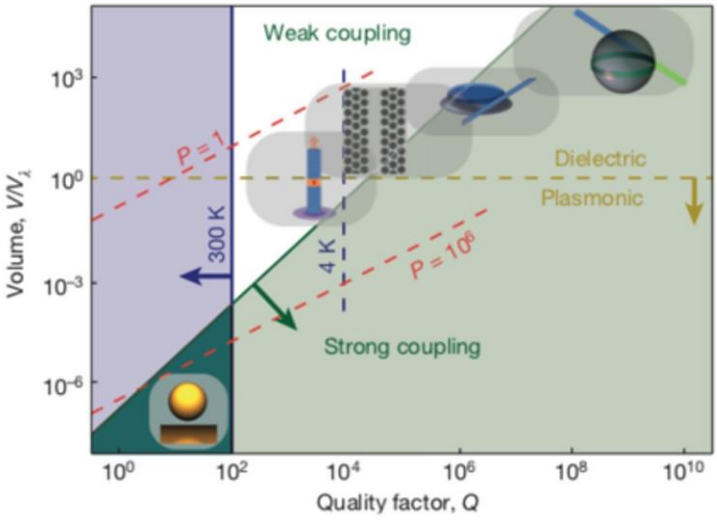

Figure 1.9: The quality factor (Q) of a nanocavity versus its effective volume (V/V_λ). The green, blue and orange arrows indicate strong-coupling, room-temperature, and plasmonic regimes for single emitters, respectively. The icons (from right) in this figure illustrate whispering gallery spheres, microdisks, photonic crystals, micropillars, and nanoparticle-on-mirror configuration (NPoM). *P* is Purcell factor, which shows the emission-rate enhancement.[46] Reproduced with permission from ref 46. Copyright 2016 Springer Nature.

1.3 Goal and Organization

The goals of this dissertation can be divided into three categories: (1) to explore plasmon-induced resonance energy transfer for fundamental understanding of the physical mechanism of the resonance energy transfer between plasmonic nanostructure and dye molecules, QDs and 2D materials, and its potential applications in biomedical imaging, sensing and solar harvesting; (2) to develop active plasmonic devices by combining the switchable functional materials such as photochromic dyes with plasmonic nanostructures. The large switchable modulation of light is achieved by the realization of strong plasmon-induced fluorescence enhancement and strong plasmon-exciton coupling; (3) to study the tunable Fano resonance and plasmon-exciton coupling in the hybrid system consisting of plasmonic nanoparticles and transition metal dichalcogenide monolayers (TMDCs). The

tunability of plasmon-exciton interaction is achieved by varying the excitonic properties of TMDCs and LSPRs of plasmonic NPs. The first category contains two chapters. In chapter 2, we demonstrated the molecular-fluorescence enhancement via blue-shifted plasmon-induced resonance energy transfer. In chapter 3, plasmon-trion and plasmon-exciton resonance energy transfer from a single plasmonic nanoparticle to monolayer MoS_2 was observed. The following two chapters are included in the second category. In chapter 4, by using photoswitchable molecule-spiropyran we achieved photoswitchable Rabi splitting in the hybrid plasmon-waveguide mode. In chapter 5, we realized the control of plasmon-enhanced fluorescence via intersystem crossing in photoswitchable molecules. For the final category, we used one chapter (chapter 6) to explore the tunable Fano resonance and plasmon-exciton coupling in the hybrid system consisting of an Au nanotriangle and monolayer WS_2.

1.4 REFERENCES

1. Willets, K. A.; Duyne, R. P. V., Localized Surface Plasmon Resonance Spectroscopy and Sensing. *Annu. Rev. Phys. Chem.* **2007**, 58 (1), 267-297.
2. Atwater, H. A.; Polman, A., Plasmonics for improved photovoltaic devices. *Nat. Mater.* **2010**, 9, 205.
3. Maier, S. A.; Atwater, H. A., Plasmonics: Localization and guiding of electromagnetic energy in metal/dielectric structures. *J. Appl. Phys.* **2005**, 98 (1), 011101.
4. Halas, N. J.; Lal, S.; Chang, W.-S.; Link, S.; Nordlander, P., Plasmons in Strongly Coupled Metallic Nanostructures. *Chem. Rev.* **2011**, 111 (6), 3913-3961.
5. Zayats, A. V.; Smolyaninov, I. I.; Maradudin, A. A., Nano-optics of surface plasmon polaritons. *Phys. Rep.* **2005**, 408 (3), 131-314.
6. Luther, J. M.; Jain, P. K.; Ewers, T.; Alivisatos, A. P., Localized surface plasmon resonances arising from free carriers in doped quantum dots. *Nat. Mater.* **2011**, 10, 361.
7. Anker, J. N.; Hall, W. P.; Lyandres, O.; Shah, N. C.; Zhao, J.; Van Duyne, R. P., Biosensing with plasmonic nanosensors. *Nat. Mater.* **2008**, 7, 442.

8. Eustis, S.; El-Sayed, M. A., Why gold nanoparticles are more precious than pretty gold: Noble metal surface plasmon resonance and its enhancement of the radiative and nonradiative properties of nanocrystals of different shapes. *Chem. Soc. Rev.* **2006**, 35 (3), 209-217.

9. Fan, X.; Zheng, W.; Singh, D. J., Light scattering and surface plasmons on small spherical particles. *Light Sci. Appl.* **2014**, 3, e179.

10. Luk'yanchuk, B.; Zheludev, N. I.; Maier, S. A.; Halas, N. J.; Nordlander, P.; Giessen, H.; Chong, C. T., The Fano resonance in plasmonic nanostructures and metamaterials. *Nat. Mater.* **2010**, 9, 707.

11. Jain, P. K.; Lee, K. S.; El-Sayed, I. H.; El-Sayed, M. A., Calculated Absorption and Scattering Properties of Gold Nanoparticles of Different Size, Shape, and Composition: Applications in Biological Imaging and Biomedicine. *J. Phys. Chem. B* **2006**, 110 (14), 7238-7248.

12. Hu, M.; Chen, J.; Li, Z.-Y.; Au, L.; Hartland, G. V.; Li, X.; Marquez, M.; Xia, Y., Gold nanostructures: engineering their plasmonic properties for biomedical applications. *Chem. Soc. Rev.* **2006**, 35 (11), 1084-1094.

13. Chen, H.; Shao, L.; Li, Q.; Wang, J., Gold nanorods and their plasmonic properties. *Chem. Soc. Rev.* **2013**, 42 (7), 2679-2724.

14. Yun, C. S.; Javier, A.; Jennings, T.; Fisher, M.; Hira, S.; Peterson, S.; Hopkins, B.; Reich, N. O.; Strouse, G. F., Nanometal Surface Energy Transfer in Optical Rulers, Breaking the FRET Barrier. *J. Am. Chem. Soc.* **2005**, 127 (9), 3115-3119.

15. Clapp, A. R.; Medintz, I. L.; Mattoussi, H., Förster Resonance Energy Transfer Investigations Using Quantum-Dot Fluorophores. *ChemPhysChem* **2006**, 7 (1), 47-57.

16. Li, J.; Cushing, S. K.; Meng, F.; Senty, T. R.; Bristow, A. D.; Wu, N., Plasmon-induced resonance energy transfer for solar energy conversion. *Nat. Photonics* **2015**, 9, 601.

17. Noda, S.; Fujita, M.; Asano, T., Spontaneous-emission control by photonic crystals and nanocavities. *Nat. Photonics* **2007**, 1 (8), 449-458.

18. Lakowicz, J. R., Radiative decay engineering 5: metal-enhanced fluorescence and plasmon emission. *Anal. Biochem.* **2005**, 337 (2), 171-194.

19. Pelton, M., Modified spontaneous emission in nanophotonic structures. *Nat. Photonics* **2015**, 9 (7), 427-435.

20. Cang, H.; Liu, Y.; Wang, Y.; Yin, X.; Zhang, X., Giant Suppression of Photobleaching for Single Molecule Detection via the Purcell Effect. *Nano Lett.* **2013**, 13 (12), 5949-5953.

21. Lodahl, P.; Floris van Driel, A.; Nikolaev, I. S.; Irman, A.; Overgaag, K.; Vanmaekelbergh, D.; Vos, W. L., Controlling the dynamics of spontaneous emission from quantum dots by photonic crystals. *Nature* **2004**, 430 (7000), 654-657.

22. Song, J.-H.; Atay, T.; Shi, S.; Urabe, H.; Nurmikko, A. V., Large Enhancement of Fluorescence Efficiency from CdSe/ZnS Quantum Dots Induced by Resonant Coupling to Spatially Controlled Surface Plasmons. *Nano Lett.* **2005**, 5 (8), 1557-1561.

23. Belacel, C.; Habert, B.; Bigourdan, F.; Marquier, F.; Hugonin, J. P.; Michaelis de Vasconcellos, S.; Lafosse, X.; Coolen, L.; Schwob, C.; Javaux, C.; Dubertret, B.; Greffet, J. J.; Senellart, P.; Maitre, A., Controlling Spontaneous Emission with Plasmonic Optical Patch Antennas. *Nano Lett.* **2013**, 13 (4), 1516-1521.

24. Noda, S.; Fujita, M.; Asano, T., Spontaneous-emission control by photonic crystals and nanocavities. *Nat. Photonics* **2007**, 1, 449.

25. Anger, P.; Bharadwaj, P.; Novotny, L., Enhancement and Quenching of Single-Molecule Fluorescence. *Phys. Rev. Lett.* **2006**, 96 (11), 113002.

26. Kühn, S.; Håkanson, U.; Rogobete, L.; Sandoghdar, V., Enhancement of Single-Molecule Fluorescence Using a Gold Nanoparticle as an Optical Nanoantenna. *Phys. Rev. Lett.* **2006**, 97 (1), 017402.

27. Akselrod, G. M.; Argyropoulos, C.; Hoang, T. B.; Ciracì, C.; Fang, C.; Huang, J.; Smith, D. R.; Mikkelsen, M. H., Probing the mechanisms of large Purcell enhancement in plasmonic nanoantennas. *Nat. Photonic*s **2014**, 8 (11), 835-840.

28. Rose, A.; Hoang, T. B.; McGuire, F.; Mock, J. J.; Ciracì, C.; Smith, D. R.; Mikkelsen, M. H., Control of Radiative Processes Using Tunable Plasmonic Nanopatch Antennas. *Nano Lett.* **2014**, 14 (8), 4797-4802.

29. Tovmachenko, O. G.; Graf, C.; van den Heuvel, D. J.; van Blaaderen, A.; Gerritsen, H. C., Fluorescence Enhancement by Metal-Core/Silica-Shell Nanoparticles. *Adv. Mater.* **2006**, 18 (1), 91-95.

30. Bardhan, R.; Grady, N. K.; Cole, J. R.; Joshi, A.; Halas, N. J., Fluorescence Enhancement by Au Nanostructures: Nanoshells and Nanorods. *ACS Nano* **2009**, 3 (3), 744-752.

31. Fujita, M.; Takahashi, S.; Tanaka, Y.; Asano, T.; Noda, S., Simultaneous Inhibition and Redistribution of Spontaneous Light Emission in Photonic Crystals. *Science* **2005**, 308 (5726), 1296.

32. Ming, T.; Chen, H.; Jiang, R.; Li, Q.; Wang, J., Plasmon-Controlled Fluorescence: Beyond the Intensity Enhancement. *J. Phys. Chem. Lett.* **2012**, 3 (2), 191-202.

33. Gandra, N.; Portz, C.; Tian, L.; Tang, R.; Xu, B.; Achilefu, S.; Singamaneni, S., Probing Distance-Dependent Plasmon-Enhanced Near-Infrared Fluorescence

Using Polyelectrolyte Multilayers as Dielectric Spacers. *Angew. Chem. Int. Ed.* **2014**, 53 (3), 866-870.

34. Ayala-Orozco, C.; Liu, J. G.; Knight, M. W.; Wang, Y.; Day, J. K.; Nordlander, P.; Halas, N. J., Fluorescence Enhancement of Molecules Inside a Gold Nanomatryoshka. *Nano Lett.* **2014**, 14 (5), 2926-2933.

35. Tam, F.; Goodrich, G. P.; Johnson, B. R.; Halas, N. J., Plasmonic Enhancement of Molecular Fluorescence. *Nano Lett.* **200**7, 7 (2), 496-501.

36. Giannini, V.; Fernández-Domínguez, A. I.; Heck, S. C.; Maier, S. A., Plasmonic Nanoantennas: Fundamentals and Their Use in Controlling the Radiative Properties of Nanoemitters. *Chem. Rev.* **2011**, 111 (6), 3888-3912.

37. Gu, Y.; Wang, L.; Ren, P.; Zhang, J.; Zhang, T.; Martin, O. J. F.; Gong, Q., Surface-Plasmon-Induced Modification on the Spontaneous Emission Spectrum via Subwavelength-Confined Anisotropic Purcell Factor. *Nano Lett.* **2012**, 12 (5), 2488-2493.

38. Ming, T.; Zhao, L.; Chen, H.; Woo, K. C.; Wang, J.; Lin, H.-Q., Experimental Evidence of Plasmophores: Plasmon-Directed Polarized Emission from Gold Nanorod–Fluorophore Hybrid Nanostructures. *Nano Lett.* **2011**, 11 (6), 2296-2303.

39. Kinkhabwala, A.; Yu, Z.; Fan, S.; Avlasevich, Y.; Müllen, K.; Moerner, W. E., Large single-molecule fluorescence enhancements produced by a bowtie nanoantenna. *Nat. Photonics* **2009**, 3, 654.

40. Miroshnichenko, A. E.; Flach, S.; Kivshar, Y. S., Fano resonances in nanoscale structures. *Rev. Mod. Phys.* **2010**, 82 (3), 2257-2298.

41. Fan, J. A.; Wu, C.; Bao, K.; Bao, J.; Bardhan, R.; Halas, N. J.; Manoharan, V. N.; Nordlander, P.; Shvets, G.; Capasso, F., Self-Assembled Plasmonic Nanoparticle Clusters. *Science* **2010**, 328 (5982), 1135.

42. Hao, F.; Sonnefraud, Y.; Dorpe, P. V.; Maier, S. A.; Halas, N. J.; Nordlander, P., Symmetry Breaking in Plasmonic Nanocavities: Subradiant LSPR Sensing and a Tunable Fano Resonance. *Nano Lett.* **2008**, 8 (11), 3983-3988.

43. Shafiei, F.; Monticone, F.; Le, K. Q.; Liu, X.-X.; Hartsfield, T.; Alù, A.; Li, X., A subwavelength plasmonic metamolecule exhibiting magnetic-based optical Fano resonance. *Nat. Nanotechnol.* **2013**, 8, 95.

44. Törmä, P.; Barnes, W. L., Strong coupling between surface plasmon polaritons and emitters: a review. *Rep. Prog. Phys.* **2015**, 78 (1), 013901.

45. Bellessa, J.; Bonnand, C.; Plenet, J. C.; Mugnier, J., Strong Coupling between Surface Plasmons and Excitons in an Organic Semiconductor. *Phys. Rev. Lett.* **2004**, 93 (3), 036404.

46. Chikkaraddy, R.; de Nijs, B.; Benz, F.; Barrow, S. J.; Scherman, O. A.; Rosta, E.; Demetriadou, A.; Fox, P.; Hess, O.; Baumberg, J. J., Single-molecule strong coupling at room temperature in plasmonic nanocavities. *Nature* **2016**, 535, 127.

Chapter 2 Blue-Shifted Plasmon-Induced Resonance Energy Transfer*

2.1 INTRODUCTION

Surface plasmon energy can be transferred from Au nanoparticles (AuNPs) as donors to dye molecules or semiconductors as acceptors, through plasmon-induced resonance energy transfer (PIRET) or plasmon resonance energy transfer (PRET).[1-7] Compared with dye molecule donors in Förster resonance energy transfer (FRET), AuNP donors in PIRET have advantages toward applications in biosensing and bioimaging in two main aspects. First of all, AuNP donors require incident light with lower intensity to excite acceptors than that required for dye molecule donors. Not only AuNPs have larger absorption cross-section than dye molecules (4-5 orders of magnitude larger than that of conventional dyes) due to the excitation of surface plasmons,[8-10] but additionally the energy transfer efficiency of PIRET decays more slowly when the NP-molecule distance is increased, as compared to FRET.[11-12] Therefore, NP-molecule hybrids are promising candidates for biosensing and bioimaging with low-power excitation and high signal-to-noise ratio.

Despite their clear advantages in biosensing and bioimaging via the use of low-energy, low-intensity light, the application of AuNPs as donors in blue-shifted PIRET has not been demonstrated experimentally. In previous studies, the effect of PIRET has been limited to dips in the scattering spectra of metal NPs.[1-3] In this chapter, we demonstrate the enhancement of molecular fluorescence via blue-shifted PIRET from single Au nanorods (AuNRs) to molecule fluorophores, which indicates that AuNPs as donors can enhance the fluorescence excitation of dye molecule acceptors.

---

* Wang, M.; Bangalore Rajeeva, B.; Scarabelli, L.; Perillo, E. P.; Dunn, A. K.; Liz-Marzán, L. M.; Zheng, Y., Molecular-Fluorescence Enhancement via Blue-Shifted Plasmon-Induced Resonance Energy Transfer. *J. Phys. Chem. C* 2016, 120 (27), 14820-14827.
Wang, M. carried out the experimental work and participated in the preparation of manuscript.

2.2 RESULTS AND DISCUSSION

2.2.1 Experimental section

2.2.1.1 Sample preparation

Solutions of Au nanorods (AuNRs, Alfa Aesar) were drop-coated on microscope calibration slides (AmScope) and dried naturally. We used AuNRs with three types of sizes: 12-18 nm dia. × 49-59 nm length, 19-25 nm dia. × 50-60 nm length, and 19-25 nm dia. × 63-73 nm length. We mixed spiropyran (SP, Sigma-Aldrich) and PMMA (Sigma-Aldrich) with a weight ratio of 2:1 (8 wt%: 4 wt%) in chlorobenzene to prepare PMMA films with high concentration of SP molecules. The SP-doped PMMA films were spin-coated onto the microscope slides with AuNRs. The spin coater (Laurell Technologies) was set as 2000 revolutions per minute and run for one minute. The thickness of the SP-doped PMMA film was measured as ~580 nm by a Wyko NT9100 Optical Profilometer (Veeco Instruments Inc.).

2.2.1.2 Optical measurements

A dark-field microscope (Ti-E inverted microscope, Nikon) with a halogen white light source (12V, 100 W) was employed to measure the scattering spectra of single AuNRs and the white-light-excited fluorescence of merocyanine (MC) molecules. A mercury light source (C-HGFIE, Nikon) with excitation filters was used to generate UV light (DAPI Shift Filter set, excitation: 358 nm). We used markers on microscope calibration slides to locate single AuNRs. UV light was applied to convert molecules from SP to MC isomers. We used an oil-immersion dark-field condenser in conjunction with 100x objective for single-nanoparticle spectroscopy. In some cases, a 665 nm long-pass filter was placed on the top of the condenser to partially block the white light at the shorter wavelengths.

Fluorescence lifetime imaging microscopy (FLIM) was performed using time correlated single photon counting technique. Major components of FLIM setup include a femtosecond titanium: sapphire laser tuned to 800 nm (≈200 fs) (Mira 900, Coherent), galvo scanning mirrors (6215H, Cambridge Tech.), and a GaAsP photomultiplier tube (PMT) (H7422PA-40, Hamamatsu) in non-descanned detection scheme. Before reaching the photon counting board (SPC-150, Becker and Hickl GmbH), the output current of the PMT is amplified via a preamplifier (HFAC-26, Becker and Hickl GmbH). The detailed information for FLIM setup can be found in a previous report.[13] A custom LabView interface was used to acquire data, while a custom Matlab script was used to process the FLIM datasets. Fluorescence lifetimes were recorded with an average laser power of 4 mW. The TCSPC bin resolution was 20 ps and FLIM pixel integration time was 5 ms. Lifetimes were fit at each pixel via a least squares method using a model of a single exponential decay.[14]

2.2.2 Single-nanoparticle scattering spectroscopy

We used single-nanoparticle scattering spectroscopy based on dark-field optical microscopy to investigate molecular fluorescence via blue-shifted PIRET from single AuNRs to dye molecules. The scheme of the sample and experimental setup is shown in Figure 2.1a. AuNRs were selected due to several considerations. AuNRs not only allow a high tunability of LSPR peak wavelengths,[9-10] but also have a long dephasing time,[15] which can enhance the efficiency of energy transfer to dye molecules.[4] Additionally, the narrow spectral linewidth of AuNRs allows us to better distinguish the LSPR scattering peak from the emission peak of the dye. With a small detection volume and a high sensitivity toward local environmental variations, single-nanoparticle scattering spectroscopy can eliminate the inhomogeneity and averaging effects inherent to ensemble measurements, enabling

accurate shape- and size-dependent studies of the optical properties of NPs.[16-24] Using single-nanoparticle spectroscopy, we managed to induce and measure blue-shifted PIRET by tuning the LSPR of AuNRs relative to the absorption and emission bands of adsorbed dye molecules at AuNRs, because PIRET efficiency strongly depends on the emission-absorption spectral overlap.[4]

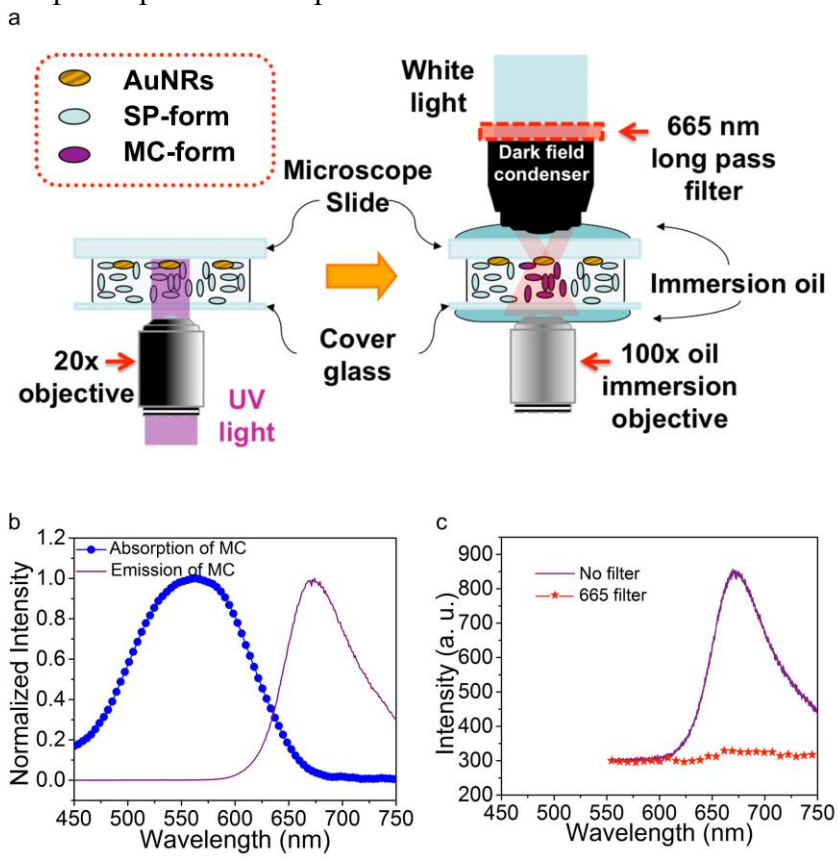

Figure 2.1: (a) Scheme of the sample and experimental setup for the study of PIRET with single-nanoparticle dark-field scattering spectroscopy. UV light induces SP-MC isomerization. (b) Absorption and emission spectra of an MC-doped PMMA film measured by a standard fluorometer. The emission spectrum was excited at 390 nm. (c) Fluorescence spectra of an MC-doped PMMA film measured by dark-field optical spectroscopy without (purple) and with (red) the use of a 665 nm long-pass filter. White light was used as excitation source. Data at short wavelengths are not available due to limitations of the grating in our spectroscopy.

Spiropyran (SP) molecules in their open form, which are known as merocyanine (MC), have a large Stokes shift between absorption and emission peak wavelengths, as shown in Figure 2.1b. Due to the difference in peak wavelength (ca. 100 nm) between the absorption and emission spectra of MC, the LSPR peak wavelength of AuNRs can be tuned to be separated from the emission band of MC while overlapping with its absorption band. As shown in Figure 2.1a, a single-nanoparticle scattering spectrum recorded with our dark-field optical spectroscopy covers the mixed signals from the LSPR scattering of AuNRs and the fluorescence of MC molecules, therefore becoming an ideal platform to study the effects of spectral overlap on the efficiency of blue-shifted PIRET. Our samples are sub-monolayers of well-separated AuNRs on glass substrates, covered by MC-doped PMMA films (Figure 2.1a). Optical measurements were made upon UV irradiation of the molecules and formation of MC isomers. The SP-MC photoisomerization is illustrated in Figure 2.2.

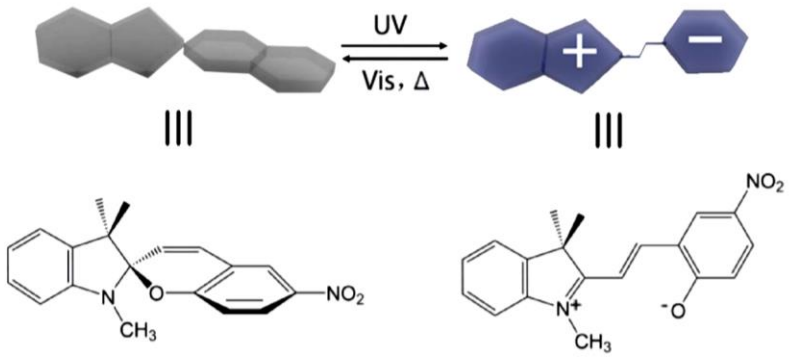

Figure 2.2: Schematics and chemical structures of reversible photoisomerization between spiropyran (SP) and merocyanine (MC).

When the LSPR peak of AuNRs is located between the absorption and emission peaks of MC, the spectral overlap between the LSPR scattering (emission) and the

absorption of MC molecules allows blue-shifted PIRET from AuNRs to MC. Meanwhile, the molecular emission band also overlaps with the LSPR absorption band, which enables red-shifted FRET from the molecules to AuNRs.[4] The net direction of energy transfer between AuNRs and MC molecules is determined by the dephasing time (T_2), which is given by:[4,15, 25]

$$\frac{1}{T_2} = \frac{1}{2T_1} + \frac{1}{T_2^*} \tag{2.1}$$

where T_1 is the recombination time that describes the relaxation from the excited state to the ground state in AuNRs (or dye molecules) and T_2* is the pure dephasing time of AuNRs (or dye molecules). Since T_2* is in the fs range and T_1 is in the ps range, T_2 is relevant to T_2*.[25] When T_2* of LSPRs is longer than that of molecular fluorescence, coherent excitons of molecules dephase more rapidly than the LSPRs of AuNRs do. Under this condition, PIRET is more efficient than FRET and energy transfers from the AuNRs to the molecules.[4]

Based on the dark-field optical microscopy study as described in Figure 2.1a, we measured the fluorescence spectra of MC molecules doped in the PMMA film under white-light excitation. Figure 2.1c shows the spectra with (indicated by "665 filter") and without (indicated by "No filter") the use of a 665 nm long-pass filter. The fluorescence spectrum without the filter matches well with the single-wavelength-excited emission spectrum from a standard fluorometer (Figure 2.1b). Both spectra exhibit the same fluorescence peak wavelength of 670 nm, confirming that dark-field optical spectroscopy allows us to excite and measure the fluorescence of MC molecules under white-light excitation. The capability of white light in exciting the fluorescence at a peak wavelength of 670 nm is also supported by the excitation spectrum (Figure 2.3), which exhibits the strong excitation efficiency within the visible-light regime.

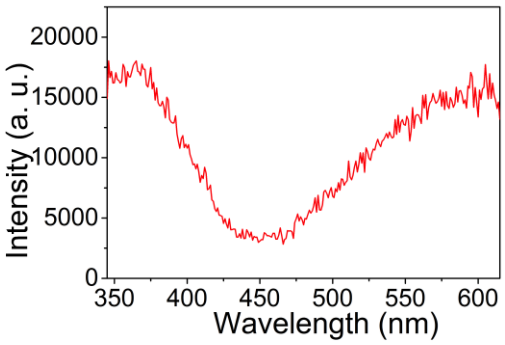

Figure 2.3: Excitation spectrum of MC molecules for an emission wavelength of 670 nm.

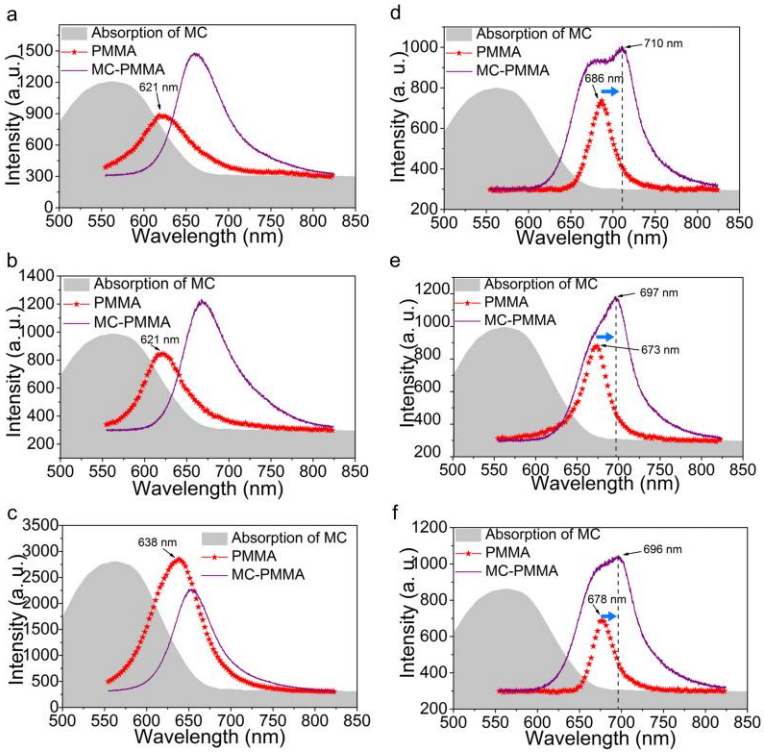

Figure 2.4: Single-nanoparticle spectra measured from AuNRs covered by MC-doped PMMA films or pure PMMA films when (a-c) the scattering spectra of AuNRs have large overlaps with the absorption band of MC molecules, and (d-f) the scattering spectra of AuNRs have minimal overlap with the absorption of MC. The black arrows label the scattering LSPR peak positions and the blue arrows indicate red shifts of the LSPR scattering peaks due to MC doping in PMMA. Also included are the absorption spectra of MC molecules measured by UV-Vis-NIR spectroscopy.

The use of a 665 nm long-pass filter however results in a significant reduction of the fluorescence of MC molecules (as indicated by the extremely weak spectrum in Figure 2.1c), which will enable us to reveal the AuNR LSPR scattering component at the wavelengths longer than 665 nm from a mixture of fluorescence and scattering signals (Figures 2.4d-f). However, the use of the long-pass filter also significantly reduces the AuNR LSPR scattering when the peak wavelengths are shorter than the cut-off wavelength (i.e., 665 nm). To identify LSPR scattering peak wavelengths that are shorter than 665 nm, we measured the scattering spectra of the same AuNRs covered by either pure PMMA films or MC-doped PMMA films. By measuring AuNRs with different LSPRs, we observe two types of scenarios. The first scenario is shown in Figure 2.4a-c, where a single resonance peak at ~670 nm is recorded for an AuNR covered by the MC-doped PMMA film, whereas for the same AuNR covered by pure PMMA, the spectrum significantly overlaps with the absorption band of MC molecules. The second scenario is shown in Figure 2.4d-f, where two peaks are observed in the spectrum of an AuNR covered by the MC-doped PMMA film and there is no obvious overlap between the scattering spectrum of the same AuNR covered by pure PMMA films and the absorption band of MC.

To better understand the two different scenarios in Figure 2.4, we fitted the spectrum in Figure 2.4d-f into two individual peaks with Lorentzian model. Take Figure 2.4a as an example, the two Lorentzian peaks are at ~670 nm and ~710 nm. The ~670 nm peak is attributed to the molecular fluorescence. To further examine the origin of the 710 nm peak, we measured the spectrum of the same AuNR covered by MC-doped PMMA film using a 665 nm long-pass filter. As a result, only the scattering peak of the AuNR at 715 nm is observed, as shown in Figure 2.5a, which matches well with the fitted peak at ~710 nm. Thus, we conclude that the two peaks in Figure 2.4d arise from both the fluorescence of MC molecules and the scattering of the AuNR. The same conclusion

applies to other similar AuNRs, as shown in Figures 2.4e and f and Figures 2.5b and c. As indicated by the blue arrows in Figure 2.4d-f, MC molecules in the PMMA film cause a red shift in the scattering peak, as compared to that of the AuNR covered by pure PMMA film, which may be attributed to the increased refractive index of the PMMA film at the presence of MC molecules. In the previous studies, similar red shifts occurred to the LSPR peak wavelengths of metal NPs when the SP was isomerized into MC in the PMMA.[26-27] In our hybrid system, the red shift further reduces the overlap between the LSPR band and the absorption band of the MC molecules.

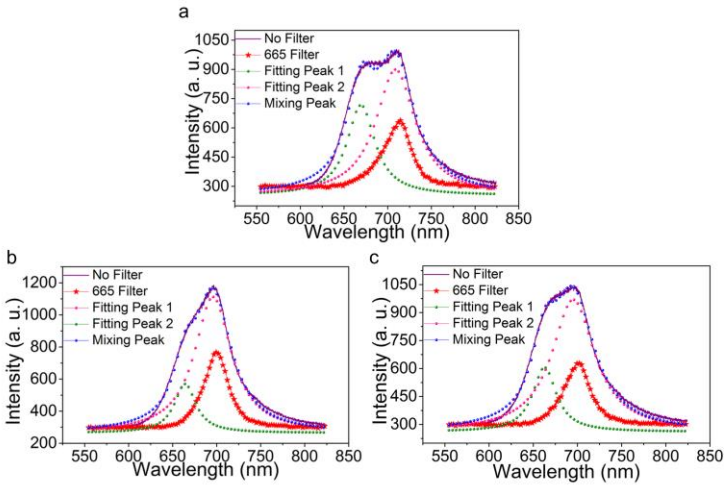

Figure 2.5: (a-c) Fitting the spectra with two peaks in Figures 2.4(d-f) with a Lorentzian model. The original spectra are indicated by "No filter". For each of the original spectra, the fitting leads to two Lorentzian peaks as indicated by "Fitting Peak 1" and "Fitting Peak 2". Cumulative spectra of two fitting spectra is indicated as "Mixing Peak". Also included is the scattering spectrum of an AuNR covered by the MC-doped PMMA film measured with the use of a 665 nm long-pass filter, as indicated by "665 filter".

The disappearance of the scattering peak in the first scenario (Figure 2.4a-c) indicates that there is energy transfer from the AuNR to MC molecules, which quenches the AuNR LSPR. The experimental observation confirms that the blue-shifted PIRET from

AuNRs to MC can occur when the LSPR band overlaps the absorption band of the molecules. Meanwhile, the red shifted FRET from MC to AuNRs can co-exist with the PIRET since there is also an overlap between the LSPR band and the emission band. When the pure dephasing time of LSPRs of AuNRs (> 10 fs) is larger than that of MC molecules,[15] the net energy transfer is from AuNRs to MC molecules, quenching the LSPR scattering.[4]

2.2.3 Plasmon-induced fluorescence enhancement and fluorescence lifetime imaging

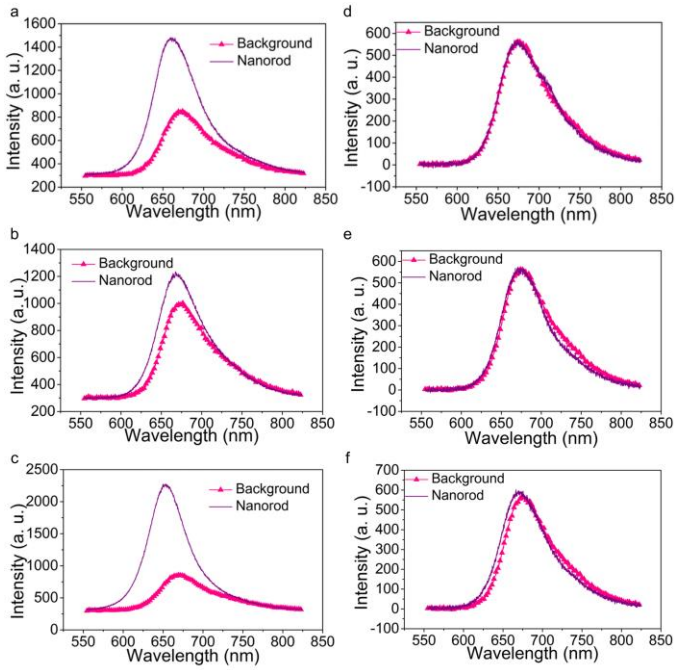

Figure 2.6: Fluorescence spectra from MC molecules at an AuNR (Nanorod) and from molecules that are far away from the AuNR (Background). (a-c) For the samples in (a-c), we observe enhanced fluorescence for the molecules at the AuNRs due to blue-shifted PIRET. (d-f) For the samples in Figures 3(d-f), no obvious fluorescence enhancement is observed. The fluorescence spectra of molecules at the AuNR were obtained by subtracting the "No Filter" spectrum with the "665 Filter" spectrum in Figure 2.4.

Besides the quenching of LSPR scattering, the resonance energy transfer is expected to enhance the molecular fluorescence.[12, 28] We observed the fluorescence

enhancement for MC molecules when the AuNR LSPR scattering band overlaps the emission band of MC molecules (Figure 2.6a-c). However, as shown in Figure 2.6d-f, no fluorescence enhancement occurs to MC molecules at the AuNRs in Figure 2.4d-f. Such a lack of fluorescence enhancement is consistent with the fact that the sample does not support blue-shifted PIRET because there is no overlap between LSPR and molecular absorption. The observed differences between Figure 2.6a-c and Figure 2.6d-f indicate that blue-shifted PIRET plays a critical role in the enhanced fluorescence of MC molecules. We also employed fluorescence lifetime imaging microscopy based on time-correlated single photon counting to measure the fluorescence lifetime of MC-doped PMMA films with and without AuNRs. The LSPR of these AuNRs overlaps with the molecular absorption band. More details on the measurements are provided in Experimental section. As shown in Figure 2.7, the average fluorescence lifetime (710.8 $\pm$ 46.3 ps) of MC-doped PMMA films with AuNRs is longer than that (636.6 $\pm$ 55.9 ps) for films without AuNRs, which further manifests that energy is transferred from AuNRs to MC molecules.[12, 29]

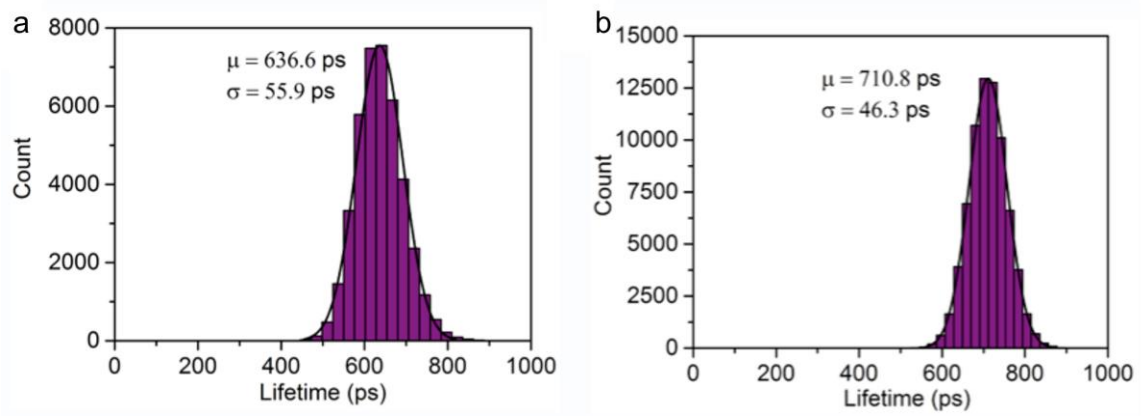

Figure 2.7: (a) Fluorescence lifetime of the MC-doped PMMA films. (b) Fluorescence lifetime of the MC-doped PMMA films with AuNRs where the LSPR spectrum overlaps with the molecular absorption spectrum.

Furthermore, we can rule out the contribution of radiative-rate modification via Purcell effect to the fluorescence enhancement.[30-32] The different results for the samples in Figures 2.6a-c and Figures 2.6d-f indicate that fluorescence enhancement occurs only when there are emission-absorption spectral overlaps. However, radiative-rate enhancement via Purcell effect does not require the emission-absorption spectral overlap, which indicates that Purcell effect is not a major factor in our fluorescence measurements.[30-32]

We further consider the differences in optical properties between AuNRs and dye molecules to identify the advantages of AuNRs over dye molecules as donors in resonant energy transfer. Compared with dye molecules, AuNRs have a larger absorption cross-section (4-5 orders larger than that of conventional dyes).[8] In addition, when the donor-acceptor distance increases, the energy transfer efficiency (Φ_{EnT}) of PIRET decays more slowly than that of FRET between two fluorophores.[11] The energy transfer efficiency (Φ_{EnT}) between the donor and the acceptor follows the equation: [11-12, 28,33]

$$\Phi_{EnT} = \frac{1}{1+\left(\frac{R}{R_0}\right)^n} \tag{2.2}$$

where R is the donor-acceptor distance, R_0 is the characteristic distance at which Φ_{EnT} is 50%, and n is 4 and 6 for PIRET and FRET, respectively, which indicates that the Φ_{EnT} in PIRET decreases more slowly than that in FRET when R increases.[11-12, 28,33] Therefore, both the larger absorption cross-section of AuNRs and the slower decay of energy transfer efficiency as a function of increased donor-acceptor distance lead to a larger amount of energy transfer through PIRET than that through FRET.

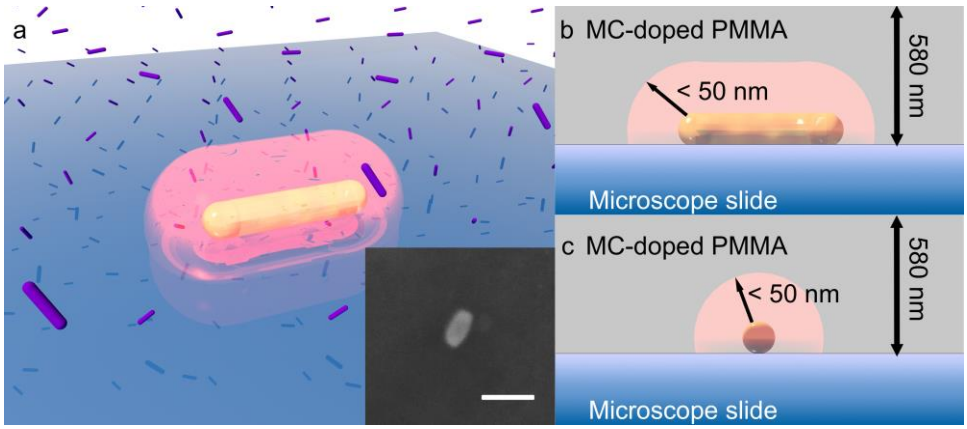

Figure 2.8: (a) Schematics of a single AuNR covered with the MC-doped PMMA thin film (thickness is 580 nm) on a glass slide. The single golden rod represents the AuNR, the purple rods illustrate MC molecules, and the red color displays the PIRET-active volume. (b) Cross-sectional view along the long axis of the AuNR in (a). (c) Cross-sectional view along the short axis of the AuNR in (a). Inset of Figure 2.8a is a representative SEM image of an individual AuNR on the substrate. Scale bar is 60 nm.

It is worth noting that there should be much larger fluorescence enhancement than our experimental measurements as shown in Figure 2.6a-c. This is because PIRET occurs within the volume near the AuNRs, which is much smaller than that from which fluorescence signals were measured. This highly confined volume accounts a small fraction of the total volume where the light signals were collected in our dark-field optical microscope since there is a dramatic decrease in the PIRET efficiency (Φ_{PIRET}) between the AuNR and molecules when the distance (R) between them increases (Equation 2.2).[11,33] However, it has remained challenging to calculate the actual average enhancement factor (EF) because of the difficulty in determining R_0, which is needed for the calculation of the PIRET-active volume in our system. Instead, we estimated a conservative average EF of up to 1854 by using the largest PIRET-active volume according to previous studies.[4, 11, 33-34] As per previous studies,[4, 11, 34] the energy transfer between dye molecules and an Au nanoparticle is limited in the volume near the particle where the donor-acceptor distance is

smaller than 50 nm. To estimate the average enhancement factors (EFs), we assume that the PIRET is limited in a volume within a distance of 50 nm[4, 11, 34] from the surfaces of AuNRs (Figure 2.8) and the MC concentration is uniform in PMMA. The average EF is defined by:

$$EF=\left(\frac{P_{AuNRs}}{P_{backgroud}}\right)\left(\frac{V_{backgroud}}{V_{AuNRs}}\right) \quad (2.3)$$

where P_{AuNRs} is the enhanced fluorescence intensity from MC molecules within the distance of 50 nm from the surfaces of AuNRs. The P_{AuNRs} is the difference between the integrated intensities of fluorescence spectra with and without an AuNR. $P_{background}$ is the integrated intensities of fluorescence spectrum without AuNRs. V_{AuNRs} is the PIRET-active volume, as indicated by red color in Figure 2.8. $V_{background}$ is the total volume from which we collected the fluorescence signals (1.92 μm × 1.92 μm × 580 nm). To calculate V_{AuNRs}, we use the largest dimensions (25 nm dia. × 73 nm length) and volumes of AuNRs from the data provided by the company that sold the AuNRs (see Experimental section). Based on Figure 2.4c, we obtain the maximum average EF of 1854. Since average EF $\propto 1/V_{AuNRs}$, the average EF is under-estimated due to the use of the maximum volume of the AuNRs. The variations in average EFs among different AuNRs and samples can be attributed to the variations in the MC concentrations. In contrast, we can see from Figures 2.6d-f that FRET hardly changes the fluorescence intensity because of the small amount of MC molecules involved in the process.

2.3 SUMMARY

In summary, we have demonstrated molecular-fluorescence enhancement through blue-shifted PIRET from single AuNRs to dye molecules. PIRET and fluorescence enhancement occur only when there is a significant spectral overlap between the light

scattering of AuNRs and the absorption of MC molecules. The fluorescence enhancement indicates that AuNRs can function as donors to enhance the fluorescence excitation of acceptors. AuNRs have two major advantages over dye molecules as donors: larger absorption cross-section and slower decay of energy transfer efficiency via donor-acceptor distance. Both effects lead to a lower intensity requirement for the incident light. Moreover, the blue-shifted PIRET allows the excitation of fluorescence of molecules near metal NPs using light of lower energy (i.e., longer wavelength). Therefore, blue-shifted PIRET provides a new pathway towards the design of NP-dye pairs for biosensing and bioimaging, with low excitation energy and high signal-to-noise ratio. In addition, the white-light excitation of both the fluorescence of dye molecules and the LSPRs of single AuNPs will enable the multiplexed sensing or imaging with different types of NP-dye pairs, using a dark-field microscope.

2.4 REFERENCES

1. Liu, G. L.; Long, Y.-T.; Choi, Y.; Kang, T.; Lee, L. P., Quantized plasmon quenching dips nanospectroscopy via plasmon resonance energy transfer. *Nat. Methods* **2007**, 4 (12), 1015-1017.
2. Choi, Y.; Kang, T.; Lee, L. P., Plasmon Resonance Energy Transfer (PRET)-based Molecular Imaging of Cytochrome c in Living Cells. *Nano Lett.* **2009**, 9 (1), 85-90.
3. Choi, Y.; Park, Y.; Kang, T.; Lee, L. P., Selective and sensitive detection of metal ions by plasmonic resonance energy transfer-based nanospectroscopy. *Nat. Nanotechnol.* **2009**, 4 (11), 742-746.
4. Li, J.; Cushing, S. K.; Meng, F.; Senty, T. R.; Bristow, A. D.; Wu, N., Plasmon-induced resonance energy transfer for solar energy conversion. *Nat. Photonics* **2015**, 9 (9), 601-607.
5. Cushing, S. K.; Li, J.; Meng, F.; Senty, T. R.; Suri, S.; Zhi, M.; Li, M.; Bristow, A. D.; Wu, N., Photocatalytic Activity Enhanced by Plasmonic Resonant Energy Transfer from Metal to Semiconductor. *J. Am. Chem. Soc.* **2012**, 134 (36), 15033-15041.
6. Cushing, S. K.; Li, J.; Bright, J.; Yost, B. T.; Zheng, P.; Bristow, A. D.; Wu, N., Controlling Plasmon-Induced Resonance Energy Transfer and Hot Electron

Injection Processes in Metal@TiO_2 Core–Shell Nanoparticles. *J. Phys. Chem. C* **2015**, 119 (28), 16239-16244.

7. Li, J.; Cushing, S. K.; Zheng, P.; Meng, F.; Chu, D.; Wu, N., Plasmon-induced photonic and energy-transfer enhancement of solar water splitting by a hematite nanorod array. *Nat. Commun.* **2013**, 4, 2651.

8. Jain, P. K.; Lee, K. S.; El-Sayed, I. H.; El-Sayed, M. A., Calculated Absorption and Scattering Properties of Gold Nanoparticles of Different Size, Shape, and Composition: Applications in Biological Imaging and Biomedicine. *J. Phys. Chem. B* **2006**, 110 (14), 7238-7248.

9. Hu, M.; Chen, J.; Li, Z.-Y.; Au, L.; Hartland, G. V.; Li, X.; Marquez, M.; Xia, Y., Gold nanostructures: engineering their plasmonic properties for biomedical applications. *Chem. Soc. Rev*. **2006**, 35 (11), 1084-1094.

10. Chen, H.; Shao, L.; Li, Q.; Wang, J., Gold nanorods and their plasmonic properties. *Chem. Soc. Rev.* **2013**, 42 (7), 2679-2724.

11. Yun, C. S.; Javier, A.; Jennings, T.; Fisher, M.; Hira, S.; Peterson, S.; Hopkins, B.; Reich, N. O.; Strouse, G. F., Nanometal Surface Energy Transfer in Optical Rulers, Breaking the FRET Barrier. *J. Am. Chem. Soc.* **2005**, 127 (9), 3115-3119.

12. Clapp, A. R.; Medintz, I. L.; Mattoussi, H., Förster Resonance Energy Transfer Investigations Using Quantum-Dot Fluorophores. *ChemPhysChem* **2006**, 7 (1), 47-57.

13. Perillo, E. P.; Liu, Y.-L.; Huynh, K.; Liu, C.; Chou, C.-K.; Hung, M.-C.; Yeh, H.-C.; Dunn, A. K., Deep and high-resolution three-dimensional tracking of single particles using nonlinear and multiplexed illumination. *Nat. Commun.* **2015**, 6 (7874).

14. Warren, S. C.; A. M., Alibhai, D.; J. Kelly, D.; Talbot, C.; Alexandrov, Y.; Munro, I.; Katan, M.; Dunsby, C.; French, P. M. W., Rapid Global Fitting of Large Fluorescence Lifetime Imaging Microscopy Datasets, *PLoS ONE* **2013**, 8, e70687.

15. Sönnichsen, C.; Franzl, T.; Wilk, T.; von Plessen, G.; Feldmann, J.; Wilson, O.; Mulvaney, P., Drastic Reduction of Plasmon Damping in Gold Nanorods. *Phys. Rev. Lett.* **2002**, 88 (7), 077402.

16. Ringe, E.; Sharma, B.; Henry, A.-I.; Marks, L. D.; Van Duyne, R. P., Single nanoparticle plasmonics. *Phys. Chem. Chem. Phys.* **2013**, 15 (12), 4110-4129.

17. Rajeeva, B. B.; Hernandez, D. S.; Wang, M.; Perillo, E.; Lin, L.; Scarabelli, L.; Pingali, B.; Liz-Marzán, L. M.; Dunn, A. K.; Shear, J. B.; Zheng, Y., Regioselective Localization and Tracking of Biomolecules on Single Gold Nanoparticles. *Adv. Sci.* **2015**, 2 (11), 1500232.

18. Ni, W.; Ambjörnsson, T.; Apell, S. P.; Chen, H.; Wang, J., Observing Plasmonic−Molecular Resonance Coupling on Single Gold Nanorods. *Nano Lett.* **2010**, 10 (1), 77-84.

19. Anker, J. N.; Hall, W. P.; Lyandres, O.; Shah, N. C.; Zhao, J.; Van Duyne, R. P., Biosensing with plasmonic nanosensors. *Nat. Mater.* **2008**, 7 (6), 442-453.

20. Ming, T.; Zhao, L.; Yang, Z.; Chen, H.; Sun, L.; Wang, J.; Yan, C., Strong Polarization Dependence of Plasmon-Enhanced Fluorescence on Single Gold Nanorods. *Nano Lett.* **2009**, 9 (11), 3896-3903.

21. Ming, T.; Zhao, L.; Xiao, M.; Wang, J., Resonance-Coupling-Based Plasmonic Switches. *Small* **2010**, 6 (22), 2514-2519.

22. McFarland, A. D.; Van Duyne, R. P., Single Silver Nanoparticles as Real-Time Optical Sensors with Zeptomole Sensitivity. *Nano Lett.* **2003**, 3 (8), 1057-1062.

23. Sherry, L. J.; Jin, R.; Mirkin, C. A.; Schatz, G. C.; Van Duyne, R. P., Localized Surface Plasmon Resonance Spectroscopy of Single Silver Triangular Nanoprisms. *Nano Lett.* **2006**, 6 (9), 2060-2065.

24. Sherry, L. J.; Chang, S.-H.; Schatz, G. C.; Van Duyne, R. P.; Wiley, B. J.; Xia, Y., Localized Surface Plasmon Resonance Spectroscopy of Single Silver Nanocubes. *Nano Lett.* **2005**, 5 (10), 2034-2038.

25. Link, S.; El-Sayed, M. A., Size and Temperature Dependence of the Plasmon Absorption of Colloidal Gold Nanoparticles. *J. Phys. Chem. B* **1999**, 103 (21), 4212-4217.

26. Dintinger, J.; Klein, S.; Ebbesen, T. W., Molecule–Surface Plasmon Interactions in Hole Arrays: Enhanced Absorption, Refractive Index Changes, and All-Optical Switching. *Adv. Mater.* **2006**, 18 (10), 1267-1270.

27. Zheng, Y. B.; Kiraly, B.; Cheunkar, S.; Huang, T. J.; Weiss, P. S., Incident-Angle-Modulated Molecular Plasmonic Switches: A Case of Weak Exciton–Plasmon Coupling. *Nano Lett.* **2011**, 11 (5), 2061-2065.

28. Sapsford, K. E.; Berti, L.; Medintz, I. L., Materials for Fluorescence Resonance Energy Transfer Analysis: Beyond Traditional Donor–Acceptor Combinations. *Angew. Chem. Int. Ed.* **2006**, 45 (28), 4562-4589.

29. Kagan, C. R.; Murray, C. B.; Nirmal, M.; Bawendi, M. G., Electronic Energy Transfer in CdSe Quantum Dot Solids. *Phys. Rev. Lett.* **1996**, 76 (9), 1517-1520.

30. Anger, P.; Bharadwaj, P.; Novotny, L., Enhancement and Quenching of Single-Molecule Fluorescence. *Phys. Rev. Lett.* **2006**, 96 (11), 113002.

31. Rose, A.; Hoang, T. B.; McGuire, F.; Mock, J. J.; Ciracì, C.; Smith, D. R.; Mikkelsen, M. H., Control of Radiative Processes Using Tunable Plasmonic Nanopatch Antennas. *Nano Lett.* **2014**, 14 (8), 4797-4802.

32. Akselrod, G. M.; Argyropoulos, C.; Hoang, T. B.; Ciracì, C.; Fang, C.; Huang, J.; Smith, D. R.; Mikkelsen, M. H., Probing the mechanisms of large Purcell enhancement in plasmonic nanoantennas. *Nat. Photonics* **2014**, 8 (11), 835-840.

33. Sen, T.; Sadhu, S.; Patra, A., Surface energy transfer from rhodamine 6G to gold nanoparticles: A spectroscopic ruler. *Appl. Phys. Lett.* **2007**, 91 (4), 043104.

34. Griffin, J.; Singh, A. K.; Senapati, D.; Rhodes, P.; Mitchell, K.; Robinson, B.; Yu, E.; Ray, P. C., Size- and Distance-Dependent Nanoparticle Surface-Energy Transfer (NSET) Method for Selective Sensing of Hepatitis C Virus RNA. Chem. Eur. J. **2009**, 15 (2), 342-351.

Chapter 3 Plasmon-Trion and Plasmon-Exciton Resonance Energy Transfer from a Single Plasmonic Nanoparticle to Monolayer MoS_2*

3.1 INTRODUCTION

Among different 2D materials, MoS_2 monolayers have been extensively studied as key components in optoelectronic devices,[1-5] to achieve high ON/OFF current ratios, negligible OFF current, low sub-threshold switching, strong photoluminescence, controllable valley polarization and high thermal stability.[5-11] Despite its large absorption coefficient, optical absorption of excitons in monolayer MoS_2 is weak (<11%) due to its atomic thickness, thereby limiting its optoelectronic applications.[12-13] Because of the ability of surface plasmons (SPs) to concentrate light beyond the diffraction limit, plasmonic metal NPs have been exploited to enhance light-matter interactions in 2D materials.[14-22]

Moreover, energy and electron transfer can occur between plasmonic metal NPs and the nearby 2D materials.[12, 23-25] It is theoretically predicted that RET between plasmonic metal NPs and transition metal dichalcogenide (TMD) monolayers such as monolayer MoS_2 is highly efficient. Briefly, by considering the exciton as a hydrogen-like system and solving a hydrogen Schrődinger equation in a 2D space, it has been concluded that the exciton binding energy of 2D excitons in monolayer MoS_2 is 4-fold that of its 3D counterpart.[26-27] In addition, the reduced dielectric screening derived from the atomic thickness of monolayer MoS_2 strengthens the Coulomb interaction between the electron and hole of excitons, which is expected to further increase exciton binding energy. This large exciton binding energy yields a large oscillator strength,[28] thus boosting the efficiency

* Wang, M.; Li, W.; Scarabelli, L.; Rajeeva, B. B.; Terrones, M.; Liz-Marzán, L. M.; Akinwande, D.; Zheng, Y., Plasmon–trion and plasmon–exciton resonance energy transfer from a single plasmonic nanoparticle to monolayer MoS_2. *Nanoscale* 2017, 9 (37), 13947-13955.
Wang, M. carried out the experimental work and participated in the preparation of manuscript.

of RET between SPs and excitons in hybrids made of metal NPs and monolayer MoS_2 (see Equation 3.1).[29]

Additionally, the increased exciton binding energy makes it feasible to observe charged excitons (i.e., trions) in monolayer MoS_2 at room temperature, with a population that can be tuned by varying the dielectric constant of the environment.[11, 30] Therefore, the NP-MoS2 hybrid is a unique platform toward exploring the interactions between SPs and trions at room temperature. Understanding and controlling the SP-trion interaction will lead to new devices that benefit from the light-induced charge transport and negative photoconductivity via trion excitation.[31-32]

Herein, we report the first observation and tuning of plasmon-trion and plasmon-exciton RET from a single plasmonic NP to monolayer MoS_2. We achieved these through rational design of hybrid NP-2D systems and single-nanoparticle measurements. By combining experiments with theoretical calculations, we conclude that large quantum confinement and reduced dielectric screening in monolayer MoS_2 allow for efficient RET between SPs of metal NPs and excitons or trions in monolayer MoS_2, and enable the study of the plasmon-trion interactions at room temperature.[33]

3.2 RESULTS AND DISCUSSION

3.2.1 Experimental section

3.2.1.1 CVD growth and transfer process for MoS2

The atomic-layer MoS_2 was grown by chemical vapor deposition using a Thermo Scientific Lindberg/Blue M Tube Furnace. Alumina crucible with 15 mg MoO_3 powder was loaded at the middle zone of a quartz tube with an inner diameter of 22 mm, and a surface-cleaned Si substrate (with 285 nm SiO_2 on the surface) was located right above the

MoO_3 source crucible. Another alumina crucible containing 1g sulfur powder was loaded outside the heating zone of the furnace and heated independently.

After loading the starting material and the substrates, the tube was pumped down to base pressure (< 10 mTorr), and purged by flowing in Ultra High Purity N_2 gas at 200 sccm. After 4 purging cycles, the tube was filled with N_2 gas to 1 atm pressure at flow rate of 10 sccm. The temperature of the furnace was raised to 850°C at a rate of 50°C/min, and the sulfur was heated to 150°C (+/- 5°C) using a heating tape. The growth lasted for 5 min at 850 °C, and the furnace was cooled down to room temperature. When the furnace temperature was reduced to 650°C, the heating of sulfur was cut off.

The as-grown MoS_2 was transferred from the SiO_2/Si substrate to a glass substrate using wet transfer process. Briefly, PMMA was spin-coated onto the MoS_2 at 4000 rpm for 40 s and baked at 180 ˚C for 2 min. The coating and baking process were repeated for ten times and the thickness of the resulted PMMA layer was about 2 μm. Buffered oxide etch (BOE) solution was used to etch away the SiO_2 under MoS_2. This enabled the PMMA-supported MoS_2 to be separated from the Si substrate, which was transferred onto a glass substrate. After the transfer, the sample was kept in the desiccator for 12 hours and baked at 180 ˚C for 2 min to improve the adhesion between MoS_2 and substrate. Finally, the PMMA layer was dissolved by soaking the sample in acetone for 2 hours.

3.2.1.2 AuNT synthesis

AuNTs were synthesized with our established method.[34] The initial Au seed solution was prepared by the standard CTAC/$NaBH_4$ procedure: 25 μL of a 0.05 M $HAuCl_4$ solution was added to 4.7 mL of 0.1 M CTAC solution, and then 300 μL of a 0.01 M $NaBH_4$ solution was injected under vigorous stirring. Excess borohydride was consumed by keeping the seed solution for 2 hours at room temperature before use. To synthesize, e.g.,

40mL of AuNT solution, two different solutions were prepared. The first solution (solution 1) was obtained by adding 1.6 mL of a 0.1 M CTAC solution to 8 mL of Milli-Q water, followed by 40 μL of 0.05 M $HAuCl_4$ solution and 15 μL of a 0.01 M NaI solution; the second solution (solution 2) was gained by adding 500 μL of a 0.05 M $HAuCl_4$ solution to 40 mL of 0.05 M CTAC, followed by 300 μL of a 0.01 M NaI solution. The solution 1 was employed to grow Au seeds into larger nanoparticles, while the solution 2 was used as the AuNT growth batch. Before the AuNT growth proceeding, the initial seed solution was diluted 10 times in a 0.1 M CTAC solution. Following that, 40 and 400 μL of 0.1 M AA solution were added to solutions 1 and 2, respectively. Both solution 1 and 2 were then manually stirred until the complete transparency of solutions was achieved. Finally, to grow 150 nm or 60 nm AuNTs, 100 or 1200 μL of the diluted seed solution was added to solution 1 (and manually stirred for 1 second), and immediately 3.2 mL of this solution was added to solution 2 (and manually stirred for several seconds). The obtained AuNT solution was left undisturbed at room temperature for at least 1 hour.

3.2.1.3 Optical meansurements

AuNTs were drop-coated on the top of monolayer MoS_2. Scattering spectra of single AuNTs and transmission spectra of monolayer MoS_2 were measured through an optical microscope (Ti-E inverted microscope, Nikon) integrated with a spectrograph and an EMCCD (Andor). A halogen white light source (12V, 100 W) is used. The interparticle separation was controlled to be several μm, which is large enough to extract signals from a single nanoparticle. Then the scattering signal from a targeted single nanoparticle was obtained by blocking all the irrelevant scattering signals from other nanoparticles through

a slit in the spectrograph and selected pixels of an EMCCD camera. To measure the sample that was surrounded by hexane, toluene, ethanol or water, we sandwiched the solvent between the sample and a cover glass. Raman and fluorescence spectra were obtained with a micro-Raman system (Witec Micro-Raman Spectrometer Alpha 300) with a 488 nm excitation laser.

3.2.1.4 FDTD simulation

Our FDTD simulations were conducted using a commercially available software package (FDTD Solutions, Lumerical). A plane wave was applied as the incident light source. The scattered light was collected in a transmission manner. The wavelength-dependent dielectric functions of Au were adapted from Johnson and Christy.[35]

3.2.2 Design of hybrid plasmon-TMDCs system

We chose to study hybrid systems consisting of Au nanotriangles (AuNTs) deposited on CVD-grown monolayer MoS_2 (Figure 3.1a), which are expected to have large RET efficiency. Theoretical studies have revealed that RET efficiency strongly depends on the relative orientation of the excited dipoles of donors and acceptors, as indicated by:[29]

$$k_{\mathrm{RET}} = \frac{q_e^2 \kappa^2}{16\pi m_e^2 (4\pi\varepsilon_0)^2 n^2 R^6} \int \frac{f_{eD}(v) f_{aA}(v) dv}{v^2} \tag{3.1}$$

where f_{eD} and f_{aA} are the oscillator strengths for the donor and acceptor, q_{e} is the charge of an electron, m_{e} is the mass of an electron, n is the refractive index of the medium, ε_0 is the permittivity of vacuum, κ is a coefficient that depends on the relative orientation between donor and acceptor (κ^2 changes from 0 from 4 when the relative orientation between the donor and acceptor varies from orthogonal to parallel orientation),[36] R is the distance between the donor and acceptor, and v is the frequency. When the orientation of excited

dipoles in the donor has the same orientation as that in the acceptors (i.e., κ is higher), RET is enhanced.[29, 37]

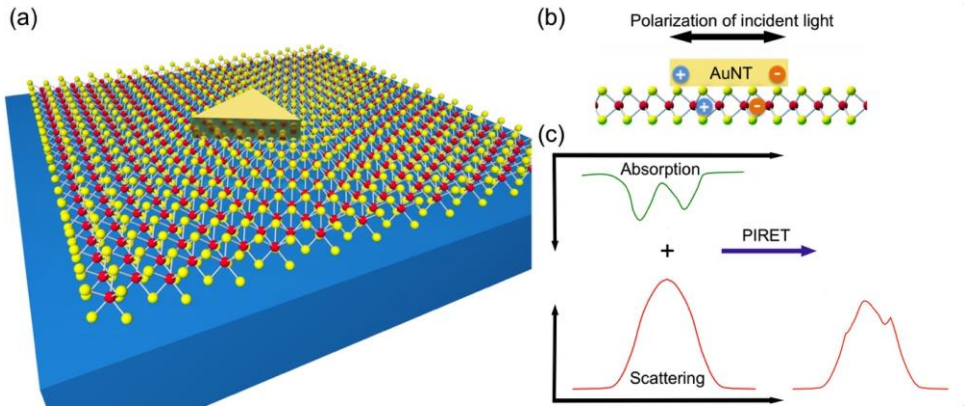

Figure 3.1: Schematics of (a) the sample configuration; (b) the relative orientation between a dipole in a single AuNT and that in monolayer MoS_2; and (c) PIRET-induced dips in the scattering spectrum of hybrid metal NP and monolayer MoS_2 where the absorption peaks of MoS_2 overlap the scattering peak of the NP. On the left-hand side of (c), the green spectrum is the inverted absorption spectrum of monolayer MoS_2 and the red spectrum is the scattering of the NP. On the right-hand side of (c), the red spectrum is the scattering of hybrid metal NP and monolayer MoS_2, which displays dips matching the absorption peaks of monolayer MoS_2.

For MoS_2 monolayers, the exciton orientation is confined along the in-plane direction due to strong geometric confinement. Chemically synthesized AuNTs can accommodate strong in-plane plasmon resonances[34, 38-44] and make intimate contact with monolayer MoS_2 due to their atomically flat surfaces, as shown in Figure 3.1a. Therefore, in hybrid systems of AuNTs on monolayer MoS_2, the dipole orientation of AuNTs can be properly aligned with the exciton orientation of MoS_2 to maximize k_{RET} (Figure 3.1b). Moreover, monolayer MoS_2 is a direct band gap semiconductor with large exciton binding energy,[8, 33, 45] which can support trions at room temperature.[33] Therefore, we hypothesize

that it should be possible to observe both plasmon-exciton and plasmon-trion RET in the hybrid systems.

3.2.3 Setups for optical measurement

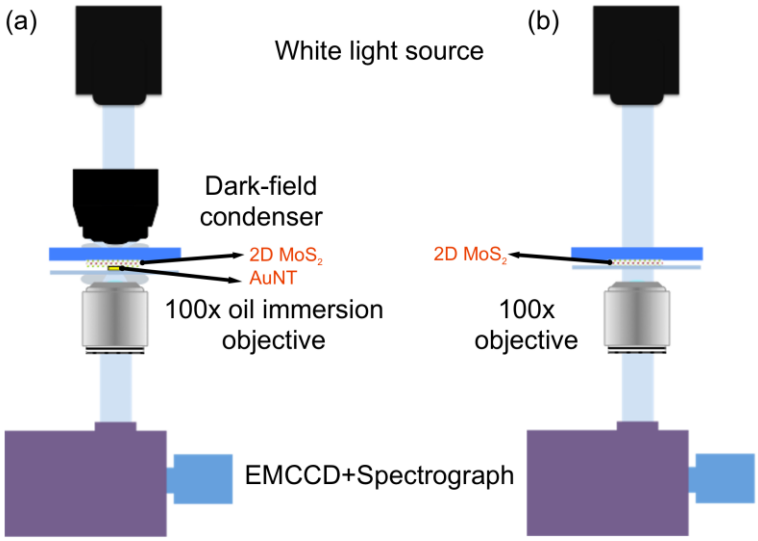

Figure 3.2: Schematic of optical setups for (a) dark-field scattering measurement and (b) transmission measurement.

Because the light absorption by excitons in monolayer MoS_2 is low (<11%),[13] without interaction with LSPR absorption, plasmon-exciton and plasmon-trion RET are weak and difficult to detect. At the single-NP level, the plasmon resonance peak wavelength can be precisely tuned via NP geometric control,[42, 46-47] and thus a good match can be achieved with the absorption peak wavelength of monolayer MoS_2, which is required to achieve the maximum RET rate. Moreover, it has been reported that PIRET can exhibit resonance dips in the scattering spectrum of a plasmonic NP, corresponding to the absorption peaks of acceptors (Figure 3.1c).[48-49] Detailed information on the experimental method and optical setup can be found in Experimental section and Figure 3.2. We

employed single-NP optical spectroscopy to study RET processes in the hybrid systems, due to its high sensitivity and resolution.

3.2.4 Characterization of monolayer MoS_2

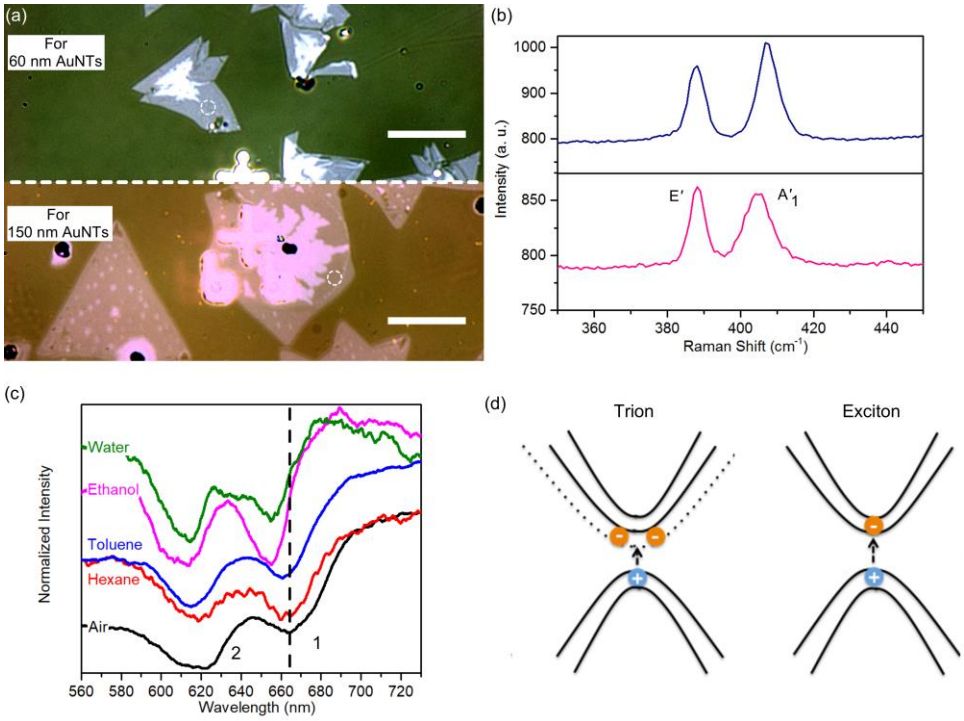

Figure 3.3: (a) Optical image of pieces of monolayer MoS_2 on a glass substrate, which were covered with (top) 60 nm and (bottom) 150 nm AuNTs after transmission and Raman measurements, respectively. Scale bar is 20 μm (b) Raman scattering spectra from selected areas of monolayer MoS_2 as indicated by the white dashed circles in (a). The top (bottom) spectrum corresponds to top (bottom) monolayer MoS_2 in (a). (c) Transmission spectra of monolayer MoS_2 in the top panel of (a) with 5 different surrounding media: air (black), hexane (red), toluene (blue), ethanol (pink), and water (green). 1 and 2 in (c) indicate the transmission dips of A and B excitons, respectively. (d) Schematics of the band structures of trion and exciton of monolayer MoS_2.

CVD-grown monolayers of MoS_2 were employed to study RET between monolayer MoS_2 and AuNTs with two different sizes (edge lengths of 150 nm and 60 nm). Optical

images of monolayer MoS_2 on a glass substrate are shown in Figure 3.3a. Monolayer MoS_2 was grown on a SiO_2/Si substrate by CVD and transferred onto glass substrates using a wet transfer process (more details in Experimental section). The monolayer MoS_2 was covered with 150 or 60 nm AuNTs. Markers were created on the glass substrates to locate the targeted MoS_2 and AuNTs. The monolayer MoS_2 can be identified based on the image contrast (e.g., those indicated by white circles in Figure 3.3a).[50] Raman scattering spectra from the areas within white circles were collected to confirm the presence of monolayer MoS_2.[50-52] As shown in Figure 3.3b, the Raman spectra display two peaks at about 386 cm^{-1} and 406 cm^{-1} that match the out-of-plane E′ mode and the in-plane A'_1 mode of monolayer MoS_2, respectively.[53-54] An AFM image of a MoS_2 flake is shown in Figure 3.4, which further confirms the atomic thickness of our CVD-grown monolayer MoS_2. The transmission spectra in Figure 3.3c indicate that monolayer MoS_2 in air has two absorption peaks at 664 nm and 620 nm (dip 1 and dip 2), which match the absorption peak wavelengths of A exciton and B exciton of monolayer MoS_2, respectively.[12] In air, the A exciton absorption peak (or transmission dip 1 in Figure 3.3c) is a mixture of absorption by uncharged exciton and charged exciton.[11, 32-33, 55] Hereafter, we denote the uncharged A exciton as A exciton and the charged A exciton as A^- trion.

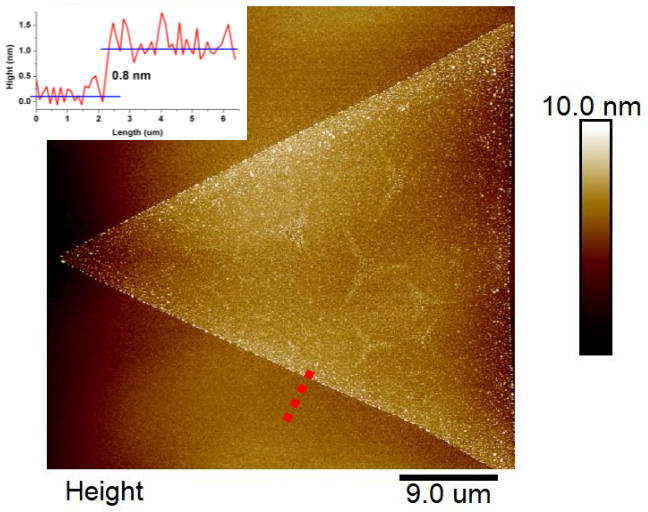

Figure 3.4: AFM image of a triangular MoS_2 crystal. Inset is step-height measurement from substrate to monolayer (0.8 nm), as indicated by the red dash line.

It has been reported that a surrounding medium with high dielectric constant increases the dielectric screening, which in turn reduces the exciton binding energy and thus the trion population.[11, 30] As shown in Figure 3.3d, the absorption band energy of trions is smaller than that of excitons. Without strong dielectric screening, the 1 transmission dip is a superposition of the exciton and trion absorption peaks. Thus, the reduction in the trion population will weaken the trion absorption and shift the absorption peak of the mixture of excitons and trions (i.e., transmission dip 1 in Figure 3.3c) to shorter wavelengths. Moreover, for the same reason, the reduction of the trion absorption also reduces the full width at half maximum (FWHM) of transmission dip 1. In order to verify our analysis experimentally, 4 non-ionic solvents with different static dielectric constants (ε_r: hexane-1.9, toluene-2.4, ethanol-25.3 and DI-water-80.1) were used to tune the exciton binding energy and trion population. It should be noticed that ε_r is not a permittivity at optical frequency, but a relative permittivity obtained under a static or low-frequency E-field. The use of nonionic solvents prevents the potential doping of monolayer MoS_2 from ions.[11] The

transmission spectra of monolayer MoS_2 covered by air and the 4 different solvents are shown in Figure 3.3c. A blue shift of A and B exciton absorption peaks (9 nm and 10 nm) is observed. The blue shift of B exciton absorption peak can also arise from an increase in dielectric screening. Since the absorption peak of B excitons is away from the scattering peak of AuNTs, we will not further discuss the changes in B excitons. Transmission spectra of monolayer MoS_2 surrounded by air and ethanol are shown in Figure 3.5a, to clearly reveal the spectral changes. When monolayer MoS_2 is surrounded by air, the transmission dip 1 is located at 664 nm. When ethanol covers the monolayer MoS_2, the transmission dip 1 shifts to 655 nm with a reduced FWHM (from ~26 nm to ~18 nm). The peak positions of A exciton absorption, obtained from 5 different areas, are summarized in Figure 3.5b and Table 3.1. Figure 3.5b indicates that no further blue shift occurs when ε_r is increased from 25.3 to 80.1. Consistent with the previously reported results, the saturation of the blue-shift is derived from the extremely small trion binding energy in high ε_r solvents.[11]

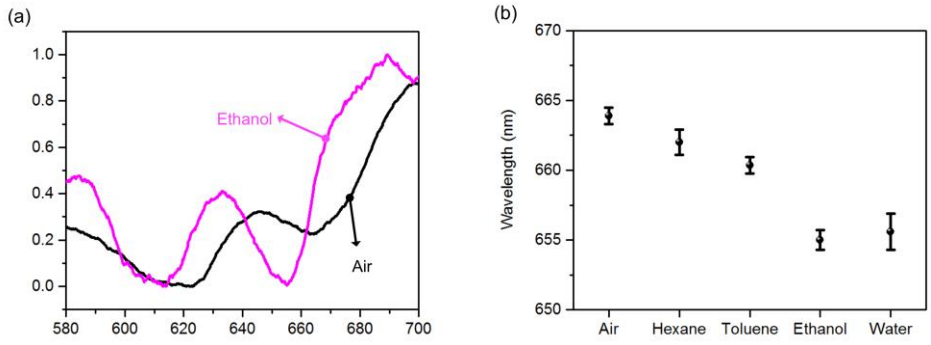

Figure 3.5: (a) Transmission spectra of monolayer MoS_2 covered by air (black) and ethanol (pink). (b) Medium-dependent wavelengths of the dip 1 in the transmission spectra in Figure 3.3c. Five different areas were measured for each medium.

Surrounding medium	ε_r	n	Transmission dip (nm)
Air	1	1	663.9±0.6
Hexane	1.89	1.375	662.0±0.9
Toluene	2.38	1.497	660.4±0.6
Ethanol	25.3	1.361	655.5±0.7
Water	80.1	1.333	655.6±1.3

Table 3.1: Dielectric constant (ε_r) and refractive index (n) of five different surrounding media along with the dip wavelengths of the transmission spectra in Figure 3.5b.

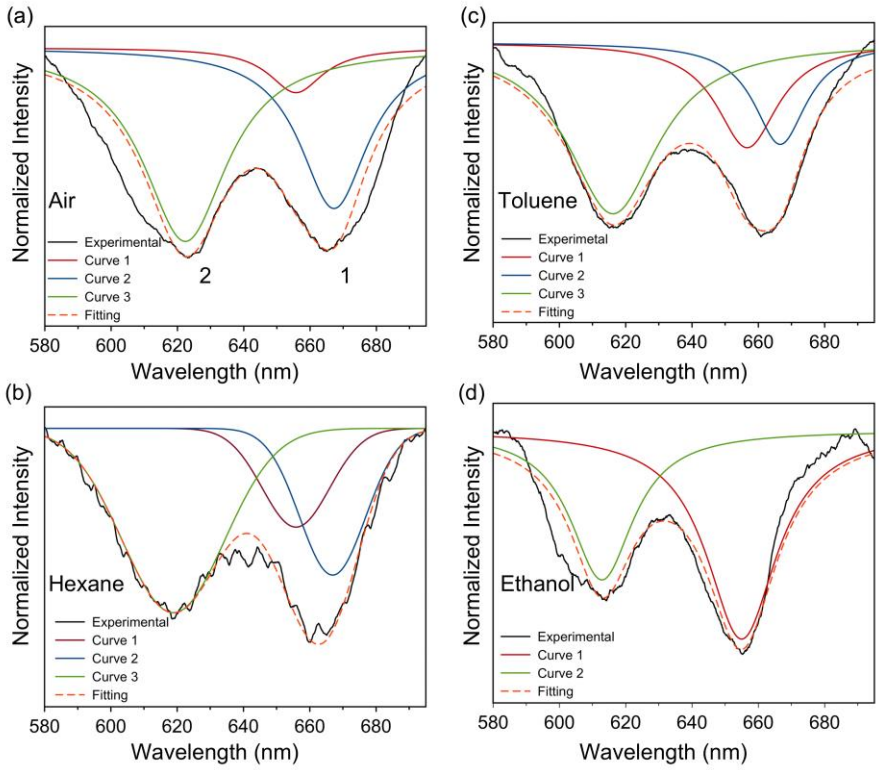

Figure 3.6. The fitting curves of the transmission spectra of monolayer MoS_2 in air (a), hexane (b), toluene (c) and ethanol (d). The peaks of the red and blue curve are fixed at 655 nm and 670 nm, respectively.

To further analyze the spectral contribution of excitons and trions to dip 1, we fitted the transmission spectra in Figure 3.3c with Lorentzians, as shown in Figure 3.6. Because the absorption peaks of A excitons and A^- trions are at ~655 nm and ~670 nm at room temperature, respectively,[56] we fixed two Lorentzian peaks (the red and blue curve) in Figures 3.6a, b and c at these two wavelengths for fitting the dip 1. Figures 3.6a, b and c also show that the depth of A exciton dip (red) increases while that of the A^- trion dip (blue) decrease with the dielectric constant of surroudning media. Table 3.2 summarizes the contribution of excitons and trions to the dip 1. Moreover, as can be seen in Figure 3.3c, when monolayer MoS_2 was surrounded by ethanol or water, the dip 1 was at ~655 nm. In this situation, we assumed that there were only excitons in monolayer MoS_2, and the fitted transmission spectrum of monolayer MoS_2 surrounded by ethanol is shown in Figure 3.6d as an example. We also found that the contribution of exitons to the transmission dip 1 has a linear relationship with the wavelength of the dip 1, as shown in Figure 3.7. Therefore, we assumed the scattering dip 1' in Figure 3.12e also follows the same relationship and estimated the contribution of plasmon-exciton and plasmon-trion RET to dip 1' with different surrounding media, as listed in Table 3.2.

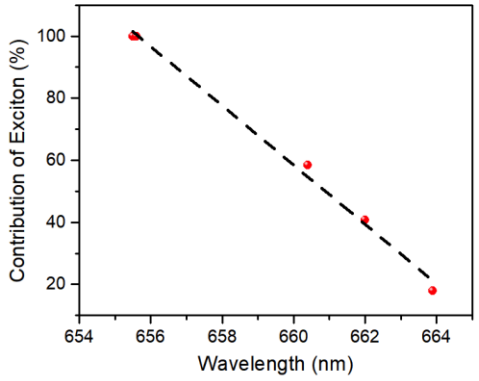

Figure 3.7: The linear relationship between the contribution of excitons to dip 1 and the dip 1 wavelength.

Surrounding medium	Contribution of exciton (%)	Contribution of trion (%)	Contribution of plasmon-exciton RET (%)	Contribution of plasmon-trion RET (%)
Air	17.9	82.1	20.2	79.8
Hexane	40.8	59.2	58.4	41.6
Toluene	54.8	45.2	77.5	22.5
Ethanol	~100.0	~0	87.0	13.0
Water	~100.0	~0	96.6	3.4

Table 3.2: The estimated contribution of excitons and trions to dip 1 in Figure 3.3c and plasmon-exciton and plasmon-trion RET to dip 1' in Figure 3.12e.

3.2.5 Plasmon-trion and plasmon-exciton resonance energy transfer

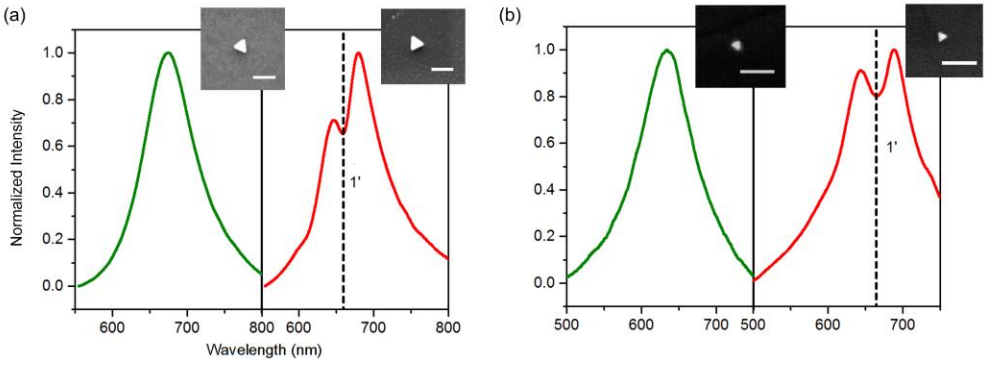

Figure 3.8: (a) Scattering spectra of single 150 nm AuNTs on a glass substrate (green) and on MoS_2 (red). (b) Scattering spectra of single 60 nm AuNTs on a glass substrate (green) and on MoS_2 (red). Insets are SEM images of the corresponding AuNTs and the scale bars are 250 nm.

The scattering spectra of single 150 nm and 60 nm AuNTs on a glass substrate are presented in the left panels of Figures 3.8a and b, respectively. Optical absorption spectra of the AuNTs are shown in Figure 3.9.[34] The spectra indicate that single 150 or 60 nm

AuNTs have localized surface plasmon resonance (LSPR) peaks at about 674 or 630 nm, which are close to the A exciton absorption peak wavelength (664 nm in air) of monolayer MoS_2.[8] The LSPR peak positions of single 150 nm and 60 nm AuNTs were also confirmed by FDTD simulations, as shown in Figure 3.10. The scattering spectra of single 150 nm and 60 nm AuNTs on monolayer MoS_2 show a dip at about 664 nm (as indicated by 1'; right panels of Figure 3.8a and 3.8b), which matches the absorption of the mixed A exciton and A^- trion of monolayer MoS_2 in air.[8, 33] Figure 3.8 also shows that the scattering dip 1' position was not affected by the LSPR peak, which further confirms that the dip 1' arises from the absorption of A excitons.

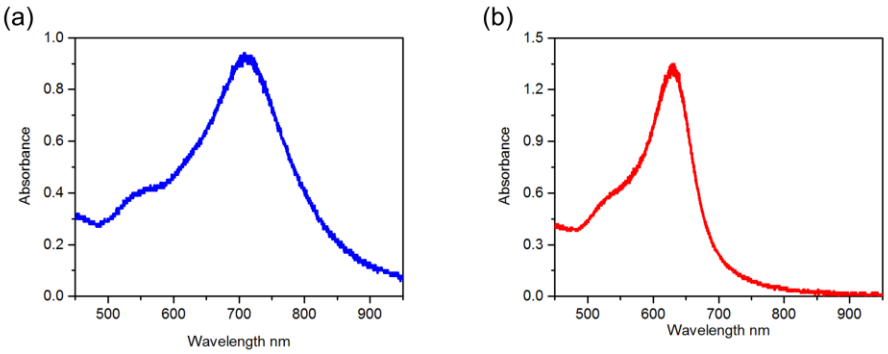

Figure 3.9: Absorption spectra of (a) 150 nm and (b) 60 nm AuNTs in solution.

It should be noted that the scattering dips show more than 20% decrease of the maximum intensity. This implies that the obtained scattering spectra of AuNT-MoS_2 hybrids cannot be a mere superposition of the optical absorption (less than 11%) of monolayer MoS_2 and the scattering of AuNTs with no interaction between monolayer MoS_2 and AuNTs. The dips in the scattering spectra indicate that either plasmon-induced RET or plasmon-enhanced absorption occur in our system. We believe that the plasmon-induced RET and plasmon-enhanced absorption in our AuNT-MoS_2 hybrids are essentially the same phenomena. In order to achieve plasmon-enhanced absorption, LSPRs of AuNTs

need to be excited first. When LSPRs are excited, the electromagnetic local density of states of AuNT-MoS_2 hybrids is increased and the absorption of the whole hybrid is enhanced.[57-58] In the meantime, monolayer MoS_2 and AuNTs exchange energy coherently until the exciton of MoS_2 or the plasmon of AuNTs decays. Eventually, the energy transfers to the region that has the longer dephasing time.[37, 59] Since the dephasing time of excitons in monolayer MoS_2 is longer than that of LSPRs of AuNTs,[37, 60-61] the energy eventually transfers from AuNTs to monolayer MoS_2. When referring to the interaction between monolayer MoS_2 and AuNTs, we conclude that our result manifests as plasmon-induced RET. When considering monolayer MoS_2, we conclude that our result indicates plasmon-enhanced absorption. Therefore, the dips in the scattering spectra suggest that plasmon-exciton and plasmon-trion RET occur from single AuNTs to monolayer MoS_2. It should be mentioned that the energy exchange between plasmons and excitons can also lead to the Fano resonance.[62-63] We exclude the possibility of the Fano resonance because no obvious asymmetric spectral feature (which is a characteristic of the Fano resonance) was observed in the spectra. In addition, the Fano resonance arises from quantum interactions between a broad "bright" mode and a narrow "dark" mode. The relatively broad absorption ("dark" mode) of monolayer MoS_2 indicates that the resonance dips are due to RET rather than the Fano resonance.[63]

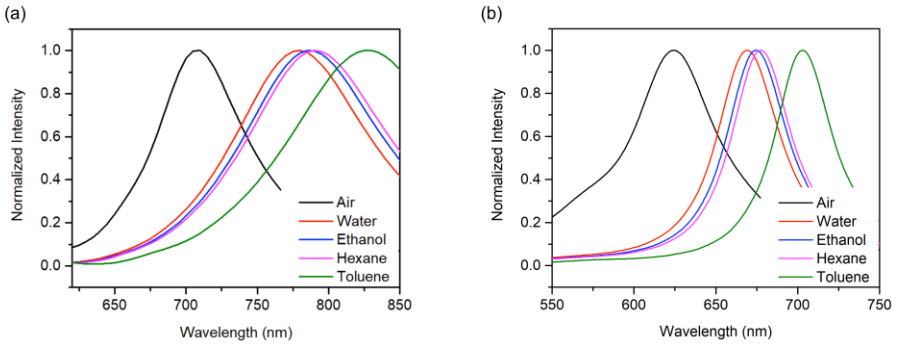

Figure 3.10: Simulated scattering spectra of a single 150 nm (a) and 60 nm (b) AuNT.

Comparing Figure 3.8a and 3.8b, we can observe that the dip in the scattering spectrum of 150 nm AuNTs is deeper than that of 60 nm AuNTs. This indicates that RET from a 150 nm AuNT to monolayer MoS_2 is more efficient than that from a 60 nm AuNT. A possible reason for this difference is that the LSPR peak of 150 nm AuNTs in air is closer to the exciton peak of monolayer MoS_2. In addition, the larger dipole moment of the larger AuNTs makes RET from 150 AuNTs to MoS_2 to be stronger than that from 60 nm AuNTs to MoS_2. The energy transfer potential between the donor and the acceptor is directly proportional to their dipole moments, as given by:[37]

$$V_{DA} = \frac{\kappa}{4\pi\varepsilon_0}\frac{\mu_D \mu_A}{R^3} \tag{3.2}$$

where V_{DA} is the energy transfer potential, and μ_D and μ_A are the dipole moment of the donor and acceptor, respectively. Therefore, the V_{DA} increases when the dipole moment of the donor and acceptor becomes larger.

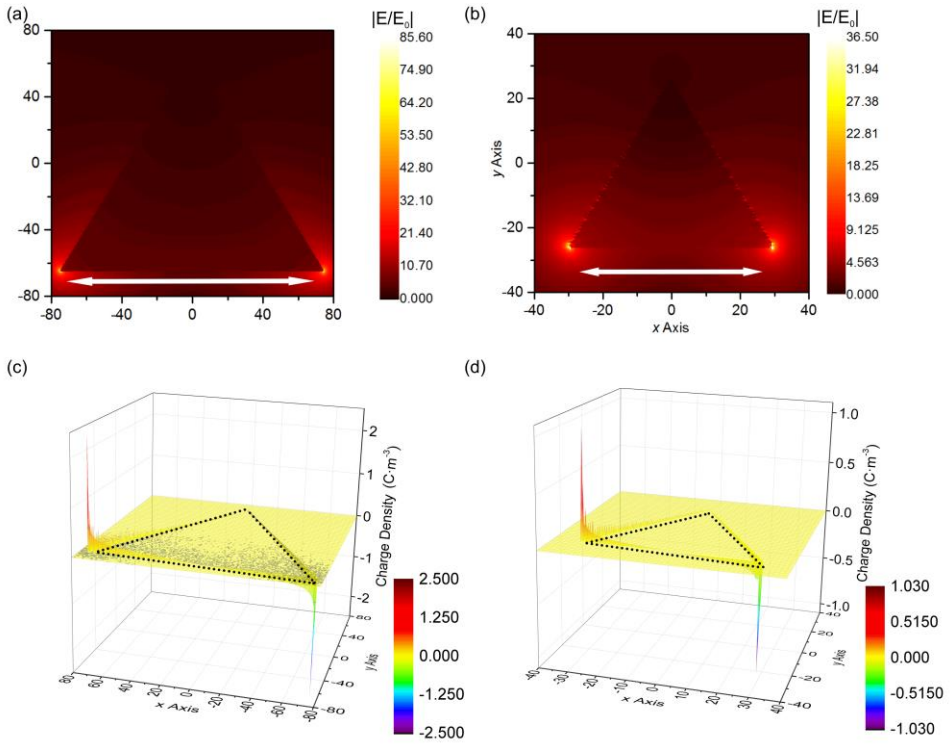

Figure 3.11: E-field distribution of (a) 150 nm AuNTs and (b) 60 nm AuNTs at the LSPR peak wavelength. The white arrows show the polarization of incident light. Charge distribution of (c) 150 nm AuNTs and (d) 60 nm AuNTs at the LSPR peak wavelength. The positive value shows the density of positive charges while the negative value indicates the density of negative charges.

In order to study the dipole moment of AuNTs with different sizes and to compare V_{DA} between 2D materials and the different AuNTs, we used finite-difference time-domain (FDTD) simulations of the E-field and charge distribution of AuNTs at LSPR wavelengths. Figures 3.11a and b show that the E-field is highly confined and enhanced at the tips of AuNTs upon excitation of LSPRs. The charge density is $\rho = \varepsilon_0 \nabla \bullet E$, where E is the E-field and ε_0 is the permittivity of vacuum. Since we only consider the unbound charges in the metal, ε_0 is used instead of $\varepsilon_{material}$ (the permittivity of material). We obtained the charge distribution from the divergence of the E-field in Figures 3.11a and b. As shown in Figures

3.11c and d, the much higher electron density exists at the tips of the AuNTs. Based on the charge distribution, the dipole moment of AuNT, i.e., μ_{AuNT}, can be calculated as:

$$\mu_{AuNT} = \left| \int_V \rho_i (r_i - r_{ref}) dr^3 \right| \quad (3.3)$$

where V is the volume of the AuNT, ρ_i is the charge density of the ith point in the AuNT, and r_i and r_{ref} are the vector of ith point and the reference point (one conventional choice is the mass center). From Equation 3.3, we estimated that the dipole moment of 150 nm AuNTs is about 13 times that of 60 nm AuNTs. Due to the larger dipole moment, RET from 150 AuNTs to MoS_2 is stronger than that from 60 nm AuNTs to MoS_2, leading to a deeper dip in the scattering spectrum of the 150 nm AuNT.

To further verify our observation of plasmon-trion RET and to achieve the active tuning of plasmon-trion and plasmon-exciton RET, we surrounded the hybrids of AuNTs and monolayer MoS_2 with 4 different solvents in order to vary the trion population. As schematically shown in Figure 3.12a, due to weak dielectric screening in air, the trion population of monolayer MoS_2 is large and the energy of LSPR can transfer to A^- trions. However, if monolayer MoS_2 was covered by a medium with large ε_r, the trion population deceases dramatically and the energy mainly transfers to A excitons (Figure 3.12b). Thus, it is expected that the scattering dips will follow the same shift to the shorter wavelength when ε_r of the surrounding medium is increased.

The FDTD simulation (detailed information is in Experimental part) was used to simulate the scattering spectra of a single 150 nm (a) and 60 nm (b) AuNT, as shown in Figure 3.10. The reflective indexes of air (1), water (1.333), ethanol (1.361), hexane (1.375) and toluene (1.497) were used to define those of the surrounding media. It is worth noticing that the experimental scattering peaks of a single 150 nm AuNT are at slightly shorter wavelengths than the simulated ones. This may be caused by the shape deviation of the

synthesized AuNTs to the prefect triangle used in the simulation and the defects in synthesized nanocrystals.

It should also be noted that the LSPR peak wavelength gets redshifted when the surrounding medium changes from air to a solvent with higher n.[64-65] FDTD simulations were used to verify this redshift. The simulated spectra are shown in Figure 3.10 and are in good agreement with the experimental results. The LSPR peak of the 150 nm AuNT shifts to a much longer wavelength than the absorption peak wavelength of monolayer MoS_2, when n of the surrounding medium is increased (Figure 3.12c). The LSPR peak of the 60 nm AuNT shifts to a wavelength close to the absorption peak of A excitons (or A^- trions; Figure 3.12d). Therefore, we chose 60 nm AuNTs to study the shift of the scattering peak as ε_r is increased.

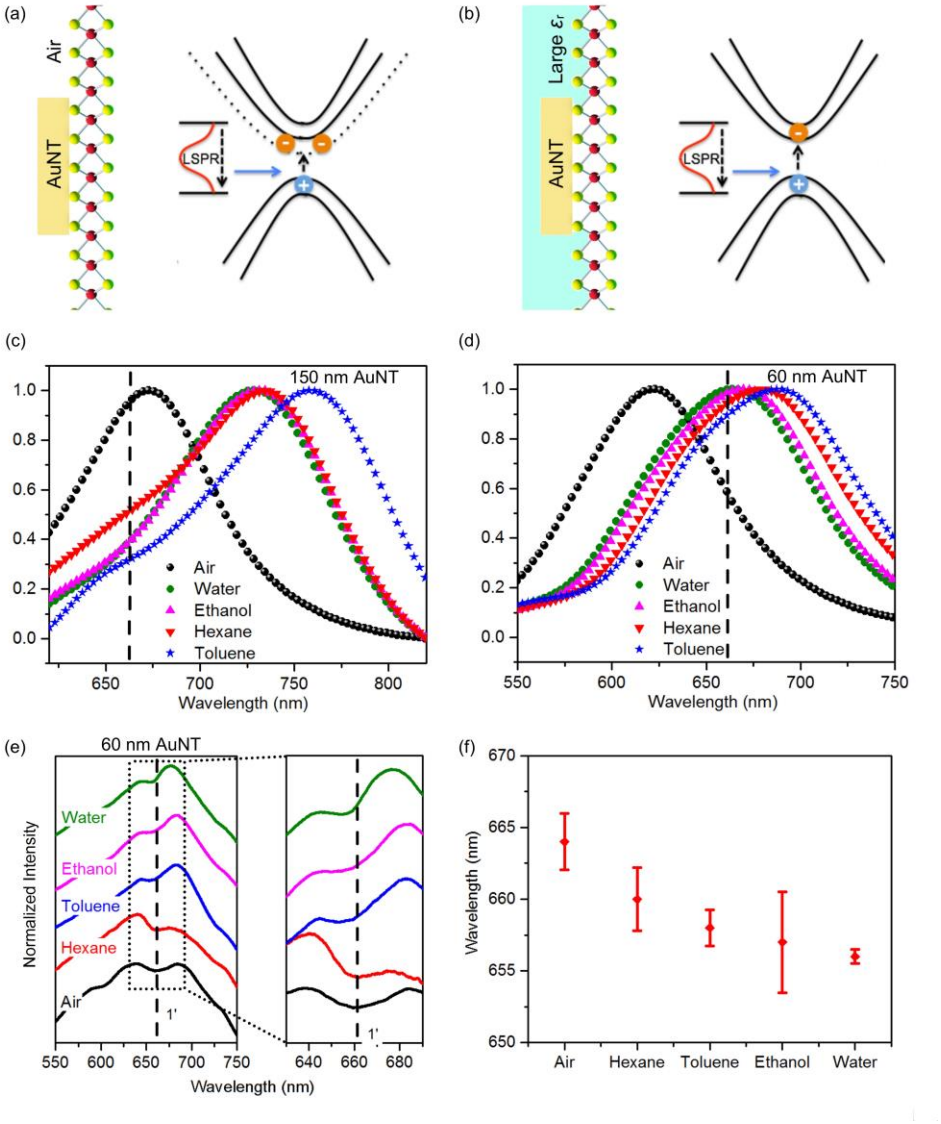

Figure 3.12: Schematics of (a) plasmon-trion RET and (b) plasmon-exciton RET. (c) Scattering spectra of the 150 nm AuNT when covered by air and various solvents. (d) Scattering spectra of the 60 nm AuNT when covered by air and various solvents. (e) Left plane: 5 scattering spectra (with dip 1') of a single 60 nm AuNT on monolayer MoS_2 covered by air (black), hexane (red), toluene (blue), ethanol (pink) and water (green), respectively. Right panel: enlarged scattering spectra in the area indicated by the black dotted square in the left panel. (f) Dip 1' wavelengths in the scattering spectra of single AuNTs on monolayer MoS_2 covered by 5 different media. 4 AuNTs were measured for each of the media.

Figure 3.12e shows that the wavelength of the dip 1' in the scattering spectra of an AuNT on monolayer MoS_2 gradually shifts from 664 nm to 656 nm when the surrounding medium changes from air to different solvents. Figure 3.12f summarizes dip 1' wavelengths in the scattering spectra of single AuNTs on monolayer MoS_2 for the 5 different surrounding media. Four different AuNTs were measured for each surrounding medium. From Figures 3.5b and 3.12f, we can observe that the wavelength of scattering dips is close to the dip wavelength of the transmission spectra of monolayer MoS_2 for each of the surrounding media. The good wavelength match indicates that the dips in the scattering spectra of AuNT-MoS_2 hybrid arose from the plasmon-trion and plasmon-exciton RET from the AuNTs to the monolayer MoS_2, and the active tuning of RET can be achieved by changing ε_r of the surrounding medium. Moreover, we estimated the spectral contribution of plasmon-exciton and plasmon-trion RET to dip 1' with different surrounding media, as listed in Table 3.2.

3.3 SUMMARY

In conclusion, the large exciton binding energy and reduced dielectric screening enables effective RET from plasmonic metal NPs to monolayer MoS_2, as well as the observation of trions at room temperature. Based on rationally designed AuNT-MoS_2 hybrids, we demonstrated room-temperature plasmon-trion and plasmon-exciton RET from a single AuNT to monolayer MoS_2, using single-nanoparticle measurements. We expect that such RET phenomena can be extended to other metal nanoparticle-2D materials systems. Moreover, tuning of the trion population in MoS_2 and the RET were achieved by varying the dielectric constant of the medium surrounding the AuNT-MoS_2 hybrids. Alternative RET tuning methods could include tuning the electronic properties of monolayer MoS_2 through chemical doping or external electric field, and varying the LSPRs

of AuNTs. Plasmon-trion and plasmon-exciton RET pave the way towards synergizing the nanoscale light control of plasmonic NPs and the superior properties of 2D materials for high-performance devices. The externally tunable RET will drive the development of novel active devices (e.g., modulators and switches) and sensors.

3.4 REFERENCE

1. Mak, K. F.; Shan, J., Photonics and optoelectronics of 2D semiconductor transition metal dichalcogenides. *Nat. Photonics* **2016**, 10 (4), 216-226.
2. Xia, F.; Wang, H.; Xiao, D.; Dubey, M.; Ramasubramaniam, A., Two-dimensional material nanophotonics. *Nat. Photonics* **2014**, 8 (12), 899-907.
3. Wang, Q. H.; Kalantar-Zadeh, K.; Kis, A.; Coleman, J. N.; Strano, M. S., Electronics and optoelectronics of two-dimensional transition metal dichalcogenides. *Nat. Nanotechnol.* **2012**, 7 (11), 699-712.
4. Gupta, A.; Sakthivel, T.; Seal, S., Recent development in 2D materials beyond graphene. *Prog. Mater. Sci.* **2015**, 73, 44-126.
5. Jariwala, D.; Sangwan, V. K.; Lauhon, L. J.; Marks, T. J.; Hersam, M. C., Emerging Device Applications for Semiconducting Two-Dimensional Transition Metal Dichalcogenides. *ACS Nano* **2014**, 8 (2), 1102-1120.
6. Lopez-Sanchez, O.; Lembke, D.; Kayci, M.; Radenovic, A.; Kis, A., Ultrasensitive photodetectors based on monolayer MoS_2. *Nat. Nanotechnol.* **2013**, 8 (7), 497-501.
7. Choi, M. S.; Qu, D.; Lee, D.; Liu, X.; Watanabe, K.; Taniguchi, T.; Yoo, W. J., Lateral MoS_2 p–n Junction Formed by Chemical Doping for Use in High-Performance Optoelectronics. *ACS Nano* **2014**, 8 (9), 9332-9340.
8. Mak, K. F.; Lee, C.; Hone, J.; Shan, J.; Heinz, T. F., Atomically Thin MoS_2: A New Direct-Gap Semiconductor. *Phys. Rev. Lett.* **2010**, 105 (13), 136805.
9. Sundaram, R. S.; Engel, M.; Lombardo, A.; Krupke, R.; Ferrari, A. C.; Avouris, P.; Steiner, M., Electroluminescence in Single Layer MoS_2. *Nano Lett.* **2013**, 13 (4), 1416-1421.
10. Mak, K. F.; He, K.; Shan, J.; Heinz, T. F., Control of valley polarization in monolayer MoS_2 by optical helicity. *Nat. Nanotechnol.* **2012**, 7 (8), 494-498.
11. Lin, Y.; Ling, X.; Yu, L.; Huang, S.; Hsu, A. L.; Lee, Y.-H.; Kong, J.; Dresselhaus, M. S.; Palacios, T., Dielectric Screening of Excitons and Trions in Single-Layer MoS_2. *Nano Lett.* **2014**, 14 (10), 5569-5576.

12. Li, Z.; Xiao, Y.; Gong, Y.; Wang, Z.; Kang, Y.; Zu, S.; Ajayan, P. M.; Nordlander, P.; Fang, Z., Active Light Control of the MoS_2 Monolayer Exciton Binding Energy. *ACS Nano* **2015**, 9 (10), 10158-10164.

13. Liu, J.-T.; Wang, T.-B.; Li, X.-J.; Liu, N.-H., Enhanced absorption of monolayer MoS_2 with resonant back reflector. *J. Appl. Phys.* **2014**, 115 (19), 193511.

14. Sobhani, A.; Lauchner, A.; Najmaei, S.; Ayala-Orozco, C.; Wen, F.; Lou, J.; Halas, N. J., Enhancing the photocurrent and photoluminescence of single crystal monolayer MoS_2 with resonant plasmonic nanoshells. *Appl. Phys. Lett.* **2014**, 104 (3), 031112.

15. Kern, J.; Trügler, A.; Niehues, I.; Ewering, J.; Schmidt, R.; Schneider, R.; Najmaei, S.; George, A.; Zhang, J.; Lou, J.; Hohenester, U.; Michaelis de Vasconcellos, S.; Bratschitsch, R., Nanoantenna-Enhanced Light–Matter Interaction in Atomically Thin WS_2. *ACS Photonics* **2015**, 2 (9), 1260-1265.

16. Wang, S.; Li, S.; Chervy, T.; Shalabney, A.; Azzini, S.; Orgiu, E.; Hutchison, J. A.; Genet, C.; Samorì, P.; Ebbesen, T. W., Coherent Coupling of WS2 Monolayers with Metallic Photonic Nanostructures at Room Temperature. *Nano Lett.* **2016**, 16 (7), 4368-4374.

17. Liu, W.; Lee, B.; Naylor, C. H.; Ee, H.-S.; Park, J.; Johnson, A. T. C.; Agarwal, R., Strong Exciton–Plasmon Coupling in MoS2 Coupled with Plasmonic Lattice. *Nano Lett.* **2016**, 16 (2), 1262-1269.

18. Lee, B.; Park, J.; Han, G. H.; Ee, H.-S.; Naylor, C. H.; Liu, W.; Johnson, A. T. C.; Agarwal, R., Fano Resonance and Spectrally Modified Photoluminescence Enhancement in Monolayer MoS_2 Integrated with Plasmonic Nanoantenna Array. *Nano Lett.* **2015**, 15 (5), 3646-3653.

19. Najmaei, S.; Mlayah, A.; Arbouet, A.; Girard, C.; Léotin, J.; Lou, J., Plasmonic Pumping of Excitonic Photoluminescence in Hybrid MoS_2–Au Nanostructures. *ACS Nano* **2014**, 8 (12), 12682-12689.

20. Zhou, H.; Yu, F.; Guo, C. F.; Wang, Z.; Lan, Y.; Wang, G.; Fang, Z.; Liu, Y.; Chen, S.; Sun, L.; Ren, Z., Well-oriented epitaxial gold nanotriangles and bowties on MoS_2 for surface-enhanced Raman scattering. *Nanoscale* **2015**, 7 (20), 9153-9157.

21. Kang, Y.; Gong, Y.; Hu, Z.; Li, Z.; Qiu, Z.; Zhu, X.; Ajayan, P. M.; Fang, Z., Plasmonic hot electron enhanced MoS_2 photocatalysis in hydrogen evolution. *Nanoscale* **2015**, 7 (10), 4482-4488.

22. Zhang, P.; Fujitsuka, M.; Majima, T., Hot electron-driven hydrogen evolution using anisotropic gold nanostructure assembled monolayer MoS_2. *Nanoscale* **2017**, 9 (4), 1520-1526.

23. Kang, Y.; Najmaei, S.; Liu, Z.; Bao, Y.; Wang, Y.; Zhu, X.; Halas, N. J.; Nordlander, P.; Ajayan, P. M.; Lou, J.; Fang, Z., Plasmonic Hot Electron Induced

Structural Phase Transition in a MoS_2 Monolayer. *Adv. Mater.* **2014**, 26 (37), 6467-6471.

24. Li, Z.; Li, Y.; Han, T.; Wang, X.; Yu, Y.; Tay, B.; Liu, Z.; Fang, Z., Tailoring MoS_2 Exciton–Plasmon Interaction by Optical Spin–Orbit Coupling. *ACS Nano* **2017**, 11 (2), 1165-1171.

25. Yu, Y.; Ji, Z.; Zu, S.; Du, B.; Kang, Y.; Li, Z.; Zhou, Z.; Shi, K.; Fang, Z., Ultrafast Plasmonic Hot Electron Transfer in Au Nanoantenna/MoS_2 Heterostructures. *Adv. Funct. Mater.* **2016**, 26 (35), 6394-6401.

26. Mathieu, H.; Lefebvre, P.; Christol, P., Simple analytical method for calculating exciton binding energies in semiconductor quantum wells. *Phys. Rev. B* **1992**, 46 (7), 4092-4101.

27. He, X.-F., Excitons in anisotropic solids: The model of fractional-dimensional space. *Phys. Rev. B* **1991**, 43 (3), 2063-2069.

28. Naeem, A.; Masia, F.; Christodoulou, S.; Moreels, I.; Borri, P.; Langbein, W., Giant exciton oscillator strength and radiatively limited dephasing in two-dimensional platelets. *Phys. Rev. B* **2015**, 91 (12), 121302.

29. Meer, B. W. v. d., Förster Theory. In FRET – Förster Resonance Energy Transfer: From Theory to Applications, First Edition., Igor Medintz, N. H., Ed. Wiley-VCH Verlag GmbH & Co. KGaA.: 2014; pp 23-62.

30. Mao, N.; Chen, Y.; Liu, D.; Zhang, J.; Xie, L., Solvatochromic Effect on the Photoluminescence of MoS_2 Monolayers. *Small* **2013**, 9 (8), 1312-1315.

31. Sanvitto, D.; Pulizzi, F.; Shields, A. J.; Christianen, P. C. M.; Holmes, S. N.; Simmons, M. Y.; Ritchie, D. A.; Maan, J. C.; Pepper, M., Observation of Charge Transport by Negatively Charged Excitons. *Science* **2001**, 294 (5543), 837.

32. Lui, C. H.; Frenzel, A. J.; Pilon, D. V.; Lee, Y. H.; Ling, X.; Akselrod, G. M.; Kong, J.; Gedik, N., Trion-Induced Negative Photoconductivity in Monolayer MoS_2. *Phys. Rev. Lett.* **2014**, 113 (16), 166801.

33. Mak, K. F.; He, K.; Lee, C.; Lee, G. H.; Hone, J.; Heinz, T. F.; Shan, J., Tightly bound trions in monolayer MoS_2. *Nat. Mater.* **2013**, 12 (3), 207-211.

34. Scarabelli, L.; Coronado-Puchau, M.; Giner-Casares, J. J.; Langer, J.; Liz-Marzán, L. M., Monodisperse Gold Nanotriangles: Size Control, Large-Scale Self-Assembly, and Performance in Surface-Enhanced Raman Scattering. *ACS Nano* **2014**, 8 (6), 5833-5842.

35. Johnson, P. B.; Christy, R. W., Optical Constants of the Noble Metals. *Phys. Rev. B* **1972**, 6 (12), 4370-4379.

36. Clapp, A. R.; Medintz, I. L.; Mauro, J. M.; Fisher, B. R.; Bawendi, M. G.; Mattoussi, H., Fluorescence Resonance Energy Transfer Between Quantum Dot

Donors and Dye-Labeled Protein Acceptors. *J. Am. Chem. Soc.* **2004**, 126 (1), 301-310.

37. Li, J.; Cushing, S. K.; Meng, F.; Senty, T. R.; Bristow, A. D.; Wu, N., Plasmon-induced resonance energy transfer for solar energy conversion. *Nat. Photonics* **2015**, 9 (9), 601-607.

38. Losquin, A.; Zagonel, L. F.; Myroshnychenko, V.; Rodríguez-González, B.; Tencé, M.; Scarabelli, L.; Förstner, J.; Liz-Marzán, L. M.; García de Abajo, F. J.; Stéphan, O.; Kociak, M., Unveiling Nanometer Scale Extinction and Scattering Phenomena through Combined Electron Energy Loss Spectroscopy and Cathodoluminescence Measurements. *Nano Lett.* **2015**, 15 (2), 1229-1237.

39. Scarabelli, L.; Sánchez-Iglesias, A.; Pérez-Juste, J.; Liz-Marzán, L. M., A "Tips and Tricks" Practical Guide to the Synthesis of Gold Nanorods. *J. Phys. Chem. Lett.* **2015**, 6 (21), 4270-4279.

40. Gole, A.; Murphy, C. J., Seed-Mediated Synthesis of Gold Nanorods: Role of the Size and Nature of the Seed. *Chem. Mater.* **2004**, 16 (19), 3633-3640.

41. Pérez-Juste, J.; Pastoriza-Santos, I.; Liz-Marzán, L. M.; Mulvaney, P., Gold nanorods: Synthesis, characterization and applications. *Coord. Chem. Rev.* **2005**, 249 (17–18), 1870-1901.

42. Chen, H.; Shao, L.; Li, Q.; Wang, J., Gold nanorods and their plasmonic properties. *Chem. Soc. Rev.* **2013**, 42 (7), 2679-2724.

43. Eustis, S.; El-Sayed, M. A., Why gold nanoparticles are more precious than pretty gold: Noble metal surface plasmon resonance and its enhancement of the radiative and nonradiative properties of nanocrystals of different shapes. *Chem. Soc. Rev.* **2006**, 35 (3), 209-217.

44. Hu, M.; Chen, J.; Li, Z.-Y.; Au, L.; Hartland, G. V.; Li, X.; Marquez, M.; Xia, Y., Gold nanostructures: engineering their plasmonic properties for biomedical applications. *Chem. Soc. Rev.* **2006**, 35 (11), 1084-1094.

45. Komsa, H.-P.; Krasheninnikov, A. V., Effects of confinement and environment on the electronic structure and exciton binding energy of MoS_2 from first principles. *Phys. Rev. B* **2012**, 86 (24), 241201.

46. Zhao, L.; Ming, T.; Chen, H.; Liang, Y.; Wang, J., Plasmon-induced modulation of the emission spectra of the fluorescent molecules near gold nanorods. *Nanoscale* **2011**, 3 (9), 3849-3859.

47. Jiang, R.; Li, B.; Fang, C.; Wang, J., Metal/Semiconductor Hybrid Nanostructures for Plasmon-Enhanced Applications. *Adv. Mater.* **2014**, 26 (31), 5274-5309.

48. Choi, Y.; Kang, T.; Lee, L. P., Plasmon Resonance Energy Transfer (PRET)-based Molecular Imaging of Cytochrome c in Living Cells. *Nano Lett.* **2009**, 9 (1), 85-90.

49. Liu, G. L.; Long, Y.-T.; Choi, Y.; Kang, T.; Lee, L. P., Quantized plasmon quenching dips nanospectroscopy via plasmon resonance energy transfer. *Nat. Methods* **2007**, 4 (12), 1015-1017.

50. Li, H.; Lu, G.; Yin, Z.; He, Q.; Li, H.; Zhang, Q.; Zhang, H., Optical Identification of Single- and Few-Layer MoS_2 Sheets. *Small* **2012**, 8 (5), 682-686.

51. Li, H.; Zhang, Q.; Yap, C. C. R.; Tay, B. K.; Edwin, T. H. T.; Olivier, A.; Baillargeat, D., From Bulk to Monolayer MoS2: Evolution of Raman Scattering. *Adv. Funct. Mater.* **2012**, 22 (7), 1385-1390.

52. Rao, C. N. R.; Ramakrishna Matte, H. S. S.; Maitra, U., Graphene Analogues of Inorganic Layered Materials. *Angew. Chem. Int. Ed.* **2013**, 52 (50), 13162-13185.

53. Terrones, H.; Corro, E. D.; Feng, S.; Poumirol, J. M.; Rhodes, D.; Smirnov, D.; Pradhan, N. R.; Lin, Z.; Nguyen, M. A. T.; Elías, A. L.; Mallouk, T. E.; Balicas, L.; Pimenta, M. A.; Terrones, M., New First Order Raman-active Modes in Few Layered Transition Metal Dichalcogenides. *Sc*i. Rep. **2014**, 4, 4215.

54. Lin, Z.; Thee, M. T.; Elías, A. L.; Feng, S.; Zhou, C.; Fujisawa, K.; Perea-López, N.; Carozo, V.; Terrones, H.; Terrones, M., Facile synthesis of MoS_2 and MoxW1-xS2 triangular monolayers. *APL Mater.* **2014**, 2 (9), 092514.

55. Mouri, S.; Miyauchi, Y.; Matsuda, K., Tunable Photoluminescence of Monolayer MoS2 via Chemical Doping. *Nano Lett.* **2013**, 13 (12), 5944-5948.

56. Soklaski, R.; Liang, Y.; Yang, L., Temperature effect on optical spectra of monolayer molybdenum disulfide. *Appl. Phys. Lett.* **2014**, 104 (19), 193110.

57. Anger, P.; Bharadwaj, P.; Novotny, L., Enhancement and Quenching of Single-Molecule Fluorescence. *Phys. Rev. Lett.* **2006**, 96 (11), 113002.

58. Pelton, M., Modified spontaneous emission in nanophotonic structures. *Nat. Photonics* **2015**, 9 (7), 427-435.

59. Wang, M.; Bangalore Rajeeva, B.; Scarabelli, L.; Perillo, E. P.; Dunn, A. K.; Liz-Marzán, L. M.; Zheng, Y., Molecular-Fluorescence Enhancement via Blue-Shifted Plasmon-Induced Resonance Energy Transfer. *J. Phys. Chem. C* **2016**, 120 (27), 14820-14827.

60. Shi, H.; Yan, R.; Bertolazzi, S.; Brivio, J.; Gao, B.; Kis, A.; Jena, D.; Xing, H. G.; Huang, L., Exciton Dynamics in Suspended Monolayer and Few-Layer MoS_2 2D Crystals. *ACS Nano* **2013**, 7 (2), 1072-1080.

61. Sönnichsen, C.; Franzl, T.; Wilk, T.; von Plessen, G.; Feldmann, J.; Wilson, O.; Mulvaney, P., Drastic Reduction of Plasmon Damping in Gold Nanorods. *Phys. Rev. Lett.* **2002**, 88 (7), 077402.

62. Zhang, W.; Govorov, A. O.; Bryant, G. W., Semiconductor-Metal Nanoparticle Molecules: Hybrid Excitons and the Nonlinear Fano Effect. *Phys. Rev. Lett.* **2006**, 97 (14), 146804.

63. Miroshnichenko, A. E.; Flach, S.; Kivshar, Y. S., Fano resonances in nanoscale structures. *Rev. Mod. Phys.* **2010**, 82 (3), 2257-2298.

64. Anker, J. N.; Hall, W. P.; Lyandres, O.; Shah, N. C.; Zhao, J.; Van Duyne, R. P., Biosensing with plasmonic nanosensors. *Nat. Mater.* **2008**, 7 (6), 442-453.

65. Maier, S. A.; Atwater, H. A., Plasmonics: Localization and guiding of electromagnetic energy in metal/dielectric structures. *J. Appl. Phys.* **2005**, 98 (1), 011101.

Chapter 4 Photoswitchable Rabi Splitting in Hybrid Plasmon-Waveguide Modes*

4.1 INTRODUCTION

The enhanced interaction between light and photon emitters occurs when the emitters are placed in an optical cavity, where the local density of electromagnetic modes is dramatically increased.[1-8] In the weak-coupling region, where the emitter-cavity energy exchange rate is lower than the cavity decay rate, one obtains enhanced light extraction from the emitter. More significant effects emerge in the strong-coupling region when the emitter-cavity coupling strength is higher than their individual decay rates, i.e., $2g > \gamma$ or κ,[4] where g is the coupling energy, γ is the emitter scattering rate and κ is the cavity loss rate. In this region, the emitter and cavity coherently exchange energy and lead to the Rabi oscillations, manifesting as a resonant peak splitting in the optical spectra. High-quality cavities with small effective cavity volume V ($g \propto 1/\sqrt{V}$) and high quality factor Q ($Q \propto 1/\sqrt{\kappa}$) are expected to support these strongly coupled mixed states for such applications as low-threshold emission [9-10] and ultrafast switching.[11-13]

The strong coupling has been demonstrated in a variety of optical cavities, including optical microcavities,[14-16] optical waveguides,[17-18] and plasmonic cavities.[5, 19-28] Most of the dielectric-based microcavities unavoidably suffer from a large cavity volume and active-area footprint. Metal nanoparticles, which support localized surface plasmon resoancnes (LSPRs) with tremendous electric field enhancement in the deep subwavelength volumes,[29-38] provide improved mode confinement and coupling strength. Specifically, Rabi splitting in hybrids of plasmonic nanostructures and molecules has attracted intense interests for both fundamental research and applications in sensing,

* Lin, L.; Wang, M.; Wei, X.; Peng, X.; Xie, C.; Zheng, Y., Photoswitchable Rabi Splitting in Hybrid Plasmon–Waveguide Modes. *Nano Letters* 2016, 16 (12), 7655-7663.
Wang, M. carried out the experimental work and participated in the preparation of manuscript.

information processing, and nanolasers. Plasmon-molecule strong couplings have been studied in the systems consisted of molecule aggregates[22, 24, 39-40] (or single molecule[5, 41]) and plasmonic nanoparticle arrays[22-24, 28] (or single-particle cavity[21, 40, 42-43]). Meanwhile, plasmonic switches have been demonstrated based on hybrids of plasmonic nanoparticles and photochromic molecules.[44] However, plasmonic cavities experience intrinsic loss due to resistive heating in metals, which limits the coupling strength between plasmons and molecular excitons and impedes their application in the long-range optical guiding and switching. To enable the long-distance guiding of surface plasmons with strong subwavelength confinement, researchers have been exploring new modes that arise from the hybridization between surface plasmon and dielectric waveguides,[45-51] which has been achieved in hybrid plasmonic waveguides. However, it has remained unknown how to excite and control Rabi splitting in these hybrid plasmon-waveguide modes (HPWMs).

In this chapter, we demonstrate the photoswitchable Rabi splitting in the HPWMs supported by Al nanodisk arrays covered by a thin polymethyl methacrylate (PMMA) waveguide layer that is doped with spiropyran (SP)-based photochromic molecules. The HPWMs exhibit both subwavelength mode confinement with intense localized electric field and long-range light waveguiding. More interestingly, we show that the HPWMs in the hybrid systems can couple strongly with molecular excitons, leading to Rabi splitting. By harnessing the photoswitchable configurations of the molecules, i.e., switching between their closed form (SP) and open form-merocyanine (MC), we can reversibly control Rabi splitting and achieve all-optical light modulation. Furthermore, we demonstrate a concept of optically rewritable waveguides using the photoswitchable Rabi splitting in the HPWMs. With their advantages of low optical loss, subwavelength confinement of light and reversible light modulation, the HPWMs with the photoswitchalbe Rabi splitting will open

up new opportunities for applications in both standalone active optical devices and lab-on-a-chip systems.[52]

4.2 Results and Discussion

4.2.1 Experimental section

4.2.1.1 Sample preparation

Al nanodisk arrays were fabricated on glass substrates by electron beam lithography (EBL, 6000 FSE, JEOL) and electron beam deposition (Cooke Vacuum Products). A 2 nm Cr layer was used as an adhesion layer between a 30 nm Al layer and a glass substrate. An atomic force microscope (AFM, Park Systems) was employed for morphology characterization of the Al nanodisk arrays. Spiropyran (SP, Sigma-Aldrich) molecules were mixed with PMMA (Sigma-Aldrich) with a weight ratio of 1:1 in chlorobenzene (2 wt% of SP in chlorobenzene). The mixture was spin-coated onto the Al nanodisk arrays at 2000 rpm for one minute. The thickness and dielectric function of the SP-doped PMMA films were determined by ellipsometry (M-2000, J.A. Woollam Co.).

4.2.1.2 Optical measurements

A dark-field microscope (Ti-E inverted microscope, Nikon) with a halogen white light source (12V, 100 W) and an oil-immersion 100x objective were utilized to measure the transmission spectra of the samples. A linear polarizer (Thorlabs) was added between the light source and samples to generate the polarized light. A mercury light source (C-HGFIE, Nikon) with excitation filters was used to generate UV light (DAPI Shift Filter set, excitation wavelength: 325-375 nm) or green light (TRITC HYQ Shift Filter set, excitation wavelength: 530-560 nm) to switch molecules between their closed form (SP) and open form (MC). The schematic of the experimental procedure is shown in Figure 4.2. All the

transmission spectra were normalized with the background signal from the sample consisted of molecule (SP or MC)-doped PMMA thin film on glass substrate without Al nanodisk arrays.

4.2.1.3 Optical writing of the waveguides

A UV lamp was used to switch SP molecules to their MC form in the whole samples before the optical writing. A 532 nm laser beam (Coherent, the maximum power is 1.1 W) was employed to write the waveguides on the Al nanodisk arrays covered with the MC-doped PMMA film. A half-wave plate was employed to control the polarization of the laser beam. A 5× beam expander was used to expand the laser beam. A square-patterned laser beam was generated by the DMD and focused onto the samples. The size of the beam was reduced by 500 times after being relayed by a 1000 mm doublet lens, a 200 mm doublet lens, an infinity-corrected tube lens and a 100× objective (NA=0.9). Either DMD or motorized stage in the optical microscope was utilized to scan the laser beam on the samples for the writing process. Optical images and videos were recorded with a color digital microscope camera (Nikon).

4.2.1.4 FDTD simulations

FDTD simulations were performed using a commercial software (Lumerical Solutions). A linear-polarized plane-wave light source was launched normally from the side of the glass substrate and a detector was placed on the top of the sample to collect the transmission signal. Symmetric and asymmetric boundary conditions were applied in both $\pm x$ and $\pm y$ direction and perfect matching layers were applied in $\pm z$ direction. The refractive index of the glass substrate was set as 1.52, while the thickness and refractive index of the SP molecule-doped PMMA was taken from the ellipsometry measurement. An ultra-fine

mesh size (1 nm) was used in the simulations. The simulated transmission spectra with MC molecules are normalized by the background signal from the structure consisted of MC molecule-doped PMMA thin film on glass substrate without Al nanodisk arrays.

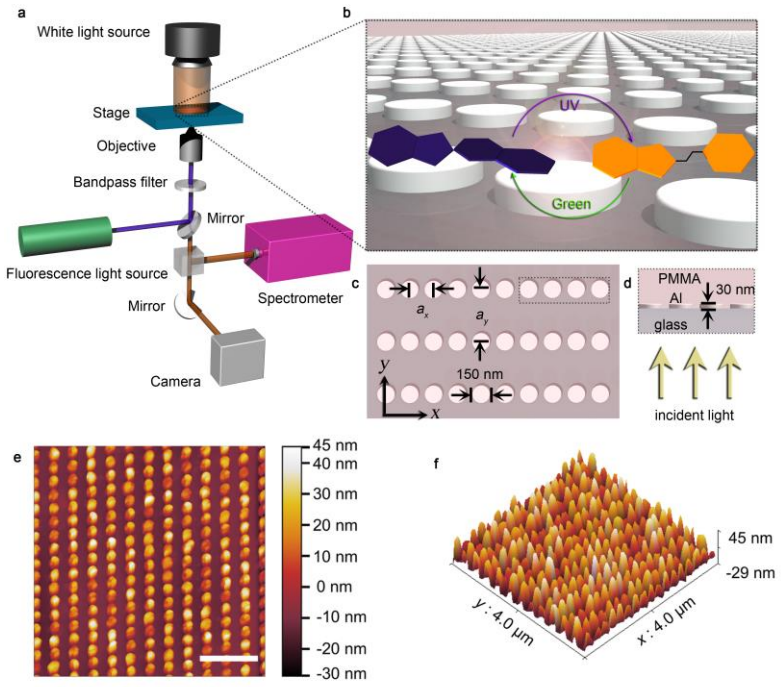

Figure 4.1: Optical setup for the study of photoswithcable Rabi splitting between HPWMs and molecular excitons, as well as sample design and characterization. (a) Schematic of the optical setup. (b) Tilted schematic view of the sample consisted of Al nanodisk arrays covered by PMMA thin films doped with SP-based photochromic molecules. The photochromic molecules undergo reversible isomerization between their SP form and MC form upon alternative illumination of UV light and green light. The MC molecules exhibit exciton absorption at visible wavelength, which will couple with the properly designed HPWMs. The exciton absorption is switched off under SP form. (c) Top view of the rectangular Al nanodisk array. The diameter of the Al nanodisks is 150 nm. We set lattice constants a_x=200 nm and ay ranging from 360 nm to 440 nm. (d) Cross-sectional view of the Al nanodisk array. The height of Al nanodisks is 30 nm. The thickness of PMMA film is 280 nm. (e) 2D and (f) 3D AFM images of the Al nanodisk array with a_y = 360 nm. Scale bar in (e): 1 μm.

4.2.2 Design of hybrid plasmon-waveguide system and optical setup

Figures 4.1a and 4.1b show the schematic of our sample and optical setup for characterizing the photoswitchable Rabi splitting in the HPWMs (also see Figure 4.2 for more details on the optical characterization). Our samples are consisted of a glass substrate, Al nanodisk arrays, and PMMA thin film doped with SP molecules (see Methods for sample fabrication details). The regular Al nanodisk arrays were embedded in the PMMA waveguide layer at the glass-PMMA interface to hybridize LSPRs with propagating waveguides. SP-doped PMMA layer was spin-coated onto the substrate. It is known that an increase in the molecule concentration can enhance the Rabi splitting. However, the maximum concentration is limited by the solubility of SP molecules in the organic solvent and PMMA and the higher concentration of molecules could result in the poor-quality PMMA films. In our experiments, we chose the suitable molecule concentration as per previous work[53-54]. A normal-incident white light with E_x polarization was launched from the side of the glass substrate to interact with the Al nanodisk arrays, exciting both LSPRs and diffraction waves. The latter allows total internal reflection at the PMMA-substrate and PMMA-air interfaces to confine light within the PMMA waveguide layer. The coupling between scattering light from the Al nanodisks and light of transverse electric (TE) mode in the PMMA layer leads to the HPWMs.[48, 55] We optimized the thickness of PMMA waveguide layer using finite-difference time-domain (FDTD) simulation in order to tune the wavelengths of the HPWMs towards the absorption wavelength of the MC molecules without introducing the higher-order waveguide modes. Excited with a fluorescence light source, reversible photoisomerization of the molecules between their SP form (irradiated with green light) and MC form (irradiated with ultraviolet light) allows photoswitchable strong coupling between the molecular excitons and the HPWMs. The

zero-order transmitted light, which was modulated with the photoswitchable Rabi splitting, was collected by an oil objective and directed towards a spectrometer for analysis.

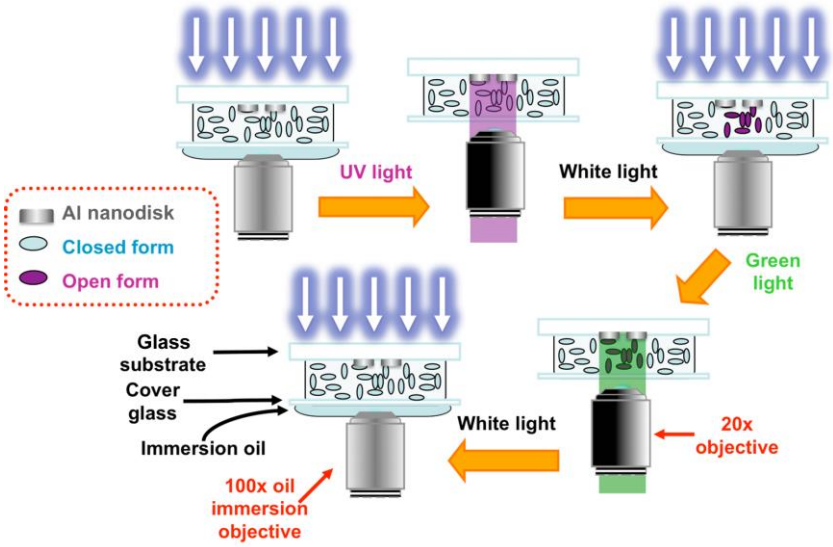

Figure 4.2: Schematic of a series of optical transmission measurements of the sample upon alternative irradiation of UV and green light. White light with TE polarization was directed normally onto Al nanodisk arrays from the side of glass substrate. The transmission signals were collected by an oil-immersion objective (100×) and directed towards a spectrometer for analysis. UV and green light irradiated the sample through the 20× objective for 1 minute and 2 minutes, respectively, to switch the molecules.

Figures 4.1c and 4.1d show planar and cross-sectional views of our samples that support the HPWMs, respectively. The diameter and height of Al nanodisks are 150 nm and 30 nm, respectively. The lattice constant along x-axis (*i.e.,* a_x) is set as 200 nm to introduce near-field coupling between adjacent Al nanodisks for the further enhancement of the localized electric field. The lattice constant along y-axis (*i.e.,* a_y) ranges from 360 nm to 440 nm to tune the resonant wavelength of the HPWMs in order to match the absorption wavelength of molecular excitons. Two-dimensional (2D) and three-

dimensional (3D) atomic force micrographs (AFM) of representative Al nanodisk arrays fabricated with electron beam lithogtaphy (EBL) are displayed in Figures 4.1e and f, respectively. We chose Al as plasmonic materials because of its wide-range optical responses from ultraviolet to visible region, technical compatibility with current CMOS-based integrated circuits, abundance in the earth's crust, and high stability with passivation by oxide layer.[23, 56-59]

4.2.3 Photoswitchable Rabi splitting

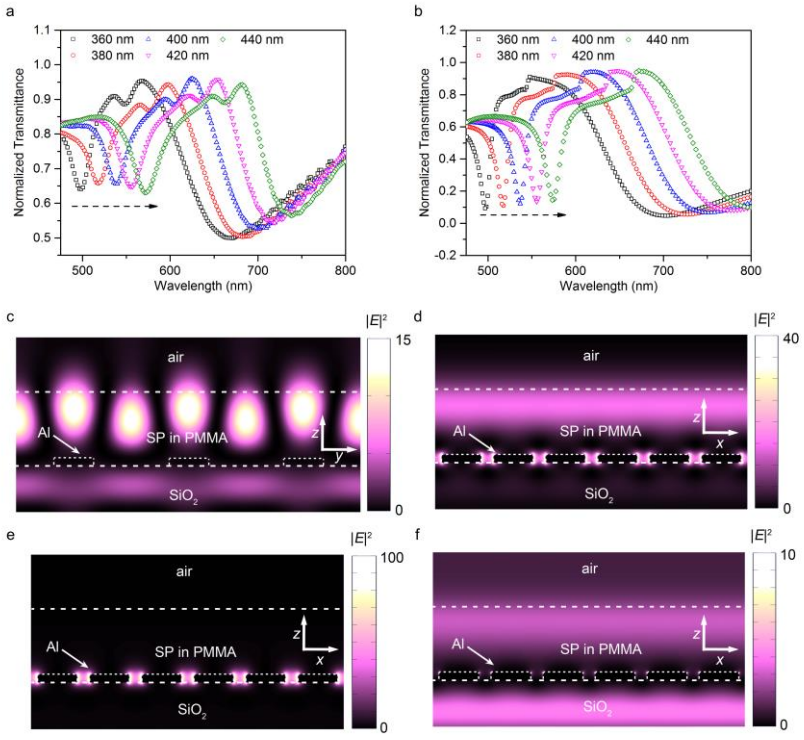

Figure 4.3: Normalized transmission spectra and electromagnetic field distributions for different modes in the spectra (a) Experimental spectra of a series of samples and (b) simulated transmission spectra of the samples with the lattice constants ay from 360 to 440 nm. (c-f) Simulated distributions of the electric field intensity at different wavelengths in the spectrum (with the lattice constant a_y=440 nm) of Figure 4.3b: (c) λ=574 nm in the *yz* plane; (d) λ=574 nm in the *xz* plane; (e) λ=800 nm in the *xz* plane; and (f) λ=625 nm in the *xz* plane.

To study the hybridization between LSPRs and waveguide modes, we measured transmission spectra of the samples with variable lattice constants a_y when photochromic molecules were in their SP form. As shown in Figure 4.3a, the broad transmission dips from 670 nm to 750 nm originate from the intrinsic LSPRs of the Al nanodisks with near-field coupling. The dips at the shorter wavelengths, which display the much narrower linewidth (and thus higher quality factor Q), arise from the HPWMs. For comparison, the transmission spectra of the bare Al nanodisk arrays on the glass substrate are shown in Figure 4.4a. We can see that the LSPR modes at the same lattice constants are located at the shorter wavelengths due to the lower refractive index of air than that of PMMA. In addition, the asymmetric surrounding environments (without the molecule-doped PMMA layer) weaken the far-field diffractive coupling between the Al nanodisks along y-axis. The resonant wavelength of HPWMs can be tuned from 500 nm to 574 nm by changing the lattice constant a_y. Considering the absorption peak wavelength of MC molecules at 570 nm (Figure 4.4b), we can have a large spectral overlap between the HPWMs and molecular excitons to achieve the strong coupling. We can also observe small dips between the intrinsic LSPRs and the HPWMs in Figure 4.3a (or the sudden jump in Figure 4.3b). The small dips arise from the diffraction orders at the Al nanodisk arrays. However, a robust coupling between the diffraction orders and the LSPRs does not exist because the thin layer of PMMA (280 nm) leads to an asymmetric refractive index of media surrounding the nanodisk arrays. Rather than generating lattice plasmon modes with narrow linewidth down to a couple of ten nanometers and below, the coupling is weak and leads to a slight redshift of the resonant wavelength and a slight narrowing of the linewidth of the LSPRs when the diffractive wavelength approaches the LSPR wavelength. Due to the diffractive coupling, we did not observe the broadened linewidth in the LSPRs when the LSPRs approach the interband transition energy of Al (1.5 eV, ~829 nm). [60-61] In addition, we have

compared the transmission spectra of PMMA-coated Al nanodisk arrays on glass substrates with and without doping of SP molecules. The LSPRs make a redshift upon the doping of SP molecules due to an increased refractive index of the PMMA layer (Figures 4.4c and 4.4d).

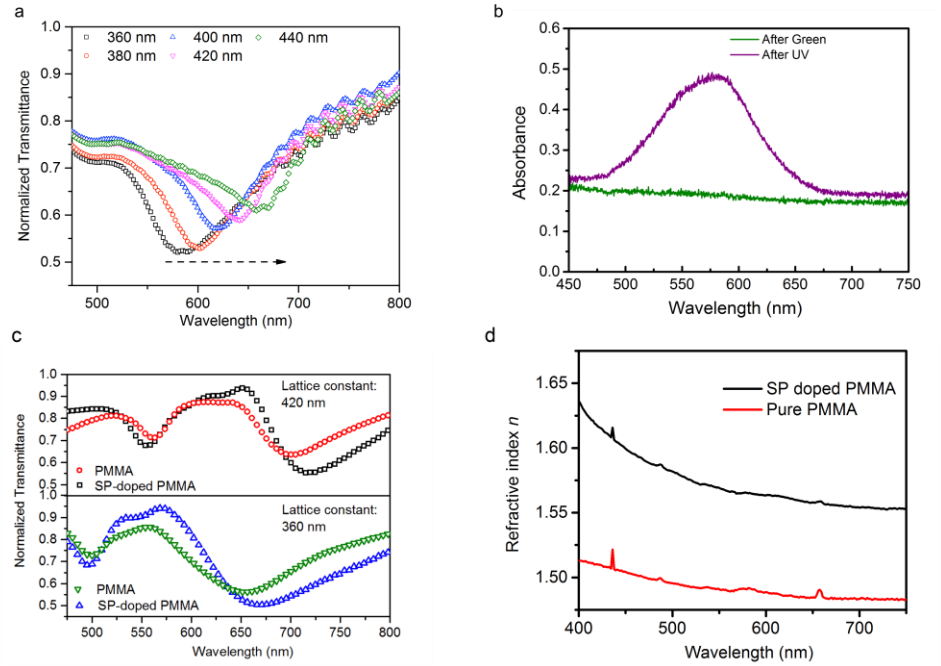

Figure 4.4: (a) Experimental transmission spectra of bare Al nanodisk arrays with different lattice constants ay. (b) Experimental absorption spectra of MC (After UV) and SP molecules (After Green). (c) Comparison of the experimental transmission spectra of PMMA coated Al nanodisk arrays with and without doping of SP molecules at two different lattice constants: a_y=420 nm and a_y=360 nm. (d) Measured refractive index of the PMMA layer with and without doping of SP molecules.

Our FDTD simulation results (Figure 4.3b) agree well with the experimental spectra. In the simulations, the dielectric function and thickness of the PMMA waveguide layer doped with SP molecules were taken from the ellipsometry measurement. It is worth noting that, different from the hybrid waveguide-plasmon polaritons (HWPPs) near zero

detuning,[46, 48, 55] we keep the HPWMs at large detuning in order to avoid the strong coupling between the waveguide modes and the LSPRs, which will cause the splitting of the hybrid modes and electromagnetically induced transparency (EIT) at the resonant wavelength.[51, 55]

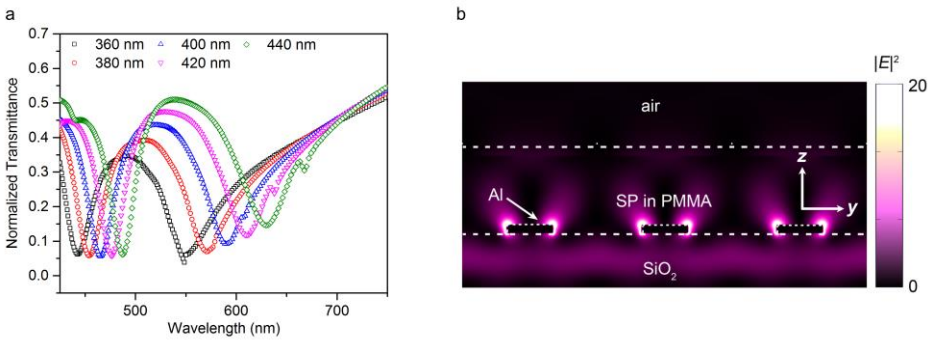

Figure 4.5: (a) Simulated transmission spectra of Al nanodisk arrays with variable lattice constants ay with the incident light of TM polarization (along y-axis). (b) Cross-sectional view of the simulated distribution of electric field intensity at the wavelength of 630 nm (TM polarization) for the Al nanodisk array with a_y=440 nm.

To better understand the nature of the HPWMs, we simulated the electric field distributions for different modes revealed by the transmission spectrum of the sample with a_y=440 nm. As shown in Figure 4.3c, at the resonant wavelength of the HPWM (λ=574 nm), A TE propagating waveguide mode (*x*-polarized and propagating along *y*-axis) is observed in the *yz* plane. We attribute this to constructive interference between total reflection light at the PMMA-air interface and diffraction waves from the periodic Al nanodisk arrays. For the same wavelength, as shown in Figure 4.3d, the LSPR-like dipole mode with near-field coupling between adjacent nanodisks is excited along *x* direction in the *xz* plane. For comparison, Figure 4.5 shows both the optical spectra and electric field distribution under the excitation of TM-polarized light. We believe that the LSPR-like

mode in the HPWMs originates from the multiple interactions between the propagating light in the waveguide layer and the Al nanodisk arrays, which cause collective coupling between the individual Al nanodisks and improve the electric field intensity of the plasmonic dipoles.

Although the resonant wavelength of 574 nm is far away from the resonant wavelength of LSPRs at 800 nm (*i.e.,* there is a large detuning), we demonstrate that the HPWMs exhibit feature of the LSPRs, which is different from the bare waveguide mode. For comparison, the electric field distribution of the LSPR mode at 800 nm is displayed in Figure 4.3e. This electric field distribution reveals a bare dipolar LSPR mode without any signatures of propagating waveguide. Moreover, the electric field distribution at λ=625 nm, which is closer to the LSPR at 800 nm but not on resonance with HPWM, reveals that the sample is transparent to this incident light without an observation of plasmonic dipole mode. Thus, we conclude that the plasmonic dipole observed in the HPWM (λ=574 nm) does not originate from the intrinsic LSPRs around 800 nm (Figure 4.3f). It is worth noting that the hybridization between the LSPRs and the waveguide mode significantly reduce the full-width at half-maximum (FWHM) of the HPWMs, which ranges from 106 meV to 132 meV according to the transmission spectra in Figure 4.3a. In contrast, the bare LSPR modes at the longer wavelength show the much broader linewidth. The FWHM is 520 meV for the sample with a_y=360 nm.

To demonstrate the strong coupling between the excitons of MC molecules and the HPWMs, we irradiated the samples in Figure 4.3 with UV light and measured the transmission spectra. Upon UV irradiation, the photochromic molecules isomerized from SP form to MC form that features an absorption peak at the wavelength of 570 nm (Figure 4.4b). The spectral overlap between the HPWMs and MC molecules leads to strong coupling between them and the Rabi splitting occurs.[62-64] As shown in Figure 4.6a, the

single transmission dips of the HPWMs have developed into two dips, with the maximum Rabi splitting energy of 572 meV at a_y=430 nm. It should be noted that a redshift of the LSPRs was also observed when the SP molecules was switched to its MC form (Figures 4.3a and 4.6a), which is caused by the photoisomerization-induced refractive index change in the molecules.[54] The energy transfer between the HPWMs and molecules upon strong coupling creates two new polaritonic states: upper polaritonic state (P_+) and lower polaritonic state (P_-) (Figure 4.6b), which are separated by the Rabi splitting energy Ω as defined below:[4]

$$\Omega = \frac{N}{V}\frac{f_0 e^2}{\varepsilon_0 m} \tag{4.1}$$

where N is the number of coupled molecules in the system, V is the effective mode volume, f_0 is the oscillator strength of molecules, ε_0 is the vacuum permittivity, e is the electron charge, and m is the electron mass. To further confirm that Rabi splitting is responsible for the observed spectral evolution, we show that the criterion of Rabi splitting is satisfied herein: $\Omega > (\gamma_{HPWM+} \gamma_0)/2$,[65-66] where γ_{HPWM} = 141 meV is FWHM of the HPWMs, and γ_0 = 497 meV is FWHM of the absorption band of MC molecules. For the largest splitting energy, λ=572 meV > $(\gamma_{HPMW+}\gamma_0)/2$ = 319 meV.

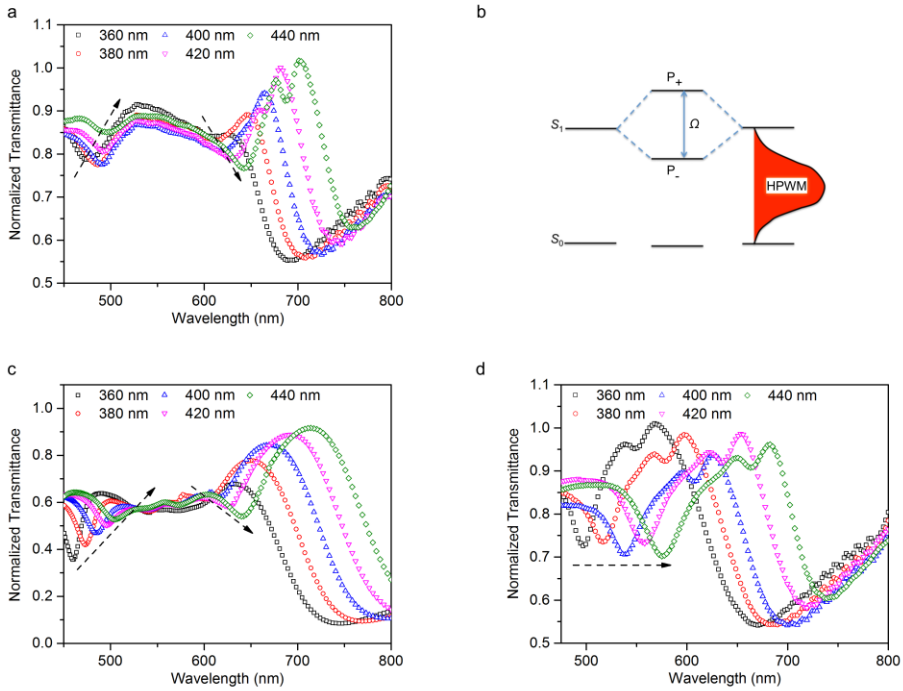

Figure 4.6: Normalized transmission spectra of a series of samples upon alternative UV and green light irradiation, which exhibit photoswitchable Rabi splitting in the HPWMs. (a) Experimental transmission spectra after UV light irradiation. (b) Schematic of strong coupling between MC molecules and the HPWM, which leads to Rabi splitting. S_0 and S_1 are ground state and first excited state of MC molecules, respectively. Two new polaritonic states (P_+ and P_-) are formed with separation of Rabi splitting energy (Ω). (c) Simulated transmission spectra after UV light irradiation. (d) Experimental transmission spectra of the same series of samples as in (a) after green light irradiation. The black arrows indicate the shifts in dip wavelengths upon an increase of the lattice constant a_y.

We simulated the transmission spectra of the series of samples at the strong coupling between the HPWMs and MC molecules, with the frequency-dependent permittivity of MC molecules treated as the dimensionless Lorentz oscillator:[23, 40]

$$\varepsilon(\omega) = \varepsilon_\infty + \frac{f\,\omega_X^2}{\omega_X^2 - \omega^2 - i\gamma\omega} \tag{4.2}$$

where ε_∞=2.46 is the bound electron permittivity taken from the ellipsometry results of SP molecules, ω_X=3.35×10^{15} rad/s is the oscillator frequency of the molecules as calculated

from the absorption wavelength, $\gamma = 2\times10^{14}$ rad/s is the damping constant determined from the linewidth of the absorption band, and f=0.17 is the oscillator strength. The simulated transmission spectra (Figure 4.6c) agree well with the experimental spectra (Figure 4.6a). The further examination of the electric field profiles at the two transmission dip wavelengths reveals that two separated HPWMs exist at these two wavelengths, confirming the occurrence of Rabi splitting (Figure 4.7). Besides the large oscillator strength of MC molecules at room temperature,[4, 64] which determines the permittivity change around the oscillator frequency (Equation 4.2), an improved quality factor of the HPWMs strengthens their strong coupling with the molecular exciton and thus leads to a large Rabi splitting observed herein. Since $\frac{\Omega}{2\gamma_P} \sim Q\sqrt{N/V}$,[43] Assuming that the ratio of coupled molecules to uncoupled molecules is constant among the total mode volume of the HPWMs, a large quality factor Q (23.6 when a_x = 360 nm) and a larger plasmon damping γ_P (defined as v/Q, where v is the frequency of HPWMs)[43] lead to a larger coupling strength.

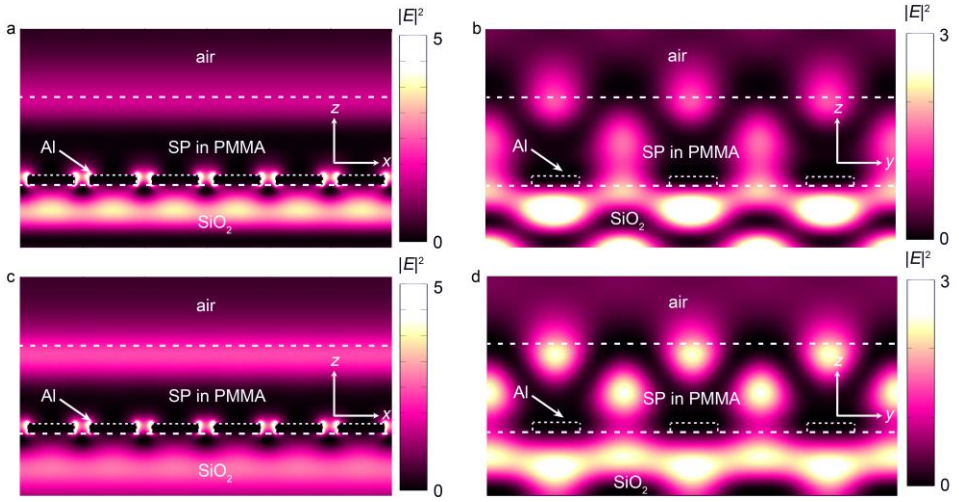

Figure 4.7: Electric field distributions of the HPWMs after Rabi splitting with the lattice constant a_y=440 nm. (a) λ=504 nm in the *xz* plane; (b) λ=504 nm in the *yz* plane; (c) λ=640 nm in the *xz* plane; and (d) λ=640 nm in the *yz* plane.

Another signature of the strong coupling between the HPWMs and MC molecular excitons and Rabi splitting is the energy anticrossing.[4] The energies of the HPWMs before and after UV light illumination and the absorption energy of the MC molecules are summarized in Figure 4.8a. The dispersions were fitted using the two-coupled-oscillators model. When the energies of HPWMs are tuned (by changing the lattice constant a_y of the Al nanodisk arrays) across the exciton energy of MC molecules (*i.e.,* 2.18 eV as indicated by black dash line), two dispersive dip branches, *i.e.,* the upper and lower polaritons P_+ and P_-, undergo an anticrossing at the exciton energy. Since all the data points are close to the zero-detuning point, the energy differences among these lattice constants are small. One application example of the photoswitchable Rabi splitting in the HPWMs is to achieve the all-optical modulation. As displayed in Figure 4.8b, the transmission spectrum for the as-prepared sample features a dip at the wavelength of 560 nm (*i.e.,* the resonance wavelength of the HPWM with a_y = 430 nm). This dip develops into two dips with wavelengths shifted to 500 nm and 640 nm after UV light irradiation on the sample, which isomerizes the

molecules to MC form and leads to the Rabi splitting. The single dip at the wavelength of 560 nm is restored after green light irradiation, which isomerizes the molecules back to SP form and the Rabi splitting disappears. Thus, one can devise all-optical modulators based on this photoswitchable Rabi splitting.[67]

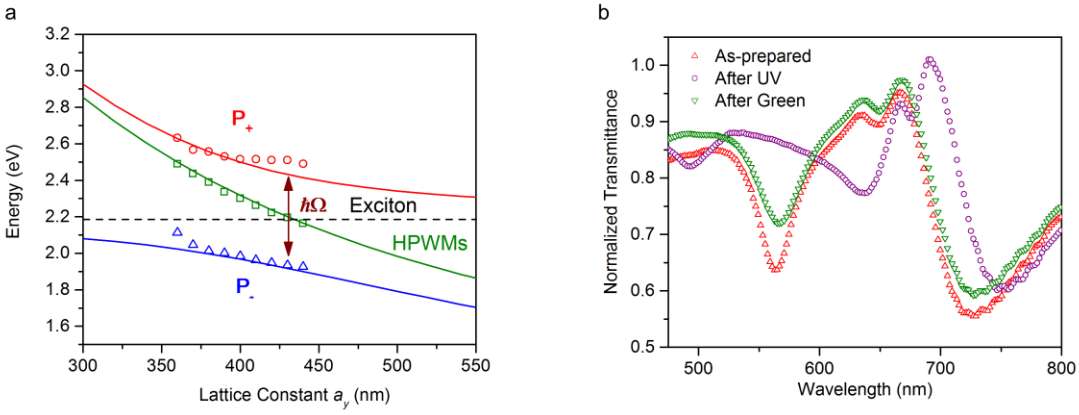

Figure 4.8: Energy anticrossing and largest photoswitchable Rabi splitting in our samples. (a) Energies of HPWMs (green squares) experiences an anticrossing near the exciton energy of MC molecules (black dash line) due to the strong coupling. Red circles and blue triangles indicate the energies of P_+ state and P_- state, respectively, as a function of lattice constant a_y (as shown in Figure 4.1c). The dispersive dip branches of P_+ and P_- states are fitted using the two-coupled-oscillators model. The energies of the HPWMs were extended using simulation data. (b) Largest photoswitchable Rabi splitting occurs to the sample with $a_y = 430$ nm.

4.2.4 Optically rewritable waveguides.

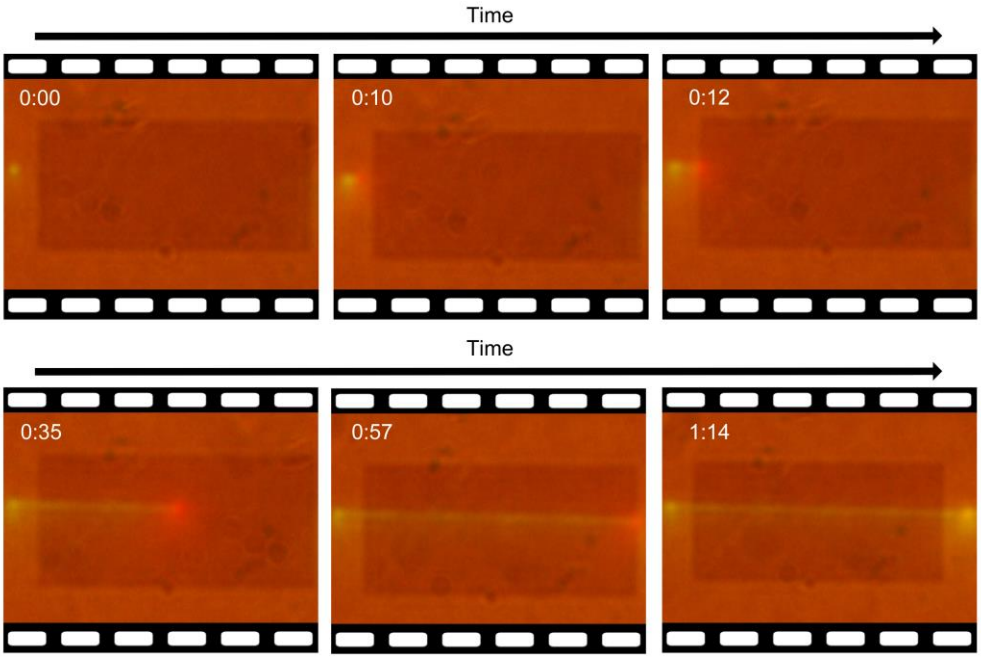

Figure 4.9: Successive optical images of the optical writing of a waveguide (as a straight line) on the MC-molecule-doped PMMA on Al nanodisk array. The writing process was completed within 1 min. The dark rectangular regime corresponds to the Al nanodisk array. Both DMD and motorized stage were applied to control a green laser beam for the waveguide writing. Upon green laser irradiation, the photochromic molecules were switched from MC to SP form.

So far, we have shown that our hybrid systems can support the photoswitchable Rabi splitting in the HPWMs, which enables us to optically tune the resonant wavelengths of HPWMs. We hypothesize that the photoswitchable resonant wavelengths of the HPWMs could be harnessed for optically rewritable waveguides. As shown in Figure 4.9, a focused green (532 nm) laser beam was applied to write a waveguide on the MC-molecule-doped PMMA thin film on Al nanodisk arrays (a_y=430 nm). Briefly, the MC molecules in the area that was exposed to the green laser beam were switched to SP form to create a waveguide, which is a straight line with a width of 2 μm in this example. A digital micromirror device

(DMD) was integrated into our optical setup to scan the laser beam with controllable power, size and speed. The straight line with SP form can support HPWMs at the wavelength of 560 nm while the unexposed areas with MC form can support HPWMs at the wavelengths of 500 nm and 640 nm (Figure 4.8b). Thus, light with a wavelength of 560 nm can be guided along the straight line, leading to the optical creation of a waveguide. In principle, with our DMD-based control of the writing laser beam, we can optically create waveguides with arbitrary designs.

To further characterize the light propagation in the optically written waveguides, we chose Al nanodisk array with a_y=370 nm that was covered by the molecule-doped PMMA thin film. The hybrid system supports HPWM with the peak wavelength close to that of our diode-pumped solid-state laser (532 nm) when the molecules are at SP state, as shown in Figure 4.10a (see spectrum "After green"). The HPWM can be repeatedly switched on and off by alternative irradiation on the sample with UV and green light due to the photoswitchable Rabi splitting (Figure 4.10b). It should be noted that the photoswitchability of SP molecules can be compromised due to the fatigue of the photochromism after many cycles. As displayed in Figure 4.10c, we wrote a linear waveguide on the hybrid structure (*i.e.,* MC molecule-doped PMMA + Al nanodisk array) by scanning green laser beam along the *y*-axis of the sample. When a focused 532 nm laser beam (diameter = 2 μm) was normally incident onto the waveguide, we observed that the light was extended to both left and right sides along the waveguide. We attributed the yellow color of light to the mixture of red fluorescence of MC molecules [68] and green light coupled to the waveguide. Figure 4.11 shows the fluorescence and excitation spectra of the MC molecules. The fluorescence and scattering light in the waveguide (mainly at the boundaries) allowed us to visualize the light coupling and propagation in the far field. In contrast, the same line pattern optically written on the MC molecule-doped PMMA without

Al nanodisk array did not exhibit similar light coupling and propagation behavior, as shown in Figure 4.10d. Furthermore, we have demonstrated the waveguides are optically rewritable in our HPWM samples. As shown in Figure 4.10e, we can erase and rewrite the waveguides by alternative UV light irradiation and green laser scanning.[69]

4.3 SUMMARY

In summary, we have demonstrated the photoswitchable Rabi splitting (up to 572 meV) in the HPWMs based on hybrid systems of molecule-doped-PMMA thin films on Al nanodisk arrays. The Rabi splitting arises from the strong coupling between the HPWMs and molecular excitons. Reversible photoisomerization of the molecules leads to the photoswitchable strong coupling and Rabi splitting. The photoswitchable Rabi splitting enables the development of all-optical light modulators and optically rewritable waveguides. With the advantages of HPWMs in the long-range propagation of light with the subwavelength confinement, the reconfigurable optical elements based on the photoswitchable Rabi splitting will open up a new window of opportunities for compact photonic devices and lab-on-a-chip systems.

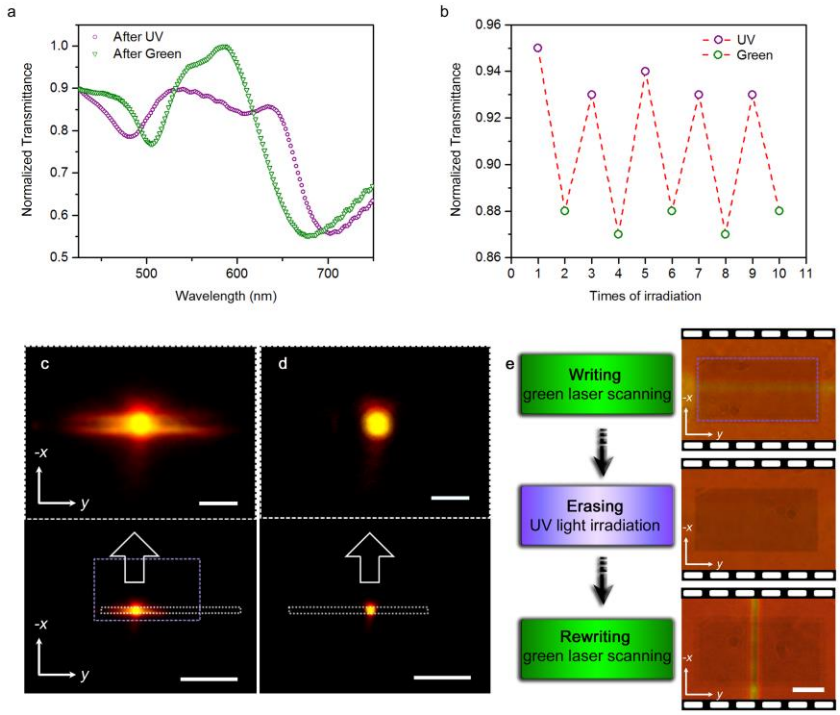

Figure 4.10: (a) Photoswitchable Rabi splitting in the HPWMs of the sample with a_y=370 nm. The single HPWM after green light irradiation has a peak wavelength of 510 nm. (b) Reversible modulation of the transmission intensity upon alternative UV and green light irradiation. Each irradiation time was 2 minutes. (c) A 532 nm laser beam is observed to couple to and propagate in an optically written waveguide on the molecule-doped PMMA on the Al nanodisk array. The yellow light propagates along the written waveguide outlined by the white dashed rectangle in the optical image at the bottom. The purple dashed rectangle indicates the Al nanodisk array. (d) No light coupling and propagation is observed when the same laser beam irradiated an optically written waveguide (outlined by the white dashed rectangle) on the molecule-doped PMMA without Al nanodisk array, which does not support the HPWMs. The white arrows indicate the enlarged images at the light spots. (e) Time-resolved optical images of the optically rewritable waveguides. The dark rectangular region outlined by the purple dashed rectangle is the Al nanodisk array. A waveguide (shown as a straight line) on the MC-molecule-doped PMMA on Al nanodisk array is written with a focused green laser beam controlled by the DMD and a motorized stage. With green laser irradiation, the photochromic molecules were switched from MC to SP form. The waveguide was erased by UV light irradiation, and rewritten by green laser again. Scale bars: 5 μm for the top images and 20 μm for the bottom images in (c) and (d); 10 μm in (e).

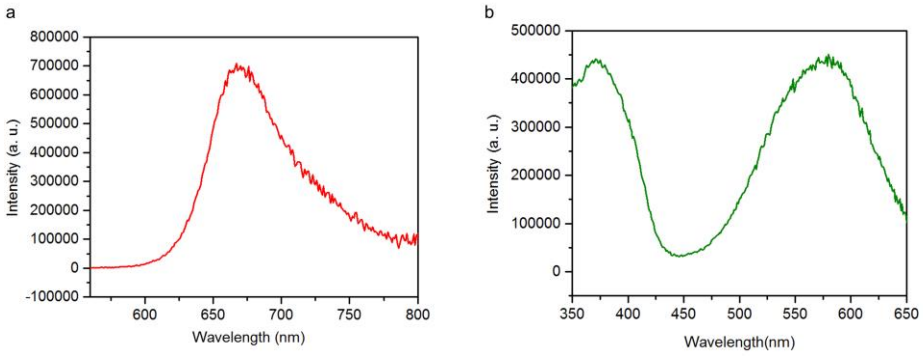

Figure 4.11: (a) Fluorescence spectrum of MC molecules at the excitation wavelength of 532 nm. (b) Excitation spectrum of MC molecules at the emission wavelength of 667 nm.

4.4 REFERENCES

1. Englund, D.; Fattal, D.; Waks, E.; Solomon, G.; Zhang, B.; Nakaoka, T.; Arakawa, Y.; Yamamoto, Y.; Vučković, J., Controlling the Spontaneous Emission Rate of Single Quantum Dots in a Two-Dimensional Photonic Crystal. *Phys. Rev. Lett.* **2005**, 95 (1), 013904.
2. Hennessy, K.; Badolato, A.; Winger, M.; Gerace, D.; Atature, M.; Gulde, S.; Falt, S.; Hu, E. L.; Imamoglu, A., Quantum nature of a strongly coupled single quantum dot-cavity system. *Nature* **2007**, 445 (7130), 896-899.
3. Press, D.; Götzinger, S.; Reitzenstein, S.; Hofmann, C.; Löffler, A.; Kamp, M.; Forchel, A.; Yamamoto, Y., Photon Antibunching from a Single Quantum-Dot-Microcavity System in the Strong Coupling Regime. *Phys. Rev. Lett.* **2007**, 98 (11), 117402.
4. Törmä, P.; Barnes, W. L., Strong coupling between surface plasmon polaritons and emitters: a review. *Rep. Prog. Phys.* **2015**, 78 (1), 013901.
5. Chikkaraddy, R.; de Nijs, B.; Benz, F.; Barrow, S. J.; Scherman, O. A.; Rosta, E.; Demetriadou, A.; Fox, P.; Hess, O.; Baumberg, J. J., Single-molecule strong coupling at room temperature in plasmonic nanocavities. *Nature* **2016**, 535, 127.
6. Konrad, A.; Kern, A. M.; Brecht, M.; Meixner, A. J., Strong and Coherent Coupling of a Plasmonic Nanoparticle to a Subwavelength Fabry–Pérot Resonator. *Nano Lett.* **2015**, 15, 4423-4428.
7. Weisbuch, C.; Nishioka, M.; Ishikawa, A.; Arakawa, Y., Observation of the coupled exciton-photon mode splitting in a semiconductor quantum microcavity. *Phys. Rev. Lett.* **1992**, 69 (23), 3314-3317.

8. Tassone, F.; Yamamoto, Y., Exciton-exciton scattering dynamics in a semiconductor microcavity and stimulated scattering into polaritons. *Phys. Rev. B* **1999**, 59 (16), 10830-10842.

9. Christopoulos, S.; von Högersthal, G. B. H.; Grundy, A. J. D.; Lagoudakis, P. G.; Kavokin, A. V.; Baumberg, J. J.; Christmann, G.; Butté, R.; Feltin, E.; Carlin, J. F.; Grandjean, N., Room-Temperature Polariton Lasing in Semiconductor Microcavities. *Phys. Rev. Lett.* **2007**, 98 (12), 126405.

10. Noda, S.; Fujita, M.; Asano, T., Spontaneous-emission control by photonic crystals and nanocavities. *Nat. Photonics* **2007**, 1 (8), 449-458.

11. Volz, T.; Reinhard, A.; Winger, M.; Badolato, A.; Hennessy, K. J.; Hu, E. L.; Imamoglu, A., Ultrafast all-optical switching by single photons. *Nat. Photonics* **2012**, 6 (9), 605-609.

12. Vasa, P.; Pomraenke, R.; Cirmi, G.; De Re, E.; Wang, W.; Schwieger, S.; Leipold, D.; Runge, E.; Cerullo, G.; Lienau, C., Ultrafast Manipulation of Strong Coupling in Metal−Molecular Aggregate Hybrid Nanostructures. *ACS Nano* **2010**, 4 (12), 7559-7565.

13. Gunter, G.; Anappara, A. A.; Hees, J.; Sell, A.; Biasiol, G.; Sorba, L.; De Liberato, S.; Ciuti, C.; Tredicucci, A.; Leitenstorfer, A.; Huber, R., Sub-cycle switch-on of ultrastrong light-Matter interaction. *Nature* **2009**, 458 (7235), 178-181.

14. Daskalakis, K. S.; Maier, S. A.; Murray, R.; Kéna-Cohen, S., Nonlinear interactions in an organic polariton condensate. *Nat. Mater.* **2014**, 13 (3), 271-278.

15. Plumhof, J. D.; Stöferle, T.; Mai, L.; Scherf, U.; Mahrt, R. F., Room-temperature Bose–Einstein condensation of cavity exciton–polaritons in a polymer. *Nat. Mater.* **2014**, 13 (3), 247-252.

16. Lidzey, D. G.; Bradley, D. D. C.; Virgili, T.; Armitage, A.; Skolnick, M. S.; Walker, S., Room Temperature Polariton Emission from Strongly Coupled Organic Semiconductor Microcavities. *Phys. Rev. Lett.* **1999**, 82 (16), 3316-3319.

17. van Vugt, L. K.; Rühle, S.; Ravindran, P.; Gerritsen, H. C.; Kuipers, L.; Vanmaekelbergh, D., Exciton Polaritons Confined in a ZnO Nanowire Cavity. *Phys. Rev. Lett.* **2006**, 97 (14), 147401.

18. Takazawa, K.; Inoue, J.-i.; Mitsuishi, K.; Takamasu, T., Fraction of a Millimeter Propagation of Exciton Polaritons in Photoexcited Nanofibers of Organic Dye. *Phys. Rev. Lett.* **2010**, 105 (6), 067401.

19. Sugawara, Y.; Kelf, T. A.; Baumberg, J. J.; Abdelsalam, M. E.; Bartlett, P. N., Strong Coupling between Localized Plasmons and Organic Excitons in Metal Nanovoids. *Phys. Rev. Lett.* **2006**, 97 (26), 266808.

20. Fofang, N. T.; Park, T.-H.; Neumann, O.; Mirin, N. A.; Nordlander, P.; Halas, N. J., Plexcitonic Nanoparticles: Plasmon−Exciton Coupling in Nanoshell−J-Aggregate Complexes. *Nano Lett.* **2008**, 8 (10), 3481-3487.

21. Schlather, A. E.; Large, N.; Urban, A. S.; Nordlander, P.; Halas, N. J., Near-Field Mediated Plexcitonic Coupling and Giant Rabi Splitting in Individual Metallic Dimers. *Nano Lett.* **2013**, 13 (7), 3281-3286.

22. Väkeväinen, A. I.; Moerland, R. J.; Rekola, H. T.; Eskelinen, A. P.; Martikainen, J. P.; Kim, D. H.; Törmä, P., Plasmonic Surface Lattice Resonances at the Strong Coupling Regime. *Nano Lett.* **2013**, 14 (4), 1721-1727.

23. Eizner, E.; Avayu, O.; Ditcovski, R.; Ellenbogen, T., Aluminum Nanoantenna Complexes for Strong Coupling between Excitons and Localized Surface Plasmons. *Nano Lett.* **2015**, 15 (9), 6215-6221.

24. Todisco, F.; D'Agostino, S.; Esposito, M.; Fernández-Domínguez, A. I.; De Giorgi, M.; Ballarini, D.; Dominici, L.; Tarantini, I.; Cuscuná, M.; Della Sala, F.; Gigli, G.; Sanvitto, D., Exciton–Plasmon Coupling Enhancement via Metal Oxidation. *ACS Nano* **2015**, 9 (10), 9691-9699.

25. Pirruccio, G.; Ramezani, M.; Rodriguez, S. R.-K.; Rivas, J. G., Coherent Control of the Optical Absorption in a Plasmonic Lattice Coupled to a Luminescent Layer. *Phys. Rev. Lett*. **2016**, 116 (10), 103002.

26. Zengin, G.; Gschneidtner, T.; Verre, R.; Shao, L.; Antosiewicz, T. J.; Moth-Poulsen, K.; Käll, M.; Shegai, T., Evaluating Conditions for Strong Coupling between Nanoparticle Plasmons and Organic Dyes Using Scattering and Absorption Spectroscopy. *J. Phys. Chem. C* **2016**, 120 (37), 20588–20596.

27. Zhou, N.; Yuan, M.; Gao, Y.; Li, D.; Yang, D., Silver Nanoshell Plasmonically Controlled Emission of Semiconductor Quantum Dots in the Strong Coupling Regime. *ACS Nano* **2016**, 10, 4154-4163.

28. Shi, L.; Hakala, T. K.; Rekola, H. T.; Martikainen, J. P.; Moerland, R. J.; Törmä, P., Spatial Coherence Properties of Organic Molecules Coupled to Plasmonic Surface Lattice Resonances in the Weak and Strong Coupling Regimes. *Phys. Rev. Lett.* **2014**, 112 (15), 153002.

29. Klar, T.; Perner, M.; Grosse, S.; von Plessen, G.; Spirkl, W.; Feldmann, J., Surface-plasmon resonances in single metallic nanoparticles. *Phys. Rev. Lett.* **1998**, 80 (19), 4249-4252.

30. Bukasov, R.; Ali, T. A.; Nordlander, P.; Shumaker-Parry, J. S., Probing the plasmonic near-field of gold nanocrescent antennas. *ACS Nano* **2010**, 4 (11), 6639-6650.

31. Halas, N. J.; Lal, S.; Chang, W. S.; Link, S.; Nordlander, P., Plasmons in strongly coupled metallic nanostructures. *Chem. Rev.* **2011**, 111 (6), 3913-3961.

32. Lin, L.; Zheng, Y., Optimizing plasmonic nanoantennas via coordinated multiple coupling. *Sci. Rep.* **2015**, 5, 14788.

33. O'Brien, M. N.; Jones, M. R.; Kohlstedt, K. L.; Schatz, G. C.; Mirkin, C. A., Uniform Circular Disks With Synthetically Tailorable Diameters: Two-Dimensional Nanoparticles for Plasmonics. *Nano Lett.* **2015**, 15 (2), 1012-1017.

34. Fan, J. A.; Bao, K.; Sun, L.; Bao, J.; Manoharan, V. N.; Nordlander, P.; Capasso, F., Plasmonic Mode Engineering with Templated Self-Assembled Nanoclusters. *Nano Lett.* **2012**, 12 (10), 5318-5324.

35. Fan, J. A.; He, Y.; Bao, K.; Wu, C.; Bao, J.; Schade, N. B.; Manoharan, V. N.; Shvets, G.; Nordlander, P.; Liu, D. R.; Capasso, F., DNA-Enabled Self-Assembly of Plasmonic Nanoclusters. *Nano Lett.* **2011**, 11 (11), 4859-4864.

36. Yao, J.; Le, A.-P.; Gray, S. K.; Moore, J. S.; Rogers, J. A.; Nuzzo, R. G., Nanostructured Plasmonic Materials: Functional Nanostructured Plasmonic Materials. *Adv. Mater.* **2010**, 22 (10), 1102–1110.

37. Russell, K. J.; Yeung, K. Y. M.; Hu, E., Measuring the mode volume of plasmonic nanocavities using coupled optical emitters. *Phys. Rev. B* **2012**, 85 (24), 245445.

38. Russell, K. J.; Hu, E. L., Gap-mode plasmonic nanocavity. *Appl. Phys. Lett.* **2010**, 97 (16), 163115.

39. Wurtz, G. A.; Evans, P. R.; Hendren, W.; Atkinson, R.; Dickson, W.; Pollard, R. J.; Zayats, A. V.; Harrison, W.; Bower, C., Molecular Plasmonics with Tunable Exciton−Plasmon Coupling Strength in J-Aggregate Hybridized Au Nanorod Assemblies. *Nano Lett.* **2007**, 7 (5), 1297-1303.

40. Zengin, G.; Johansson, G.; Johansson, P.; Antosiewicz, T. J.; Käll, M.; Shegai, T., Approaching the strong coupling limit in single plasmonic nanorods interacting with J-aggregates. *Sci. Rep.* **2013**, 3, 3074.

41. Trügler, A.; Hohenester, U., Strong coupling between a metallic nanoparticle and a single molecule. *Phys. Rev. B* **2008**, 77 (11), 115403.

42. Ni, W.; Ambjörnsson, T.; Apell, S. P.; Chen, H.; Wang, J., Observing Plasmonic−Molecular Resonance Coupling on Single Gold Nanorods. *Nano Lett.* **2010**, 10 (1), 77-84.

43. Zengin, G.; Wersäll, M.; Nilsson, S.; Antosiewicz, T. J.; Käll, M.; Shegai, T., Realizing Strong Light-Matter Interactions between Single-Nanoparticle Plasmons and Molecular Excitons at Ambient Conditions. *Phys. Rev. Lett.* **2015**, 114 (15), 157401.

44. Ming, T.; Zhao, L.; Xiao, M.; Wang, J., Resonance-Coupling-Based Plasmonic Switches. *Small* **2010**, 6 (22), 2514-2519.

45. Alam, M. Z.; Aitchison, J. S.; Mojahedi, M., A marriage of convenience: Hybridization of surface plasmon and dielectric waveguide modes. *Laser Photonics Rev*. **2014**, 8 (3), 394-408.

46. Christ, A.; Tikhodeev, S. G.; Gippius, N. A.; Kuhl, J.; Giessen, H., Waveguide-Plasmon Polaritons: Strong Coupling of Photonic and Electronic Resonances in a Metallic Photonic Crystal Slab. *Phys. Rev. Lett.* **2003**, 91 (18), 183901.

47. Yannopapas, V.; Paspalakis, E.; Vitanov, N. V., Electromagnetically induced transparency and slow light in an array of metallic nanoparticles. *Phys. Rev. B* **2009**, 80 (3), 035104.

48. Zentgraf, T.; Zhang, S.; Oulton, R. F.; Zhang, X., Ultranarrow coupling-induced transparency bands in hybrid plasmonic systems. *Phys. Rev. B* **2009**, 80 (19), 195415.

49. Bernal Arango, F.; Kwadrin, A.; Koenderink, A. F., Plasmonic Antennas Hybridized with Dielectric Waveguides. *ACS Nano* **2012**, 6 (11), 10156-10167.

50. Février, M.; Gogol, P.; Aassime, A.; Mégy, R.; Delacour, C.; Chelnokov, A.; Apuzzo, A.; Blaize, S.; Lourtioz, J.-M.; Dagens, B., Giant Coupling Effect between Metal Nanoparticle Chain and Optical Waveguide. *Nano Lett.* **2012**, 12 (2), 1032-1037.

51. Oulton, R. F.; Sorger, V. J.; Genov, D. A.; Pile, D. F. P.; Zhang, X., A hybrid plasmonic waveguide for subwavelength confinement and long-range propagation. *Nat. Photonics* **2008**, 2 (8), 496-500.

52. Yang, X.; Liu, Y.; Oulton, R. F.; Yin, X.; Zhang, X., Optical Forces in Hybrid Plasmonic Waveguides. *Nano Lett.* **2011**, 11 (2), 321-328.

53. Dintinger, J.; Klein, S.; Ebbesen, T. W., Molecule–Surface Plasmon Interactions in Hole Arrays: Enhanced Absorption, Refractive Index Changes, and All-Optical Switching. *Adv. Mater.* **2006**, 18 (10), 1267-1270.

54. Zheng, Y. B.; Kiraly, B.; Cheunkar, S.; Huang, T. J.; Weiss, P. S., Incident-Angle-Modulated Molecular Plasmonic Switches: A Case of Weak Exciton–Plasmon Coupling. *Nano Lett.* **2011**, 11 (5), 2061-2065.

55. Rodriguez, S. R. K.; Murai, S.; Verschuuren, M. A.; Rivas, J. G., Light-Emitting Waveguide-Plasmon Polaritons. *Phys. Rev. Lett.* **2012**, 109 (16), 166803.

56. Knight, M. W.; King, N. S.; Liu, L.; Everitt, H. O.; Nordlander, P.; Halas, N. J., Aluminum for Plasmonics. *ACS Nano* **2014**, 8 (1), 834-840.

57. Zheng, B. Y.; Wang, Y.; Nordlander, P.; Halas, N. J., Color-Selective and CMOS-Compatible Photodetection Based on Aluminum Plasmonics. *Adv. Mater.* **2014**, 26 (36), 6318-6323.

58. Olson, J.; Manjavacas, A.; Basu, T.; Huang, D.; Schlather, A. E.; Zheng, B.; Halas, N. J.; Nordlander, P.; Link, S., High Chromaticity Aluminum Plasmonic Pixels for Active Liquid Crystal Displays. *ACS Nano* **2016**, 10 (1), 1108-1117.

59. Ross, M. B.; Schatz, G. C., Aluminum and Indium Plasmonic Nanoantennas in the Ultraviolet. *J. Phys. Chem. C* **2014**, 118 (23), 12506-12514.

60. Chan, G. H.; Zhao, J.; Schatz, G. C.; Duyne, R. P. V., Localized Surface Plasmon Resonance Spectroscopy of Triangular Aluminum Nanoparticles. *J. Phys. Chem. C* **2008**, 112 (36), 13958-13963.

61. Langhammer, C.; Schwind, M.; Kasemo, B.; Zorić, I., Localized Surface Plasmon Resonances in Aluminum Nanodisks. *Nano Lett.* **2008**, 8 (5), 1461-1471.

62. Hutchison, J. A.; Liscio, A.; Schwartz, T.; Canaguier-Durand, A.; Genet, C.; Palermo, V.; Samorì, P.; Ebbesen, T. W., Tuning the Work-Function Via Strong Coupling. *Adv. Mater.* **2013**, 25 (17), 2481-2485.

63. Hutchison, J. A.; Schwartz, T.; Genet, C.; Devaux, E.; Ebbesen, T. W., Modifying Chemical Landscapes by Coupling to Vacuum Fields. *Angew. Chem. Int. Ed.* **2012**, 51 (7), 1592-1596.

64. Schwartz, T.; Hutchison, J. A.; Genet, C.; Ebbesen, T. W., Reversible Switching of Ultrastrong Light-Molecule Coupling. *Phys. Rev. Lett.* **2011**, 106 (19), 196405.

65. Khitrova, G.; Gibbs, H. M.; Kira, M.; Koch, S. W.; Scherer, A., Vacuum Rabi splitting in semiconductors. *Nat. Phys.* **2006**, 2 (2), 81-90.

66. Savasta, S.; Saija, R.; Ridolfo, A.; Di Stefano, O.; Denti, P.; Borghese, F., Nanopolaritons: Vacuum Rabi Splitting with a Single Quantum Dot in the Center of a Dimer Nanoantenna. *ACS Nano* 20**10**, 4 (11), 6369-6376.

67. Baudrion, A.-L.; Perron, A.; Veltri, A.; Bouhelier, A.; Adam, P.-M.; Bachelot, R., Reversible Strong Coupling in Silver Nanoparticle Arrays Using Photochromic Molecules. *Nano Lett.* **2013**, 13 (1), 282-286.

68. Wang, M.; Bangalore Rajeeva, B.; Scarabelli, L.; Perillo, E. P.; Dunn, A. K.; Liz-Marzán, L. M.; Zheng, Y., Molecular-Fluorescence Enhancement via Blue-Shifted Plasmon-Induced Resonance Energy Transfer. *J. Phys. Chem. C* **2016**, 120 (27), 14820-14827.

69. Klajn, R., Spiropyran-based dynamic materials. *Chem. Soc. Rev.* **2014**, 43 (1), 148-184.

Chapter 5 Controlling Plasmon-Enhanced Fluorescence via Intersystem Crossing in Photoswitchable Molecules*

5.1 INTRODUCTION

Extensive studies on plasmon-enhanced fluorescence have focused on applying plasmonic nanostructures with large field enhancement and low optical loss to increase the excitation and radiative-decay rates of fluorophores. However, the fluorescence quantum yield (QY) is also influenced by non-radiative decay rates that can be increased by the plasmon-induced high electromagnetic fields. The non-radiative decay channels vary in different molecular systems. In the presence of a strong spin-orbit coupling, an additional decay channel occurs when the first excited singlet state transfers to the triplet state, a process known as intersystem crossing (ISC). So far, most of the studies on plasmon-enhanced fluorescence have ignored the possible influence of ISC.[1-10] However, for some dye molecules such as spiropyran (SP)-derived merocyanine (MC) molecules, ISC can be an efficient non-radiative decay pathway of the first excited singlet state.[11-12] Therefore, understanding and controlling the effects of ISC on plasmon-enhanced fluorescence may advance both fundamental research and applications.

In this chapter, we explore and exploit the intrinsic ISC of photochromic molecules to control their plasmon-enhanced fluorescence. Specifically, we used hybrid systems comprising photochromic SP molecules and a single plasmonic nanoparticle (NP) or NP aggregates, as platforms to demonstrate that (1) ISC-mediated plasmon-enhanced

* Wang, M.; Hartmann, G.; Wu, Z.; Scarabelli, L.; Rajeeva, B. B.; Jarrett, J. W.; Perillo, E. P.; Dunn, A. K.; Liz-Marzán, L. M.; Hwang, G. S.; Zheng, Y., Controlling Plasmon-Enhanced Fluorescence via Intersystem Crossing in Photoswitchable Molecules. *Small* 2017, 13 (38), 1701763.
Wang, M. carried out the experimental work and participated in the preparation of manuscript.

fluorescence of photoswitchabe molecules leads to a large modulation of light emission from the hybrid systems, and (2) as a non-radiative decay pathway, counterintuitively, ISC can improve the plasmonic enhancement of the fluorescence of molecules when there is strong electromagnetic field enhancement and the ISC rate is sufficiently fast.

5.2 Results and Discussion

5.2.1 Experimental section

5.2.1.1 Sample Preparation

Au nanospheres (AuNSs, Sigma Aldrich) with a diameter of 60 nm and Au nanotriangles (AuNTs) of variable sizes[18] were drop-coated on microscope calibration slides (AmScope) and dried naturally. Chlorobenzene (Fisher Scientific) was used to dissolve spiropyran (SP, Sigma-Aldrich) and PMMA (Sigma-Aldrich) with a weight ratio of 2:1 (SP:PMMA) to prepare PMMA films with a high concentration of SP molecules (8 wt%). A spin coater (Laurell Technologies) was employed to create SP-doped PMMA films on microscope slides with AuNSs or AuNTs. The spin coater was run with a speed of 2000 revolutions per minute for one minute.

5.2.1.2 Optical measurements

The optical scattering spectra and the white-light-excited fluorescence of merocyanine (MC) molecules were measured via a dark-field optical microscope (Ti-E inverted microscope, Nikon) with a halogen white light source (12V, 100 W). UV light and green light were obtained by a mercury light source (C-HGFIE, power: 130 W, Nikon) with excitation filters (DAPI Shift Filter set, excitation: 358 nm; TRITC HYQ Shift Filter set, excitation: 530-560 nm). Microscope calibration slides with markers were used to

locate individual gold nanosphere (AuNS) aggregates and gold nanotriangles (AuNTs). The UV or green light (irradiation time was one minute) was applied to convert molecules from SP to MC isomers or from MC to SP isomers. An oil-immersion dark-field condenser in conjunction with 100× objective was used for single-particle and single-aggregate spectroscopy. Scanning electron microscopy (S5500, Hitachi) and transmission electron microscopy (JEM1400PLUS, JEOL) were used to measure the morphology of AuNS aggregates and AuNTs.

5.2.1.3 Temperature measurement

A thermometer was used to measure the temperature increase at the samples due to the photothermal effects. Upon irradiation with white light, the sample temperature increased from 22 °C to 31 °C within two minutes. The supply voltage of the white light source was 6 V. It should be noted that the thermometer was directly placed under the white light source and the head of thermometer is much larger than the irradiated spot in the dark-field optical measurement. Therefore, we believe that the actual temperature increase rate was faster than the measured value.

5.2.1.4. FDTD simulation

A commercially available software package (FDTD Solutions, Lumerical) was employed to conduct the finite-difference time-domain (FDTD) simulations. The AuNSs and AuNT were positioned at the top of a glass substrate (modeled with refractive index n=1.4). The refractive index of background environment was set as 1.49 to represent the PMMA films. A plane wave was applied as the incident light source, and the scattered light was collected in transmission mode to obtain the optical scattering spectra. The

wavelength-dependent dielectric functions of Au were adapted from Johnson and Christy.[19]

5.2.1.5 DFT simulation

Our density functional theory (DFT) and time-dependent density functional theory (TDDFT) calculations were performed using the Gaussian 09 suite of programs.[20] Semilocal (PBE[21])- and hybrid (B3LYP[22])-generalized gradient approximations were both considered. The 6-311G(d,p) and 6-311+G(2d,p) levels of theory were employed for configuration/total energy and vertical excitation calculations, respectively. The environment of the molecule within a PMMA matrix was simulated by applying a polarizable continuum model within integral equation formalism.[23]

5.2.1.6 Fluorescence lifetime imaging microscopy

A femtosecond titanium: sapphire laser tuned to 800 nm (≈200 fs) (Mira 900, Coherent), galvo scanning mirrors (6215H, Cambridge Tech.), and a GaAsP photomultiplier tube (PMT) (H7422PA-40, Hamamatsu) in non-descanned detection scheme were utilized to constitute the FLIM setup. Before the signal reached the photon counting board (SPC-150, Becker and Hickl GmbH), a preamplifier (HFAC-26, Becker and Hickl GmbH) was used to ampilfy the output current of the PMT. The average laser power, TCSPC bin resolution, and FLIM pixel integration time were set to 4 mW, 20 ps, and 5 ms, respectively, when recording the fluorescence lifetime. A least squares method using a model of a single exponential decay was then used to fit the fluorescence lifetime.[24]

5.2.2 Design and working principle

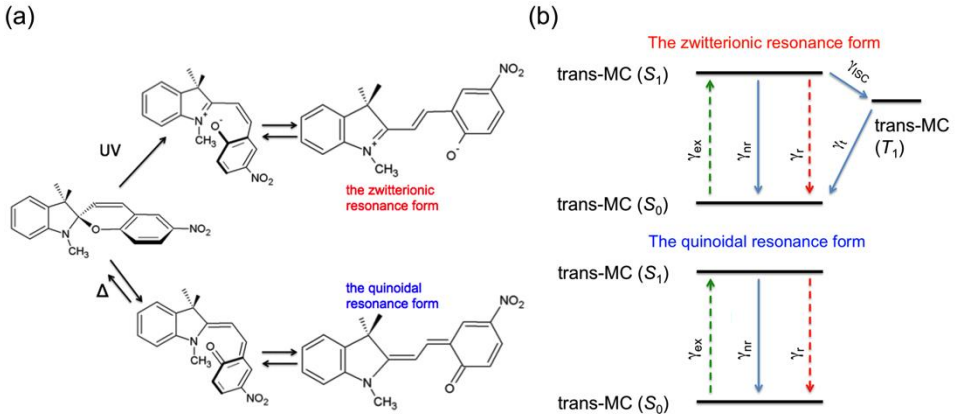

Figure 5.1: (a) Schematic representation of the photochemical (up pathway) and thermal (down pathway) ring-opening reactions of SP molecules. (b) Jablonski diagram with the relevant energy states for both forms. γ_{ex} is the excitation rate, γ_r is the radiative decay rate, γ_{nr} is the non-radiative decay rate, γ_{ISC} is the rate of intersystem crossing, and γ_t is the triplet decay rate.

It has been known that SP molecules can convert to MC via either photochemical ring-opening or thermal ring-opening reactions.[13-14] Photochemical ring-opening reactions proceed through a heterolytic C-O bond cleavage, producing the zwitterionic MC form. Thermal ring-opening reactions follow a 6*p* electro-cyclic ring opening, producing the quinoidal MC form, (Figure 5.1a). A zwitterionic character in the singlet wave function, which contains a positive and a negative charge, is favorable for ISC.[15-17] While the zwitterionic MC form has efficient ISC,[11-12] the quinoidal MC form lacks the zwitterionic character and thus the ISC. Therefore, the decay channels of the first excited singlet state are different in the zwitterionic and the quinoidal MC forms, as indicated in Figure 5.1b. Thus, the fluorescence QY of zwitterionic MC molecules (ϕ_0) and quinoidal MC molecules (ϕ_0'), without plasmonic nanostructures, can be expressed as[1, 4, 10]:

$$\phi_0 = \frac{\gamma_r}{\gamma_r + \gamma_{nr} + \gamma_{\mathrm{ISC}}} \tag{5.1}$$

and

$$\phi_0 = \frac{\gamma_r'}{\gamma_r' + \gamma_{nr}'} \tag{5.2}$$

where γ_r, γ_{nr} and γ_{ISC} represent the radiative decay rate, non-radiative (excluding ISC) decay rate, and ISC rate of zwitterionic MC molecules, respectively. γ_r' and γ_{nr}' are the radiative and non-radiative decay rates of quinoidal MC molecules, respectively. We use (′) to distinguish the parameters of the quinoidal MC molecule from those of the zwitterionic MC molecule.

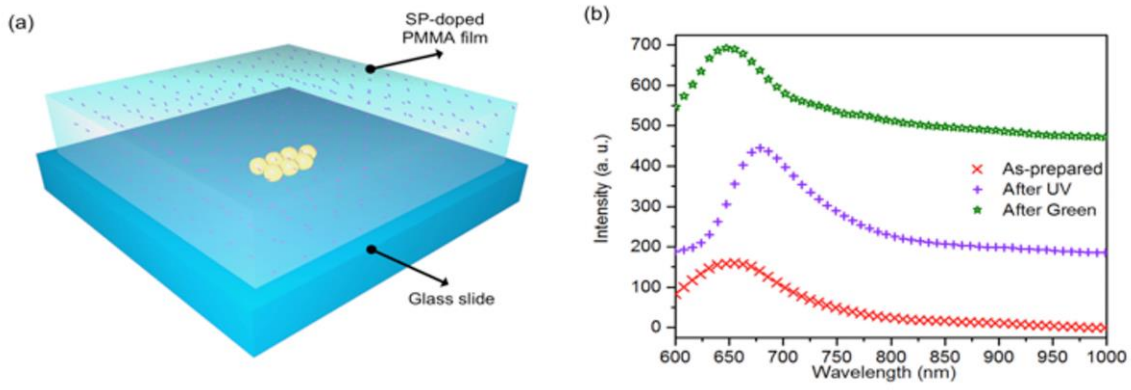

Figure 5.2: (a) Schematic view of a sample comprising a single AuNS aggregate on a glass substrate, covered by an SP-doped PMMA thin film. (b) Photoswitchable fluorescence of pure photochromic molecules. Specifically, the curve made of red crosses represents the molecular fluorescence before irradiation on the sample. The curves made of purple and green symbols represent molecular fluorescence after UV and green light irradiation on the sample, respectively. An intensity-axis offset was added for clarity.

Our samples were prepared by drop-casting AuNSs and AuNTs on glass slides,[18] followed by spin-coating of SP-doped PMMA films to cover the AuNSs and AuNTs, as shown in Figure 5.2a. The photoisomerization of SP in the PMMA matrix was confirmed by FTIR and UV-vis absorption spectra under different light irradiation (see Figures 5.3a and b). Upon white light excitation of the molecules, photoswitchable fluorescence can be observed in a dark-field optical microscope after alternating UV and green light irradiation, as shown in Figure 5.2b.[25] The fluorescence of zwitterionic MC molecules, which are formed via photochemical ring opening reaction upon UV irradiation, features an emission band centered at 670 nm (Figure 5.2b, purple line), which is in good agreement with the fluorescence measured in a conventional fluorometer.[26-28] The zwitterionic MC molecules are stable in the PMMA matrix due to the increased polarity of their microenvironment.[29-32] This increased polarity arises from the formation of a large number of zwitterionic MC molecules in the PMMA matrix during UV irradiation. Both the as-prepared sample and the sample after green irradiation feature emission bands centered at ~650 nm (Figure 5.2b, red and green lines). The emission cannot be attributed to SP molecules, which were reported to have an emission band centered around ~530 nm under UV light excitation (our white halogen light source does not contain UV light, see spectrum in Figure 5.3c.[13] We attribute the ~650 nm emission to the quinoidal MC molecules, which are formed through a thermal ring-opening reaction (see Figure 5.4).[13] The thermal ring-opening reaction occurs in our experiments due to temperature increase (see detailed information in the Experimental section) at the optically irradiated spots. Therefore, our molecular system combined with plasmonic nanoparticles provides an ideal platform to investigate how the intrinsic ISC affects plasmon-enhanced fluorescence.

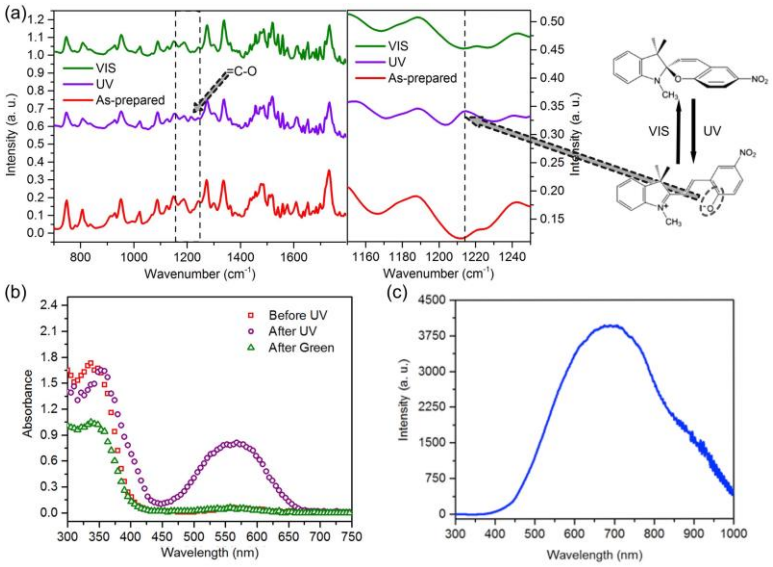

Figure 5.3: (a) FTIR spectra of molecules under different light irradiation. The right panel is zoom-in spectra for the part indicated by dashed lines in the left panel. The dashed line in right panel indicates additional peak at 1214 cm^{-1}. The chemical structures of the molecules under isomerization are shown. (b) UV-vis absorption spectra of molecules under different light irradiation. (c) Optical spectrum of the halogen light source. The supply voltage of the light source is 6V.

The fluorescence of a molecular emitter is enhanced when the molecule is near a plasmonic nanostructure that exhibits a localized surface plasmon resonance (LSPR) at a wavelength matching the fluorescence peak of the emitter.[10, 33] The radiative decay rate enhancement is calculated by:[10, 33]

$$\frac{\gamma_r}{\gamma_{r0}} = \left| \mathbf{n}_p + k^2 \frac{1}{\varepsilon_0} \ddot{\alpha}(\omega) \ddot{\mathbf{G}}(\mathbf{r}_p, \mathbf{r}_0; \omega) \mathbf{n}_p \right|^2 \tag{5.3}$$

where γ_r is the radiative decay rate in the presence of the plasmonic nanostructure, γ_{r0} is the radiative decay rate without the plasmonic nanostructure, $\mathbf{n}_p$ is the unit vector in the direction of the molecule's dipole moment, k is the wavevector of emitted light, ω is frequency of emitted light, $\ddot{\alpha}$ is the particle's polarizability, $\ddot{\mathbf{G}}$ is the system's dyadic

Green's function, $\mathbf{r}_0$ is the position vector of the molecules, and $\mathbf{r}_p$ is the position vector of the particles.

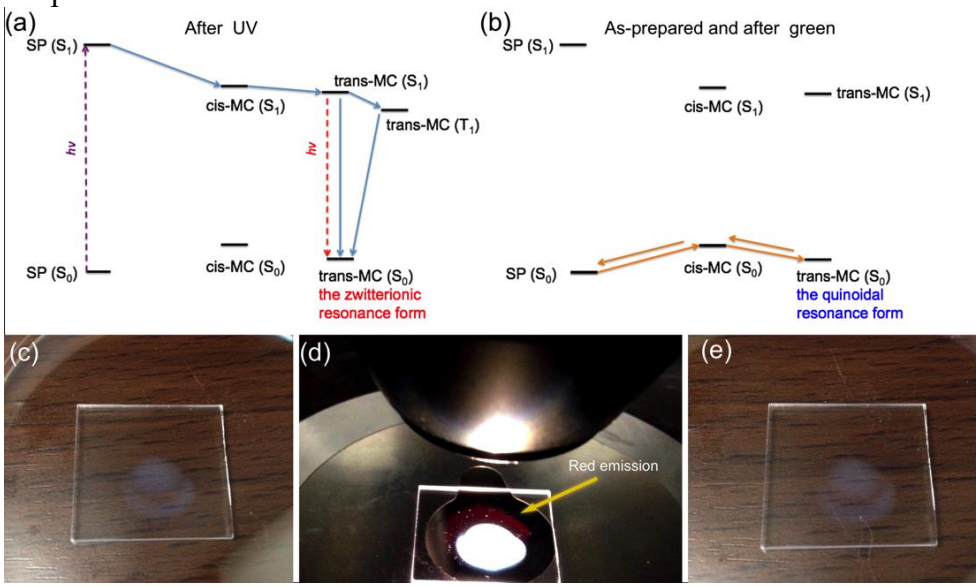

Figure 5.4: (a) Schematic of the photochemical pathway. (b) Schematic of the thermal pathway. (c) Photo of SP-doped PMMA film before white light irradiation. (d) Red fluorescence from the SP-doped PMMA film immediately after white light irradiation. (e) Photo of SP-doped PMMA film after 1 minute of white light irradiation.

The enhanced E-field by the plasmonic nanostructure, $\mathrm{E}_p(\mathbf{r}_0)$, equals:[33]

$$\mathrm{E}_p(\mathbf{r}_0) = k^2 \frac{1}{\varepsilon_0} \ddot{\alpha}(\omega) \ddot{\mathbf{G}}(\mathbf{r}_p, \mathbf{r}_0; \omega) \mathbf{n}_p \mathrm{E}_0(\mathbf{r}_p) \tag{5.4}$$

where $\mathrm{E}_0(\mathbf{r}_p)$ is the E-field of the incident light. By combining Equations 5.3 and 5.4, we obtain:

$$\frac{\gamma_r}{\gamma_{r0}} = \left| \mathbf{n}_p + \frac{\mathrm{E}_p(\mathbf{r}_0)}{\mathrm{E}_0(\mathbf{r}_p)} \mathbf{n}_p \right|^2 \tag{5.5}$$

From Equation 5.5, it is clear that a larger E-field enhancement leads to a larger radiative decay rate enhancement, and when $\mathrm{E}_p(\mathbf{r}_0)$ is much larger than $E_0(\mathbf{r}_p)$ approximately $\frac{\gamma_r}{\gamma_{r0}} \propto \left|\mathrm{E}_p(\mathbf{r}_0)\right|^2$.

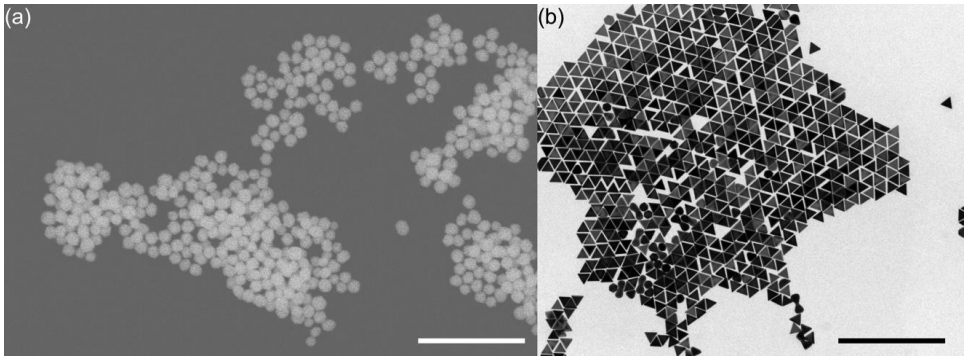

Figure 5.5: (a) SEM image of AuNSs. Scale bar is 500 nm. (b) TEM image of AuNTs. Scale bar is 500 nm.

5.2.3 Optical measurements and FDTD simulation

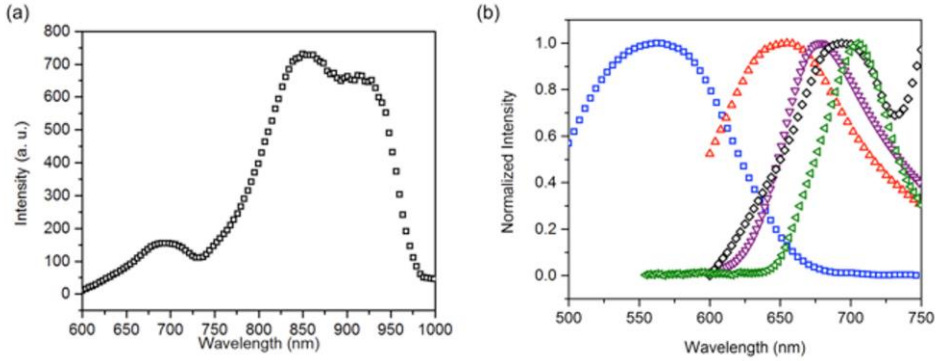

Figure 5.6: (a) Scattering spectrum of an AuNS aggregate covered with a pure PMMA film. (b) Normalized scattering spectra of the AuNS aggregate (black diamonds) and a single AuNT (green triangles); fluorescence spectra of the as-prepared sample (red triangles) and the sample after UV irradiation (purple triangles); and absorption spectrum of the sample after UV irradiation (blue squares). The cutoff of some of the spectra in (b) is due to the limited working range of the grating in our spectrometer.

Since both plasmonic NP aggregates with small inter-particle gaps and NPs with sharp tips can lead to a large E-field enhancement,[18, 34-37] we selected for our experiments self-assembled AuNS aggregates with small inter-particle gaps and single gold nanotriangles AuNTs featuring sharp tips. Self-assembly is chosen to obtain AuNS

aggregates with small inter-particle gaps, which are difficult to be obtained by other methods, such as the electron-beam lithography. In the former case we use AuNSs with a diameter of 60 nm (see SEM image of AuNSs in Figure 5.5a). AuNTs have an average edge length of 60 nm and an average thickness of 30 nm (see TEM image in Figure 5.5b). Most importantly, both systems were carefully chosen to have an optical scattering peak at ~700 nm (when covered with PMMA films or SP-doped PMMA films) that can match the fluorescence rather than the absorption of MC molecules (Figures 5.6a and b). This peak wavelength can avoid the influence from the fluorescence enhancement by the plasmon-induced excitation enhancement and resonance energy transfer.[25, 38] Moreover, this particular aggregate was selected because it shows the largest fluorescence enhancement during repeated measurements. It is also worth mentioning that, the energy bandgap of ISC is smaller than that of the molecule's emission, as shown in Figure 5.1b. Since the LSPR bands of AuNS aggregates and AuNTs match the emission band of the molecules, there is also a mismatch between the energy bands of LSPRs and ISC. Therefore, the influence from LSPRs on the ISC process is weak.

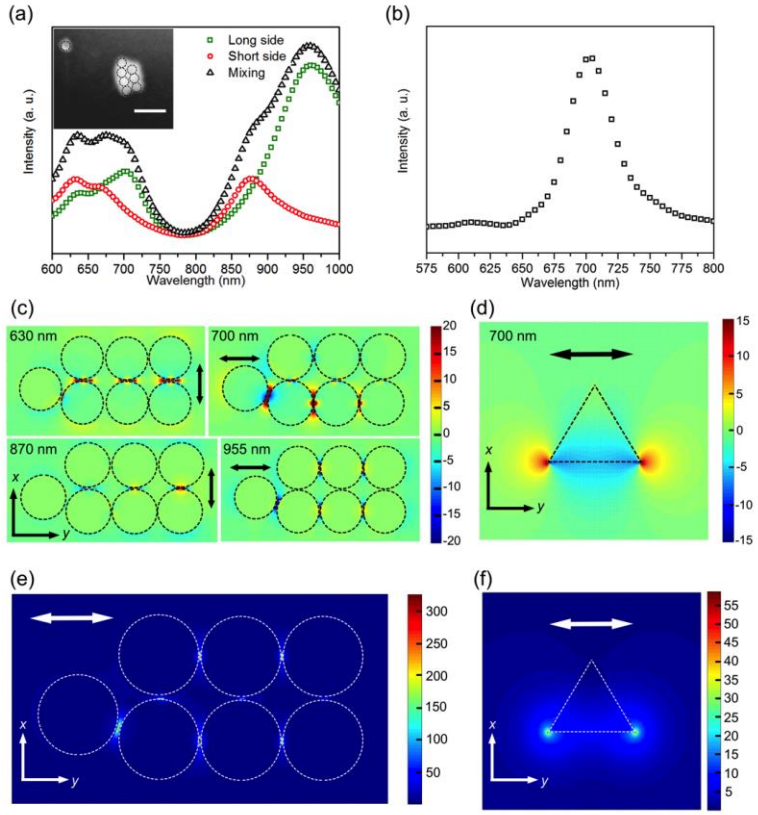

Figure 5.7: (a) Simulated scattering spectra of an AuNS aggregate under different polarizations of incident light. SEM image in inset shows an AuNS aggregate and a single AuNS. The dashed circles indicate the AuNSs. (b) Simulated scattering spectrum of a single AuNT. (c) *x* components and y components of E-field distributions, which indicate gap dipole modes of the AuNS aggregate at 630 nm and 700 nm, and dipole modes of the AuNS aggregate at 870 nm and 955 nm. (d) E-field distribution of the dipole mode of the AuNT at 700 nm (e) Absolute E-field distribution of the AuNS aggregate at 700 nm (f) Absolute E-field distribution of the AuNT at 700 nm. The double-headed arrows show the polarization of the incident light.

The dark-field scattering spectrum of the AuNS aggregate in Figure 5.7a (see the SEM image in the inset of Figure 5.7a) displays three scattering peaks. In order to identify the plasmonic mode of each peak, we conducted FDTD calculations to simulate the scattering spectrum of an AuNS aggregate covered by PMMA, as shown in Figure 5.7. The

E-field distribution of the simulated scattering peak at 700 nm (Figure 5.7c) indicates that the experimentally measured scattering peak at 695 nm is derived from the gap plasmon mode between two nearby AuNSs along the *y* axis. It can also be seen that the scattering peaks at 630 nm, 854 nm and 915 nm arise from the plasmon gap mode along the *x* axis, the near-field coupling between two AuNSs along the *x* axis, and the near-field coupling among three AuNSs along the *y* axis, respectively. Figure 5.7b shows the simulated scattering spectrum of the AuNT when the polarization of the incident light is along one side of the AuNT. The scattering peak wavelength matches well our experimental spectrum (green triangles curve in Figure 5.6b and scattering spectra in Figure 5.8), which arises from the plasmon dipole mode. Figures 5.7e and f illustrate the absolute E-field distributions of the AuNS aggregate and the AuNT, respectively. From the absolute E-field distributions, we know the E-field enhancement near the AuNS aggregate is 50-60 times larger than that near the single AuNT.

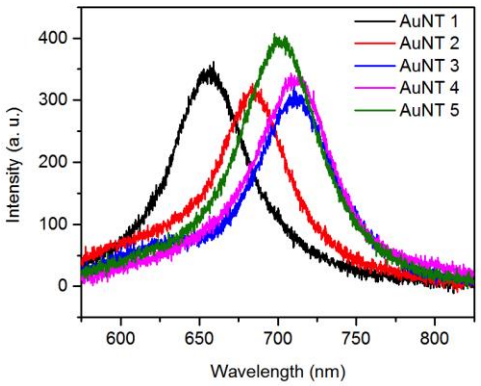

Figure 5.8: Optical scattering spectra of 5 single AuNTs coverd by PMMA.

The broad absorption spectrum (blue square) in Figure 5.6b is likely attributed to different stereoisomers of trans-MC (Figure 5.9), which were created by UV irradiation. As presented in Table 5.1, there is a small energy difference (< 0.1 eV) between the

stereoisomers, and their absorption peak wavelengths (λ_{max}), varying by 20-25 nm depending on the exchange-correlation function employed in density functional theory (DFT) calculations. We also considered the possibility that MC molecules may exist in both non-polar quinoidal and dipolar zwitterionic states, depending on the polarization of the local environment. However, the influence of polarization on λ_{max} (e.g., $\Delta\lambda_{max}\approx$10 nm, when the dielectric constant changes from 4 to 78.4, as shown in Table 5.2, is found to be not as significant as that of isomerization; this implies that the absorption spectra due to the quinoidal and zwitterionic MC forms, even if they coexist in our samples, would be hard to distinguish.

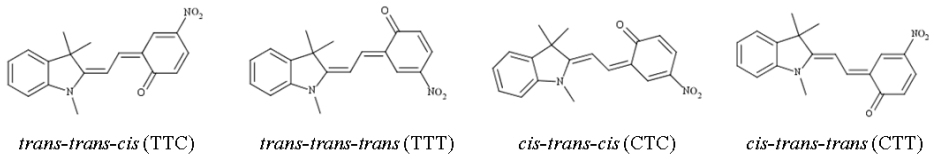

Figure 5.9: Skeletal formula of four trans-MC isomers.

	ΔE (eV)	$\Delta E_{HOMO\text{-}LUMO}$ (eV)	λ_{max} (nm)
TTC	0.00 (0.00)	2.76 (1.63)	505 (573)
TTT	0.05 (0.05)	2.66 (1.59)	530 (595)
CTC	0.08 (0.08)	2.76 (1.63)	506 (574)
CTT	0.11 (0.11)	2.67 (1.54)	529 (595)

Table 5.1: Predicted relative stabilities (ΔE), HOMO-LUMO gaps ($\Delta E_{HOMO\text{-}LUMO}$), and maximum absorption wavelengths (λ_{max}) of four trans-MC isomers shown above from implicit solvent DFT calculations using the B3LYP hybrid functional.

ε	$\Delta E_{\text{HOMO-LUMO}}$ (eV)	λ_{max} (nm)
2	2.72 (1.60)	510 (578)
4	2.76 (1.63)	505 (573)
6.32	2.77 (1.64)	502 (570)
78.4	2.82 (1.68)	495 (563)

Table 5.2: Predicted HOMO-LUMO gap ($\Delta E_{\text{HOMO-LUMO}}$) and maximum absorption wavelength (λ_{max}) of the most stable trans-MC isomer (TTC) for variation of the dielectric constant (ε) of solvent from implicit solvent DFT calculations using the B3LYP (PBE) functional.

5.2.4 Photoswitchable plasmon-enhanced fluorescence

Figure 5.10a illustrates the large photoswitchable fluorescence from SP molecules near an AuNS aggregate. After UV irradiation, the emission peak at 675 nm matches the fluorescence peak of zwitterionic MC (purple curve in Figure 5.6b) and has a higher intensity than that of the zwitterionic MC and the scattering peak of the AuNS aggregate at 695 nm (Figure 5.6a). The integrated intensity of the enhanced fluorescence from the hybrid is approximately 32 times that of pure MC molecules. To avoid interference with scattering peaks at longer wavelengths (Figure 5.6a), the integration is limited to a wavelength range from 600 to 725 nm. In contrast, the integrated intensity of the fluorescence (with removal of pure scattering by the AuNS aggregate) from the hybrid after green light radiation, is only 1.3 times that of pure MC molecules (Figure 5.10b, curve of green squares). Therefore, no obvious fluorescence enhancement or quenching is observed for the quinoidal MC form. The fluorescence enhancements obtained from the molecules near 5 different AuNS aggregates that exhibit LSPR bands overlapping the fluorescence band of MC molecules are listed in Table 5.3. Not all AuNS aggregates lead to an equally large fluorescence enhancement. The enhancement differences cannot be attributed to the relative orientation of molecules with respect to AuNS aggregates because

there are a large number of randomly oriented molecules near the AuNS aggregates; however, it may arise from the difference in the total number of molecules at plasmonic hot spots, since the number and size of hot spots vary for different AuNS aggregates.

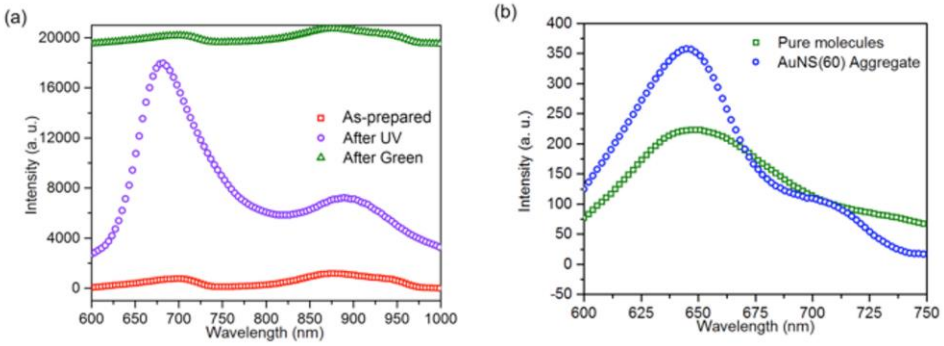

Figure 5.10: (a) Large photoswitchable fluorescence enhancement from a hybrid containing MC molecules and an AuNS aggregate. The intensity-axis offset is added for clarity. (b) Fluorescence spectra measured near and far away from the AuNS aggregate covered by the SP-doped PMMA film after green light irradiation. The fluorescence spectrum of molecules near the AuNS aggregate is obtained by removing the scattering by the AuNS aggregate.

Single AuNS aggregate	Enhancement rate	Single AuNT	Enhancement rate
Aggregate 1	31.7	AuNT 1	1.3
Aggregate 2	15.4	AuNT 2	1.6
Aggregate 3	3.9	AuNT 3	1.1
Aggregate 4	7.5	AuNT 4	0.8
Aggregate 5	3.3	AuNT 5	1.3

Table 5.3: Comparison between the fluorescence enhancements near single AuNS aggregates and single AuNTs.

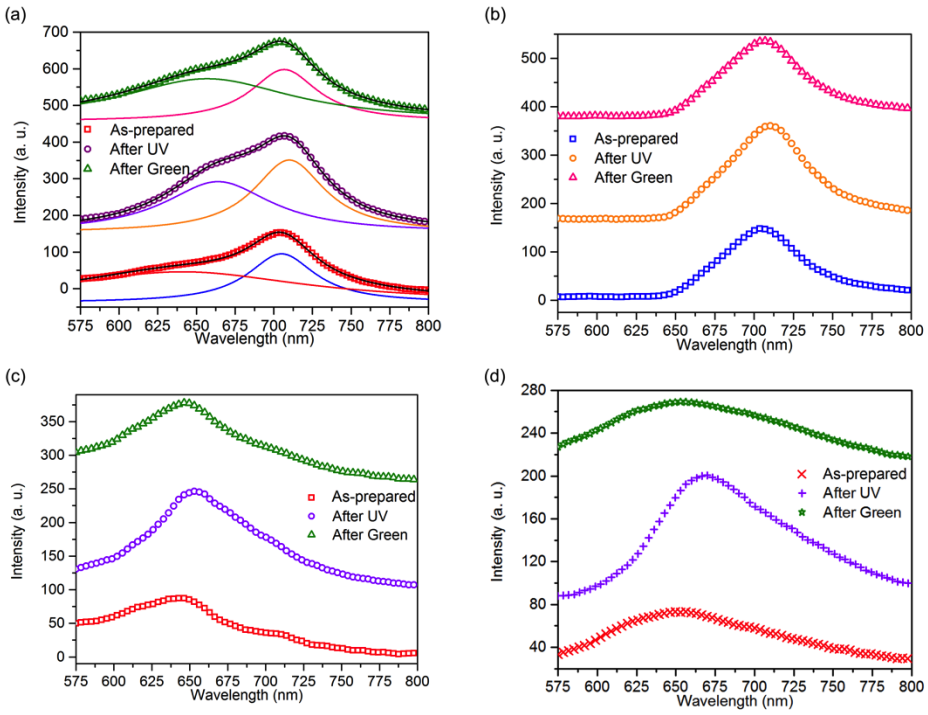

Figure 5.11: (a) Dark-field optical spectra of a single AuNT covered by an SP-doped PMMA film under different light irradiation. The solid lines were obtained by fitting the dark-field spectra into two Lorentzian peaks. The peak wavelengths of the fitted blue, orange and pink solid lines match those in the scattering spectra in (b). The peak wavelengths of red, purple and green solid lines are close to the fluorescence peak wavelengths of the pure molecules as shown in (d). (b) Scattering spectra of the same single AuNT as in (a), under different light irradiation. The scattering spectra were obtained by blocking the fluorescence of molecules with a 665 long pass filter, because the absorption peak of zwitterionic MC molecules is at 560 nm (Figure 5.6b). The slight redshift of the scattering peak after UV irradiation can be explained by a change in the refractive index around the AuNT since zwitterionic MC molecules have a larger refractive index than SP molecules. (c) Fluorescence spectra of molecules near the same AuNT as in (a) under different light irradiation. These spectra were acquired by subtracting the scattering spectra in (b) from the dark-field spectra in (a). (d) Fluorescence spectra of molecules away from AuNTs under different light irradiation in the same sample. The intensity-axis offset is added for clarity.

For the sample consisting of AuNTs covered by a molecule-doped PMMA film, two peaks appear in the dark-field optical spectra of a single AuNT (Figure 5.11a). By

removing the scattering signal from the pure AuNT (Figure 5.11b), we obtain the fluorescence signals from the molecules near the AuNT (Figure 5.11c). No obvious fluorescence enhancement is observed for the molecules near the AuNT when compared to the molecules without the AuNT in Figure 5.11d. The fluorescence enhancement factors for the molecules near 5 different AuNTs are listed in Table 5.3. All the enhancement factors are close to 1.

To clarify why the large fluorescence enhancement of zwitterionic MC molecules occurs near AuNS aggregates rather than near AuNTs, we explore the difference in the radiative decay rate enhancements between these two systems and assume $\frac{\gamma_r}{\gamma_{r0}} = k_r$. Since $k_r \propto \left|\mathrm{E}_p(\mathbf{r}_0)\right|^2$, we can further assume $k_r = \alpha_{\mathrm{n}} \mathrm{A} \mathrm{E}_{\mathrm{n}}^2$ (for the nth molecule near the plasmonic nanostructure), where α_{n} is a constant determined by the relative orientation of the nth molecule to the plasmonic nanostructure, E_{n} is the intensity of the enhanced E-field at the nth molecule, and A is a constant determined by the type of molecule. The fluorescence enhancement factor is obtained from the integrated fluorescence intensity of molecules at the AuNS aggregate (or AuNT) divided by that of the pure molecules, which is an average signal from the whole measured region. Accordingly, we compare the average emission rate enhancement: $\bar{k}_r = \frac{\sum \alpha_{\mathrm{n}} \mathrm{A} \mathrm{E}_{\mathrm{n}}^2}{\mathrm{m}}$, where n is the number of molecules in all hot spots and m is the total number of molecules in the measured region. For the randomly distributed molecules (i.e., the effect of $\alpha_{\mathrm{n}} \mathrm{A}$ is negligible), the square of E-field intensity ($\mathrm{E}_{\mathrm{n}}^2$) increases by several orders of magnitude when n is much smaller than m, leading to an obvious fluorescence enhancement. Because the molecules located at the hot spots of AuNS aggregates and those of AuNTs only account for a small fraction of the total number of the molecules in the measured areas, our observation of fluorescence enhancement of

zwitterionic MC molecules near AuNS aggregates rather than near AuNTs suggests that the E-field enhancement by the AuNS aggregates is larger than that by the AuNTs.

In fact, surface-enhanced Raman scattering (SERS) studies have demonstrated that the E-field enhancement by gap plasmonic modes at plasmonic NP aggregates can be significantly larger than that of single AuNTs.[37, 39-42] Our FDTD simulations also show that the E-field of gap modes in the AuNS aggregate can be 50-60 times larger than that at single AuNTs (Figures 5.7e, f). This larger E-field enhancement at the interparticle gaps of the AuNS aggregate leads to a larger (250-360 times) emission rate enhancement of zwitterionic MC. Thus, we conclude that the large fluorescence enhancement arises from the large E-field at the AuNS aggregates. However, the large E-field cannot explain the observed photoswitchable fluorescence near the AuNS aggregates. To elucidate the physical principle of the photoswitchable fluorescence, we further explore the difference in fluorescence QY between zwitterionic MC and the quinoidal MC molecules near plasmonic nanostructures.

We assume that the MC molecule is a classic dipole and the non-radiative rate is determined by Ohmic loss in the environment:[10]

$$\gamma_{nr} \propto \frac{\gamma_{r0}}{P_0}\left|\mathrm{E_m}\right|^2 \tag{5.6}$$

where γ_0 is the free-space decay rate, P_0 is the power emitted by the MC molecule, and $\mathrm{E_m}$ is the E-field emitted by the molecule. For our molecule-plasmon hybrid nanostructures, $\mathrm{E_m}$ equates $\mathrm{E_{0m}} + E_p(\mathbf{r}_0)$, where $\mathrm{E_{0m}}$ is the E-field emitted by the molecule without plasmonic nanostructures. When $E_p(\mathbf{r}_0)$ is much larger than $\mathrm{E_{0m}}$, because $\gamma_{r0} = \frac{\gamma_{r0}}{\phi_0}$, we obtain:

$$\gamma_{nr} \propto \frac{\gamma_{r0}}{\phi_0 P_0}\left|\mathrm{E}_p(\mathbf{r}_0)\right|^2 \tag{5.7}$$

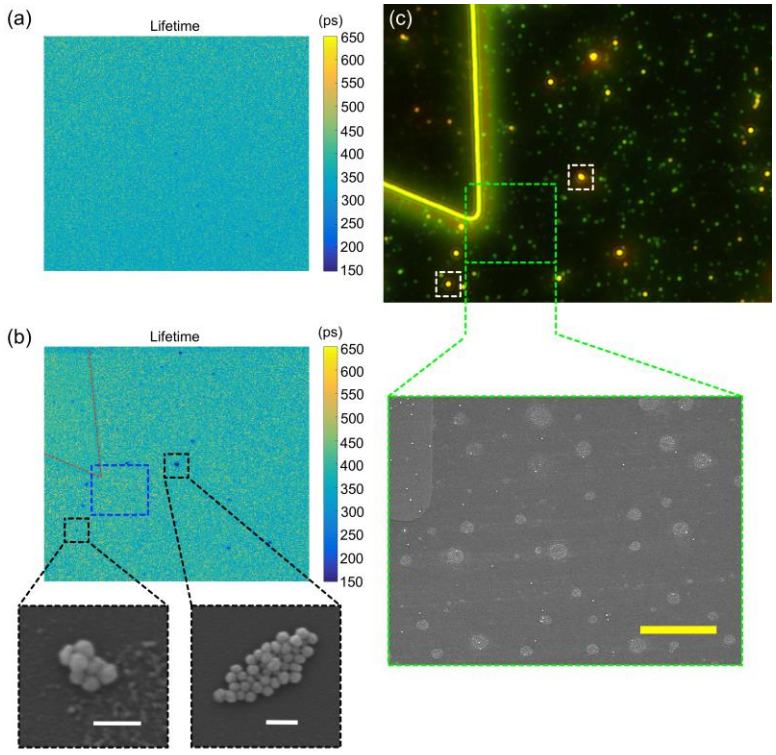

Figure 5.12: (a) FLIM image of MC-doped PMMA without AuNSs after UV irradiation (b) FLIM image of MC-doped PMMA with 60 nm AuNSs after UV irradiation. SEM images of AuNS aggregates obtained from the spots of the shorter lifetime in the black dashed rectangles. Red dashed lines outline the position of the marker. (c) Dark-field optical image of the same area of the sample as shown in (b). SEM image is obtained from the area indicated by the green dashed rectangle, which corresponds to the blue dashed rectangle in the FLIM image of (b). The white dashed rectangles correspond to the black dashed rectangles in the FLIM image of b). The large circular regions with light color in the SEM image are residual PMMA on the glass substrate. White scale bars in SEM image of (b) are 200 nm and yellow scale bar in SEM image of (c) is 5 μm.

According to Equations 5.6 and 5.7, we assume that the radiative rate and non-radiative rate of molecules near the AuNT be $\gamma_r = \alpha_{\mathrm{n}} \mathrm{AE}_{\mathrm{n}}^2 \gamma_{r0}$ and $\gamma_{nr} = \beta_{\mathrm{n}} \mathrm{BE}_{\mathrm{n}}^2 \frac{\gamma_{r0}}{\phi_0 P_0}$, respectively. β_{n} is a constant determined by the relative orientation of the nth molecule to the plasmonic nanostructure and B is a constant determined by the type of the molecule.

E_n depends on the type of plasmonic nanostructures and the degree of the spectral overlap between the LSPRs and the molecular fluorescence. We further denote $E_{1,n}$ as E_n for zwitterionic MC molecules near the AuNT, $E_{2,n}$ as E_n for zwitterionic MC molecules near the AuNS aggregate, $E_{3,n}$ as E_n for quinoidal MC molecules near the AuNT, and $E_{4,n}$ as E_n for quinoidal MC molecules near the AuNS aggregate.

Based on Equations 5.1 and 5.2, we define the average QY of zwitterionic MC molecules near the AuNT ($\bar{\phi}_{NT}$) and near the AuNS aggregate ($\bar{\phi}_{Agg}$) and the average QY of quinoidal MC molecules near the AuNT ($\bar{\phi}'_{NT}$) and near the AuNS aggregate ($\bar{\phi}'_{Agg}$) as:

$$\bar{\phi}_{NT} = \frac{\bar{\alpha}_{NT} A \bar{E}_1^2 \gamma_{r0}}{\bar{\alpha}_{NT} A \bar{E}_1^2 \gamma_{r0} + \bar{\beta}_{NT} B \bar{E}_1^2 \frac{\gamma_{r0}}{\phi_0 P_0} + \gamma_{ISC}} = \frac{\bar{\alpha}_{NT} A}{\bar{\alpha}_{NT} A + \frac{\bar{\beta}_{NT} B}{\phi_0 P_0} + \frac{\gamma_{ISC}}{\bar{E}_1^2 \gamma_{r0}}} \tag{5.8}$$

$$\bar{\phi}_{Agg} = \frac{\bar{\alpha}_{Agg} A \bar{E}_1^2 \gamma_{r0}}{\bar{\alpha}_{Agg} A \bar{E}_1^2 \gamma_{r0} + \bar{\beta}_{Agg} B \bar{E}_1^2 \frac{\gamma_{r0}}{\phi_0 P_0} + \gamma_{ISC}} = \frac{\bar{\alpha}_{Agg} A}{\bar{\alpha}_{Agg} A + \frac{\bar{\beta}_{Agg} B}{\phi_0 P_0} + \frac{\gamma_{ISC}}{\bar{E}_1^2 \gamma_{r0}}} \tag{5.9}$$

$$\bar{\phi}'_{NT} = \frac{\bar{\alpha}_{NT} A' \bar{E}_3^2 \gamma'_{r0}}{\bar{\alpha}_{NT} A' \bar{E}_3^2 \gamma'_{r0} + \bar{\beta}_{NT} B' \bar{E}_3^2 \frac{\gamma'_{r0}}{\phi'_0 P'_0}} = \frac{\bar{\alpha}_{NT} A'}{\bar{\alpha}_{NT} A + \frac{\bar{\beta}_{NT} B'}{\phi'_0 P'_0}} \tag{5.10}$$

and

$$\bar{\phi}'_{Agg} = \frac{\bar{\alpha}_{Agg} A' \bar{E}_4^2 \gamma'_{r0}}{\bar{\alpha}_{Agg} A' \bar{E}_4^2 \gamma'_{r0} + \bar{\beta}_{Agg} B' \bar{E}_4^2 \frac{\gamma'_{r0}}{\phi'_0 P'_0}} = \frac{\bar{\alpha}_{Agg} A'}{\bar{\alpha}_{Agg} A + \frac{\bar{\beta}_{Agg} B'}{\phi'_0 P'_0}} \tag{5.11}$$

where $\bar{\alpha}_{NT}$ and $\bar{\beta}_{NT}$ are the average α and β of molecules near the AuNT; $\bar{\alpha}_{Agg}$ and $\bar{\beta}_{Agg}$ are the average α and β of molecules near the AuNS aggregate; and $\bar{E}_x^2 = \frac{\sum E_{x,n}^2}{n}$ where x=1, 2, 3 or 4. Since no obvious enhancement or quenching was observed for quinoidal MC molecules near the AuNT and AuNS aggregate, we assume $\bar{\phi}'_{ANT} \approx \bar{\phi}'_{Agg} \approx \phi'_0$, which leads to $\bar{\alpha}_{NT} \approx \bar{\alpha}_{Agg}$ and $\bar{\beta}_{NT} \approx \bar{\beta}_{Agg}$. From Equations 5.8 and 5.9, we know that, if $\frac{\gamma_{ISC}}{\gamma_{r0}}$ is large, fluorescence QY can be significantly increased when the E-field is strongly

increased. This QY increase indicates that, even if the plasmon-induced non-radiative rate enhancement is equivalent to the plasmon-induced radiative rate enhancement, a large fluorescence enhancement can be still obtained due to the large ISC rate. Moreover, the fluorescence can be tuned by controlling the ISC rate.

We further investigated the fluorescence lifetime of zwitterionic MC molecules at single AuNS aggregates. We employed fluorescence lifetime imaging microscopy (FLIM) to achieve single-nanostructure resolution (see detailed information in Experimental section).[25, 43] As a control experiment, the FLIM image of MC-doped PMMA film without AuNSs is shown in Figure 5.12a. The image was taken after UV irradiation of the film, which reveals that the zwitterionic MC molecules in the PMMA film have a fluorescence lifetime of ~ 400 ps. The FLIM image of MC-doped PMMA film that covers 60 nm AuNSs is shown in Figure 5.12b. Most parts of the MC-doped PMMA film have a fluorescence lifetime of ~400 ps, while some regions have a reduced fluorescence lifetime down to ~150 ps. The regions with shorter lifetimes contain the AuNS aggregates, which are confirmed by SEM (Figure 5.12b). Two examples of the AuNS aggregates are marked by black dashed rectangles in Figure 5.12b. Figure 5.12c shows the dark-field optical microscopy image of the same sample covered with a pure PMMA film. By comparing the dark-field optical image with the FLIM image, we conclude that the fluorescence signals of reduced lifetime are obtained from the larger orange spots with the stronger optical scattering in the dark-field optical image. In addition, green spots with weaker scattering in the dark-field optical image are individual 60 nm AuNSs, which have an LSPR peak wavelength around 545 nm (Figure 5.13). We verified the individual AuNSs by an SEM image shown in the green dashed rectangle. No obvious reduction of lifetime occurs at the green spots, meaning that the reduced fluorescence lifetime of zwitterionic MC molecules at the aggregates arises from the strong E-field enhancement at interparticle gaps. Since fluorescence

lifetime is $\tau = \frac{1}{\gamma_r}$, the lifetime measurements indicate that the average k_r is less than 3. Since both γ_r and γ_{nr} increase with E-field enhancement, Equations 5.1 and 5.9 indicate that, without changes in γ_{ISC}, the fluorescence QY enhancement is smaller than k_r. Therefore, the QY enhancement (as listed in Table 5.3) larger than k_r proves that the ISC in zwitterionic MC molecules can further enhance the fluorescence when the E-field enhancement is large.

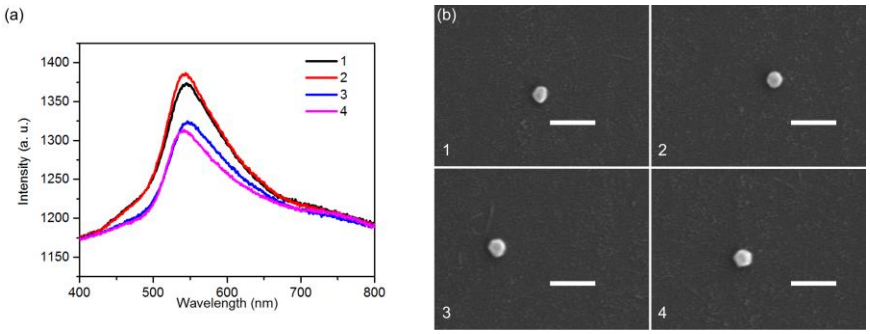

Figure 5.13: (a) Scattering spectra of 4 single 60 nm AuNSs. (b) SEM image of single 60 nm AuNSs of (a). Scale bar is 200 nm.

5.3 SUMMARY

In summary, we elucidate how ISC influences the plasmon-enhanced fluorescence based on hybrid systems of plasmonic nanostructures and SP-derived MC molecules. Due to the high ISC rate, a large fluorescence enhancement can be obtained even if the plasmon-induced non-radiative rate enhancement is equivalent to the plasmon-induced radiative rate enhancement. The ISC-mediated fluorescence enhancement by the plasmonic nanostructures represents a new phenomenon in molecular plasmonics, which provides a new insight into how to select and design molecule-plasmon hybrid nanostructures to obtain a large plasmon-induced fluorescence enhancement. In addition, spiropyran and

merocyanine molecules are sensitive to external stimuli and environmental changes, such as light with different wavelengths, temperature changes and pH changes. Therefore, we propose that ISC-mediated fluorescence enhancement can be used for applications such as optical modulators, optical switches, biosensing and bioimaging.[13, 26, 44-46]

5.4 REFERENCES

1. Holzmeister, P.; Pibiri, E.; Schmied, J. J.; Sen, T.; Acuna, G. P.; Tinnefeld, P., Quantum yield and excitation rate of single molecules close to metallic nanostructures. *Nat. Commun.* **2014**, 5, 5356.
2. Fu, Y.; Zhang, J.; Lakowicz, J. R., Plasmon-Enhanced Fluorescence from Single Fluorophores End-Linked to Gold Nanorods. *J. Am. Chem. Soc.* **2010**, 132 (16), 5540-5541.
3. Ming, T.; Zhao, L.; Yang, Z.; Chen, H.; Sun, L.; Wang, J.; Yan, C., Strong Polarization Dependence of Plasmon-Enhanced Fluorescence on Single Gold Nanorods. *Nano Lett.* **2009**, 9 (11), 3896-3903.
4. Tovmachenko, O. G.; Graf, C.; van den Heuvel, D. J.; van Blaaderen, A.; Gerritsen, H. C., Fluorescence Enhancement by Metal-Core/Silica-Shell Nanoparticles. *Adv. Mater.* **2006**, 18 (1), 91-95.
5. Tam, F.; Goodrich, G. P.; Johnson, B. R.; Halas, N. J., Plasmonic Enhancement of Molecular Fluorescence. *Nano Lett.* **2007**, 7 (2), 496-501.
6. Kinkhabwala, A.; Yu, Z.; Fan, S.; Avlasevich, Y.; Mullen, K.; Moerner, W. E., Large single-molecule fluorescence enhancements produced by a bowtie nanoantenna. *Nat. Photonics* **2009**, 3 (11), 654-657.
7. Akselrod, G. M.; Argyropoulos, C.; Hoang, T. B.; Ciracì, C.; Fang, C.; Huang, J.; Smith, D. R.; Mikkelsen, M. H., Probing the mechanisms of large Purcell enhancement in plasmonic nanoantennas. *Nat. Photonics* **2014**, 8 (11), 835-840.
8. Rose, A.; Hoang, T. B.; McGuire, F.; Mock, J. J.; Ciracì, C.; Smith, D. R.; Mikkelsen, M. H., Control of Radiative Processes Using Tunable Plasmonic Nanopatch Antennas. *Nano Lett.* **2014**, 14 (8), 4797-4802.
9. Pelton, M., Modified spontaneous emission in nanophotonic structures. *Nat. Photonics* **2015**, 9 (7), 427-435.
10. Anger, P.; Bharadwaj, P.; Novotny, L., Enhancement and Quenching of Single-Molecule Fluorescence. *Phys. Rev. Lett.* **2006**, 96 (11), 113002.

11. Gorner, H., Photochromism of nitrospiropyrans: effects of structure, solvent and temperature. *Phys. Chem. Chem. Phys.* **2001**, 3 (3), 416-423.

12. Chibisov, A. K.; Görner, H., Singlet versus triplet photoprocesses in indodicarbocyanine dyes and spiropyran-derived merocyanines. *J. Photochem. Photobiol., A* **1997**, 105 (2), 261-267.

13. Klajn, R., Spiropyran-based dynamic materials. *Chem. Soc. Rev.* **2014**, 43 (1), 148-184.

14. Ming, T.; Zhao, L.; Xiao, M.; Wang, J., Resonance-Coupling-Based Plasmonic Switches. *Small* **2010**, 6 (22), 2514-2519.

15. Kita, F.; Adam, W.; Jordan, P.; Nau, W. M.; Wirz, J., 1,3-Cyclopentanediyl Diradicals: Substituent and Temperature Dependence of Triplet−Singlet Intersystem Crossing. *J. Am. Chem. Soc.* **1999**, 121 (40), 9265-9275.

16. Cogan, S.; Haas, Y.; Zilberg, S., Intersystem crossing at singlet conical intersections. *J. Photochem. Photobiol., A* **2007**, 190 (2–3), 200-206.

17. Salem, L.; Rowland, C., The Electronic Properties of Diradicals. *Angew. Chem. Int. Ed.* **1972**, 11 (2), 92-111.

18. Scarabelli, L.; Coronado-Puchau, M.; Giner-Casares, J. J.; Langer, J.; Liz-Marzán, L. M., Monodisperse Gold Nanotriangles: Size Control, Large-Scale Self-Assembly, and Performance in Surface-Enhanced Raman Scattering. *ACS Nano* **2014**, 8 (6), 5833-5842.

19. Johnson, P. B.; Christy, R. W., Optical Constants of the Noble Metals. *Phys. Rev. B* **1972**, 6 (12), 4370-4379.

20. M. J. Frisch, G. W. T., H. B. Schlegel, G. E. Scuseria, M. A. Robb, J. R. Cheeseman, G. Scalmani, V. Barone, B. Mennucci, G. A. Petersson, H. Nakatsuji, M. Caricato, X. Li, H. P. Hratchian, A. F. Izmaylov, J. Bloino, G. Zheng, J. L. Sonnenberg, M. Hada, M. Ehara, K. Toyota, R. Fukuda, J. Hasegawa, M. Ishida, T. Nakajima, Y. Honda, O. Kitao, H. Nakai, T. Vreven, J.A.Montgomery,J. E. Peralta,F.Ogliaro, M. Bearpark,J.J.Heyd, E. Brothers,K.N.Kudin, V.N. Staroverov, T. Keith, R. Kobayashi, J. Normald, K. Raghavachari, A. Rendell, J. C. Burant,S.S.Iyengar, J. Tomasi, M. Cossi,N.Rega, J. M. Millam, M. Klene, J. E. Knox, J. B. Cross, V. Bakken, C. Adamo, J. Jaramillo,R.Gomperts,R. E.Stratmann,O. Yazyev,A.J.Austin, R. Cammi, C. Pomelli, J. W. Ochterski, R. L. Martin, K. Morokuma,V. G. Zakrzewski, G. A. Voth,P.Salvador, J. J. Dannenberg,S.Dapprich, A. D. Daniels, O. Farkas,J.B. Foresman,J.V.Ortiz, J.Cioslowskiand, D. J. Fox, Gaussian 09 Revis. C.01, Gaussian, Inc., Wallingord CT, 2010.

21. Perdew, J. P.; Burke, K.; Ernzerhof, M., Generalized Gradient Approximation Made Simple. *Phys. Rev. Lett.* **1996**, 77 (18), 3865-3868.

22. Becke, A. D., Density-functional thermochemistry. III. The role of exact exchange. *J. Chem. Phys.* **1993**, 98 (7), 5648-5652.

23. Mennucci, B.; Cancès, E.; Tomasi, J., Evaluation of Solvent Effects in Isotropic and Anisotropic Dielectrics and in Ionic Solutions with a Unified Integral Equation Method: Theoretical Bases, Computational Implementation, and Numerical Applications. *J. Phys. Chem. B* **1997**, 101 (49), 10506-10517.

24. Sean C. Warren, A. M., Dominic Alibhai, Douglas J. Kelly, Clifford Talbot, Yuriy Alexandrov, Ian Munro, Matilda Katan, Chris Dunsby, Paul M. W. French *PLoS ONE* **2013**, 8, e70687.

25. Wang, M.; Bangalore Rajeeva, B.; Scarabelli, L.; Perillo, E. P.; Dunn, A. K.; Liz-Marzán, L. M.; Zheng, Y., Molecular-Fluorescence Enhancement via Blue-Shifted Plasmon-Induced Resonance Energy Transfer. *J. Phys. Chem. C* **2016**, 120 (27), 14820-14827.

26. Zhu, M.-Q.; Zhu, L.; Han, J. J.; Wu, W.; Hurst, J. K.; Li, A. D. Q., Spiropyran-Based Photochromic Polymer Nanoparticles with Optically Switchable Luminescence. *J. Am. Chem. Soc.* **2006**, 128 (13), 4303-4309.

27. Xue, Y.; Tian, J.; Tian, W.; Gong, P.; Dai, J.; Wang, X., Significant Fluorescence Enhancement of Spiropyran in Colloidal Dispersion and Its Light-Induced Size Tunability for Release Control. *J. Phys. Chem. C* **2015**, 119 (35), 20762-20772.

28. Tian, W.; Tian, J., Synergy of Different Fluorescent Enhancement Effects on Spiropyran Appended onto Cellulose. *Langmuir* **2014**, 30 (11), 3223-3227.

29. Song, X.; Zhou, J.; Li, Y.; Tang, Y., Correlations between solvatochromism, Lewis acid-base equilibrium and photochromism of an indoline spiropyran. *J. Photochem. Photobiol., A* **1995**, 92 (1), 99-103.

30. Wu, Y.; Sasaki, T.; Kazushi, K.; Seo, T.; Sakurai, K., Interactions between Spiropyrans and Room-Temperature Ionic Liquids: Photochromism and Solvatochromism. *J. Phys. Chem. B* **2008**, 112 (25), 7530-7536.

31. Rosario, R.; Gust, D.; Hayes, M.; Springer, J.; Garcia, A. A., Solvatochromic Study of the Microenvironment of Surface-Bound Spiropyrans. *Langmuir* **2003**, 19 (21), 8801-8806.

32. Wojtyk, J. T. C.; Wasey, A.; Kazmaier, P. M.; Hoz, S.; Buncel, E., Thermal Reversion Mechanism of N-Functionalized Merocyanines to Spiropyrans: A Solvatochromic, Solvatokinetic, and Semiempirical Study. *J. Phys. Chem. A* **2000**, 104 (39), 9046-9055.

33. Bharadwaj, P.; Novotny, L., Spectral dependence of single molecule fluorescence enhancement. *Opt. Express* **2007**, 15 (21), 14266-14274.

34. Xiong, Y.; McLellan, J. M.; Chen, J.; Yin, Y.; Li, Z.-Y.; Xia, Y., Kinetically Controlled Synthesis of Triangular and Hexagonal Nanoplates of Palladium and Their SPR/SERS Properties. *J. Am. Chem. Soc.* **2005**, 127 (48), 17118-17127.

35. Rycenga, M.; Camargo, P. H. C.; Li, W.; Moran, C. H.; Xia, Y., Understanding the SERS Effects of Single Silver Nanoparticles and Their Dimers, One at a Time. *J. Phys. Chem. Lett.* **2010**, 1 (4), 696-703.

36. Sun, Y.; Xia, Y., Shape-Controlled Synthesis of Gold and Silver Nanoparticles. *Science* **2002**, 298 (5601), 2176-2179.

37. Wustholz, K. L.; Henry, A.-I.; McMahon, J. M.; Freeman, R. G.; Valley, N.; Piotti, M. E.; Natan, M. J.; Schatz, G. C.; Duyne, R. P. V., Structure−Activity Relationships in Gold Nanoparticle Dimers and Trimers for Surface-Enhanced Raman Spectroscopy. *J. Am. Chem. Soc.* **2010**, 132 (31), 10903-10910.

38. Kühn, S.; Håkanson, U.; Rogobete, L.; Sandoghdar, V., Enhancement of Single-Molecule Fluorescence Using a Gold Nanoparticle as an Optical Nanoantenna. *Phys. Rev. Lett.* **2006**, 97 (1), 017402.

39. Kleinman, S. L.; Sharma, B.; Blaber, M. G.; Henry, A.-I.; Valley, N.; Freeman, R. G.; Natan, M. J.; Schatz, G. C.; Van Duyne, R. P., Structure Enhancement Factor Relationships in Single Gold Nanoantennas by Surface-Enhanced Raman Excitation Spectroscopy. *J. Am. Chem. Soc.* **2013**, 135 (1), 301-308.

40. Kleinman, S. L.; Frontiera, R. R.; Henry, A.-I.; Dieringer, J. A.; Van Duyne, R. P., Creating, characterizing, and controlling chemistry with SERS hot spots. *Phys. Chem. Chem. Phys.* **2013**, 15 (1), 21-36.

41. Camden, J. P.; Dieringer, J. A.; Wang, Y.; Masiello, D. J.; Marks, L. D.; Schatz, G. C.; Van Duyne, R. P., Probing the Structure of Single-Molecule Surface-Enhanced Raman Scattering Hot Spots. *J. Am. Chem. Soc.* **2008**, 130 (38), 12616-12617.

42. Pazos-Perez, N.; Wagner, C. S.; Romo-Herrera, J. M.; Liz-Marzán, L. M.; García de Abajo, F. J.; Wittemann, A.; Fery, A.; Alvarez-Puebla, R. A., Organized Plasmonic Clusters with High Coordination Number and Extraordinary Enhancement in Surface-Enhanced Raman Scattering (SERS). *Angew. Chem. Int. Ed.* **2012**, 51 (51), 12688-12693.

43. Perillo, E. P.; Liu, Y.-L.; Huynh, K.; Liu, C.; Chou, C.-K.; Hung, M.-C.; Yeh, H.-C.; Dunn, A. K., Deep and high-resolution three-dimensional tracking of single particles using nonlinear and multiplexed illumination. *Nat. Commun.* **2015**, 6, 7874.

44. Zhu, M.-Q.; Zhang, G.-F.; Li, C.; Aldred, M. P.; Chang, E.; Drezek, R. A.; Li, A. D. Q., Reversible Two-Photon Photoswitching and Two-Photon Imaging of Immunofunctionalized Nanoparticles Targeted to Cancer Cells. *J. Am. Chem. Soc.* **2011**, 133 (2), 365-372.

45. Zhu, M.-Q.; Zhang, G.-F.; Hu, Z.; Aldred, M. P.; Li, C.; Gong, W.-L.; Chen, T.; Huang, Z.-L.; Liu, S., Reversible Fluorescence Switching of Spiropyran-Conjugated Biodegradable Nanoparticles for Super-Resolution Fluorescence Imaging. *Macromolecules* **2014**, 47 (5), 1543-1552.

46. Berkovic, G.; Krongauz, V.; Weiss, V., Spiropyrans and Spirooxazines for Memories and Switches. *Chem. Rev.* **2000**, 100 (5), 1741-1754.

Chapter 6 Tunable Fano Resonance and Plasmon-Exciton Coupling in Single Au Nanotriangles on Monolayer WS_2 at Room Temperature*

6.1 INTRODUCTION

Plasmon-exciton systems have attracted strong interest as platforms for studying light-matter interactions through mechanisms such as Fano interference,[1-7] strong coupling,[8-13] plasmon-induced resonance energy transfer,[14-16] plasmon-enhanced absorption and emission.[17-19] In particular, Fano resonances and Rabi splitting phenomena in plasmon-exciton systems are promising for the development of new optical devices, including nanolasers, biosensors, and single-photon switches.[4, 20-22] So far, both Fano resonances and Rabi splitting have been observed in plasmonic systems incorporating dye molecules[8-12, 23-24] and quantum dots (QDs).[2-4, 25] Due to the lack of efficient ways to tune the excitonic properties of dye molecules and QDs, active control of Fano interference and plasmon-exciton coupling relies on varying surface plasmons or incident light, which has limited the degree of control of Fano asymmetric lineshape and coupling strength to specific light wavelengths and polarizations.[8-12, 26-33] In addition, it remains unclear how to distinguish Fano interference and Rabi splitting in such plasmon-exciton systems.

Semiconducting transition metal dichalcogenide (TMDC) monolayers exhibit excitonic properties that can be tuned by external signals, such as electrical bias and temperature.[34-36] Different from dye molecules and QDs, two-dimensional (2D) TMDC monolayers possess excitons highly confined in the in-plane direction, thus making it convenient to align the orientation of excitons with the one of surface plasmons for effective dipole-dipole interactions.[16] We propose that these unique features of TMDC

* Wang, M.; Krasnok, A.; Zhang, T.; Scarabelli, L.; Liu, H.; Wu, Z.; Liz-Marzán L. M.; Terrones, M.; Alù, A.; Zheng, Y., Tunable Fano Resonance and Plasmon–Exciton Coupling in Single Au Nanotriangles on Monolayer WS_2 at Room Temperature. *Advanced Materials* 2018, 30 (22), 1705779.
Wang, M. carried out the experimental work and participated in the preparation of manuscript.

monolayers, combined with their other exceptional physical and chemical properties, make hybrid systems of TMDC monolayers and plasmonic NPs ideal platforms for studying tunable Fano resonances and plasmon-exciton coupling.[36-40]

In this chapter, we discuss tunable Fano resonances and plasmon-exciton coupling in atomically thin WS_2-AuNT hybrids (schematically shown in Figure 6.1a) at room temperature. Tuning was then demonstrated by active control of the WS_2 exciton binding energy and dipole-dipole interaction. Single-nanoparticle measurements were employed to avoid inhomogeneous spectral broadening brought by ensemble measurements.

6.2 Results and Discussion

6.2.1 Design and characterization of monolayer WS_2, single AuNTs and hybrid systems

We first synthesized monolayer WS_2 by chemical vapor deposition (CVD) and transferred the as-grown monolayer flakes onto a glass substrate.[41] Figure 6.1b shows an optical image of a representative WS_2 flake on the substrate. The monolayer nature of the WS_2 flake was confirmed by the optical contrast and the strong photoluminescence (PL) signal (Figure 6.1c), which is typical of direct bandgap semiconductors.[42] The PL spectrum at 300K under ambient conditions shows a single intense peak centered at 630 nm (1.97 eV), which matches the reported exciton emission of CVD-grown monolayer WS_2.[43] The monolayer nature of CVD-grown WS_2 was further verified by atomic force microscopy (AFM) (Figures 6.2a and b). We further examined the degree of crystallinity of the monolayer WS_2 by measuring the Raman scattering spectrum with a 488 nm excitation laser (Figure 6.1c). The Raman spectrum is dominated by three peaks at 352 cm^{-1}, 360 cm^{-1} and 421 cm^{-1}, which correspond to the second-order longitudinal acoustic 2LA(M) mode, the first-order out-of-plane E′ mode, and the first-order in-plane A'_1 mode of monolayer

WS_2, respectively.[44-45] Colloidal AuNTs with edge lengths of 60 nm and 150 nm (referred to as 60 nm and 150 nm AuNTs) and thickness of 30 nm were synthesized by a previously reported method.[46] The obtained AuNTs have atomically flat surfaces, major in-plane dipoles, and strong E-field enhancement at the tip positions. Transmission electron microscopy (TEM) was used to image the 60 nm and 150 nm AuNTs as shown in Figures 6.2c and d.

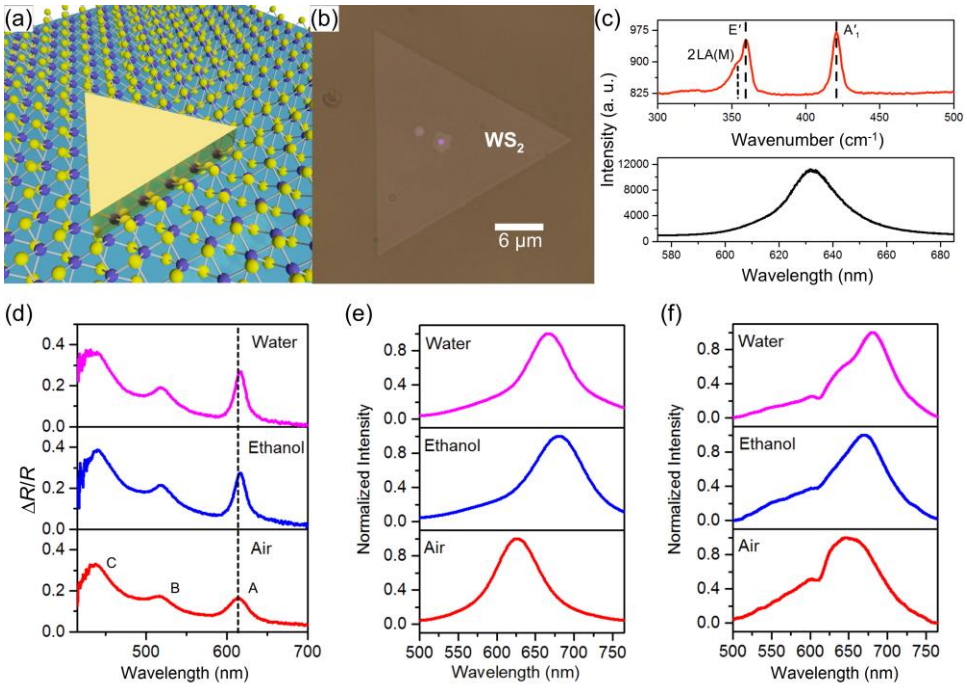

Figure 6.1: (a) Schematic view of a sample comprising a single AuNT on monolayer WS_2. (b) Optical image of triangular WS_2 monolayer. (c) Raman (top) and PL (bottom) spectra of the monolayer WS_2 in air (the excitation wavelength is 488 nm). (d) Vis-NIR differential reflectance spectra of monolayer WS_2 immersed in air, ethanol and water. A, B, and C label peaks of exciton A, B and C, respectively. (e) Scattering spectra of a single 60 nm AuNT in air, ethanol and water. (f) Scattering spectra of a single 60 nm AuNT on monolayer WS_2 in air, ethanol and water.

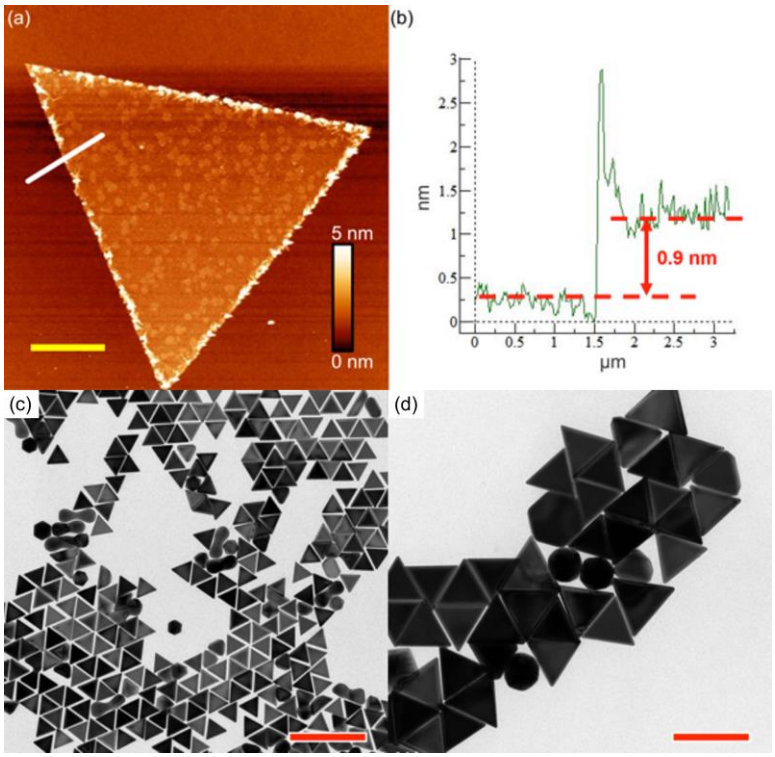

Figure 6.2: (a) AFM image of monolayer WS_2. (b) Height profile of the white line in a. The color bar is 2.8 μm. (c) TEM image of 60 AuNTs. (d) TEM image of 150 AuNTs. Scale bars are 200 nm.

We hypothesize that Fano resonances may arise from the interference between the discrete exciton band of monolayer WS_2 and the broad plasmonic mode of an individual AuNT.[4, 20, 47-48] Due to the low dielectric screening, the exciton binding energy of monolayer WS_2 can be tuned by the dielectric constant of the surrounding environment at room temperature.[49-50] Thus, we hypothesized that it should be possible to dynamically control Fano interference and plasmon-exciton coupling in the hybrids consisting of monolayer WS_2 and AuNTs under ambient conditions, by simply changing the surrounding solvents. It should be mentioned that when dealing with the dielectric screening in monolayer WS_2, the static dielectric constant instead of the permittivity at optical frequencies of the surrounding solvents should be considered.[49-50]

In order to verify our hypothesis, we used an optical microscope integrated with a spectrometer and an EMCCD camera to measure reflectance and dark-field scattering spectra from a series of samples.[13, 16] The differential reflectance spectra of monolayer WS_2 in different solvents are shown in Figure 6.1d. Monolayer WS_2 in air has an obvious peak around 615 nm (known as exciton A (neutral exciton), 2.02 eV). The two peaks at shorter wavelengths correspond to excitons B and C.[51] The peak of exciton A red-shifts as the dielectric constant of the solvent increases (Figure 6.1d), in agreement with previous reports.[49-50] Ethanol and water were chosen because of their large dielectric constants (25.3 and 80.1, respectively) that in turn lead to a large variation of exciton binding energies.[49-50]

We then studied the 60 nm AuNTs on monolayer WS_2 in different environments (i.e., air, ethanol and water). The 60 nm AuNTs exhibit a LSPR peak wavelength of ~620 nm in air (Figure 6.1e). Their E-field enhancement is stronger than the one of 150 nm AnNTs at the exciton A absorption peak wavelength of monolayer WS_2, when AuNTs are on monolayer WS_2/SiO_2 substrates and in air (Figures 6.3). Figure 6.1e shows that the optical scattering peak wavelength of a single 60 nm AuNT (see the SEM image of the 60 nm AuNT in Figure 6.6a) on a glass substrate red-shifts when ethanol or water is added to the sample, because of the increased refractive index.[52] The scattering spectra of a WS_2-AuNT hybrid are shown in Figure 6.1f (see SEM image of the 60 nm AuNT in Figure 6.6b). In air or ethanol, the scattering spectrum shows a dip at the absorption peak wavelength of monolayer WS_2. In contrast, an asymmetric Fano spectral shape, which brings an additional shoulder near the scattering peak, was obtained from the hybrids in water.

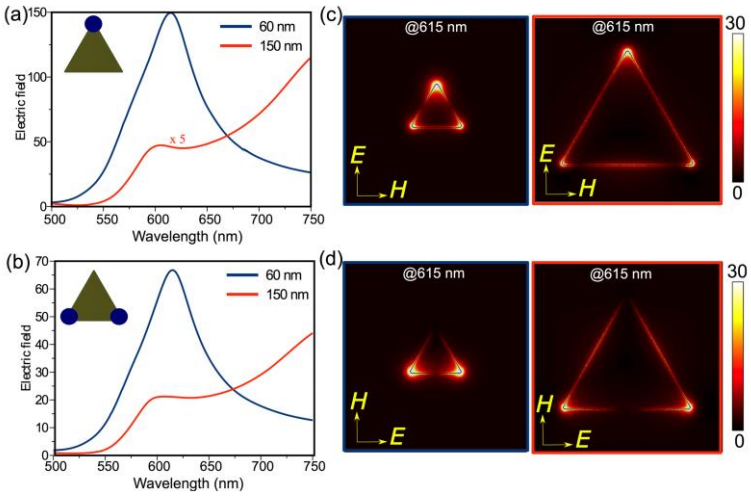

Figure 6.3: (a), (b) Absolute value of electric field strength in the near field of AuNTs on SiO_2 substrate (in air) as a function of light wavelength; blue curves and red curves correspond to 60 nm and 150 nm AuNTs. The radii of AuNT tips are about 2 nm. Insets show the points where the spectra are calculated. (c), (d) Electric-field distribution profiles at the wavelength of 615 nm (i.e., exciton A absorption peak wavelength of monolayer WS_2).

6.2.2 A theoretical fitting of tunable Fano resonances

We employed a theoretical approach to describe the Fano resonance and explain the variations in the observed spectra measured from the WS_2-AuNT hybrids,.[53-54] This approach is an expansion of the original Fano model to non-Hermitian systems with sufficient intrinsic dissipative losses.[53-54] The essential part of this approach is that the scattering cross-section spectra $\sigma_t(\omega)$ of a nanostructure supporting dark and bright modes can be expressed in the following form:

$$\sigma_t(\omega) = \sigma_{ex}(\omega)\sigma_{pl}(\omega) \tag{6.1}$$

where the partial multipliers represent an interference between the radiation continuum and a nonradiative (dark) mode $\sigma_{ex}(\omega)$ and the radiation continuum coupled to a (bright) mode $\sigma_{pl}(\omega)$. These coefficients are given by:

$$\sigma_{ex}(\omega)=\frac{\left(\frac{\omega^2-\omega_{ex}^2}{2W_{ex}\omega_{ex}}+q\right)+b}{\left(\frac{\omega^2-\omega_{ex}^2}{2W_{ex}\omega_{ex}}\right)^2+1},\sigma_{pl}(\omega)=\frac{a^2}{\left(\frac{\omega^2-\omega_{pl}^2}{2W_{pl}\omega_{pl}}\right)^2+1} \tag{6.2}$$

where ω_{ex}, W_{ex} and ω_{pl}, W_{pl} are the resonant frequency and the half-width of resonance line at half maximum of the exciton and plasmonic resonances, respectively, q is the Fano asymmetry parameter, b is the damping parameter originating from intrinsic losses, a is the maximal amplitude of the resonance. We note that Equation 6.2 assumes $W_{ex} << \omega_{ex}$. It then follows that the Fano resonance results from the competition between the two modes, and thus the Fano lineshape depends on the coupling between the relative dipole strengths. The quantity q represents this relative strength and can be deduced from Fano's original theory:[55-56]

$$q=\frac{1}{\pi L_{pl} g}\times\frac{D_{ex}}{d_{pl}} \tag{6.3}$$

where L_{pl} is the electromagnetic density of states at the plasmon resonance and g is the coupling strength between the surface plasmon (SP) and the exciton, D_{ex} is the total dipole moment of excitons, and d_{pl} is the dipole moment of the NP at the plasmon resonance. Commonly, the SPs have much stronger dipole moment compared to excitons in TMDC monolayers, which causes $|q|<<1$ in a plasmon-exciton system and the asymmetrical Fano lineshapes are undistinguishable. However, this theoretical modeling indicates that, when the dipole moment of the exciton subsystem (which depends on the number of excitons) is comparable to that of SPs, i.e. $|q|\approx 1$, more distinct asymmetrical Fano lineshapes appear, as shown in Figure 6.4a. Our experimental and simulated data indicate that q is negative in our system and, therefore, we only show this particular case. Figure 6.4a also demonstrates the behavior of the Fano resonance, which can be deduced from Equations 6.1 and 6.2, as we vary the Fano parameter q.

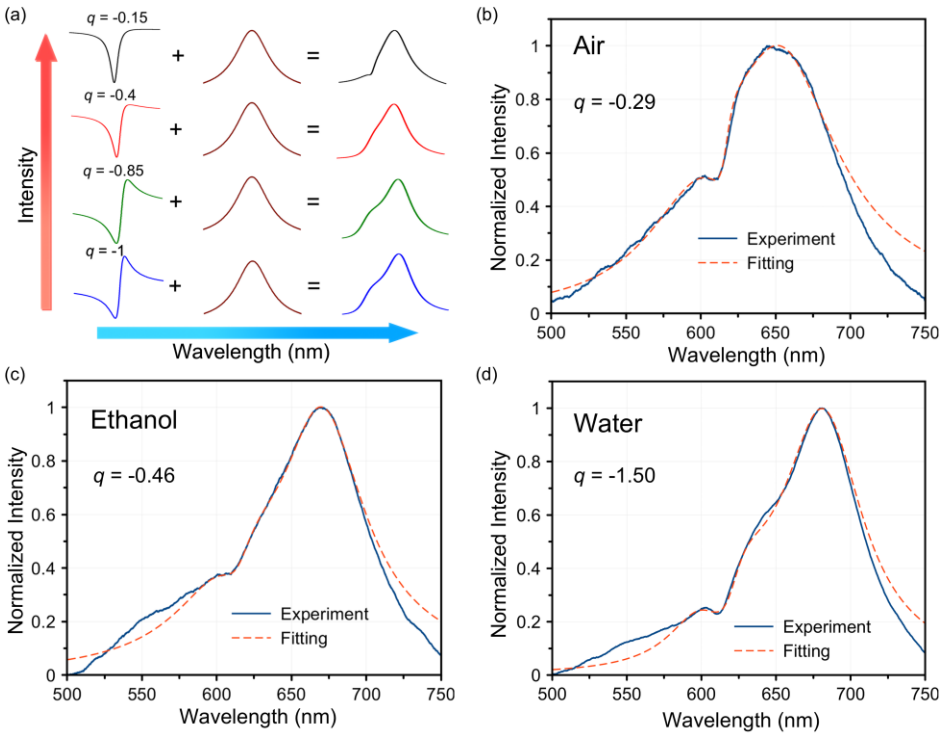

Figure 6.4: (a) Illustration of how Fano lineshape evolves as a function of the asymmetry Fano parameter q. Left curves show the Fano lineshapes for q values of -0.15, -0.4, -0.85 and -1, respectively. The middle curves represent the scattering spectra of single AuNTs. Right curves show the scattering spectra of WS_2-AuNT hybrids for q = -0.15, -0.4, -0.85 and -1, respectively. (b-d) Scattering spectra of a single 60 nm AuNT on monolayer WS_2 in air (b), ethanol (c) and water (d) (blue curves), and the results of theoretical analysis (red dashed curves) of the experimentally obtained scattering spectra.

In air, the dipole moment of SPs is stronger than the one of excitons, thus in WS_2-AuNT hybrids the SPs are dominating and $|q| << 1$. When the dielectric constant of the solvent increases, asymmetrical lineshapes appear in the scattering spectra (Figure 6.1f), which implies that $|q|$ becomes larger and close to 1. In order to understand this spectral change, Equations 6.1 and 6.2 were used to fit scattering spectra in Figure 6.1f. However, it should be noted that the scattering spectra of single AuNTs are not single Lorentzian-like spectra, and instead presented flat shoulders at short wavelengths, which are caused

by an additional plasmonic resonance in AuNTs (out-of-plane), excited by light with a large incident angle.[46] Since this additional resonance does not get involved into Fano scattering because of its mismatch with the orientation of exciton transition dipoles, we fitted the experimental results (Figure 6.1f) by adding an additional Lorentzian-like scattering peak to Equation 6.1. The results of our analysis are summarized in Figure 6.4b-d (detailed information is provided in Figure 6.5). Thus, we conclude that, by increasing the dielectric constant of the solvent, we obtain an increase of $|q|$ from 0.29 (air) to 1.50 (water), while holding its negative value.

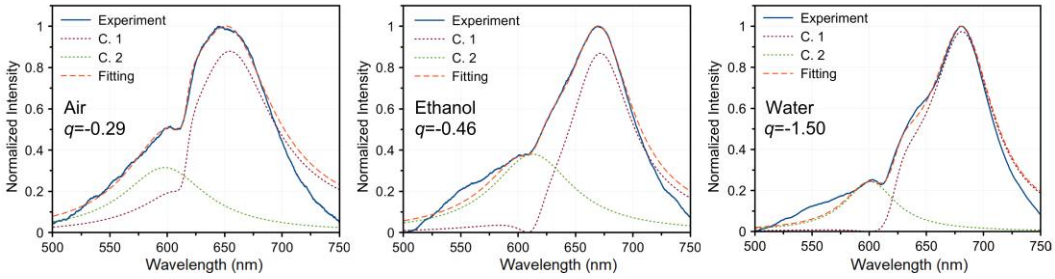

Figure 6.5: Scattering spectra of a single 60 nm AuNT on monolayer WS_2 in air (a), ethanol (b) and water (c) (blue curves), and the results of theoretical analysis (red dashed curves) of the experimentally obtained scattering spectra. The curves C.1 (brown dashed ones) correspond to Equations 6.1 and 6.2, whereas the curves C.2 (green dashed ones) are the additional Lorentzian signals, which are caused by other surface plasmon resonances.

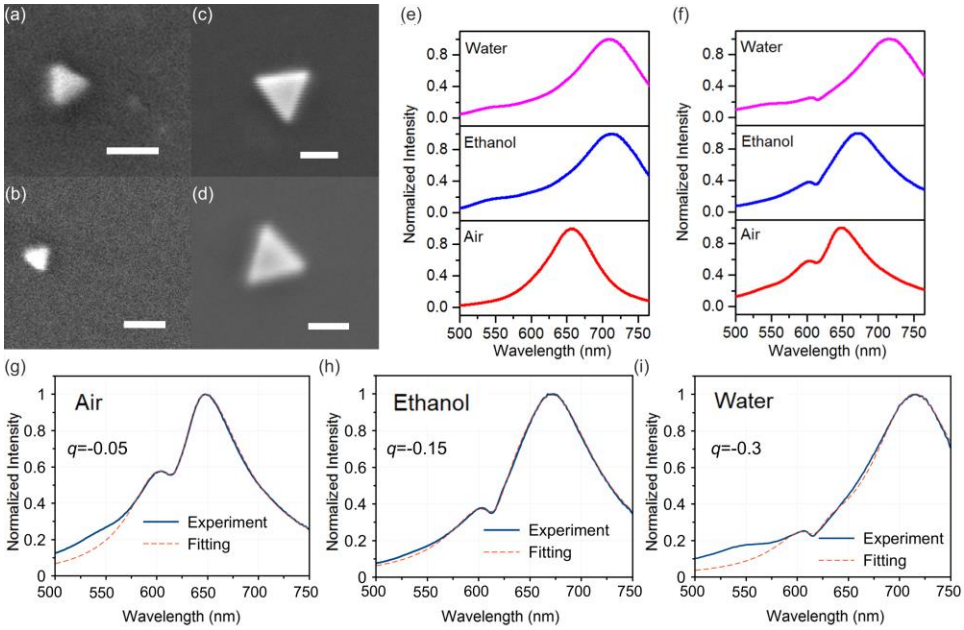

Figure 6.6: (a-d) SEM images of a 60 nm AuNT on a glass substrate (a), a 60 nm AuNT on monolayer WS_2 (b), a 150 nm AuNT on a glass substrate (c), and a 150 nm AuNT on monolayer WS_2 (d). The scale bars are 100 nm. (e) Scattering spectra of a single 150 nm AuNT on a glass substrate in air (red curve), ethanol (blue curve) and water (pink curve). f) Scattering spectra of a single 150 nm AuNT on monolayer WS_2 in air (red curve), ethanol (blue curve) and water (pink curve). Scattering spectra (blue curves) and the results of the theoretical analysis (red dashed curves) of the experimentally obtained scattering spectra of a single 150 nm AuNT on monolayer WS_2 in air (g), ethanol (h) and water (i).

The increase in $|q|$ is due to the increase in dipole moment (Equation 6.3), which derives from the decrease in exciton binding energy. The exciton binding energy E_b of a 2D excitonic system is given by:[57]

$$E_b = 4\frac{m_0 \cdot R_H \cdot a_H^2}{\mu \cdot a_0^2} \tag{6.4}$$

where m_0 and μ are the free-electron mass and exciton reduced mass, respectively. The parameters R_H, a_H and a_0 are the Rydberg constant, Bohr radius and effective Bohr radius, respectively. Since a larger effective Bohr radius represents a larger separation between

positive and negative charges, the smaller binding energy leads to a larger dipole moment of excitons. The increase of the exciton dipole moment was verified by the increasing PL intensity when solvents with larger dielectric constant were used.[50] This is because the PL intensity is directly proportional to the square of the total dipole moment of all excitons in the system $D_{ex} \sim d_{ex} \cdot N$, where N is the number of excitons and decreases when the solvent changes from air to water.[58] Note that the differential reflectance spectra demonstrate only slight changes in the bare TMDC light absorption in different solvents, thus indicating that the excitation processes play a minor role in the PL emission enhancement.

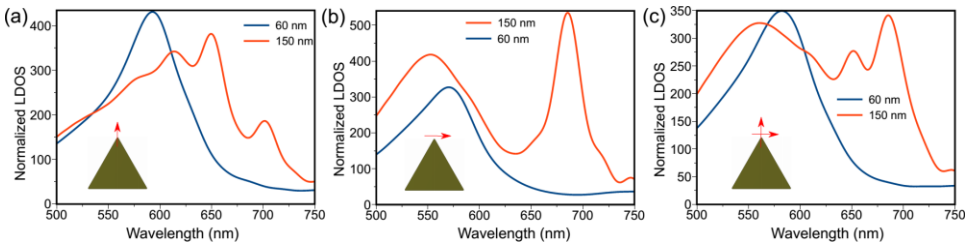

Figure 6.7: (a), (b) Normalized LDOS spectra for the dipole emitter located close to an AuNT tip (the distance between the emitter and AuNT is 5 nm). Insets show the relative arrangements of the source and nanoantenna in each case. (c) Average normalized LDOS factor for the 60 nm and 150 nm AuNTs; blue and red curves correspond to a 60 nm and 150 nm AuNT, respectively.

From Equation 6.3, it can be seen that the Fano lineshape also depends on L_{pl} and d_{pl} of SPs, and g between the SP and the excitons. Therefore, changes in plasmonic NPs can tune the Fano lineshape as well. To reveal how this works, we compare 60 nm AuNTs with 150 nm AuNTs (SEM images of 150 nm AuNTs are shown in Figures 6.6c and d). The scattering spectra of 150 nm AuNTs on a glass substrate and on monolayer WS_2 with different solvents are shown in Figure 6.6e and Figure 6.6f, respectively. By comparing Figure 6.6f to Figure 6.6e no obvious asymmetrical Fano lineshape is observed in the 150

nm AuNT sample. To understand this difference, we compared L_{pl}, g, and d_{pl} of 60 nm AuNTs with those of 150 nm AuNTs. For L_{pl} comparison the numerically calculated normalized local density of states (LDOS) distributions over AuNTs on SiO_2 substrate are used. The calculation approach we used is outlined in our previous work.[59] The results presented in Figures 6.7 reveal that both 60 nm and 150 nm AuNTs exhibit the maximum normalized LDOS of ~275 at 615 nm nearby their tips (Figure 6.7). This result implies that L_{pl} is approximately the same for 60 nm and 150 nm AuNTs. As shown in Figures 6.8 and 6.9, our coupled harmonic oscillator model calculation indicates that, in air and ethanol, the hybrids with 60 nm AuNTs have the smaller g than those with 150 nm AuNTs. However, in water, g for the hybrid with a 60 nm AuNT is ~1.7 times of that of the hybrid with a 150 nm AuNT. Moreover, we calculated the electric dipole moment **d** induced in 60 nm AuNT and 150 nm AuNT for s- and p-polarized plane wave excitation (with respect to the AuNT center) by:

$$\mathbf{d} = \varepsilon_0 \int_V \mathbf{r}\,\mathrm{div}(\mathbf{E}) dV \tag{6.5}$$

where ε_0 is the dielectric constant, $\mathbf{r}$ is the radius vector, V is the integration volume, which includes the whole AuNT. The results are presented in Figure 6.8.

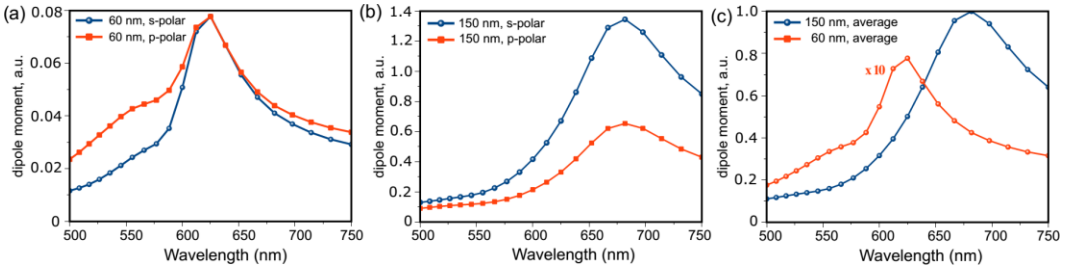

Figure 6.8: (a, b) Absolute value of the electric dipole moment (calculated with respect to the AuNT center) induced in a 60 nm AuNT a) and a 150 nm AuNT b) for s- and p-polarized plane wave excitation. c) Average electric dipole moment of the 60 nm and 150 nm AuNTs; blue and red curves correspond to a 60 nm and 150 nm AuNT, respectively. All results were normalized equally such that the average electric dipole of the 150 nm AuNT equals 1.

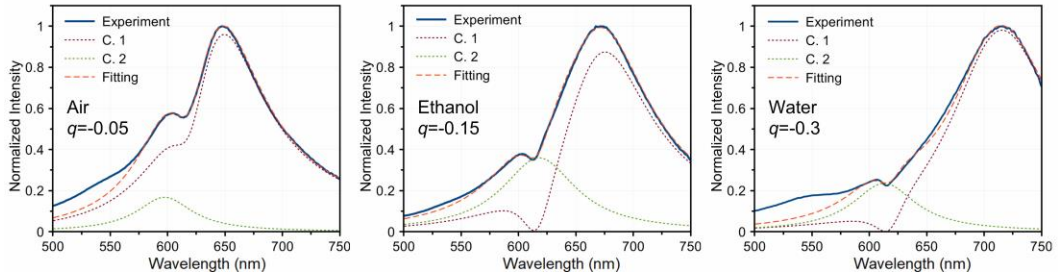

Figure 6.9: Scattering spectra of a single 150 nm AuNT on monolayer WS_2 in air (a), ethanol (b) and water (c) (blue curves), and the results of theoretical analysis (red dashed curves) of the experimentally obtained scattering spectra. The curves C.1 (brown dashed ones) correspond to Equations 6.1 and 6.2, whereas the curves C.2 (green dashed ones) are the additional Lorentzian signals, which are caused by other surface plasmon resonances.

The results in Figure 6.8 indicate that 150 nm AuNTs have a larger d_{pl} when compared to 60 nm AuNTs (more than 10 times) with the same solvent. By combining the results of L_{pl}, g, and d_{pl}, we obtain that $|q|$ for 150 nm AuNTs is smaller than that for 60 nm AuNTs. This is consistent with the results obtained from fitting the scattering spectra in Figure 6.6f, which are shown in Figures 6.6g, h and i (detailed information is in Figure 6.9). The fittings show that $|q|$ values for the 150 nm AuNT are 0.05, 0.15 and 0.3 in air,

ethanol and water, respectively, and are all smaller than those for the 60 nm AuNT in the same solvents

6.2.3 Coupled oscillators model of the exciton-plasmon coupling

In order to analyze the coupling strength in our system, which cannot be directly obtained from Fano's original theory, we further used the coupled harmonic oscillator model to simulate the scattering spectra.[60-61] In the coupled oscillators model, each component (the plasmonic nanoparticle and the exciton) of the coupled system is described as a harmonic oscillator with its own resonance frequency and damping. The coupling between the nanoparticle and WS_2 excitations is mediated via inductive terms proportional to the oscillator velocities. Dynamics of the full system are therefore modeled by two coupled equations:[60-61]

$$\begin{aligned} \ddot{x}_{pl} + 2W'_{pl}\dot{x}_{pl} + \omega'^2_{pl}x_{pl} + g\dot{x}_{ex} &= -eE(t) \\ \ddot{x}_{ex} + 2W'_{ex}\dot{x}_{ex} + \omega'^2_{ex}x_{ex} + g\dot{x}_{pl} &= 0 \end{aligned} \tag{6.6}$$

where x_{pl} and x_{ex} represent coordinates of the cavity and exciton oscillators, respectively, $E(t)$ is the driving electric field, e is the elementary charge, g is the plasmon-exciton coupling strength, the parameters ω'_{ex}, W'_{ex} and ω'_{pl}, W'_{pl} are the resonant frequency and half-width of resonance line at half maximum (*bare*) of the exciton and the plasmonic resonance, respectively. We assume that only the nanoantenna interacts directly with the incident field, which reflects the fact that the exciton extinction is negligible compared to that of the plasmonic nanostructure. The scattering cross-section of the coupled system, being dominated by the nanoparticle dipole moment radiation, can be estimated in this phenomenological approach as:

$$\sigma_{scat} \propto \omega^4 \left|x_{pl}\right|^2 \propto \left|\frac{\omega^2 \tilde{\omega}_{ex}^2}{\tilde{\omega}_{ex}^2 \tilde{\omega}_{pl}^2 - \omega^2 g^2}\right|^2 \tag{6.7}$$

Here $\tilde{\omega}_{ex}^2 = (\omega^2 - \omega_{ex}'^2 + 2iW_{ex}'\omega)$, $\tilde{\omega}_{pl}^2 = (\omega^2 - \omega_{pl}'^2 + 2iW_{pl}'\omega)$. However, Equation 6.7 is not suitable for the $|q| \approx 1$ case,[62-63] because the conventional coupled oscillator model doesn't account the retardation phase shifts in resonances and there is a π/2 phase difference between the exciton and the plasmonic resonance when $|q| \approx 1$.[64-65] Hence, the modified solutions of Equation 6.6 considering the π/2 phase difference should be employed for the single 60 nm AuNT on monolayer WS_2 in water ($|q| = 1.5$), and the scattering cross-section of the modified coupled system follows:[62]

$$\sigma_{scat} \propto \left| \frac{\omega^2 \tilde{\omega}_{ex}^2}{\tilde{\omega}_{ex}^2 \tilde{\omega}_{pl}^2 + \omega^2 g^2} \right|^2 \tag{6.8}$$

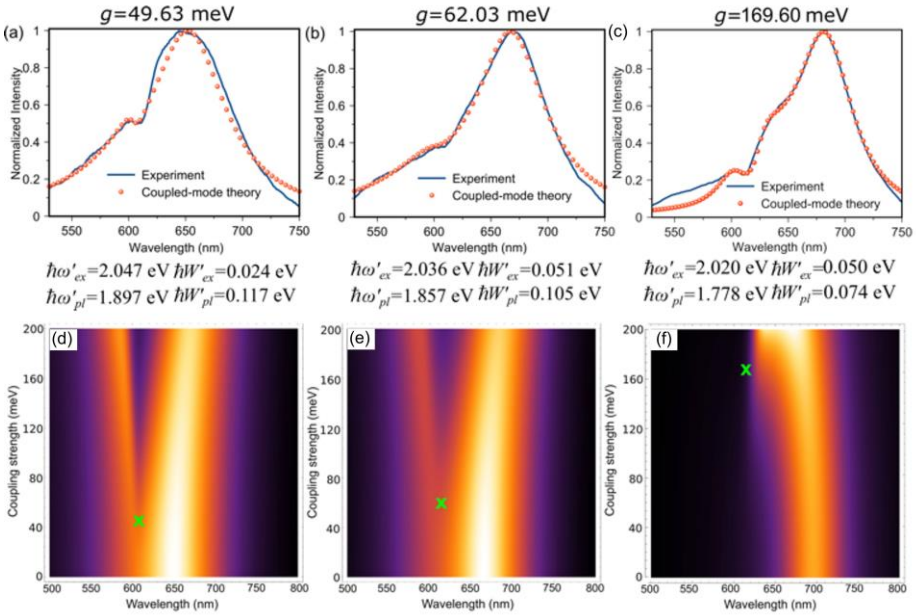

Figure 6.10: Results of theoretical analysis of the experimentally measured scattering spectra of a single 60 nm AuNT on monolayer WS_2 in air (a), ethanol (b) and water (c) (blue curves) by the coupled oscillators model (red dotted curves). The coupling strength *g* has been converted into the energy value. Scattering cross-section dependences on the wavelength and coupling strength *g* of the hybrid system with 60 nm AuNTs in air (d), ethanol (e), and water (f). The green crosses show the experimentally achieved values of the coupling strength.

For the hybrids with 60 nm AuNTs, we observe that the coupled oscillator model reproduces the experimental results exceptionally well, as shown in Figure 6.10. The important observation is that the coupling strength of the hybrid system increases from 49.63 meV (air) to 169.60 meV (water). Since the coupling strength is determined by the transition dipole moment, the increase in the coupling strength matches the augment of the PL intensity of monolayer WS_2 from air to water. The increase of coupling strength and reduction of dissipative losses of the system when changing the solvent suggest that the *strong coupling regime* may be achieved in this system. By considering the detuning, the splitting between the upper plexcitonic state (E_+) and the lower plexcitonic state (E_-) equates:[66]

$$E_+ - E_- = \sqrt{4g^2 + (\hbar\delta - i(\hbar W'_{ex} - \hbar W'_{pl}))^2} \tag{6.9}$$

where W'_{ex} is the half-width of resonance line at half maximum of excitons, W'_{pl} is the half-width of resonance line at half maximum of plasmon resonances, $\hbar$ is the reduced Planck constant, and δ is the detuning that equates ω_{pl} - ω_{ex}. However, the usually used criterion for the strong coupling- $\hbar\Omega_0 > \hbar W'_{ex} + \hbar W'_{pl}$, where $\hbar\Omega_0$ is Rabi splitting at zero detuning, cannot be directly applied to a system with detuning. Thus, an extended criterion is demanded. When the detuning is smaller than ω_{ex}, the splitting of plexcitonic states can be approximately expressed in the form of $\hbar\Omega_0$ through the classic description of strong coupling:[67-68] $E_+ - E_- = \sqrt{(\hbar\Omega_0)^2 + (\hbar\delta - i(\hbar W'_{ex} - \hbar W'_{pl}))^2}$. When $\hbar\Omega_0 > \hbar W'_{ex} + \hbar W'_{pl}$, the system achieves the strong coupling regime. Hence, we come to conclusion that when $2g > \hbar W'_{ex} + \hbar W'_{pl}$ the system with detuning achieves the strong coupling regime. In our case, this criterion is satisfied only for the system in water, where the $\hbar W'_{ex} + \hbar W'_{pl}$ equals to 153.76 meV, whereas 2*g* equals 339.20 meV. Thus, we can conclude that for the hybrid system with 60 nm AuNTs in water, we achieve strong coupling regime, where Rabi splitting sufficiently perturbs the scattering spectrum. The other parameters of the system

in different solvents correspond to those shown in Figure 6.10a-c. The corresponding results for 150 nm AuNTs in different solvents are presented in Figure 6.11a-c. For 150 nm AuNTs, the strong coupling is again only achieved in water, where $\hbar W'_{ex} + \hbar W'_{pl}$ and $2g$ equal to 182.71 meV and 198.51 meV, respectively. Figure 6.10d-f and Figure 6.11d-f demonstrate the dependence of the scattering cross-section on the wavelength and coupling strength g of the hybrid system with 60 nm and 150 nm AuNTs in air (a), ethanol (b), and water (c), respectively. The green crosses indicate the experimentally achieved values of the coupling strength.

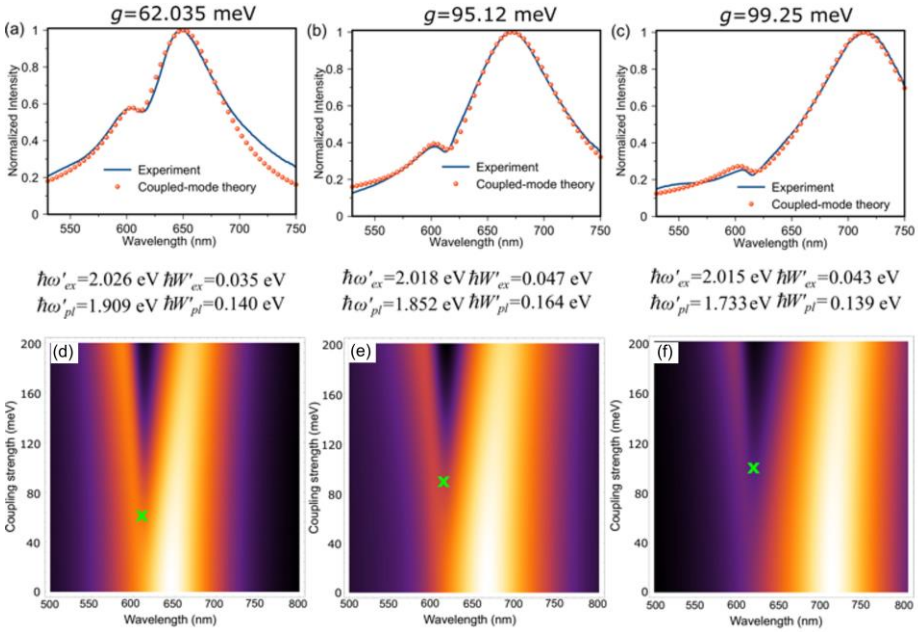

Figure 6.11: Results of theoretical analysis of the experimentally measured scattering spectra of a single 150 nm AuNT on monolayer WS_2 in air (a), ethanol (b) and water (c) (blue curves) by the coupled oscillators model (red dotted curves). The coupling strength g has been converted into the energy value. Scattering cross-section dependencies on the wavelength and coupling strength g of the hybrid system with 150 nm AuNTs in air (d), ethanol (e), and water (f). The green crosses show the experimentally achieved values of the coupling strength.

6.3 SUMMARY

In summary, tunable Fano resonances and plasmon-exciton coupling in monolayer WS_2-AuNT hybrids have been demonstrated. Fano resonances can be controlled by tuning the exciton binding energy or the LSPR strength through the dielectric constant of surrounding solvents or the dimension of AuNTs. Similarly, a transition from weak to strong plasmon-exciton coupling has been achieved by changing the dielectric constant of surrounding solvents. Large coupling strength of 50-170 meV occur at room temperature due to the strong field localization of the AuNTs and large transition dipole moment of the WS_2 exciton. Our experiments are supported by numerical simulations, which provide a guidance on systematic tuning of the Fano lineshape and Rabi splitting energies. Our demonstrated tunable Fano resonance and Rabi splitting will pave the way towards active devices based on TMDC-plasmonic systems such as optical switches and tunable lasers.[69-70]

6.4 REFERENCES

1. Frimmer, M.; Coenen, T.; Koenderink, A. F., Signature of a Fano Resonance in a Plasmonic Metamolecule's Local Density of Optical States. *Phys. Rev. Lett.* **2012**, 108 (7), 077404.
2. Zhang, W.; Govorov, A. O., Quantum theory of the nonlinear Fano effect in hybrid metal-semiconductor nanostructures: The case of strong nonlinearity. *Phys. Rev. B* **2011**, 84 (8), 081405.
3. Ridolfo, A.; Di Stefano, O.; Fina, N.; Saija, R.; Savasta, S., Quantum Plasmonics with Quantum Dot-Metal Nanoparticle Molecules: Influence of the Fano Effect on Photon Statistics. *Phys. Rev. Lett.* **2010**, 105 (26), 263601.
4. Miroshnichenko, A. E.; Flach, S.; Kivshar, Y. S., Fano resonances in nanoscale structures. *Rev. Mod. Phys.* **2010**, 82 (3), 2257-2298.
5. Luk'yanchuk, B.; Zheludev, N. I.; Maier, S. A.; Halas, N. J.; Nordlander, P.; Giessen, H.; Chong, C. T., The Fano resonance in plasmonic nanostructures and metamaterials. *Nat. Mater.* **2010**, 9, 707.

6. Lassiter, J. B.; Sobhani, H.; Fan, J. A.; Kundu, J.; Capasso, F.; Nordlander, P.; Halas, N. J., Fano Resonances in Plasmonic Nanoclusters: Geometrical and Chemical Tunability. *Nano Lett.* **2010**, 10 (8), 3184-3189.

7. Frontiera, R. R.; Gruenke, N. L.; Van Duyne, R. P., Fano-Like Resonances Arising from Long-Lived Molecule-Plasmon Interactions in Colloidal Nanoantennas. *Nano Lett.* **2012**, 12 (11), 5989-5994.

8. Bellessa, J.; Bonnand, C.; Plenet, J. C.; Mugnier, J., Strong Coupling between Surface Plasmons and Excitons in an Organic Semiconductor. *Phys. Rev. Lett.* **2004**, 93 (3), 036404.

9. Wurtz, G. A.; Evans, P. R.; Hendren, W.; Atkinson, R.; Dickson, W.; Pollard, R. J.; Zayats, A. V.; Harrison, W.; Bower, C., Molecular Plasmonics with Tunable Exciton−Plasmon Coupling Strength in J-Aggregate Hybridized Au Nanorod Assemblies. *Nano Lett.* **2007**, 7 (5), 1297-1303.

10. Roller, E.-M.; Argyropoulos, C.; Högele, A.; Liedl, T.; Pilo-Pais, M., Plasmon–Exciton Coupling Using DNA Templates. *Nano Lett.* 2016, 16 (9), 5962-5966.

11. Balci, S.; Kocabas, C.; Ates, S.; Karademir, E.; Salihoglu, O.; Aydinli, A., Tuning surface plasmon-exciton coupling via thickness dependent plasmon damping. *Phys. Rev. B* **2012**, 86 (23), 235402.

12. Ni, W.; Ambjörnsson, T.; Apell, S. P.; Chen, H.; Wang, J., Observing Plasmonic−Molecular Resonance Coupling on Single Gold Nanorods. *Nano Lett.* **2010**, 10 (1), 77-84.

13. Lin, L.; Wang, M.; Wei, X.; Peng, X.; Xie, C.; Zheng, Y., Photoswitchable Rabi Splitting in Hybrid Plasmon–Waveguide Modes. *Nano Lett.* **2016**, 16 (12), 7655-7663.

14. Li, J.; Cushing, S. K.; Meng, F.; Senty, T. R.; Bristow, A. D.; Wu, N., Plasmon-induced resonance energy transfer for solar energy conversion. *Nat. Photonics* **2015**, 9, 601.

15. Liu, G. L.; Long, Y.-T.; Choi, Y.; Kang, T.; Lee, L. P., Quantized plasmon quenching dips nanospectroscopy via plasmon resonance energy transfer. *Nat. Methods* **2007**, 4, 1015.

16. Wang, M.; Bangalore Rajeeva, B.; Scarabelli, L.; Perillo, E. P.; Dunn, A. K.; Liz-Marzán, L. M.; Zheng, Y., Molecular-Fluorescence Enhancement via Blue-Shifted Plasmon-Induced Resonance Energy Transfer. *J. Phys. Chem. C* **2016**, 120 (27), 14820-14827.

17. Ming, T.; Zhao, L.; Yang, Z.; Chen, H.; Sun, L.; Wang, J.; Yan, C., Strong Polarization Dependence of Plasmon-Enhanced Fluorescence on Single Gold Nanorods. *Nano Lett.* **2009**, 9 (11), 3896-3903.

18. Wang, M.; Hartmann, G.; Wu, Z.; Scarabelli, L.; Rajeeva, B. B.; Jarrett, J. W.; Perillo, E. P.; Dunn, A. K.; Liz-Marzán, L. M.; Hwang, G. S.; Zheng, Y., Controlling Plasmon-Enhanced Fluorescence via Intersystem Crossing in Photoswitchable Molecules. *Small* **2017**, 13 (38), 1701763.

19. Akselrod, G. M.; Argyropoulos, C.; Hoang, T. B.; Ciracì, C.; Fang, C.; Huang, J.; Smith, D. R.; Mikkelsen, M. H., Probing the mechanisms of large Purcell enhancement in plasmonic nanoantennas. *Nat. Photonics* **2014**, 8, 835.

20. Luk'yanchuk, B.; Zheludev, N. I.; Maier, S. A.; Halas, N. J.; Nordlander, P.; Giessen, H.; Chong, C. T., The Fano resonance in plasmonic nanostructures and metamaterials. *Nat. Mater.* **2010**, 9 (9), 707-715.

21. Chikkaraddy, R.; de Nijs, B.; Benz, F.; Barrow, S. J.; Scherman, O. A.; Rosta, E.; Demetriadou, A.; Fox, P.; Hess, O.; Baumberg, J. J., Single-molecule strong coupling at room temperature in plasmonic nanocavities. *Nature* **2016**, 535 (7610), 127-130.

22. Giannini, V.; Fernández-Domínguez, A. I.; Heck, S. C.; Maier, S. A., Plasmonic Nanoantennas: Fundamentals and Their Use in Controlling the Radiative Properties of Nanoemitters. *Chem. Rev.* **2011**, 111 (6), 3888-3912.

23. Fofang, N. T.; Grady, N. K.; Fan, Z.; Govorov, A. O.; Halas, N. J., Plexciton Dynamics: Exciton−Plasmon Coupling in a J-Aggregate−Au Nanoshell Complex Provides a Mechanism for Nonlinearity. *Nano Lett.* **2011**, 11 (4), 1556-1560.

24. DeLacy, B. G.; Miller, O. D.; Hsu, C. W.; Zander, Z.; Lacey, S.; Yagloski, R.; Fountain, A. W.; Valdes, E.; Anquillare, E.; Soljačić, M.; Johnson, S. G.; Joannopoulos, J. D., Coherent Plasmon-Exciton Coupling in Silver Platelet-J-aggregate Nanocomposites. *Nano Lett.* **2015**, 15 (4), 2588-2593.

25. Artuso, R. D.; Bryant, G. W., Optical Response of Strongly Coupled Quantum Dot−Metal Nanoparticle Systems: Double Peaked Fano Structure and Bistability. *Nano Lett.* **2008**, 8 (7), 2106-2111.

26. Schlather, A. E.; Large, N.; Urban, A. S.; Nordlander, P.; Halas, N. J., Near-Field Mediated Plexcitonic Coupling and Giant Rabi Splitting in Individual Metallic Dimers. *Nano Lett.* **2013**, 13 (7), 3281-3286.

27. Fofang, N. T.; Park, T.-H.; Neumann, O.; Mirin, N. A.; Nordlander, P.; Halas, N. J., Plexcitonic Nanoparticles: Plasmon−Exciton Coupling in Nanoshell−J-Aggregate Complexes. *Nano Lett.* **2008**, 8 (10), 3481-3487.

28. Zheng, Y. B.; Juluri, B. K.; Lin Jensen, L.; Ahmed, D.; Lu, M.; Jensen, L.; Huang, T. J., Dynamic Tuning of Plasmon–Exciton Coupling in Arrays of Nanodisk–J-aggregate Complexes. *Adv. Mater.* **2010**, 22 (32), 3603-3607.

29. Ni, W.; Yang, Z.; Chen, H.; Li, L.; Wang, J., Coupling between Molecular and Plasmonic Resonances in Freestanding Dye−Gold Nanorod Hybrid Nanostructures. *J. Am. Chem. Soc.* **2008**, 130 (21), 6692-6693.

30. Nan, F.; Zhang, Y.-F.; Li, X.; Zhang, X.-T.; Li, H.; Zhang, X.; Jiang, R.; Wang, J.; Zhang, W.; Zhou, L.; Wang, J.-H.; Wang, Q.-Q.; Zhang, Z., Unusual and Tunable One-Photon Nonlinearity in Gold-Dye Plexcitonic Fano Systems. *Nano Lett.* **2015**, 15 (4), 2705-2710.

31. Zhang, W.; Govorov, A. O.; Bryant, G. W., Semiconductor-Metal Nanoparticle Molecules: Hybrid Excitons and the Nonlinear Fano Effect. *Phys. Rev. Lett.* **2006**, 97 (14), 146804.

32. Zengin, G.; Wersäll, M.; Nilsson, S.; Antosiewicz, T. J.; Käll, M.; Shegai, T., Realizing Strong Light-Matter Interactions between Single-Nanoparticle Plasmons and Molecular Excitons at Ambient Conditions. *Phys. Rev. Lett.* **2015**, 114 (15), 157401.

33. Manjavacas, A.; Abajo, F. J. G. d.; Nordlander, P., Quantum Plexcitonics: Strongly Interacting Plasmons and Excitons. *Nano Lett.* **2011**, 11 (6), 2318-2323.

34. Wang, Q. H.; Kalantar-Zadeh, K.; Kis, A.; Coleman, J. N.; Strano, M. S., Electronics and optoelectronics of two-dimensional transition metal dichalcogenides. *Nat. Nanotechnol.* **2012**, 7 (11), 699-712.

35. Jariwala, D.; Sangwan, V. K.; Lauhon, L. J.; Marks, T. J.; Hersam, M. C., Emerging Device Applications for Semiconducting Two-Dimensional Transition Metal Dichalcogenides. *ACS Nano* **2014**, 8 (2), 1102-1120.

36. Abid, I.; Chen, W.; Yuan, J.; Bohloul, A.; Najmaei, S.; Avendano, C.; Péchou, R.; Mlayah, A.; Lou, J., Temperature-Dependent Plasmon–Exciton Interactions in Hybrid Au/$MoSe_2$ Nanostructures. *ACS Photonics* **2017**, 4 (7), 1653-1660.

37. Koperski, M.; Molas Maciej, R.; Arora, A.; Nogajewski, K.; Slobodeniuk Artur, O.; Faugeras, C.; Potemski, M., Optical properties of atomically thin transition metal dichalcogenides: observations and puzzles. *Nanophotonics* **2017**, 6(6), 1289–1308.

38. Manzeli, S.; Ovchinnikov, D.; Pasquier, D.; Yazyev, O. V.; Kis, A., 2D transition metal dichalcogenides. *Nat. Rev. Mater.* **2017**, 2, 17033.

39. Mak, K. F.; Shan, J., Photonics and optoelectronics of 2D semiconductor transition metal dichalcogenides. *Nat. Photonics* **2016**, 10 (4), 216-226.

40. Wen, J.; Wang, H.; Wang, W.; Deng, Z.; Zhuang, C.; Zhang, Y.; Liu, F.; She, J.; Chen, J.; Chen, H.; Deng, S.; Xu, N., Room-Temperature Strong Light–Matter Interaction with Active Control in Single Plasmonic Nanorod Coupled with Two-Dimensional Atomic Crystals. *Nano Lett.* **2017**, 17 (8), 4689-4697.

41. Carozo, V.; Wang, Y.; Fujisawa, K.; Carvalho, B. R.; McCreary, A.; Feng, S.; Lin, Z.; Zhou, C.; Perea-López, N.; Elías, A. L.; Kabius, B.; Crespi, V. H.; Terrones, M., Optical identification of sulfur vacancies: Bound excitons at the edges of monolayer tungsten disulfide. *Sci. Adv.* **2017**, 3 (4).

42. Zhang, Y.; Zhang, Y.; Ji, Q.; Ju, J.; Yuan, H.; Shi, J.; Gao, T.; Ma, D.; Liu, M.; Chen, Y.; Song, X.; Hwang, H. Y.; Cui, Y.; Liu, Z., Controlled Growth of High-Quality Monolayer WS2 Layers on Sapphire and Imaging Its Grain Boundary. *ACS Nano* **20**13, 7 (10), 8963-8971.

43. Cong, C.; Shang, J.; Wu, X.; Cao, B.; Peimyoo, N.; Qiu, C.; Sun, L.; Yu, T., Synthesis and Optical Properties of Large-Area Single-Crystalline 2D Semiconductor WS2 Monolayer from Chemical Vapor Deposition. *Adv. Opt. Mater.* **2014**, 2 (2), 131-136.

44. Terrones, H.; Corro, E. D.; Feng, S.; Poumirol, J. M.; Rhodes, D.; Smirnov, D.; Pradhan, N. R.; Lin, Z.; Nguyen, M. A. T.; Elías, A. L.; Mallouk, T. E.; Balicas, L.; Pimenta, M. A.; Terrones, M., New First Order Raman-active Modes in Few Layered Transition Metal Dichalcogenides. *Sci. Rep.* **2014**, 4, 4215.

45. Berkdemir, A.; Gutiérrez, H. R.; Botello-Méndez, A. R.; Perea-López, N.; Elías, A. L.; Chia, C.-I.; Wang, B.; Crespi, V. H.; López-Urías, F.; Charlier, J.-C.; Terrones, H.; Terrones, M., Identification of individual and few layers of WS_2 using Raman Spectroscopy. *Sci. Rep.* **2013**, 3, 1755.

46. Scarabelli, L.; Coronado-Puchau, M.; Giner-Casares, J. J.; Langer, J.; Liz-Marzán, L. M., Monodisperse Gold Nanotriangles: Size Control, Large-Scale Self-Assembly, and Performance in Surface-Enhanced Raman Scattering. *ACS Nano* **2014**, 8 (6), 5833-5842.

47. Shafiei, F.; Monticone, F.; Le, K. Q.; Liu, X.-X.; Hartsfield, T.; Alu, A.; Li, X., A subwavelength plasmonic metamolecule exhibiting magnetic-based optical Fano resonance. *Nat. Nanotechnol.* **2013**, 8 (2), 95-99.

48. Argyropoulos, C.; Monticone, F.; D'Aguanno, G.; Alù, A., Plasmonic nanoparticles and metasurfaces to realize Fano spectra at ultraviolet wavelengths. *Appl. Phys. Lett.* **2013**, 103 (14), 143113.

49. Mao, N.; Chen, Y.; Liu, D.; Zhang, J.; Xie, L., Solvatochromic Effect on the Photoluminescence of MoS_2 Monolayers. *Small* **2013**, 9 (8), 1312-1315.

50. Lin, Y.; Ling, X.; Yu, L.; Huang, S.; Hsu, A. L.; Lee, Y.-H.; Kong, J.; Dresselhaus, M. S.; Palacios, T., Dielectric Screening of Excitons and Trions in Single-Layer MoS_2. *Nano Lett.* **2014**, 14 (10), 5569-5576.

51. Zhu, B.; Chen, X.; Cui, X., Exciton Binding Energy of Monolayer WS_2. *Sci. Rep.* **2015**, 5, 9218.

52. Anker, J. N.; Hall, W. P.; Lyandres, O.; Shah, N. C.; Zhao, J.; Van Duyne, R. P., Biosensing with plasmonic nanosensors. *Nat. Mater.* **2008**, 7 (6), 442-453.

53. Gallinet, B.; Martin, O. J. F., Influence of Electromagnetic Interactions on the Line Shape of Plasmonic Fano Resonances. *ACS Nano* **2011**, 5 (11), 8999-9008.

54. Gallinet, B.; Martin, O. J. F., Ab initio. *Phys. Rev. B* **2011**, 83 (23), 235427.

55. Fano, U., Effects of Configuration Interaction on Intensities and Phase Shifts. P*hys. Rev.* **1961**, 124 (6), 1866-1878.

56. Tang, T.-T.; Zhang, Y.; Park, C.-H.; Geng, B.; Girit, C.; Hao, Z.; Martin, M. C.; Zettl, A.; Crommie, M. F.; Louie, S. G.; Shen, Y. R.; Wang, F., A tunable phonon-exciton Fano system in bilayer graphene. *Nat. Nanotechnol.* **2010**, 5 (1), 32-36.

57. Mathieu, H.; Lefebvre, P.; Christol, P., Simple analytical method for calculating exciton binding energies in semiconductor quantum wells. P*hys. Rev. B* **1992**, 46 (7), 4092-4101.

58. Baranov, D. G.; Savelev, R. S.; Li, S. V.; Krasnok, A. E.; Alù, A., Modifying magnetic dipole spontaneous emission with nanophotonic structures. *Laser Photonics Rev.* **2017,** 11 (3), 1600268.

59. Krasnok, A. E.; Slobozhanyuk, A. P.; Simovski, C. R.; Tretyakov, S. A.; Poddubny, A. N.; Miroshnichenko, A. E.; Kivshar, Y. S.; Belov, P. A., An antenna model for the Purcell effect. *Sci. Rep.* **2015**, 5, 12956.

60. Wu, X.; Gray, S. K.; Pelton, M., Quantum-dot-induced transparency in a nanoscale plasmonic resonator. *Opt. Express* **2010**, 18 (23), 23633-23645.

61. Zengin, G.; Johansson, G.; Johansson, P.; Antosiewicz, T. J.; Käll, M.; Shegai, T., Approaching the strong coupling limit in single plasmonic nanorods interacting with J-aggregates. *Sci. Rep.* **2013**, 3, 3074.

62. Kelly, C.; Khosravi Khorashad, L.; Gadegaard, N.; Barron, L. D.; Govorov, A. O.; Karimullah, A. S.; Kadodwala, M., Controlling Metamaterial Transparency with Superchiral Fields. *ACS Photonics* **2018**, 5 (2), 535-543.

63. Riffe, D. M., Classical Fano oscillator. Phys. Rev. B **201**1, 84 (6), 064308.

64. Ott, C.; Kaldun, A.; Raith, P.; Meyer, K.; Laux, M.; Evers, J.; Keitel, C. H.; Greene, C. H.; Pfeifer, T., Lorentz Meets Fano in Spectral Line Shapes: A Universal Phase and Its Laser Control. *Science* **2013**, 340 (6133), 716.

65. Limonov, M. F.; Rybin, M. V.; Poddubny, A. N.; Kivshar, Y. S., Fano resonances in photonics. *Nat. Photonics* **2017**, 11, 543.

66. Baranov, D. G.; Wersäll, M.; Cuadra, J.; Antosiewicz, T. J.; Shegai, T., Novel Nanostructures and Materials for Strong Light–Matter Interactions. *ACS Photonics* **2018**, 5 (1), 24–4.

67. Törmä, P.; Barnes, W. L., Strong coupling between surface plasmon polaritons and emitters: a review. *Rep. Prog. Phys.* **2015**, 78 (1), 013901.

68. Tserkezis, C.; Wubs, M.; Mortensen, N. A., Robustness of the Rabi Splitting under Nonlocal Corrections in Plexcitonics. *ACS Photonics* **2017**.

69. Argyropoulos, C.; Chen, P.-Y.; Monticone, F.; D'Aguanno, G.; Alù, A., Nonlinear Plasmonic Cloaks to Realize Giant All-Optical Scattering Switching. *Phys. Rev. Lett.* **2012**, 108 (26), 263905.

70. Sun, Z.; Martinez, A.; Wang, F., Optical modulators with 2D layered materials. *Nat. Photonics* **2016**, 10 (4), 227-238.

Bibliography

Chapter 1

1. Willets, K. A.; Duyne, R. P. V., Localized Surface Plasmon Resonance Spectroscopy and Sensing. *Annu. Rev. Phys. Chem.* **2007**, 58 (1), 267-297.
2. Atwater, H. A.; Polman, A., Plasmonics for improved photovoltaic devices. *Nat. Mater.* **2010**, 9, 205.
3. Maier, S. A.; Atwater, H. A., Plasmonics: Localization and guiding of electromagnetic energy in metal/dielectric structures. *J. Appl. Phys.* **2005**, 98 (1), 011101.
4. Halas, N. J.; Lal, S.; Chang, W.-S.; Link, S.; Nordlander, P., Plasmons in Strongly Coupled Metallic Nanostructures. *Chem. Rev.* **2011**, 111 (6), 3913-3961.
5. Zayats, A. V.; Smolyaninov, I. I.; Maradudin, A. A., Nano-optics of surface plasmon polaritons. *Phys. Rep.* **2005**, 408 (3), 131-314.
6. Luther, J. M.; Jain, P. K.; Ewers, T.; Alivisatos, A. P., Localized surface plasmon resonances arising from free carriers in doped quantum dots. *Nat. Mater.* **201**1, 10, 361.
7. Anker, J. N.; Hall, W. P.; Lyandres, O.; Shah, N. C.; Zhao, J.; Van Duyne, R. P., Biosensing with plasmonic nanosensors. *Nat. Mater.* **2008**, 7, 442.
8. Eustis, S.; El-Sayed, M. A., Why gold nanoparticles are more precious than pretty gold: Noble metal surface plasmon resonance and its enhancement of the radiative and nonradiative properties of nanocrystals of different shapes. *Chem. Soc. Rev.* **2006**, 35 (3), 209-217.
9. Fan, X.; Zheng, W.; Singh, D. J., Light scattering and surface plasmons on small spherical particles. *Light Sci. Appl.* **2014**, 3, e179.
10. Luk'yanchuk, B.; Zheludev, N. I.; Maier, S. A.; Halas, N. J.; Nordlander, P.; Giessen, H.; Chong, C. T., The Fano resonance in plasmonic nanostructures and metamaterials. *Nat. Mater.* **2010**, 9, 707.
11. Jain, P. K.; Lee, K. S.; El-Sayed, I. H.; El-Sayed, M. A., Calculated Absorption and Scattering Properties of Gold Nanoparticles of Different Size, Shape, and Composition: Applications in Biological Imaging and Biomedicine. *J. Phys. Chem. B* **2006**, 110 (14), 7238-7248.
12. Hu, M.; Chen, J.; Li, Z.-Y.; Au, L.; Hartland, G. V.; Li, X.; Marquez, M.; Xia, Y., Gold nanostructures: engineering their plasmonic properties for biomedical applications. *Chem. Soc. Rev.* **2006**, 35 (11), 1084-1094.
13. Chen, H.; Shao, L.; Li, Q.; Wang, J., Gold nanorods and their plasmonic properties. *Chem. Soc. Rev.* **2013**, 42 (7), 2679-2724.

14. Yun, C. S.; Javier, A.; Jennings, T.; Fisher, M.; Hira, S.; Peterson, S.; Hopkins, B.; Reich, N. O.; Strouse, G. F., Nanometal Surface Energy Transfer in Optical Rulers, Breaking the FRET Barrier. *J. Am. Chem. Soc.* **2005**, 127 (9), 3115-3119.

15. Clapp, A. R.; Medintz, I. L.; Mattoussi, H., Förster Resonance Energy Transfer Investigations Using Quantum-Dot Fluorophores. *ChemPhysChem* **2006**, 7 (1), 47-57.

16. Li, J.; Cushing, S. K.; Meng, F.; Senty, T. R.; Bristow, A. D.; Wu, N., Plasmon-induced resonance energy transfer for solar energy conversion. *Nat. Photonics* **2015**, 9, 601.

17. Noda, S.; Fujita, M.; Asano, T., Spontaneous-emission control by photonic crystals and nanocavities. *Nat. Photonics* **2007**, 1 (8), 449-458.

18. Lakowicz, J. R., Radiative decay engineering 5: metal-enhanced fluorescence and plasmon emission. *Anal. Biochem.* **2005**, 337 (2), 171-194.

19. Pelton, M., Modified spontaneous emission in nanophotonic structures. *Nat. Photonics* **2015**, 9 (7), 427-435.

20. Cang, H.; Liu, Y.; Wang, Y.; Yin, X.; Zhang, X., Giant Suppression of Photobleaching for Single Molecule Detection via the Purcell Effect. *Nano Lett.* **2013**, 13 (12), 5949-5953.

21. Lodahl, P.; Floris van Driel, A.; Nikolaev, I. S.; Irman, A.; Overgaag, K.; Vanmaekelbergh, D.; Vos, W. L., Controlling the dynamics of spontaneous emission from quantum dots by photonic crystals. *Nature* **2004**, 430 (7000), 654-657.

22. Song, J.-H.; Atay, T.; Shi, S.; Urabe, H.; Nurmikko, A. V., Large Enhancement of Fluorescence Efficiency from CdSe/ZnS Quantum Dots Induced by Resonant Coupling to Spatially Controlled Surface Plasmons. *Nano Lett.* **2005**, 5 (8), 1557-1561.

23. Belacel, C.; Habert, B.; Bigourdan, F.; Marquier, F.; Hugonin, J. P.; Michaelis de Vasconcellos, S.; Lafosse, X.; Coolen, L.; Schwob, C.; Javaux, C.; Dubertret, B.; Greffet, J. J.; Senellart, P.; Maitre, A., Controlling Spontaneous Emission with Plasmonic Optical Patch Antennas. *Nano Lett.* **2013**, 13 (4), 1516-1521.

24. Noda, S.; Fujita, M.; Asano, T., Spontaneous-emission control by photonic crystals and nanocavities. *Nat. Photonics* **2007**, 1, 449.

25. Anger, P.; Bharadwaj, P.; Novotny, L., Enhancement and Quenching of Single-Molecule Fluorescence. *Phys. Rev. Lett.* **2006**, 96 (11), 113002.

26. Kühn, S.; Håkanson, U.; Rogobete, L.; Sandoghdar, V., Enhancement of Single-Molecule Fluorescence Using a Gold Nanoparticle as an Optical Nanoantenna. *Phys. Rev. Lett.* **2006**, 97 (1), 017402.

27. Akselrod, G. M.; Argyropoulos, C.; Hoang, T. B.; Ciracì, C.; Fang, C.; Huang, J.; Smith, D. R.; Mikkelsen, M. H., Probing the mechanisms of large Purcell enhancement in plasmonic nanoantennas. *Nat. Photonic*s **2014**, 8 (11), 835-840.

28. Rose, A.; Hoang, T. B.; McGuire, F.; Mock, J. J.; Ciracì, C.; Smith, D. R.; Mikkelsen, M. H., Control of Radiative Processes Using Tunable Plasmonic Nanopatch Antennas. *Nano Lett.* **2014**, 14 (8), 4797-4802.

29. Tovmachenko, O. G.; Graf, C.; van den Heuvel, D. J.; van Blaaderen, A.; Gerritsen, H. C., Fluorescence Enhancement by Metal-Core/Silica-Shell Nanoparticles. *Adv. Mater.* **2006**, 18 (1), 91-95.

30. Bardhan, R.; Grady, N. K.; Cole, J. R.; Joshi, A.; Halas, N. J., Fluorescence Enhancement by Au Nanostructures: Nanoshells and Nanorods. *ACS Nano* **2009**, 3 (3), 744-752.

31. Fujita, M.; Takahashi, S.; Tanaka, Y.; Asano, T.; Noda, S., Simultaneous Inhibition and Redistribution of Spontaneous Light Emission in Photonic Crystals. *Science* **2005**, 308 (5726), 1296.

32. Ming, T.; Chen, H.; Jiang, R.; Li, Q.; Wang, J., Plasmon-Controlled Fluorescence: Beyond the Intensity Enhancement. *J. Phys. Chem. Lett.* **2012**, 3 (2), 191-202.

33. Gandra, N.; Portz, C.; Tian, L.; Tang, R.; Xu, B.; Achilefu, S.; Singamaneni, S., Probing Distance-Dependent Plasmon-Enhanced Near-Infrared Fluorescence Using Polyelectrolyte Multilayers as Dielectric Spacers. *Angew. Chem. Int. Ed.* **2014**, 53 (3), 866-870.

34. Ayala-Orozco, C.; Liu, J. G.; Knight, M. W.; Wang, Y.; Day, J. K.; Nordlander, P.; Halas, N. J., Fluorescence Enhancement of Molecules Inside a Gold Nanomatryoshka. *Nano Lett.* **2014**, 14 (5), 2926-2933.

35. Tam, F.; Goodrich, G. P.; Johnson, B. R.; Halas, N. J., Plasmonic Enhancement of Molecular Fluorescence. *Nano Lett.* **200**7, 7 (2), 496-501.

36. Giannini, V.; Fernández-Domínguez, A. I.; Heck, S. C.; Maier, S. A., Plasmonic Nanoantennas: Fundamentals and Their Use in Controlling the Radiative Properties of Nanoemitters. *Chem. Rev.* **2011**, 111 (6), 3888-3912.

37. Gu, Y.; Wang, L.; Ren, P.; Zhang, J.; Zhang, T.; Martin, O. J. F.; Gong, Q., Surface-Plasmon-Induced Modification on the Spontaneous Emission Spectrum via Subwavelength-Confined Anisotropic Purcell Factor. *Nano Lett.* **2012**, 12 (5), 2488-2493.

38. Ming, T.; Zhao, L.; Chen, H.; Woo, K. C.; Wang, J.; Lin, H.-Q., Experimental Evidence of Plasmophores: Plasmon-Directed Polarized Emission from Gold Nanorod–Fluorophore Hybrid Nanostructures. *Nano Lett.* **2011**, 11 (6), 2296-2303.

39. Kinkhabwala, A.; Yu, Z.; Fan, S.; Avlasevich, Y.; Müllen, K.; Moerner, W. E., Large single-molecule fluorescence enhancements produced by a bowtie nanoantenna. *Nat. Photonics* **2009**, 3, 654.

40. Miroshnichenko, A. E.; Flach, S.; Kivshar, Y. S., Fano resonances in nanoscale structures. *Rev. Mod. Phys.* 2010, 82 (3), 2257-2298.

41. Fan, J. A.; Wu, C.; Bao, K.; Bao, J.; Bardhan, R.; Halas, N. J.; Manoharan, V. N.; Nordlander, P.; Shvets, G.; Capasso, F., Self-Assembled Plasmonic Nanoparticle Clusters. *Science* **2010**, 328 (5982), 1135.

42. Hao, F.; Sonnefraud, Y.; Dorpe, P. V.; Maier, S. A.; Halas, N. J.; Nordlander, P., Symmetry Breaking in Plasmonic Nanocavities: Subradiant LSPR Sensing and a Tunable Fano Resonance. *Nano Lett.* **2008**, 8 (11), 3983-3988.

43. Shafiei, F.; Monticone, F.; Le, K. Q.; Liu, X.-X.; Hartsfield, T.; Alù, A.; Li, X., A subwavelength plasmonic metamolecule exhibiting magnetic-based optical Fano resonance. *Nat. Nanotechnol.* **2013**, 8, 95.

44. Törmä, P.; Barnes, W. L., Strong coupling between surface plasmon polaritons and emitters: a review. *Rep. Prog. Phys.* **2015**, 78 (1), 013901.

45. Bellessa, J.; Bonnand, C.; Plenet, J. C.; Mugnier, J., Strong Coupling between Surface Plasmons and Excitons in an Organic Semiconductor. *Phys. Rev. Lett.* **2004**, 93 (3), 036404.

46. Chikkaraddy, R.; de Nijs, B.; Benz, F.; Barrow, S. J.; Scherman, O. A.; Rosta, E.; Demetriadou, A.; Fox, P.; Hess, O.; Baumberg, J. J., Single-molecule strong coupling at room temperature in plasmonic nanocavities. *Nature* **2016**, 535, 127.

Chapter 2

1. Liu, G. L.; Long, Y.-T.; Choi, Y.; Kang, T.; Lee, L. P., Quantized plasmon quenching dips nanospectroscopy via plasmon resonance energy transfer. *Nat. Methods* **2007**, 4 (12), 1015-1017.

2. Choi, Y.; Kang, T.; Lee, L. P., Plasmon Resonance Energy Transfer (PRET)-based Molecular Imaging of Cytochrome c in Living Cells. *Nano Lett.* **2009**, 9 (1), 85-90.

3. Choi, Y.; Park, Y.; Kang, T.; Lee, L. P., Selective and sensitive detection of metal ions by plasmonic resonance energy transfer-based nanospectroscopy. *Nat. Nanotechnol.* **2009**, 4 (11), 742-746.

4. Li, J.; Cushing, S. K.; Meng, F.; Senty, T. R.; Bristow, A. D.; Wu, N., Plasmon-induced resonance energy transfer for solar energy conversion. *Nat. Photonics* **2015**, 9 (9), 601-607.

5. Cushing, S. K.; Li, J.; Meng, F.; Senty, T. R.; Suri, S.; Zhi, M.; Li, M.; Bristow, A. D.; Wu, N., Photocatalytic Activity Enhanced by Plasmonic Resonant Energy Transfer from Metal to Semiconductor. *J. Am. Chem. Soc.* **2012**, 134 (36), 15033-15041.

6. Cushing, S. K.; Li, J.; Bright, J.; Yost, B. T.; Zheng, P.; Bristow, A. D.; Wu, N., Controlling Plasmon-Induced Resonance Energy Transfer and Hot Electron Injection Processes in Metal@TiO_2 Core–Shell Nanoparticles. *J. Phys. Chem. C* **2015**, 119 (28), 16239-16244.

7. Li, J.; Cushing, S. K.; Zheng, P.; Meng, F.; Chu, D.; Wu, N., Plasmon-induced photonic and energy-transfer enhancement of solar water splitting by a hematite nanorod array. *Nat. Commun.* **2013**, 4, 2651.

8. Jain, P. K.; Lee, K. S.; El-Sayed, I. H.; El-Sayed, M. A., Calculated Absorption and Scattering Properties of Gold Nanoparticles of Different Size, Shape, and Composition: Applications in Biological Imaging and Biomedicine. *J. Phys. Chem. B* **2006**, 110 (14), 7238-7248.

9. Hu, M.; Chen, J.; Li, Z.-Y.; Au, L.; Hartland, G. V.; Li, X.; Marquez, M.; Xia, Y., Gold nanostructures: engineering their plasmonic properties for biomedical applications. *Chem. Soc. Rev*. **2006**, 35 (11), 1084-1094.

10. Chen, H.; Shao, L.; Li, Q.; Wang, J., Gold nanorods and their plasmonic properties. *Chem. Soc. Rev.* **2013**, 42 (7), 2679-2724.

11. Yun, C. S.; Javier, A.; Jennings, T.; Fisher, M.; Hira, S.; Peterson, S.; Hopkins, B.; Reich, N. O.; Strouse, G. F., Nanometal Surface Energy Transfer in Optical Rulers, Breaking the FRET Barrier. *J. Am. Chem. Soc.* **2005**, 127 (9), 3115-3119.

12. Clapp, A. R.; Medintz, I. L.; Mattoussi, H., Förster Resonance Energy Transfer Investigations Using Quantum-Dot Fluorophores. *ChemPhysChem* **2006**, 7 (1), 47-57.

13. Perillo, E. P.; Liu, Y.-L.; Huynh, K.; Liu, C.; Chou, C.-K.; Hung, M.-C.; Yeh, H.-C.; Dunn, A. K., Deep and high-resolution three-dimensional tracking of single particles using nonlinear and multiplexed illumination. *Nat. Commun.* **2015**, 6 (7874).

14. Warren, S. C.; A. M., Alibhai, D.; J. Kelly, D.; Talbot, C.; Alexandrov, Y.; Munro, I.; Katan, M.; Dunsby, C.; French, P. M. W., Rapid Global Fitting of Large Fluorescence Lifetime Imaging Microscopy Datasets, *PLoS ONE* **2013**, 8, e70687.

15. Sönnichsen, C.; Franzl, T.; Wilk, T.; von Plessen, G.; Feldmann, J.; Wilson, O.; Mulvaney, P., Drastic Reduction of Plasmon Damping in Gold Nanorods. *Phys. Rev. Lett.* **2002**, 88 (7), 077402.

16. Ringe, E.; Sharma, B.; Henry, A.-I.; Marks, L. D.; Van Duyne, R. P., Single nanoparticle plasmonics. *Phys. Chem. Chem. Phys.* **2013**, 15 (12), 4110-4129.

17. Rajeeva, B. B.; Hernandez, D. S.; Wang, M.; Perillo, E.; Lin, L.; Scarabelli, L.; Pingali, B.; Liz-Marzán, L. M.; Dunn, A. K.; Shear, J. B.; Zheng, Y., Regioselective Localization and Tracking of Biomolecules on Single Gold Nanoparticles. *Adv. Sci.* **2015**, 2 (11), 1500232.

18. Ni, W.; Ambjörnsson, T.; Apell, S. P.; Chen, H.; Wang, J., Observing Plasmonic−Molecular Resonance Coupling on Single Gold Nanorods. *Nano Lett.* **2010**, 10 (1), 77-84.

19. Anker, J. N.; Hall, W. P.; Lyandres, O.; Shah, N. C.; Zhao, J.; Van Duyne, R. P., Biosensing with plasmonic nanosensors. *Nat. Mater.* **2008**, 7 (6), 442-453.

20. Ming, T.; Zhao, L.; Yang, Z.; Chen, H.; Sun, L.; Wang, J.; Yan, C., Strong Polarization Dependence of Plasmon-Enhanced Fluorescence on Single Gold Nanorods. *Nano Lett.* **2009**, 9 (11), 3896-3903.

21. Ming, T.; Zhao, L.; Xiao, M.; Wang, J., Resonance-Coupling-Based Plasmonic Switches. *Small* **2010**, 6 (22), 2514-2519.

22. McFarland, A. D.; Van Duyne, R. P., Single Silver Nanoparticles as Real-Time Optical Sensors with Zeptomole Sensitivity. *Nano Lett.* **2003**, 3 (8), 1057-1062.

23. Sherry, L. J.; Jin, R.; Mirkin, C. A.; Schatz, G. C.; Van Duyne, R. P., Localized Surface Plasmon Resonance Spectroscopy of Single Silver Triangular Nanoprisms. *Nano Lett.* **2006**, 6 (9), 2060-2065.

24. Sherry, L. J.; Chang, S.-H.; Schatz, G. C.; Van Duyne, R. P.; Wiley, B. J.; Xia, Y., Localized Surface Plasmon Resonance Spectroscopy of Single Silver Nanocubes. *Nano Lett.* **2005**, 5 (10), 2034-2038.

25. Link, S.; El-Sayed, M. A., Size and Temperature Dependence of the Plasmon Absorption of Colloidal Gold Nanoparticles. *J. Phys. Chem. B* **1999**, 103 (21), 4212-4217.

26. Dintinger, J.; Klein, S.; Ebbesen, T. W., Molecule–Surface Plasmon Interactions in Hole Arrays: Enhanced Absorption, Refractive Index Changes, and All-Optical Switching. *Adv. Mater.* **2006**, 18 (10), 1267-1270.

27. Zheng, Y. B.; Kiraly, B.; Cheunkar, S.; Huang, T. J.; Weiss, P. S., Incident-Angle-Modulated Molecular Plasmonic Switches: A Case of Weak Exciton–Plasmon Coupling. *Nano Lett.* **2011**, 11 (5), 2061-2065.

28. Sapsford, K. E.; Berti, L.; Medintz, I. L., Materials for Fluorescence Resonance Energy Transfer Analysis: Beyond Traditional Donor–Acceptor Combinations. *Angew. Chem. Int. Ed.* **2006**, 45 (28), 4562-4589.

29. Kagan, C. R.; Murray, C. B.; Nirmal, M.; Bawendi, M. G., Electronic Energy Transfer in CdSe Quantum Dot Solids. *Phys. Rev. Lett.* **1996**, 76 (9), 1517-1520.

30. Anger, P.; Bharadwaj, P.; Novotny, L., Enhancement and Quenching of Single-Molecule Fluorescence. *Phys. Rev. Lett.* **2006**, 96 (11), 113002.

31. Rose, A.; Hoang, T. B.; McGuire, F.; Mock, J. J.; Ciracì, C.; Smith, D. R.; Mikkelsen, M. H., Control of Radiative Processes Using Tunable Plasmonic Nanopatch Antennas. *Nano Lett.* **2014**, 14 (8), 4797-4802.

32. Akselrod, G. M.; Argyropoulos, C.; Hoang, T. B.; Ciracì, C.; Fang, C.; Huang, J.; Smith, D. R.; Mikkelsen, M. H., Probing the mechanisms of large Purcell enhancement in plasmonic nanoantennas. *Nat. Photonics* **2014**, 8 (11), 835-840.

33. Sen, T.; Sadhu, S.; Patra, A., Surface energy transfer from rhodamine 6G to gold nanoparticles: A spectroscopic ruler. *Appl. Phys. Lett.* **2007**, 91 (4), 043104.

34. Griffin, J.; Singh, A. K.; Senapati, D.; Rhodes, P.; Mitchell, K.; Robinson, B.; Yu, E.; Ray, P. C., Size- and Distance-Dependent Nanoparticle Surface-Energy Transfer (NSET) Method for Selective Sensing of Hepatitis C Virus RNA. Chem. Eur. J. **2009**, 15 (2), 342-351.

Chapter 3

1. Mak, K. F.; Shan, J., Photonics and optoelectronics of 2D semiconductor transition metal dichalcogenides. *Nat. Photonics* **2016**, 10 (4), 216-226.

2. Xia, F.; Wang, H.; Xiao, D.; Dubey, M.; Ramasubramaniam, A., Two-dimensional material nanophotonics. *Nat. Photonics* **2014**, 8 (12), 899-907.

3. Wang, Q. H.; Kalantar-Zadeh, K.; Kis, A.; Coleman, J. N.; Strano, M. S., Electronics and optoelectronics of two-dimensional transition metal dichalcogenides. *Nat. Nanotechnol.* **2012**, 7 (11), 699-712.

4. Gupta, A.; Sakthivel, T.; Seal, S., Recent development in 2D materials beyond graphene. *Prog. Mater. Sci.* **2015**, 73, 44-126.

5. Jariwala, D.; Sangwan, V. K.; Lauhon, L. J.; Marks, T. J.; Hersam, M. C., Emerging Device Applications for Semiconducting Two-Dimensional Transition Metal Dichalcogenides. *ACS Nano* **2014**, 8 (2), 1102-1120.

6. Lopez-Sanchez, O.; Lembke, D.; Kayci, M.; Radenovic, A.; Kis, A., Ultrasensitive photodetectors based on monolayer MoS_2. *Nat. Nanotechnol.* **2013**, 8 (7), 497-501.

7. Choi, M. S.; Qu, D.; Lee, D.; Liu, X.; Watanabe, K.; Taniguchi, T.; Yoo, W. J., Lateral MoS_2 p–n Junction Formed by Chemical Doping for Use in High-Performance Optoelectronics. *ACS Nano* **2014**, 8 (9), 9332-9340.

8. Mak, K. F.; Lee, C.; Hone, J.; Shan, J.; Heinz, T. F., Atomically Thin MoS_2: A New Direct-Gap Semiconductor. *Phys. Rev. Lett.* **2010**, 105 (13), 136805.

9. Sundaram, R. S.; Engel, M.; Lombardo, A.; Krupke, R.; Ferrari, A. C.; Avouris, P.; Steiner, M., Electroluminescence in Single Layer MoS_2. *Nano Lett.* **2013**, 13 (4), 1416-1421.

10. Mak, K. F.; He, K.; Shan, J.; Heinz, T. F., Control of valley polarization in monolayer MoS_2 by optical helicity. *Nat. Nanotechnol.* **2012**, 7 (8), 494-498.

11. Lin, Y.; Ling, X.; Yu, L.; Huang, S.; Hsu, A. L.; Lee, Y.-H.; Kong, J.; Dresselhaus, M. S.; Palacios, T., Dielectric Screening of Excitons and Trions in Single-Layer MoS_2. *Nano Lett.* **2014**, 14 (10), 5569-5576.

12. Li, Z.; Xiao, Y.; Gong, Y.; Wang, Z.; Kang, Y.; Zu, S.; Ajayan, P. M.; Nordlander, P.; Fang, Z., Active Light Control of the MoS_2 Monolayer Exciton Binding Energy. *ACS Nano* **2015**, 9 (10), 10158-10164.

13. Liu, J.-T.; Wang, T.-B.; Li, X.-J.; Liu, N.-H., Enhanced absorption of monolayer MoS_2 with resonant back reflector. *J. Appl. Phys.* **2014**, 115 (19), 193511.

14. Sobhani, A.; Lauchner, A.; Najmaei, S.; Ayala-Orozco, C.; Wen, F.; Lou, J.; Halas, N. J., Enhancing the photocurrent and photoluminescence of single crystal monolayer MoS_2 with resonant plasmonic nanoshells. *Appl. Phys. Lett.* **2014**, 104 (3), 031112.

15. Kern, J.; Trügler, A.; Niehues, I.; Ewering, J.; Schmidt, R.; Schneider, R.; Najmaei, S.; George, A.; Zhang, J.; Lou, J.; Hohenester, U.; Michaelis de Vasconcellos, S.; Bratschitsch, R., Nanoantenna-Enhanced Light–Matter Interaction in Atomically Thin WS_2. *ACS Photonics* **2015**, 2 (9), 1260-1265.

16. Wang, S.; Li, S.; Chervy, T.; Shalabney, A.; Azzini, S.; Orgiu, E.; Hutchison, J. A.; Genet, C.; Samorì, P.; Ebbesen, T. W., Coherent Coupling of WS2 Monolayers with Metallic Photonic Nanostructures at Room Temperature. *Nano Lett.* **2016**, 16 (7), 4368-4374.

17. Liu, W.; Lee, B.; Naylor, C. H.; Ee, H.-S.; Park, J.; Johnson, A. T. C.; Agarwal, R., Strong Exciton–Plasmon Coupling in MoS2 Coupled with Plasmonic Lattice. *Nano Lett.* **2016**, 16 (2), 1262-1269.

18. Lee, B.; Park, J.; Han, G. H.; Ee, H.-S.; Naylor, C. H.; Liu, W.; Johnson, A. T. C.; Agarwal, R., Fano Resonance and Spectrally Modified Photoluminescence Enhancement in Monolayer MoS_2 Integrated with Plasmonic Nanoantenna Array. *Nano Lett.* **2015**, 15 (5), 3646-3653.

19. Najmaei, S.; Mlayah, A.; Arbouet, A.; Girard, C.; Léotin, J.; Lou, J., Plasmonic Pumping of Excitonic Photoluminescence in Hybrid MoS_2–Au Nanostructures. *ACS Nano* **2014**, 8 (12), 12682-12689.

20. Zhou, H.; Yu, F.; Guo, C. F.; Wang, Z.; Lan, Y.; Wang, G.; Fang, Z.; Liu, Y.; Chen, S.; Sun, L.; Ren, Z., Well-oriented epitaxial gold nanotriangles and bowties on MoS_2 for surface-enhanced Raman scattering. *Nanoscale* **2015**, 7 (20), 9153-9157.

21. Kang, Y.; Gong, Y.; Hu, Z.; Li, Z.; Qiu, Z.; Zhu, X.; Ajayan, P. M.; Fang, Z., Plasmonic hot electron enhanced MoS_2 photocatalysis in hydrogen evolution. *Nanoscale* **2015**, 7 (10), 4482-4488.

22. Zhang, P.; Fujitsuka, M.; Majima, T., Hot electron-driven hydrogen evolution using anisotropic gold nanostructure assembled monolayer MoS_2. *Nanoscale* **2017**, 9 (4), 1520-1526.

23. Kang, Y.; Najmaei, S.; Liu, Z.; Bao, Y.; Wang, Y.; Zhu, X.; Halas, N. J.; Nordlander, P.; Ajayan, P. M.; Lou, J.; Fang, Z., Plasmonic Hot Electron Induced Structural Phase Transition in a MoS_2 Monolayer. *Adv. Mater.* **2014**, 26 (37), 6467-6471.

24. Li, Z.; Li, Y.; Han, T.; Wang, X.; Yu, Y.; Tay, B.; Liu, Z.; Fang, Z., Tailoring MoS_2 Exciton–Plasmon Interaction by Optical Spin–Orbit Coupling. *ACS Nano* **2017**, 11 (2), 1165-1171.

25. Yu, Y.; Ji, Z.; Zu, S.; Du, B.; Kang, Y.; Li, Z.; Zhou, Z.; Shi, K.; Fang, Z., Ultrafast Plasmonic Hot Electron Transfer in Au Nanoantenna/MoS_2 Heterostructures. *Adv. Funct. Mater.* **2016**, 26 (35), 6394-6401.

26. Mathieu, H.; Lefebvre, P.; Christol, P., Simple analytical method for calculating exciton binding energies in semiconductor quantum wells. *Phys. Rev. B* **1992**, 46 (7), 4092-4101.

27. He, X.-F., Excitons in anisotropic solids: The model of fractional-dimensional space. *Phys. Rev. B* **1991**, 43 (3), 2063-2069.

28. Naeem, A.; Masia, F.; Christodoulou, S.; Moreels, I.; Borri, P.; Langbein, W., Giant exciton oscillator strength and radiatively limited dephasing in two-dimensional platelets. *Phys. Rev. B* **2015**, 91 (12), 121302.

29. Meer, B. W. v. d., Förster Theory. In FRET – Förster Resonance Energy Transfer: From Theory to Applications, First Edition., Igor Medintz, N. H., Ed. Wiley-VCH Verlag GmbH & Co. KGaA.: 2014; pp 23-62.

30. Mao, N.; Chen, Y.; Liu, D.; Zhang, J.; Xie, L., Solvatochromic Effect on the Photoluminescence of MoS_2 Monolayers. *Small* **2013**, 9 (8), 1312-1315.

31. Sanvitto, D.; Pulizzi, F.; Shields, A. J.; Christianen, P. C. M.; Holmes, S. N.; Simmons, M. Y.; Ritchie, D. A.; Maan, J. C.; Pepper, M., Observation of Charge Transport by Negatively Charged Excitons. *Science* **2001**, 294 (5543), 837.

32. Lui, C. H.; Frenzel, A. J.; Pilon, D. V.; Lee, Y. H.; Ling, X.; Akselrod, G. M.; Kong, J.; Gedik, N., Trion-Induced Negative Photoconductivity in Monolayer MoS_2. *Phys. Rev. Lett.* **2014**, 113 (16), 166801.

33. Mak, K. F.; He, K.; Lee, C.; Lee, G. H.; Hone, J.; Heinz, T. F.; Shan, J., Tightly bound trions in monolayer MoS_2. *Nat. Mater.* **2013**, 12 (3), 207-211.

34. Scarabelli, L.; Coronado-Puchau, M.; Giner-Casares, J. J.; Langer, J.; Liz-Marzán, L. M., Monodisperse Gold Nanotriangles: Size Control, Large-Scale Self-Assembly, and Performance in Surface-Enhanced Raman Scattering. *ACS Nano* **2014**, 8 (6), 5833-5842.

35. Johnson, P. B.; Christy, R. W., Optical Constants of the Noble Metals. *Phys. Rev. B* **1972**, 6 (12), 4370-4379.

36. Clapp, A. R.; Medintz, I. L.; Mauro, J. M.; Fisher, B. R.; Bawendi, M. G.; Mattoussi, H., Fluorescence Resonance Energy Transfer Between Quantum Dot Donors and Dye-Labeled Protein Acceptors. *J. Am. Chem. Soc.* **2004**, 126 (1), 301-310.

37. Li, J.; Cushing, S. K.; Meng, F.; Senty, T. R.; Bristow, A. D.; Wu, N., Plasmon-induced resonance energy transfer for solar energy conversion. *Nat. Photonics* **2015**, 9 (9), 601-607.

38. Losquin, A.; Zagonel, L. F.; Myroshnychenko, V.; Rodríguez-González, B.; Tencé, M.; Scarabelli, L.; Förstner, J.; Liz-Marzán, L. M.; García de Abajo, F. J.; Stéphan, O.; Kociak, M., Unveiling Nanometer Scale Extinction and Scattering Phenomena through Combined Electron Energy Loss Spectroscopy and Cathodoluminescence Measurements. *Nano Lett.* **2015**, 15 (2), 1229-1237.

39. Scarabelli, L.; Sánchez-Iglesias, A.; Pérez-Juste, J.; Liz-Marzán, L. M., A "Tips and Tricks" Practical Guide to the Synthesis of Gold Nanorods. *J. Phys. Chem. Lett.* **2015**, 6 (21), 4270-4279.

40. Gole, A.; Murphy, C. J., Seed-Mediated Synthesis of Gold Nanorods: Role of the Size and Nature of the Seed. *Chem. Mater.* **2004**, 16 (19), 3633-3640.

41. Pérez-Juste, J.; Pastoriza-Santos, I.; Liz-Marzán, L. M.; Mulvaney, P., Gold nanorods: Synthesis, characterization and applications. *Coord. Chem. Rev.* **2005**, 249 (17–18), 1870-1901.

42. Chen, H.; Shao, L.; Li, Q.; Wang, J., Gold nanorods and their plasmonic properties. *Chem. Soc. Rev.* **2013**, 42 (7), 2679-2724.

43. Eustis, S.; El-Sayed, M. A., Why gold nanoparticles are more precious than pretty gold: Noble metal surface plasmon resonance and its enhancement of the radiative and nonradiative properties of nanocrystals of different shapes. *Chem. Soc. Rev.* **2006**, 35 (3), 209-217.

44. Hu, M.; Chen, J.; Li, Z.-Y.; Au, L.; Hartland, G. V.; Li, X.; Marquez, M.; Xia, Y., Gold nanostructures: engineering their plasmonic properties for biomedical applications. *Chem. Soc. Rev.* **2006**, 35 (11), 1084-1094.

45. Komsa, H.-P.; Krasheninnikov, A. V., Effects of confinement and environment on the electronic structure and exciton binding energy of MoS_2 from first principles. *Phys. Rev. B* **2012**, 86 (24), 241201.

46. Zhao, L.; Ming, T.; Chen, H.; Liang, Y.; Wang, J., Plasmon-induced modulation of the emission spectra of the fluorescent molecules near gold nanorods. *Nanoscale* **2011**, 3 (9), 3849-3859.

47. Jiang, R.; Li, B.; Fang, C.; Wang, J., Metal/Semiconductor Hybrid Nanostructures for Plasmon-Enhanced Applications. *Adv. Mater.* **2014**, 26 (31), 5274-5309.

48. Choi, Y.; Kang, T.; Lee, L. P., Plasmon Resonance Energy Transfer (PRET)-based Molecular Imaging of Cytochrome c in Living Cells. *Nano Lett.* **2009**, 9 (1), 85-90.

49. Liu, G. L.; Long, Y.-T.; Choi, Y.; Kang, T.; Lee, L. P., Quantized plasmon quenching dips nanospectroscopy via plasmon resonance energy transfer. *Nat. Methods* **2007**, 4 (12), 1015-1017.

50. Li, H.; Lu, G.; Yin, Z.; He, Q.; Li, H.; Zhang, Q.; Zhang, H., Optical Identification of Single- and Few-Layer MoS_2 Sheets. *Small* **2012**, 8 (5), 682-686.

51. Li, H.; Zhang, Q.; Yap, C. C. R.; Tay, B. K.; Edwin, T. H. T.; Olivier, A.; Baillargeat, D., From Bulk to Monolayer MoS2: Evolution of Raman Scattering. *Adv. Funct. Mater.* **2012**, 22 (7), 1385-1390.

52. Rao, C. N. R.; Ramakrishna Matte, H. S. S.; Maitra, U., Graphene Analogues of Inorganic Layered Materials. *Angew. Chem. Int. Ed.* **2013**, 52 (50), 13162-13185.

53. Terrones, H.; Corro, E. D.; Feng, S.; Poumirol, J. M.; Rhodes, D.; Smirnov, D.; Pradhan, N. R.; Lin, Z.; Nguyen, M. A. T.; Elías, A. L.; Mallouk, T. E.; Balicas, L.; Pimenta, M. A.; Terrones, M., New First Order Raman-active Modes in Few Layered Transition Metal Dichalcogenides. *Sc*i. Rep. **2014**, 4, 4215.

54. Lin, Z.; Thee, M. T.; Elías, A. L.; Feng, S.; Zhou, C.; Fujisawa, K.; Perea-López, N.; Carozo, V.; Terrones, H.; Terrones, M., Facile synthesis of MoS_2 and MoxW1-xS2 triangular monolayers. *APL Mater.* **2014**, 2 (9), 092514.

55. Mouri, S.; Miyauchi, Y.; Matsuda, K., Tunable Photoluminescence of Monolayer MoS2 via Chemical Doping. *Nano Lett.* **2013**, 13 (12), 5944-5948.

56. Soklaski, R.; Liang, Y.; Yang, L., Temperature effect on optical spectra of monolayer molybdenum disulfide. *Appl. Phys. Lett.* **2014**, 104 (19), 193110.

57. Anger, P.; Bharadwaj, P.; Novotny, L., Enhancement and Quenching of Single-Molecule Fluorescence. *Phys. Rev. Lett.* **2006**, 96 (11), 113002.

58. Pelton, M., Modified spontaneous emission in nanophotonic structures. *Nat. Photonics* **2015**, 9 (7), 427-435.

59. Wang, M.; Bangalore Rajeeva, B.; Scarabelli, L.; Perillo, E. P.; Dunn, A. K.; Liz-Marzán, L. M.; Zheng, Y., Molecular-Fluorescence Enhancement via Blue-Shifted Plasmon-Induced Resonance Energy Transfer. *J. Phys. Chem. C* **2016**, 120 (27), 14820-14827.

60. Shi, H.; Yan, R.; Bertolazzi, S.; Brivio, J.; Gao, B.; Kis, A.; Jena, D.; Xing, H. G.; Huang, L., Exciton Dynamics in Suspended Monolayer and Few-Layer MoS_2 2D Crystals. *ACS Nano* **2013**, 7 (2), 1072-1080.

61. Sönnichsen, C.; Franzl, T.; Wilk, T.; von Plessen, G.; Feldmann, J.; Wilson, O.; Mulvaney, P., Drastic Reduction of Plasmon Damping in Gold Nanorods. *Phys. Rev. Lett.* **2002**, 88 (7), 077402.

62. Zhang, W.; Govorov, A. O.; Bryant, G. W., Semiconductor-Metal Nanoparticle Molecules: Hybrid Excitons and the Nonlinear Fano Effect. *Phys. Rev. Lett.* **2006**, 97 (14), 146804.

63. Miroshnichenko, A. E.; Flach, S.; Kivshar, Y. S., Fano resonances in nanoscale structures. *Rev. Mod. Phys.* **2010**, 82 (3), 2257-2298.

64. Anker, J. N.; Hall, W. P.; Lyandres, O.; Shah, N. C.; Zhao, J.; Van Duyne, R. P., Biosensing with plasmonic nanosensors. *Nat. Mater.* **2008**, 7 (6), 442-453.

65. Maier, S. A.; Atwater, H. A., Plasmonics: Localization and guiding of electromagnetic energy in metal/dielectric structures. *J. Appl. Phys.* **2005**, 98 (1), 011101.

Chapter 4

1. Englund, D.; Fattal, D.; Waks, E.; Solomon, G.; Zhang, B.; Nakaoka, T.; Arakawa, Y.; Yamamoto, Y.; Vučković, J., Controlling the Spontaneous Emission Rate of Single Quantum Dots in a Two-Dimensional Photonic Crystal. *Phys. Rev. Lett.* **2005**, 95 (1), 013904.

2. Hennessy, K.; Badolato, A.; Winger, M.; Gerace, D.; Atature, M.; Gulde, S.; Falt, S.; Hu, E. L.; Imamoglu, A., Quantum nature of a strongly coupled single quantum dot-cavity system. *Nature* **2007**, 445 (7130), 896-899.

3. Press, D.; Götzinger, S.; Reitzenstein, S.; Hofmann, C.; Löffler, A.; Kamp, M.; Forchel, A.; Yamamoto, Y., Photon Antibunching from a Single Quantum-Dot-Microcavity System in the Strong Coupling Regime. *Phys. Rev. Lett.* **2007**, 98 (11), 117402.

4. Törmä, P.; Barnes, W. L., Strong coupling between surface plasmon polaritons and emitters: a review. *Rep. Prog. Phys.* **2015**, 78 (1), 013901.

5. Chikkaraddy, R.; de Nijs, B.; Benz, F.; Barrow, S. J.; Scherman, O. A.; Rosta, E.; Demetriadou, A.; Fox, P.; Hess, O.; Baumberg, J. J., Single-molecule strong coupling at room temperature in plasmonic nanocavities. *Nature* **2016**, 535, 127.

6. Konrad, A.; Kern, A. M.; Brecht, M.; Meixner, A. J., Strong and Coherent Coupling of a Plasmonic Nanoparticle to a Subwavelength Fabry–Pérot Resonator. *Nano Lett.* **2015**, 15, 4423-4428.

7. Weisbuch, C.; Nishioka, M.; Ishikawa, A.; Arakawa, Y., Observation of the coupled exciton-photon mode splitting in a semiconductor quantum microcavity. *Phys. Rev. Lett.* **1992**, 69 (23), 3314-3317.

8. Tassone, F.; Yamamoto, Y., Exciton-exciton scattering dynamics in a semiconductor microcavity and stimulated scattering into polaritons. *Phys. Rev. B* **1999**, 59 (16), 10830-10842.

9. Christopoulos, S.; von Högersthal, G. B. H.; Grundy, A. J. D.; Lagoudakis, P. G.; Kavokin, A. V.; Baumberg, J. J.; Christmann, G.; Butté, R.; Feltin, E.; Carlin, J. F.; Grandjean, N., Room-Temperature Polariton Lasing in Semiconductor Microcavities. *Phys. Rev. Lett.* **2007**, 98 (12), 126405.

10. Noda, S.; Fujita, M.; Asano, T., Spontaneous-emission control by photonic crystals and nanocavities. *Nat. Photonics* **2007**, 1 (8), 449-458.

11. Volz, T.; Reinhard, A.; Winger, M.; Badolato, A.; Hennessy, K. J.; Hu, E. L.; Imamoglu, A., Ultrafast all-optical switching by single photons. *Nat. Photonics* **2012**, 6 (9), 605-609.

12. Vasa, P.; Pomraenke, R.; Cirmi, G.; De Re, E.; Wang, W.; Schwieger, S.; Leipold, D.; Runge, E.; Cerullo, G.; Lienau, C., Ultrafast Manipulation of Strong Coupling in Metal−Molecular Aggregate Hybrid Nanostructures. *ACS Nano* **2010**, 4 (12), 7559-7565.

13. Gunter, G.; Anappara, A. A.; Hees, J.; Sell, A.; Biasiol, G.; Sorba, L.; De Liberato, S.; Ciuti, C.; Tredicucci, A.; Leitenstorfer, A.; Huber, R., Sub-cycle switch-on of ultrastrong light-Matter interaction. *Nature* **2009**, 458 (7235), 178-181.

14. Daskalakis, K. S.; Maier, S. A.; Murray, R.; Kéna-Cohen, S., Nonlinear interactions in an organic polariton condensate. *Nat. Mater.* **2014**, 13 (3), 271-278.

15. Plumhof, J. D.; Stöferle, T.; Mai, L.; Scherf, U.; Mahrt, R. F., Room-temperature Bose–Einstein condensation of cavity exciton–polaritons in a polymer. *Nat. Mater.* **2014**, 13 (3), 247-252.

16. Lidzey, D. G.; Bradley, D. D. C.; Virgili, T.; Armitage, A.; Skolnick, M. S.; Walker, S., Room Temperature Polariton Emission from Strongly Coupled Organic Semiconductor Microcavities. *Phys. Rev. Lett.* **1999**, 82 (16), 3316-3319.

17. van Vugt, L. K.; Rühle, S.; Ravindran, P.; Gerritsen, H. C.; Kuipers, L.; Vanmaekelbergh, D., Exciton Polaritons Confined in a ZnO Nanowire Cavity. *Phys. Rev. Lett.* **2006**, 97 (14), 147401.

18. Takazawa, K.; Inoue, J.-i.; Mitsuishi, K.; Takamasu, T., Fraction of a Millimeter Propagation of Exciton Polaritons in Photoexcited Nanofibers of Organic Dye. *Phys. Rev. Lett.* **2010**, 105 (6), 067401.

19. Sugawara, Y.; Kelf, T. A.; Baumberg, J. J.; Abdelsalam, M. E.; Bartlett, P. N., Strong Coupling between Localized Plasmons and Organic Excitons in Metal Nanovoids. *Phys. Rev. Lett.* **2006**, 97 (26), 266808.

20. Fofang, N. T.; Park, T.-H.; Neumann, O.; Mirin, N. A.; Nordlander, P.; Halas, N. J., Plexcitonic Nanoparticles: Plasmon−Exciton Coupling in Nanoshell−J-Aggregate Complexes. *Nano Lett.* **2008**, 8 (10), 3481-3487.

21. Schlather, A. E.; Large, N.; Urban, A. S.; Nordlander, P.; Halas, N. J., Near-Field Mediated Plexcitonic Coupling and Giant Rabi Splitting in Individual Metallic Dimers. *Nano Lett.* **2013**, 13 (7), 3281-3286.

22. Väkeväinen, A. I.; Moerland, R. J.; Rekola, H. T.; Eskelinen, A. P.; Martikainen, J. P.; Kim, D. H.; Törmä, P., Plasmonic Surface Lattice Resonances at the Strong Coupling Regime. *Nano Lett.* **2013**, 14 (4), 1721-1727.

23. Eizner, E.; Avayu, O.; Ditcovski, R.; Ellenbogen, T., Aluminum Nanoantenna Complexes for Strong Coupling between Excitons and Localized Surface Plasmons. *Nano Lett.* **2015**, 15 (9), 6215-6221.

24. Todisco, F.; D'Agostino, S.; Esposito, M.; Fernández-Domínguez, A. I.; De Giorgi, M.; Ballarini, D.; Dominici, L.; Tarantini, I.; Cuscuná, M.; Della Sala, F.; Gigli, G.; Sanvitto, D., Exciton–Plasmon Coupling Enhancement via Metal Oxidation. *ACS Nano* **2015**, 9 (10), 9691-9699.

25. Pirruccio, G.; Ramezani, M.; Rodriguez, S. R.-K.; Rivas, J. G., Coherent Control of the Optical Absorption in a Plasmonic Lattice Coupled to a Luminescent Layer. *Phys. Rev. Lett*. **2016**, 116 (10), 103002.

26. Zengin, G.; Gschneidtner, T.; Verre, R.; Shao, L.; Antosiewicz, T. J.; Moth-Poulsen, K.; Käll, M.; Shegai, T., Evaluating Conditions for Strong Coupling between Nanoparticle Plasmons and Organic Dyes Using Scattering and Absorption Spectroscopy. *J. Phys. Chem. C* **2016**, 120 (37), 20588–20596.

27. Zhou, N.; Yuan, M.; Gao, Y.; Li, D.; Yang, D., Silver Nanoshell Plasmonically Controlled Emission of Semiconductor Quantum Dots in the Strong Coupling Regime. *ACS Nano* **2016**, 10, 4154-4163.

28. Shi, L.; Hakala, T. K.; Rekola, H. T.; Martikainen, J. P.; Moerland, R. J.; Törmä, P., Spatial Coherence Properties of Organic Molecules Coupled to Plasmonic Surface Lattice Resonances in the Weak and Strong Coupling Regimes. *Phys. Rev. Lett.* **2014**, 112 (15), 153002.

29. Klar, T.; Perner, M.; Grosse, S.; von Plessen, G.; Spirkl, W.; Feldmann, J., Surface-plasmon resonances in single metallic nanoparticles. *Phys. Rev. Lett.* **1998**, 80 (19), 4249-4252.

30. Bukasov, R.; Ali, T. A.; Nordlander, P.; Shumaker-Parry, J. S., Probing the plasmonic near-field of gold nanocrescent antennas. *ACS Nano* **2010**, 4 (11), 6639-6650.

31. Halas, N. J.; Lal, S.; Chang, W. S.; Link, S.; Nordlander, P., Plasmons in strongly coupled metallic nanostructures. *Chem. Rev.* **2011**, 111 (6), 3913-3961.

32. Lin, L.; Zheng, Y., Optimizing plasmonic nanoantennas via coordinated multiple coupling. *Sci. Rep.* **2015**, 5, 14788.

33. O'Brien, M. N.; Jones, M. R.; Kohlstedt, K. L.; Schatz, G. C.; Mirkin, C. A., Uniform Circular Disks With Synthetically Tailorable Diameters: Two-Dimensional Nanoparticles for Plasmonics. *Nano Lett.* **2015**, 15 (2), 1012-1017.

34. Fan, J. A.; Bao, K.; Sun, L.; Bao, J.; Manoharan, V. N.; Nordlander, P.; Capasso, F., Plasmonic Mode Engineering with Templated Self-Assembled Nanoclusters. *Nano Lett.* **2012**, 12 (10), 5318-5324.

35. Fan, J. A.; He, Y.; Bao, K.; Wu, C.; Bao, J.; Schade, N. B.; Manoharan, V. N.; Shvets, G.; Nordlander, P.; Liu, D. R.; Capasso, F., DNA-Enabled Self-Assembly of Plasmonic Nanoclusters. *Nano Lett.* **2011**, 11 (11), 4859-4864.

36. Yao, J.; Le, A.-P.; Gray, S. K.; Moore, J. S.; Rogers, J. A.; Nuzzo, R. G., Nanostructured Plasmonic Materials: Functional Nanostructured Plasmonic Materials. *Adv. Mater.* **2010**, 22 (10), 1102–1110.

37. Russell, K. J.; Yeung, K. Y. M.; Hu, E., Measuring the mode volume of plasmonic nanocavities using coupled optical emitters. *Phys. Rev. B* **2012**, 85 (24), 245445.

38. Russell, K. J.; Hu, E. L., Gap-mode plasmonic nanocavity. *Appl. Phys. Lett.* **2010**, 97 (16), 163115.

39. Wurtz, G. A.; Evans, P. R.; Hendren, W.; Atkinson, R.; Dickson, W.; Pollard, R. J.; Zayats, A. V.; Harrison, W.; Bower, C., Molecular Plasmonics with Tunable Exciton−Plasmon Coupling Strength in J-Aggregate Hybridized Au Nanorod Assemblies. *Nano Lett.* **2007**, 7 (5), 1297-1303.

40. Zengin, G.; Johansson, G.; Johansson, P.; Antosiewicz, T. J.; Käll, M.; Shegai, T., Approaching the strong coupling limit in single plasmonic nanorods interacting with J-aggregates. *Sci. Rep.* **2013**, 3, 3074.

41. Trügler, A.; Hohenester, U., Strong coupling between a metallic nanoparticle and a single molecule. *Phys. Rev. B* **2008**, 77 (11), 115403.

42. Ni, W.; Ambjörnsson, T.; Apell, S. P.; Chen, H.; Wang, J., Observing Plasmonic−Molecular Resonance Coupling on Single Gold Nanorods. *Nano Lett.* **2010**, 10 (1), 77-84.

43. Zengin, G.; Wersäll, M.; Nilsson, S.; Antosiewicz, T. J.; Käll, M.; Shegai, T., Realizing Strong Light-Matter Interactions between Single-Nanoparticle Plasmons and Molecular Excitons at Ambient Conditions. *Phys. Rev. Lett.* **2015**, 114 (15), 157401.

44. Ming, T.; Zhao, L.; Xiao, M.; Wang, J., Resonance-Coupling-Based Plasmonic Switches. *Small* **2010**, 6 (22), 2514-2519.

45. Alam, M. Z.; Aitchison, J. S.; Mojahedi, M., A marriage of convenience: Hybridization of surface plasmon and dielectric waveguide modes. *Laser Photonics Rev*. **2014**, 8 (3), 394-408.

46. Christ, A.; Tikhodeev, S. G.; Gippius, N. A.; Kuhl, J.; Giessen, H., Waveguide-Plasmon Polaritons: Strong Coupling of Photonic and Electronic Resonances in a Metallic Photonic Crystal Slab. *Phys. Rev. Lett.* **2003**, 91 (18), 183901.

47. Yannopapas, V.; Paspalakis, E.; Vitanov, N. V., Electromagnetically induced transparency and slow light in an array of metallic nanoparticles. *Phys. Rev. B* **2009**, 80 (3), 035104.

48. Zentgraf, T.; Zhang, S.; Oulton, R. F.; Zhang, X., Ultranarrow coupling-induced transparency bands in hybrid plasmonic systems. *Phys. Rev. B* **2009**, 80 (19), 195415.

49. Bernal Arango, F.; Kwadrin, A.; Koenderink, A. F., Plasmonic Antennas Hybridized with Dielectric Waveguides. *ACS Nano* **2012**, 6 (11), 10156-10167.

50. Février, M.; Gogol, P.; Aassime, A.; Mégy, R.; Delacour, C.; Chelnokov, A.; Apuzzo, A.; Blaize, S.; Lourtioz, J.-M.; Dagens, B., Giant Coupling Effect between Metal Nanoparticle Chain and Optical Waveguide. *Nano Lett.* **2012**, 12 (2), 1032-1037.

51. Oulton, R. F.; Sorger, V. J.; Genov, D. A.; Pile, D. F. P.; Zhang, X., A hybrid plasmonic waveguide for subwavelength confinement and long-range propagation. *Nat. Photonics* **2008**, 2 (8), 496-500.

52. Yang, X.; Liu, Y.; Oulton, R. F.; Yin, X.; Zhang, X., Optical Forces in Hybrid Plasmonic Waveguides. *Nano Lett.* **2011**, 11 (2), 321-328.

53. Dintinger, J.; Klein, S.; Ebbesen, T. W., Molecule–Surface Plasmon Interactions in Hole Arrays: Enhanced Absorption, Refractive Index Changes, and All-Optical Switching. *Adv. Mater.* **2006**, 18 (10), 1267-1270.

54. Zheng, Y. B.; Kiraly, B.; Cheunkar, S.; Huang, T. J.; Weiss, P. S., Incident-Angle-Modulated Molecular Plasmonic Switches: A Case of Weak Exciton–Plasmon Coupling. *Nano Lett.* **2011**, 11 (5), 2061-2065.

55. Rodriguez, S. R. K.; Murai, S.; Verschuuren, M. A.; Rivas, J. G., Light-Emitting Waveguide-Plasmon Polaritons. *Phys. Rev. Lett.* **2012**, 109 (16), 166803.

56. Knight, M. W.; King, N. S.; Liu, L.; Everitt, H. O.; Nordlander, P.; Halas, N. J., Aluminum for Plasmonics. *ACS Nano* **2014**, 8 (1), 834-840.

57. Zheng, B. Y.; Wang, Y.; Nordlander, P.; Halas, N. J., Color-Selective and CMOS-Compatible Photodetection Based on Aluminum Plasmonics. *Adv. Mater.* **2014**, 26 (36), 6318-6323.

58. Olson, J.; Manjavacas, A.; Basu, T.; Huang, D.; Schlather, A. E.; Zheng, B.; Halas, N. J.; Nordlander, P.; Link, S., High Chromaticity Aluminum Plasmonic Pixels for Active Liquid Crystal Displays. *ACS Nano* **2016**, 10 (1), 1108-1117.

59. Ross, M. B.; Schatz, G. C., Aluminum and Indium Plasmonic Nanoantennas in the Ultraviolet. *J. Phys. Chem. C* **2014**, 118 (23), 12506-12514.

60. Chan, G. H.; Zhao, J.; Schatz, G. C.; Duyne, R. P. V., Localized Surface Plasmon Resonance Spectroscopy of Triangular Aluminum Nanoparticles. *J. Phys. Chem. C* **2008**, 112 (36), 13958-13963.

61. Langhammer, C.; Schwind, M.; Kasemo, B.; Zorić, I., Localized Surface Plasmon Resonances in Aluminum Nanodisks. *Nano Lett.* **2008**, 8 (5), 1461-1471.

62. Hutchison, J. A.; Liscio, A.; Schwartz, T.; Canaguier-Durand, A.; Genet, C.; Palermo, V.; Samorì, P.; Ebbesen, T. W., Tuning the Work-Function Via Strong Coupling. *Adv. Mater.* **2013**, 25 (17), 2481-2485.

63. Hutchison, J. A.; Schwartz, T.; Genet, C.; Devaux, E.; Ebbesen, T. W., Modifying Chemical Landscapes by Coupling to Vacuum Fields. *Angew. Chem. Int. Ed.* **2012**, 51 (7), 1592-1596.

64. Schwartz, T.; Hutchison, J. A.; Genet, C.; Ebbesen, T. W., Reversible Switching of Ultrastrong Light-Molecule Coupling. *Phys. Rev. Lett.* **2011**, 106 (19), 196405.

65. Khitrova, G.; Gibbs, H. M.; Kira, M.; Koch, S. W.; Scherer, A., Vacuum Rabi splitting in semiconductors. *Nat. Phys.* **2006**, 2 (2), 81-90.

66. Savasta, S.; Saija, R.; Ridolfo, A.; Di Stefano, O.; Denti, P.; Borghese, F., Nanopolaritons: Vacuum Rabi Splitting with a Single Quantum Dot in the Center of a Dimer Nanoantenna. *ACS Nano* 20**10**, 4 (11), 6369-6376.

67. Baudrion, A.-L.; Perron, A.; Veltri, A.; Bouhelier, A.; Adam, P.-M.; Bachelot, R., Reversible Strong Coupling in Silver Nanoparticle Arrays Using Photochromic Molecules. *Nano Lett.* **2013**, 13 (1), 282-286.

68. Wang, M.; Bangalore Rajeeva, B.; Scarabelli, L.; Perillo, E. P.; Dunn, A. K.; Liz-Marzán, L. M.; Zheng, Y., Molecular-Fluorescence Enhancement via Blue-Shifted Plasmon-Induced Resonance Energy Transfer. *J. Phys. Chem. C* **2016**, 120 (27), 14820-14827.

69. Klajn, R., Spiropyran-based dynamic materials. *Chem. Soc. Rev.* **2014**, 43 (1), 148-184.

Chapter 5

1. Holzmeister, P.; Pibiri, E.; Schmied, J. J.; Sen, T.; Acuna, G. P.; Tinnefeld, P., Quantum yield and excitation rate of single molecules close to metallic nanostructures. *Nat. Commun.* **2014**, 5, 5356.

2. Fu, Y.; Zhang, J.; Lakowicz, J. R., Plasmon-Enhanced Fluorescence from Single Fluorophores End-Linked to Gold Nanorods. *J. Am. Chem. Soc.* **2010**, 132 (16), 5540-5541.

3. Ming, T.; Zhao, L.; Yang, Z.; Chen, H.; Sun, L.; Wang, J.; Yan, C., Strong Polarization Dependence of Plasmon-Enhanced Fluorescence on Single Gold Nanorods. *Nano Lett.* **2009**, 9 (11), 3896-3903.

4. Tovmachenko, O. G.; Graf, C.; van den Heuvel, D. J.; van Blaaderen, A.; Gerritsen, H. C., Fluorescence Enhancement by Metal-Core/Silica-Shell Nanoparticles. *Adv. Mater.* **2006**, 18 (1), 91-95.

5. Tam, F.; Goodrich, G. P.; Johnson, B. R.; Halas, N. J., Plasmonic Enhancement of Molecular Fluorescence. *Nano Lett.* **2007**, 7 (2), 496-501.

6. Kinkhabwala, A.; Yu, Z.; Fan, S.; Avlasevich, Y.; Mullen, K.; Moerner, W. E., Large single-molecule fluorescence enhancements produced by a bowtie nanoantenna. *Nat. Photonics* **2009**, 3 (11), 654-657.

7. Akselrod, G. M.; Argyropoulos, C.; Hoang, T. B.; Ciracì, C.; Fang, C.; Huang, J.; Smith, D. R.; Mikkelsen, M. H., Probing the mechanisms of large Purcell enhancement in plasmonic nanoantennas. *Nat. Photonics* **2014**, 8 (11), 835-840.

8. Rose, A.; Hoang, T. B.; McGuire, F.; Mock, J. J.; Ciracì, C.; Smith, D. R.; Mikkelsen, M. H., Control of Radiative Processes Using Tunable Plasmonic Nanopatch Antennas. *Nano Lett.* **2014**, 14 (8), 4797-4802.

9. Pelton, M., Modified spontaneous emission in nanophotonic structures. *Nat. Photonics* **2015**, 9 (7), 427-435.

10. Anger, P.; Bharadwaj, P.; Novotny, L., Enhancement and Quenching of Single-Molecule Fluorescence. *Phys. Rev. Lett.* **2006**, 96 (11), 113002.

11. Gorner, H., Photochromism of nitrospiropyrans: effects of structure, solvent and temperature. *Phys. Chem. Chem. Phys.* **2001**, 3 (3), 416-423.

12. Chibisov, A. K.; Görner, H., Singlet versus triplet photoprocesses in indodicarbocyanine dyes and spiropyran-derived merocyanines. *J. Photochem. Photobiol., A* **1997**, 105 (2), 261-267.

13. Klajn, R., Spiropyran-based dynamic materials. *Chem. Soc. Rev.* **2014**, 43 (1), 148-184.

14. Ming, T.; Zhao, L.; Xiao, M.; Wang, J., Resonance-Coupling-Based Plasmonic Switches. *Small* **2010**, 6 (22), 2514-2519.

15. Kita, F.; Adam, W.; Jordan, P.; Nau, W. M.; Wirz, J., 1,3-Cyclopentanediyl Diradicals: Substituent and Temperature Dependence of Triplet−Singlet Intersystem Crossing. *J. Am. Chem. Soc.* **1999**, 121 (40), 9265-9275.

16. Cogan, S.; Haas, Y.; Zilberg, S., Intersystem crossing at singlet conical intersections. *J. Photochem. Photobiol., A* **2007**, 190 (2–3), 200-206.

17. Salem, L.; Rowland, C., The Electronic Properties of Diradicals. *Angew. Chem. Int. Ed.* **1972**, 11 (2), 92-111.

18. Scarabelli, L.; Coronado-Puchau, M.; Giner-Casares, J. J.; Langer, J.; Liz-Marzán, L. M., Monodisperse Gold Nanotriangles: Size Control, Large-Scale Self-Assembly, and Performance in Surface-Enhanced Raman Scattering. *ACS Nano* **2014**, 8 (6), 5833-5842.

19. Johnson, P. B.; Christy, R. W., Optical Constants of the Noble Metals. *Phys. Rev. B* **1972**, 6 (12), 4370-4379.

20. M. J. Frisch, G. W. T., H. B. Schlegel, G. E. Scuseria, M. A. Robb, J. R. Cheeseman, G. Scalmani, V. Barone, B. Mennucci, G. A. Petersson, H. Nakatsuji, M. Caricato, X. Li, H. P. Hratchian, A. F. Izmaylov, J. Bloino, G. Zheng, J. L. Sonnenberg, M. Hada, M. Ehara, K. Toyota, R. Fukuda, J. Hasegawa, M. Ishida, T. Nakajima, Y. Honda, O. Kitao, H. Nakai, T. Vreven, J.A.Montgomery,J. E. Peralta,F.Ogliaro, M. Bearpark,J.J.Heyd, E. Brothers,K.N.Kudin, V.N. Staroverov, T. Keith, R. Kobayashi, J. Normald, K. Raghavachari, A. Rendell, J. C. Burant,S.S.Iyengar, J. Tomasi, M. Cossi,N.Rega, J. M. Millam, M. Klene, J. E. Knox, J. B. Cross, V. Bakken, C. Adamo, J. Jaramillo,R.Gomperts,R. E.Stratmann,O. Yazyev,A.J.Austin, R. Cammi, C. Pomelli, J. W. Ochterski, R. L. Martin, K. Morokuma,V. G. Zakrzewski, G. A. Voth,P.Salvador, J. J. Dannenberg,S.Dapprich, A. D. Daniels, O. Farkas,J.B. Foresman,J.V.Ortiz, J.Cioslowskiand, D. J. Fox, Gaussian 09 Revis. C.01, Gaussian, Inc., Wallingord CT, 2010.

21. Perdew, J. P.; Burke, K.; Ernzerhof, M., Generalized Gradient Approximation Made Simple. *Phys. Rev. Lett.* **1996**, 77 (18), 3865-3868.

22. Becke, A. D., Density-functional thermochemistry. III. The role of exact exchange. *J. Chem. Phys.* **1993**, 98 (7), 5648-5652.

23. Mennucci, B.; Cancès, E.; Tomasi, J., Evaluation of Solvent Effects in Isotropic and Anisotropic Dielectrics and in Ionic Solutions with a Unified Integral Equation Method: Theoretical Bases, Computational Implementation, and Numerical Applications. *J. Phys. Chem. B* **1997**, 101 (49), 10506-10517.

24. Sean C. Warren, A. M., Dominic Alibhai, Douglas J. Kelly, Clifford Talbot, Yuriy Alexandrov, Ian Munro, Matilda Katan, Chris Dunsby, Paul M. W. French *PLoS ONE* **2013**, 8, e70687.

25. Wang, M.; Bangalore Rajeeva, B.; Scarabelli, L.; Perillo, E. P.; Dunn, A. K.; Liz-Marzán, L. M.; Zheng, Y., Molecular-Fluorescence Enhancement via Blue-Shifted Plasmon-Induced Resonance Energy Transfer. *J. Phys. Chem. C* **2016**, 120 (27), 14820-14827.

26. Zhu, M.-Q.; Zhu, L.; Han, J. J.; Wu, W.; Hurst, J. K.; Li, A. D. Q., Spiropyran-Based Photochromic Polymer Nanoparticles with Optically Switchable Luminescence. *J. Am. Chem. Soc.* **2006**, 128 (13), 4303-4309.

27. Xue, Y.; Tian, J.; Tian, W.; Gong, P.; Dai, J.; Wang, X., Significant Fluorescence Enhancement of Spiropyran in Colloidal Dispersion and Its Light-Induced Size Tunability for Release Control. *J. Phys. Chem. C* **2015**, 119 (35), 20762-20772.

28. Tian, W.; Tian, J., Synergy of Different Fluorescent Enhancement Effects on Spiropyran Appended onto Cellulose. *Langmuir* **2014**, 30 (11), 3223-3227.

29. Song, X.; Zhou, J.; Li, Y.; Tang, Y., Correlations between solvatochromism, Lewis acid-base equilibrium and photochromism of an indoline spiropyran. *J. Photochem. Photobiol., A* **1995**, 92 (1), 99-103.

30. Wu, Y.; Sasaki, T.; Kazushi, K.; Seo, T.; Sakurai, K., Interactions between Spiropyrans and Room-Temperature Ionic Liquids: Photochromism and Solvatochromism. *J. Phys. Chem. B* **2008**, 112 (25), 7530-7536.

31. Rosario, R.; Gust, D.; Hayes, M.; Springer, J.; Garcia, A. A., Solvatochromic Study of the Microenvironment of Surface-Bound Spiropyrans. *Langmuir* **2003**, 19 (21), 8801-8806.

32. Wojtyk, J. T. C.; Wasey, A.; Kazmaier, P. M.; Hoz, S.; Buncel, E., Thermal Reversion Mechanism of N-Functionalized Merocyanines to Spiropyrans: A Solvatochromic, Solvatokinetic, and Semiempirical Study. *J. Phys. Chem. A* **2000**, 104 (39), 9046-9055.

33. Bharadwaj, P.; Novotny, L., Spectral dependence of single molecule fluorescence enhancement. *Opt. Express* **2007**, 15 (21), 14266-14274.

34. Xiong, Y.; McLellan, J. M.; Chen, J.; Yin, Y.; Li, Z.-Y.; Xia, Y., Kinetically Controlled Synthesis of Triangular and Hexagonal Nanoplates of Palladium and Their SPR/SERS Properties. *J. Am. Chem. Soc.* **2005**, 127 (48), 17118-17127.

35. Rycenga, M.; Camargo, P. H. C.; Li, W.; Moran, C. H.; Xia, Y., Understanding the SERS Effects of Single Silver Nanoparticles and Their Dimers, One at a Time. *J. Phys. Chem. Lett.* **2010**, 1 (4), 696-703.

36. Sun, Y.; Xia, Y., Shape-Controlled Synthesis of Gold and Silver Nanoparticles. *Science* **2002**, 298 (5601), 2176-2179.

37. Wustholz, K. L.; Henry, A.-I.; McMahon, J. M.; Freeman, R. G.; Valley, N.; Piotti, M. E.; Natan, M. J.; Schatz, G. C.; Duyne, R. P. V., Structure−Activity Relationships in Gold Nanoparticle Dimers and Trimers for Surface-Enhanced Raman Spectroscopy. *J. Am. Chem. Soc.* **2010**, 132 (31), 10903-10910.

38. Kühn, S.; Håkanson, U.; Rogobete, L.; Sandoghdar, V., Enhancement of Single-Molecule Fluorescence Using a Gold Nanoparticle as an Optical Nanoantenna. *Phys. Rev. Lett.* **2006**, 97 (1), 017402.

39. Kleinman, S. L.; Sharma, B.; Blaber, M. G.; Henry, A.-I.; Valley, N.; Freeman, R. G.; Natan, M. J.; Schatz, G. C.; Van Duyne, R. P., Structure Enhancement Factor Relationships in Single Gold Nanoantennas by Surface-Enhanced Raman Excitation Spectroscopy. *J. Am. Chem. Soc.* **2013**, 135 (1), 301-308.

40. Kleinman, S. L.; Frontiera, R. R.; Henry, A.-I.; Dieringer, J. A.; Van Duyne, R. P., Creating, characterizing, and controlling chemistry with SERS hot spots. *Phys. Chem. Chem. Phys.* **2013**, 15 (1), 21-36.

41. Camden, J. P.; Dieringer, J. A.; Wang, Y.; Masiello, D. J.; Marks, L. D.; Schatz, G. C.; Van Duyne, R. P., Probing the Structure of Single-Molecule Surface-Enhanced Raman Scattering Hot Spots. *J. Am. Chem. Soc.* **2008**, 130 (38), 12616-12617.

42. Pazos-Perez, N.; Wagner, C. S.; Romo-Herrera, J. M.; Liz-Marzán, L. M.; García de Abajo, F. J.; Wittemann, A.; Fery, A.; Alvarez-Puebla, R. A., Organized Plasmonic Clusters with High Coordination Number and Extraordinary Enhancement in Surface-Enhanced Raman Scattering (SERS). *Angew. Chem. Int. Ed.* **2012**, 51 (51), 12688-12693.

43. Perillo, E. P.; Liu, Y.-L.; Huynh, K.; Liu, C.; Chou, C.-K.; Hung, M.-C.; Yeh, H.-C.; Dunn, A. K., Deep and high-resolution three-dimensional tracking of single particles using nonlinear and multiplexed illumination. *Nat. Commun.* **2015**, 6, 7874.

44. Zhu, M.-Q.; Zhang, G.-F.; Li, C.; Aldred, M. P.; Chang, E.; Drezek, R. A.; Li, A. D. Q., Reversible Two-Photon Photoswitching and Two-Photon Imaging of Immunofunctionalized Nanoparticles Targeted to Cancer Cells. *J. Am. Chem. Soc.* **2011**, 133 (2), 365-372.

45. Zhu, M.-Q.; Zhang, G.-F.; Hu, Z.; Aldred, M. P.; Li, C.; Gong, W.-L.; Chen, T.; Huang, Z.-L.; Liu, S., Reversible Fluorescence Switching of Spiropyran-Conjugated Biodegradable Nanoparticles for Super-Resolution Fluorescence Imaging. *Macromolecules* **2014**, 47 (5), 1543-1552.

46. Berkovic, G.; Krongauz, V.; Weiss, V., Spiropyrans and Spirooxazines for Memories and Switches. *Chem. Rev.* **2000**, 100 (5), 1741-1754.

Chapter 6

1. Frimmer, M.; Coenen, T.; Koenderink, A. F., Signature of a Fano Resonance in a Plasmonic Metamolecule's Local Density of Optical States. *Phys. Rev. Lett.* **2012**, 108 (7), 077404.

2. Zhang, W.; Govorov, A. O., Quantum theory of the nonlinear Fano effect in hybrid metal-semiconductor nanostructures: The case of strong nonlinearity. *Phys. Rev. B* **2011**, 84 (8), 081405.

3. Ridolfo, A.; Di Stefano, O.; Fina, N.; Saija, R.; Savasta, S., Quantum Plasmonics with Quantum Dot-Metal Nanoparticle Molecules: Influence of the Fano Effect on Photon Statistics. *Phys. Rev. Lett.* **2010**, 105 (26), 263601.

4. Miroshnichenko, A. E.; Flach, S.; Kivshar, Y. S., Fano resonances in nanoscale structures. *Rev. Mod. Phys.* **2010**, 82 (3), 2257-2298.

5. Luk'yanchuk, B.; Zheludev, N. I.; Maier, S. A.; Halas, N. J.; Nordlander, P.; Giessen, H.; Chong, C. T., The Fano resonance in plasmonic nanostructures and metamaterials. *Nat. Mater.* **2010**, 9, 707.

6. Lassiter, J. B.; Sobhani, H.; Fan, J. A.; Kundu, J.; Capasso, F.; Nordlander, P.; Halas, N. J., Fano Resonances in Plasmonic Nanoclusters: Geometrical and Chemical Tunability. *Nano Lett.* **2010**, 10 (8), 3184-3189.

7. Frontiera, R. R.; Gruenke, N. L.; Van Duyne, R. P., Fano-Like Resonances Arising from Long-Lived Molecule-Plasmon Interactions in Colloidal Nanoantennas. *Nano Lett.* **2012**, 12 (11), 5989-5994.

8. Bellessa, J.; Bonnand, C.; Plenet, J. C.; Mugnier, J., Strong Coupling between Surface Plasmons and Excitons in an Organic Semiconductor. *Phys. Rev. Lett.* **2004**, 93 (3), 036404.

9. Wurtz, G. A.; Evans, P. R.; Hendren, W.; Atkinson, R.; Dickson, W.; Pollard, R. J.; Zayats, A. V.; Harrison, W.; Bower, C., Molecular Plasmonics with Tunable Exciton−Plasmon Coupling Strength in J-Aggregate Hybridized Au Nanorod Assemblies. *Nano Lett.* **2007**, 7 (5), 1297-1303.

10. Roller, E.-M.; Argyropoulos, C.; Högele, A.; Liedl, T.; Pilo-Pais, M., Plasmon–Exciton Coupling Using DNA Templates. *Nano Lett.* 2016, 16 (9), 5962-5966.

11. Balci, S.; Kocabas, C.; Ates, S.; Karademir, E.; Salihoglu, O.; Aydinli, A., Tuning surface plasmon-exciton coupling via thickness dependent plasmon damping. *Phys. Rev. B* **2012**, 86 (23), 235402.

12. Ni, W.; Ambjörnsson, T.; Apell, S. P.; Chen, H.; Wang, J., Observing Plasmonic−Molecular Resonance Coupling on Single Gold Nanorods. *Nano Lett.* **2010**, 10 (1), 77-84.

13. Lin, L.; Wang, M.; Wei, X.; Peng, X.; Xie, C.; Zheng, Y., Photoswitchable Rabi Splitting in Hybrid Plasmon–Waveguide Modes. *Nano Lett.* **2016**, 16 (12), 7655-7663.

14. Li, J.; Cushing, S. K.; Meng, F.; Senty, T. R.; Bristow, A. D.; Wu, N., Plasmon-induced resonance energy transfer for solar energy conversion. *Nat. Photonics* **2015**, 9, 601.

15. Liu, G. L.; Long, Y.-T.; Choi, Y.; Kang, T.; Lee, L. P., Quantized plasmon quenching dips nanospectroscopy via plasmon resonance energy transfer. *Nat. Methods* **2007**, 4, 1015.

16. Wang, M.; Bangalore Rajeeva, B.; Scarabelli, L.; Perillo, E. P.; Dunn, A. K.; Liz-Marzán, L. M.; Zheng, Y., Molecular-Fluorescence Enhancement via Blue-Shifted Plasmon-Induced Resonance Energy Transfer. *J. Phys. Chem. C* **2016**, 120 (27), 14820-14827.

17. Ming, T.; Zhao, L.; Yang, Z.; Chen, H.; Sun, L.; Wang, J.; Yan, C., Strong Polarization Dependence of Plasmon-Enhanced Fluorescence on Single Gold Nanorods. *Nano Lett.* **2009**, 9 (11), 3896-3903.

18. Wang, M.; Hartmann, G.; Wu, Z.; Scarabelli, L.; Rajeeva, B. B.; Jarrett, J. W.; Perillo, E. P.; Dunn, A. K.; Liz-Marzán, L. M.; Hwang, G. S.; Zheng, Y., Controlling Plasmon-Enhanced Fluorescence via Intersystem Crossing in Photoswitchable Molecules. *Small* **2017**, 13 (38), 1701763.

19. Akselrod, G. M.; Argyropoulos, C.; Hoang, T. B.; Ciracì, C.; Fang, C.; Huang, J.; Smith, D. R.; Mikkelsen, M. H., Probing the mechanisms of large Purcell enhancement in plasmonic nanoantennas. *Nat. Photonics* **2014**, 8, 835.

20. Luk'yanchuk, B.; Zheludev, N. I.; Maier, S. A.; Halas, N. J.; Nordlander, P.; Giessen, H.; Chong, C. T., The Fano resonance in plasmonic nanostructures and metamaterials. *Nat. Mater.* **2010**, 9 (9), 707-715.

21. Chikkaraddy, R.; de Nijs, B.; Benz, F.; Barrow, S. J.; Scherman, O. A.; Rosta, E.; Demetriadou, A.; Fox, P.; Hess, O.; Baumberg, J. J., Single-molecule strong coupling at room temperature in plasmonic nanocavities. *Nature* **2016**, 535 (7610), 127-130.

22. Giannini, V.; Fernández-Domínguez, A. I.; Heck, S. C.; Maier, S. A., Plasmonic Nanoantennas: Fundamentals and Their Use in Controlling the Radiative Properties of Nanoemitters. *Chem. Rev.* **2011**, 111 (6), 3888-3912.

23. Fofang, N. T.; Grady, N. K.; Fan, Z.; Govorov, A. O.; Halas, N. J., Plexciton Dynamics: Exciton−Plasmon Coupling in a J-Aggregate−Au Nanoshell Complex Provides a Mechanism for Nonlinearity. *Nano Lett.* **2011**, 11 (4), 1556-1560.

24. DeLacy, B. G.; Miller, O. D.; Hsu, C. W.; Zander, Z.; Lacey, S.; Yagloski, R.; Fountain, A. W.; Valdes, E.; Anquillare, E.; Soljačić, M.; Johnson, S. G.;

Joannopoulos, J. D., Coherent Plasmon-Exciton Coupling in Silver Platelet-J-aggregate Nanocomposites. *Nano Lett.* **2015**, 15 (4), 2588-2593.

25. Artuso, R. D.; Bryant, G. W., Optical Response of Strongly Coupled Quantum Dot−Metal Nanoparticle Systems: Double Peaked Fano Structure and Bistability. *Nano Lett.* **2008**, 8 (7), 2106-2111.

26. Schlather, A. E.; Large, N.; Urban, A. S.; Nordlander, P.; Halas, N. J., Near-Field Mediated Plexcitonic Coupling and Giant Rabi Splitting in Individual Metallic Dimers. *Nano Lett.* **2013**, 13 (7), 3281-3286.

27. Fofang, N. T.; Park, T.-H.; Neumann, O.; Mirin, N. A.; Nordlander, P.; Halas, N. J., Plexcitonic Nanoparticles: Plasmon−Exciton Coupling in Nanoshell−J-Aggregate Complexes. *Nano Lett.* **2008**, 8 (10), 3481-3487.

28. Zheng, Y. B.; Juluri, B. K.; Lin Jensen, L.; Ahmed, D.; Lu, M.; Jensen, L.; Huang, T. J., Dynamic Tuning of Plasmon–Exciton Coupling in Arrays of Nanodisk–J-aggregate Complexes. *Adv. Mater.* **2010**, 22 (32), 3603-3607.

29. Ni, W.; Yang, Z.; Chen, H.; Li, L.; Wang, J., Coupling between Molecular and Plasmonic Resonances in Freestanding Dye−Gold Nanorod Hybrid Nanostructures. *J. Am. Chem. Soc.* **2008**, 130 (21), 6692-6693.

30. Nan, F.; Zhang, Y.-F.; Li, X.; Zhang, X.-T.; Li, H.; Zhang, X.; Jiang, R.; Wang, J.; Zhang, W.; Zhou, L.; Wang, J.-H.; Wang, Q.-Q.; Zhang, Z., Unusual and Tunable One-Photon Nonlinearity in Gold-Dye Plexcitonic Fano Systems. *Nano Lett.* **2015**, 15 (4), 2705-2710.

31. Zhang, W.; Govorov, A. O.; Bryant, G. W., Semiconductor-Metal Nanoparticle Molecules: Hybrid Excitons and the Nonlinear Fano Effect. *Phys. Rev. Lett.* **2006**, 97 (14), 146804.

32. Zengin, G.; Wersäll, M.; Nilsson, S.; Antosiewicz, T. J.; Käll, M.; Shegai, T., Realizing Strong Light-Matter Interactions between Single-Nanoparticle Plasmons and Molecular Excitons at Ambient Conditions. *Phys. Rev. Lett.* **2015**, 114 (15), 157401.

33. Manjavacas, A.; Abajo, F. J. G. d.; Nordlander, P., Quantum Plexcitonics: Strongly Interacting Plasmons and Excitons. *Nano Lett.* **2011**, 11 (6), 2318-2323.

34. Wang, Q. H.; Kalantar-Zadeh, K.; Kis, A.; Coleman, J. N.; Strano, M. S., Electronics and optoelectronics of two-dimensional transition metal dichalcogenides. *Nat. Nanotechnol.* **2012**, 7 (11), 699-712.

35. Jariwala, D.; Sangwan, V. K.; Lauhon, L. J.; Marks, T. J.; Hersam, M. C., Emerging Device Applications for Semiconducting Two-Dimensional Transition Metal Dichalcogenides. *ACS Nano* **2014**, 8 (2), 1102-1120.

36. Abid, I.; Chen, W.; Yuan, J.; Bohloul, A.; Najmaei, S.; Avendano, C.; Péchou, R.; Mlayah, A.; Lou, J., Temperature-Dependent Plasmon–Exciton Interactions in Hybrid Au/$MoSe_2$ Nanostructures. *ACS Photonics* **2017**, 4 (7), 1653-1660.

37. Koperski, M.; Molas Maciej, R.; Arora, A.; Nogajewski, K.; Slobodeniuk Artur, O.; Faugeras, C.; Potemski, M., Optical properties of atomically thin transition metal dichalcogenides: observations and puzzles. *Nanophotonics* **2017**, 6(6), 1289–1308.

38. Manzeli, S.; Ovchinnikov, D.; Pasquier, D.; Yazyev, O. V.; Kis, A., 2D transition metal dichalcogenides. *Nat. Rev. Mater.* **2017**, 2, 17033.

39. Mak, K. F.; Shan, J., Photonics and optoelectronics of 2D semiconductor transition metal dichalcogenides. *Nat. Photonics* **2016**, 10 (4), 216-226.

40. Wen, J.; Wang, H.; Wang, W.; Deng, Z.; Zhuang, C.; Zhang, Y.; Liu, F.; She, J.; Chen, J.; Chen, H.; Deng, S.; Xu, N., Room-Temperature Strong Light–Matter Interaction with Active Control in Single Plasmonic Nanorod Coupled with Two-Dimensional Atomic Crystals. *Nano Lett.* **2017**, 17 (8), 4689-4697.

41. Carozo, V.; Wang, Y.; Fujisawa, K.; Carvalho, B. R.; McCreary, A.; Feng, S.; Lin, Z.; Zhou, C.; Perea-López, N.; Elías, A. L.; Kabius, B.; Crespi, V. H.; Terrones, M., Optical identification of sulfur vacancies: Bound excitons at the edges of monolayer tungsten disulfide. *Sci. Adv.* **2017**, 3 (4).

42. Zhang, Y.; Zhang, Y.; Ji, Q.; Ju, J.; Yuan, H.; Shi, J.; Gao, T.; Ma, D.; Liu, M.; Chen, Y.; Song, X.; Hwang, H. Y.; Cui, Y.; Liu, Z., Controlled Growth of High-Quality Monolayer WS2 Layers on Sapphire and Imaging Its Grain Boundary. *ACS Nano* **20**13, 7 (10), 8963-8971.

43. Cong, C.; Shang, J.; Wu, X.; Cao, B.; Peimyoo, N.; Qiu, C.; Sun, L.; Yu, T., Synthesis and Optical Properties of Large-Area Single-Crystalline 2D Semiconductor WS2 Monolayer from Chemical Vapor Deposition. *Adv. Opt. Mater.* **2014**, 2 (2), 131-136.

44. Terrones, H.; Corro, E. D.; Feng, S.; Poumirol, J. M.; Rhodes, D.; Smirnov, D.; Pradhan, N. R.; Lin, Z.; Nguyen, M. A. T.; Elías, A. L.; Mallouk, T. E.; Balicas, L.; Pimenta, M. A.; Terrones, M., New First Order Raman-active Modes in Few Layered Transition Metal Dichalcogenides. *Sci. Rep.* **2014**, 4, 4215.

45. Berkdemir, A.; Gutiérrez, H. R.; Botello-Méndez, A. R.; Perea-López, N.; Elías, A. L.; Chia, C.-I.; Wang, B.; Crespi, V. H.; López-Urías, F.; Charlier, J.-C.; Terrones, H.; Terrones, M., Identification of individual and few layers of WS_2 using Raman Spectroscopy. *Sci. Rep.* **2013**, 3, 1755.

46. Scarabelli, L.; Coronado-Puchau, M.; Giner-Casares, J. J.; Langer, J.; Liz-Marzán, L. M., Monodisperse Gold Nanotriangles: Size Control, Large-Scale Self-Assembly, and Performance in Surface-Enhanced Raman Scattering. *ACS Nano* **2014**, 8 (6), 5833-5842.

47. Shafiei, F.; Monticone, F.; Le, K. Q.; Liu, X.-X.; Hartsfield, T.; Alu, A.; Li, X., A subwavelength plasmonic metamolecule exhibiting magnetic-based optical Fano resonance. *Nat. Nanotechnol.* **2013**, 8 (2), 95-99.

48. Argyropoulos, C.; Monticone, F.; D'Aguanno, G.; Alù, A., Plasmonic nanoparticles and metasurfaces to realize Fano spectra at ultraviolet wavelengths. *Appl. Phys. Lett.* **2013**, 103 (14), 143113.

49. Mao, N.; Chen, Y.; Liu, D.; Zhang, J.; Xie, L., Solvatochromic Effect on the Photoluminescence of MoS_2 Monolayers. *Small* **2013**, 9 (8), 1312-1315.

50. Lin, Y.; Ling, X.; Yu, L.; Huang, S.; Hsu, A. L.; Lee, Y.-H.; Kong, J.; Dresselhaus, M. S.; Palacios, T., Dielectric Screening of Excitons and Trions in Single-Layer MoS_2. *Nano Lett.* **2014**, 14 (10), 5569-5576.

51. Zhu, B.; Chen, X.; Cui, X., Exciton Binding Energy of Monolayer WS_2. *Sci. Rep.* **2015**, 5, 9218.

52. Anker, J. N.; Hall, W. P.; Lyandres, O.; Shah, N. C.; Zhao, J.; Van Duyne, R. P., Biosensing with plasmonic nanosensors. *Nat. Mater.* **2008**, 7 (6), 442-453.

53. Gallinet, B.; Martin, O. J. F., Influence of Electromagnetic Interactions on the Line Shape of Plasmonic Fano Resonances. *ACS Nano* **2011**, 5 (11), 8999-9008.

54. Gallinet, B.; Martin, O. J. F., Ab initio. *Phys. Rev. B* **2011**, 83 (23), 235427.

55. Fano, U., Effects of Configuration Interaction on Intensities and Phase Shifts. P*hys. Rev.* **1961**, 124 (6), 1866-1878.

56. Tang, T.-T.; Zhang, Y.; Park, C.-H.; Geng, B.; Girit, C.; Hao, Z.; Martin, M. C.; Zettl, A.; Crommie, M. F.; Louie, S. G.; Shen, Y. R.; Wang, F., A tunable phonon-exciton Fano system in bilayer graphene. *Nat. Nanotechnol.* **2010**, 5 (1), 32-36.

57. Mathieu, H.; Lefebvre, P.; Christol, P., Simple analytical method for calculating exciton binding energies in semiconductor quantum wells. P*hys. Rev. B* **1992**, 46 (7), 4092-4101.

58. Baranov, D. G.; Savelev, R. S.; Li, S. V.; Krasnok, A. E.; Alù, A., Modifying magnetic dipole spontaneous emission with nanophotonic structures. *Laser Photonics Rev.* **2017,** 11 (3), 1600268.

59. Krasnok, A. E.; Slobozhanyuk, A. P.; Simovski, C. R.; Tretyakov, S. A.; Poddubny, A. N.; Miroshnichenko, A. E.; Kivshar, Y. S.; Belov, P. A., An antenna model for the Purcell effect. *Sci. Rep.* **2015**, 5, 12956.

60. Wu, X.; Gray, S. K.; Pelton, M., Quantum-dot-induced transparency in a nanoscale plasmonic resonator. *Opt. Express* **2010**, 18 (23), 23633-23645.

61. Zengin, G.; Johansson, G.; Johansson, P.; Antosiewicz, T. J.; Käll, M.; Shegai, T., Approaching the strong coupling limit in single plasmonic nanorods interacting with J-aggregates. *Sci. Rep.* **2013**, 3, 3074.

62. Kelly, C.; Khosravi Khorashad, L.; Gadegaard, N.; Barron, L. D.; Govorov, A. O.; Karimullah, A. S.; Kadodwala, M., Controlling Metamaterial Transparency with Superchiral Fields. *ACS Photonics* **2018**, 5 (2), 535-543.

63. Riffe, D. M., Classical Fano oscillator. Phys. Rev. B **201**1, 84 (6), 064308.

64. Ott, C.; Kaldun, A.; Raith, P.; Meyer, K.; Laux, M.; Evers, J.; Keitel, C. H.; Greene, C. H.; Pfeifer, T., Lorentz Meets Fano in Spectral Line Shapes: A Universal Phase and Its Laser Control. *Science* **2013**, 340 (6133), 716.

65. Limonov, M. F.; Rybin, M. V.; Poddubny, A. N.; Kivshar, Y. S., Fano resonances in photonics. *Nat. Photonics* **2017**, 11, 543.

66. Baranov, D. G.; Wersäll, M.; Cuadra, J.; Antosiewicz, T. J.; Shegai, T., Novel Nanostructures and Materials for Strong Light–Matter Interactions. *ACS Photonics* **2018**, 5 (1), 24–4.

67. Törmä, P.; Barnes, W. L., Strong coupling between surface plasmon polaritons and emitters: a review. *Rep. Prog. Phys.* **2015**, 78 (1), 013901.

68. Tserkezis, C.; Wubs, M.; Mortensen, N. A., Robustness of the Rabi Splitting under Nonlocal Corrections in Plexcitonics. *ACS Photonics* **2017**.

69. Argyropoulos, C.; Chen, P.-Y.; Monticone, F.; D'Aguanno, G.; Alù, A., Nonlinear Plasmonic Cloaks to Realize Giant All-Optical Scattering Switching. *Phys. Rev. Lett.* **2012**, 108 (26), 263905.

70. Sun, Z.; Martinez, A.; Wang, F., Optical modulators with 2D layered materials. *Nat. Photonics* **2016**, 10 (4), 227-238.